DE-CORRELATION OF TROPOSPHERIC ERROR AND HEIGHT COMPONENT ON GNSS USING COMBINED ZENITH-DEPENDENT PARAMETER

YONG-WON AHN

December 2016

TECHNICAL REPORT
NO. 306

DE-CORRELATION OF TROPOSPHERIC ERROR AND HEIGHT COMPONENT ON GNSS USING COMBINED ZENITH-DEPENDENT PARAMETER

Yong-Won Ahn

Department of Geodesy and Geomatics Engineering
University of New Brunswick
P.O. Box 4400
Fredericton, N.B.
Canada
E3B 5A3

December 2016

PREFACE

This technical report is a reproduction of a dissertation submitted in partial fulfillment of the requirements for the degree of Doctor of Philosophy in the Department of Geodesy and Geomatics Engineering, December 2016. The research was supervised by Dr. Peter Dare, and funding was provided primarily by the Natural Sciences and Engineering Research Council of Canada (NSERC) Strategic Project Grants and Discovery Grants Programs.

As with any copyrighted material, permission to reprint or quote extensively from this report must be received from the author. The citation to this work should appear as follows:

Ahn, Yong-Won (2016). *De-Correlation of Tropospheric Error and Height Component on GNSS Using Combined Zenith-Dependent Parameter*. Ph.D. dissertation, Department of Geodesy and Geomatics Engineering, Technical Report No. 306, University of New Brunswick, Fredericton, New Brunswick, Canada, 222 pp.

Dedication

For my daughter, Chelsea

Abstract

For high precision GNSS positioning, the troposphere is one of the most problematic error sources. Typically, the effect is minimal due to the spatio-temporal correlation when the baseline length is short enough in the relative positioning scenario. When a strong tropospheric anomaly effect is present, the problem can be much more complicated and the resultant positioning solution is typically no longer precise even for a baseline of a few kilometres in length. As the troposphere delay and height estimates are almost linearly correlated above a 20° elevation angle, the problem exists of how to de-correlate these two parameters to avoid such ill-conditioned cases.

To obtain reliable height estimates, and avoid ill-conditioned cases, a new method is proposed in this dissertation: these two common zenith dependent parameters are combined into a single parameter plus weighting parameters. Once the parameters are combined and corresponding weighting parameters are determined, the vertical component can be retrieved.

The feasibility of the methodology is investigated in a kinematic situation. To determine the weighting coefficient in this case, the residuals in a least-square estimator are analyzed. As the residuals can be decomposed into two different realms, either troposphere or ionosphere, the magnitude of the residual contribution of the

troposphere for each satellite pair in the double difference can be determined. This value is further used to determine the weighting parameters. Through this new method, the common zenith-dependent parameters are found to be de-correlated. A number of data sets are processed and the results are analyzed, especially during severe inhomogeneous tropospheric conditions and under humid environments.

In summary, in a kinematic scenario, the achievement is shown to be up to 20% (4 cm to 3 cm rms) with processed data. Compared to the conventional approach, the degradation of the vertical component during an anomalous weather period is almost eliminated in kinematic scenarios, which is the main goal of the research described in this dissertation. This means that this new approach is resistant to an anomalous tropospheric event.

Acknowledgements

I would like to express my gratitude to those who have had significant positive impact on my life over the past few years, as follows:

- To my supervisor, Dr. Peter Dare. Without his help, I may not have been able to effectively continue my research and studies. He gave me constant guidance, assistance, and support. Whenever I discussed with him about my research, he raised many very good questions, and constantly tried his best to encourage me, and guide me in the right direction.

- To Dr. Richard B. Langley and Dr. Marcelo C. Santos for their useful comments and advice especially during weekly GNSS group meetings. Also, I would like to thank Dr. Don Kim for his suggestion and support for some years. I would like to thank Dr. Trevor Hanson in Civil Engineering at UNB and Dr. Ahmed El-Rabbany in Geomatics Engineering at Ryerson University for reviewing my dissertation and for making invaluable comments.

- To Dr. Drew Rendall and Dr. Rice Fuller for invaluable encouragement, help and support.

- To Dr. Peter Park and Dr. James Park at Korea Astronomy & Space Institute (KASI) in South Korea for their encouragement to achieve my goal.

- To Mr. Nick Kim and Mrs. Alica Kim for consistent encouragement and invaluable help.

- To Dr. Susan Nichols, Dr. Yun Zhang at UNB, Dr. Gérard Lachapelle at University of Calgary, and Dr. Andre B. Fletcher at Curtin University for their encouragement.

- To many of my invaluable friends and former colleagues. Too many to describe here, but, especially, Mr. Wentao Zhang at Qualcomm, Mr. Chaochao Wang at Garmin, Dr. Mustafa Berber at the California State University at Fresno, Dr. Eun-Hwan Shin at Samsung Semiconductor in California. They are all incredible to me. Dr. Hui Tang and Dr. Mazder Rahman for their invaluable help and inputs are very appreciative too.

Especially, I would like to acknowledge Canada′s Natural Sciences and Engineering Research Council (NSERC), Canada Foundation for Innovation (CFI) and the New Brunswick Innovation Foundation (NBIF) for support for the research. I also thank the Astronomical Institute of University of Bern for the Bernese software with its purchase supported by the Royal Institution of Chartered Surveyors (RICS) Education Trust.

I also thank to all of office staff of the Department of Geodesy and Geomatics Engineering, and especially to Mrs. Sylvia Whittaker, who was always available to help with a smile.

Finally, I wish to thank to my family, Chelsea and Stella, and my families in Korea, who encouraged me whenever I faced many difficulties during my studies, especially my brother, Dong-Won. I deeply appreciate all the support, encouragement, and love that were freely given to me.

Table of Contents

List of Tables

List of Figures

List of Symbols

k_1	$77.60 \pm 0.09\ ^\circ K/hPa$
k_2	$69.4 \pm 2.2\ ^\circ K/hPa$
$k_2^{'}$	$22.1 \pm 2.2\ ^\circ K/hPa$
k_3	$(3.701 \pm 0.012)\ 10^5\ ^\circ K^2/hPa$
$\rho_\circ$	A priori value for geometric distance between satellite and receiver
$x_\circ$	A priori values of parameters
$\sigma_\circ^2$	A priori variance of the observations
A_D	Amplitude of the direct signal
A_R	Amplitude of the reflected signal
δr_{ant}^s	Antenna phase centre offset and variations
$\delta \vec{r}_{r,ant}$	Antenna phase center offset and variations of station
X_{k0},Y_{k0},Z_{k0}	Approximate receiver positions in ECEF coordinate system (metres)
ω_{sat}	Argument of perigee
$\delta \vec{r}_{r,atm}$	Atmospheric loading, which is due to the weight of the atmosphere on the continental plate
T_{avg}	Average noise temperature of the source across the antenna reception pattern
α_{azi}	Azimuth

$T_\circ$	Cable's ambient temperature
Q_{ll}	Cofactor matrix
Q_{xx}	Cofactor matrix of the parameters
$\hat{l}$	Column matrix of adjusted observations
l'	Column matrix of observations
x_2, x_2°	Column vector with all ambiguity parameters and column vector with the a priori values of these parameters
x_1, x_1°	Column vector with all non-ambiguity parameters and column vector with the a priori values of these parameters
l	Column matrix of $'$observed-computed$'$ (O-C)
Ψ	Computed observables
α_{mul}	Damping factor ($0 \leq \alpha_{mul} \leq 1$)
t_{mw}	Day of year for maximum winter which is set to 28 days for the northern hemisphere and 211 for the southern hemisphere
ρ_{mk}^{pq}	DD geometric range (metres)
N_{mk}^{pq}	DD integer carrier phase ambiguities (cycles)
$\gamma_{km_\lambda}^{pq}$	DD phase residual between satellites p and q
$N_{km}^{pq}(1)$	DD operator ($= N_{km}^{p}(1) - N_{km}^{q}(1)$)
$\delta I_{km,\varphi}^{pq}(t)$	DD operator ($= \delta I_{km,\varphi}^{p}(t) - \delta I_{km,\varphi}^{q}(t)$)
$\delta T_{km}^{pq}(t)$	DD operator ($= \delta T_{km}^{p}(t) - \delta T_{km}^{q}(t)$)
$\delta \rho_{km,mul,\varphi}^{pq}(t)$	DD operator ($\delta \rho_{km,mul,\varphi}^{p}(t) - \delta \rho_{km,mul,\varphi}^{q}(t)$)
$\varepsilon_{km,err,\varphi}^{pq}$	DD operator ($= \varepsilon_{km,err,\varphi}^{p} - \varepsilon_{km,err,\varphi}^{q}$)
φ_{mk}^{pq}	DD phase observables (cycles): superscripts p and q stands for the satellites, and subscripts m and k for the receivers
$\delta T_{dry,mk}^{pq}$	DD slant hydrostatic (or dry) delay (meters)
$\delta t_{k,sys}$	Delays in receiver k and its antenna
$\delta t_{r,sys}$	Delays in receiver r and its antenna

δt^s_{sys}	Delays in satellite and its antenna
ρ_d	Density of dry air ($kg\ m^{-3}$)
T_d	Dew point temperature ($^\circ K$)
$M^i_{km_\lambda}$	Differential carrier multipath error for satellite i and frequency k
dH	Differential change in height (m)
dp	Differential change in pressure ($mbar$)
Δr	Differential distance to the satellite
dh	Differential increment in height
$\delta I^i \lambda_{km_\lambda}$	Differential ionosphere group delay at frequency k
$W^i_{km_\lambda}$	Differential receiver noise error for satellite i and frequency k
δT^i	Differential troposphere delay for satellite i
e_{sat}	Eccentricity of the satellite orbit
Δr	Error of a baseline length
$\hat{x}$	Estimated parameters
A_1, A_2	First design matrix of the parameters x_1 and x_2 involving partial derivatives
$\alpha_{sn} (= 1/L_{sn})$	Fractional attenuation ($0 \leq \alpha_{sn} \leq 1$) of a cable
f_{L1}	Frequency of the GPS signal (L1)
R_d	Gas constant for dry air
φ	Geodetic latitude
α_M	Geomagnetic azimuth
ϵ_M	Geomagnetic elevation angle
θ_M	Geomagnetic pole distance
ρ^s_r, ρ	Geometrical distance between a satellite and a receiver
$\rho^p_{k,L1}(t)$	Geometrical distance between satellite(p) and a receiver(k) for L1

G_{east}	Gradient in eastward direction
G_{north}	Gradient in northward direction
g	Gravitational constant on Earth surface
g	Gravity change with height (m/s^2)
$p_1, \cdots, p_d$	Gravity field coefficients, air drag and radiation pressure parameters, etc
q	Humidity ratio (kg_{water}/kg_{dryair})
$\delta T_{h,asym}$	Hydrostatic correction term taking asymmetry into account
$\delta T_{h,sym}$	Hydrostatic delay term under the assumption of symmetry in azimuth
Φ_{IF}	IF observables
x	Improvements to the a priori parameter values
i_{sat}	Inclination of the satellite orbit
$n(s)$	Index of refraction as function of the distance s
N_r^s	Integer ambiguity for receiver r and satellite s
N_k^p	Integer ambiguity for receiver k and satellite p
Z_d^{-1}, Z_w^{-1}	Inverse compressibility factors for dry and wet air which are empirical factors
δI	Ionospheric delay
H	Jacobi matrix
f_{L1}	L1 frequency
f_{L2}	L2 frequency
λ_{L1}	L1 wavelength (metres)
φ, H_{hgt}	Latitude and height of the station
Ω_{sat}	Longitude of ascending node
$m(\epsilon)$	Mapping function

a	Mapping function coefficient, separated into average value and amplitude
m_{da}	Mass of dry air (kg)
m_{wv}	Mass of water vapour (kg)
R_E	Mean radius of the Earth
T_m	Mean temperature of water vapour in $^\circ K$
h_m	Mean value for the height of the ionosphere
r_r	Mixing ratio
ψ	Model function (mathematical relationship between observations and parameters; observation equation)
M_d	Molar weight of dry air ($= 28.9644 kg\ kmol^{-1}$)
M_w	Molar weight of wet air ($= 18.0152 kg\ kmol^{-1}$)
$\delta\rho_{mul}$	Multipath
N	Normal equation matrix
$L - \Psi(x_1^\circ, x_2^\circ)$	Observed minus computed (O-C) double difference observables ($\equiv l$)
$\delta\vec{r}_{r,sol}$	Ocean loading, which is due to the weight of the water on the continental plate during high tide
ΔR	Orbital errors
$T_s, p_s, e_s, \beta, \lambda$	Parameters for UNB3 model
p_d	Partial pressure of dry air ($mbar$); $p_d = p - e$ with p being the total pressure
e_w	Partial pressure of water vapour ($mbar$)
$\varphi^p_{k,L1}(t)$	Phase observables between satellite(p) and receiver(k) for L1
Φ_{L1}, Φ_{L2}	Phase observables for L1 frequency, L2 frequency
Φ_D	Phase position of the direct signal

Φ_R	Phase shift of the reflected signal with respect to the phase of the direct signal
θ'_M	Pole distance
$\delta\vec{r}_{r,pol}$	Pole tides, which are caused by the reaction of the elastic Earth to the change of the rotation axis due to polar motion
$\vec{r}^{s}_{i,o}$	Position vector at the centre of mass
$P_\circ$	Pressure at the surface $h = 0$
P_H	Pressure at the surface $h = H$
$\vec{r}_{r,i}(t_r)$	Receiver position at reception time t_r in inertial system
$\vec{r}_{r,e}(t_r)$	Receiver position at time t_r in Earth-fixed system
ΔX_k,ΔY_k,ΔZ_k	Receiver position increments (metres)
k_1, k_2, k_3	Refraction constants ($^\circ K/mbar$,$^\circ K/mbar$,$^\circ K/mbar^2$)
N_t	Refractive index
H_{rh}, U_w	Relative humidity (%)
$\delta\rho_{rel}$	Relativistic corrections due to special and general relativity
τ_{mk}	Relative wet zenith delay (metres)
ε_{err}	Remaining measurement errors
v	Residuals
$\varepsilon^{pq}_{mk,err}$	Residual errors (e.g., receiver system noise)
δt^s	Satellite clock correction due to satellite clock error of s
δt^p	Satellite clock correction due to satellite clock error of p
a^p	Satellite frequency offset
$\vec{r}^{s}_{i}(t^s)$	Satellite position at emission time $t_s = t_r - \tau^s_r$ in inertial system
X^q,Y^q,Z^q	Satellite positions in Earth-centered Earth-fixed (ECEF) coordinate system (metres)
e_{sw}	Saturated water vapour pressure

a_{sat}	Semi-major axis of the satellite orbit
$\varphi^{i}_{km_\lambda}$	SD carrier-phase measurement for satellite i on frequency λ (in units of cycles)
m^{pq}_{k}	SD (between satellites) non-hydrostatic (or wet) mapping coefficient at the receiver k (unitless)
$N^{p}_{km}(1)$	SD operator $(= N^{p}_{k}(1) - N^{p}_{m}(1))$
$\delta I^{p}_{km,\varphi}(t)$	SD operator $(= \delta I^{p}_{k,\varphi}(t) - \delta I^{p}_{m,\varphi}(t))$
$\delta T^{p}_{km}(t)$	SD operator $(= \delta T^{p}_{k}(t) - \delta T^{p}_{m}(t))$
$\delta t_{km,sys,\varphi}(t)$	SD operator $(= \delta t_{k,sys,\varphi}(t) - \delta t_{m,sys,\varphi}(t))$
$\delta \rho^{p}_{km,mul,\varphi}(t)$	SD operator $(= \delta \rho^{p}_{k,mul,\varphi}(t) - \delta \rho^{p}_{m,mul,\varphi}(t))$
$\varepsilon^{p}_{km,err,\varphi}$	SD operator $(= \varepsilon^{p}_{k,err,\varphi} - \varepsilon^{p}_{m,err,\varphi})$
$\tau^{s}_{r} (= \rho^{s}_{r}/c)$	Signal travel time
φ_i	Site latitude
Ω_s	Solid angular extent of the noise source
$\delta \vec{r}_{r,sol}$	Solid Earth tides which are caused by the gravitational forces by Sun and Moon
R_d	Specific gas constant for dry air $(= 287.054 J\ mol^{-1}\ ^{\circ}K^{-1})$
c	Speed of light in vacuum
δt_r	Station clock correction for station r
δt_k	Station clock correction for station k
$\delta U(0)$	Station height component
$g_\circ$	Surface gravity
h_s	Surface height
p_s	Surface pressure
$T_\circ$	Surface temperature $(^{\circ}K)$
T_c	Temperature $(^{\circ}C)$
T	Temperature $(^{\circ}K)$

T_s	Temperature at surface (or antenna) height ($^\circ K$)
α_{lr}	Temperature lapse rate ($^\circ K/km$)
t_p	Time of perigee passage
ρ_t	Total density for dry and wet air ($kg\ m^{-3}$)
$\dot{\rho}^p_{k,L1}(t)$	Topocentric range rate
δT	Tropospheric delay
$\delta T(0)$	Troposphere parameter at zenith
R_o	Universal gas constant ($= 8.31434 J\ mol^{-1}\ ^\circ K^{-1}$)
$\vec{v}_{r,e}$	Velocity of the station
e_s	Water vapour pressure at the surface ($mbar$)
λ_{km_λ}	Wavelength of frequency λ
λ	Wavelength of the GPS signal (L1 or L2)
g_m	Weighted mean gravity acceleration
P	Weight matrix
$\delta T_{w,asym}$	Wet correction term taking asymmetry into account
$\delta T_{w,sym}$	Wet delay term under the assumption of symmetry in azimuth
z or z'	Zenith angle either at observing station or at IP

List of Abbreviations

A-GPS	**A**ssisted **GPS**
ACARS	**A**ircraft **C**ommunications, **A**ddressing, and **R**eporting **S**ystem
ACs	**A**nalysis **C**entres
ARNS	**A**eronautical **R**adio **N**avigation **S**ervices
C/A code	**C**oarse **A**cquisition code
C/No	**C**arrier-to-**No**ise-density ratio
CIRA	**C**OSPAR **I**nternational **R**eference **A**tmosphere
CMC	**C**anadian **M**eteorological **C**entre
CORS	**C**ontinuously **O**perating **R**eference **S**tations
BPE	**B**ernese **P**rocessing **E**ngine
DD	**D**ouble-**D**ifferencing
DGPS	**D**ifferential **GPS**
DoT	**D**epartment **o**f **T**ransportation
DOY	**D**ay **O**f **Y**ear
ECEF	**E**arth-**c**entered **E**arth-**f**ixed
ECMWF	**E**uropean **C**entre for **M**edium Range **W**eather **F**orecast
EDM	**E**lectronic **D**istance **M**easurement
EGNOS	**E**uropean **G**eostationary **N**avigation **O**verlay **S**ervice
EM wave	**E**lectro-**M**agnetic wave

ERP	**E**arth **R**otation **P**arameter
FAA	**F**ederal **A**viation **A**dministration
FSL	**F**orecast **S**ystems **L**aboratory
GOES	**G**eostationary **O**perational **E**nvironmental **S**atellite
IERS	**I**nternational **E**arth **R**otation and Reference System **S**ervice
IF	**I**onospheric-**F**ree
IGRA	**I**ntegrated **G**lobal **R**adiosonde **A**rchive
IGS	**I**nternational **G**NSS **S**ervice
IMF	**I**sobaric **M**apping **F**unction
IP	**I**onospheric **P**oint
IPW	**I**ntegrated **P**recipitable **W**ater Vapour
ITRF	**I**nternational **T**errestrial **R**eference **F**rame
IWV	**I**ntegrated **W**ater **V**apour
GAGAN	**G**PS **A**ided **G**eo **A**ugmented **N**avigation
GEM	**G**lobal **E**nvironmental **M**ulti-scale
GF	**G**eometry-**F**ree
GNSS	**G**lobal **S**atellite **N**avigation **S**ystem
GrADS	**Gr**id **A**nalysis and **D**isplay **S**ystem
KMA	**K**orea **M**eteorological **A**dministration
LC	**L**inear **C**ombination
MODIS	**Mod**erate Resolution **I**maging **S**pectroradiometer
MSAS	**M**ulti-Functional **S**atellite **A**ugmentation **S**ystem
NASA	**N**ational **A**eronautics and **S**pace **A**dministration
NCAR	**N**ational **C**entre for **A**tmospheric **R**esearch
NCEP	**N**ational **C**enter for **E**nvironmental **P**rediction
NMF	**N**iell **M**apping **F**unction

NOAA	**N**ational **O**ceanic and **A**tmospheric **A**dministration
NWP	**N**umerical **W**eather **P**rediction
NWS	**N**ational **W**eather **S**ervice
O-C	**O**bserved minus **C**omputed
P code	**P**recise code
PPK	**P**ost-**P**rocessed **K**inematic
ppm	**p**art **p**er **m**illion
PPP	**P**recise **P**oint **P**ositioning
PRC	**P**seudo- **R**andom **C**ode
PRN	**P**seudo**R**andom **N**oise
PWV	**P**recipitable **W**ater **V**apour
RAP	**RAP**id Refresh
RASS	**R**adio **A**coustic **S**ounding **S**ystem
RF	**R**adio **F**requency
rms	**r**oot **m**ean **s**quared
RTK	**R**eal-**T**ime **K**inematic
RUC13	**R**apid **U**pdate **C**ycle **13** km
RUC	**R**apid **U**pdate **C**ycle
SED	**S**torm **E**nhanced **D**ensity
SD	**S**ingle-**D**ifferencing
SHD	**S**lant **H**ydrostatic **D**elay
SIP	**S**tochastic **I**onosphere **P**arameters
SLR	**S**atellite **L**aser **R**anging
SSM/I	**S**pecial **S**ensor **M**icrowave **I**mager
SWD	**S**lant **W**et **D**elay
TD	**T**riple-**D**ifferencing
TEC	**T**otal **E**lectron **C**ontent

TECU	**TEC U**nits
TID	**T**raveling **I**onospheric **D**isturbance
TS	**T**otal **S**tation
UNB	**U**niversity of **N**ew **B**runswick
USM	**U**niversity of **S**outhern **M**ississippi
VAD	**V**elocity-**A**zimuth **D**isplay
VLBI	**V**ery **L**ong **B**aseline **I**nterferometry
VMF	**V**ienna **M**apping **F**unction
VTEC	**V**ertical **TEC**
WASS	**W**ide **A**rea **A**ugmented **S**ystem
WGS84	**W**orld **G**eodetic **S**ystem **84**
WL	**W**ide-**L**ane
WVR	**W**ater **V**apour **R**adiometer
ZD	**Z**ero-**D**ifferencing
ZHD	**Z**enith **H**ydrostatic **D**elay
ZTD	**Z**enith **T**otal **D**elay
ZWD	**Z**enith **W**et **D**elay

Chapter 1

Introduction

In this dissertation, a novel and effective algorithm is presented for solving the problem of mitigating the Global Satellite Navigation System (GNSS) tropospheric delay. One of the most problematic error sources in GNSS positioning arises from the non-dispersive medium that exists in the lower atmosphere and in most circumstances is not dependent on the GNSS frequency [*Oguchi*, 1983]. Even if multiple frequencies of the modernized signals are available, unlike the ionospheric delay, they are not fully helpful in mitigating the tropospheric delay. The problem is much more difficult as the tropospheric delay parameters are highly correlated with the height component which can cause an ill-conditioned case to be created in the normal equations.

This dissertation presents an approach to solve correlation issue between the two parameters and to enhance the overall positioning result, especially for the height component in kinematic scenario.

1.1 Background

The use of GNSS technology is expanding rapidly and is playing an increasingly important role in many fields. It is estimated that over 99% of all GPS receivers sold are L1-only C/A code receivers [*van Diggelen*, 2009]. The remaining 1% are high precision users, mostly for engineering or scientific usages, for cm to mm positioning accuracy. This includes land surveyors, seismologist, atmospheric researchers, militaries, space agencies for low Earth orbiting satellites or space missions, geologists, astronomers, and so on.

To obtain high precision positioning results from GNSS, the current emerging positioning method and active research field is based on the precise point positioning (PPP) method which uses a single geodetic receiver. The relative positioning method, which is typically used for a high precision application, uses two or more receivers. One receiver should be used on a known control point and the other receiver must be simultaneously recording the GNSS data for RTK or later precision processing.

Depending on the accuracy and limitation, however, each method has its own strength and weakness. For dense networks, many surveyors still choose the relative positioning method because it provides higher accuracy, in general, and faster convergence in the positioning domain. If the baseline length is typically around 10 km, most of the errors affecting GNSS observables are cancelled out or much reduced due to the mathematical differencing in relative positioning.

GNSS sensing is one of the most valuable tools in the atmospheric research community, because GNSS provides relatively accurate atmospheric signal delays under all weather conditions. This sensing provides more information on the spatial distri-

bution of the water vapour near the receiver. Therefore, more accurate hydrostatic (called ′dry′) and non-hydrostatic (or ′wet′) delays can be retrieved from individual reference stations, especially when the information is combined with the results from the most advanced and accurate numerical weather prediction models. However, such applications also have a need for increasingly accurate, reliable, and timely GNSS data and products from existing and specialized networks. Modernized GNSS signals includes many different frequencies. One of the benefits of having more frequencies is to make a better model of the frequency-dependent refraction component, i.e., the ionosphere. Having more signals also allows for improved ambiguity resolution where many choices of different frequency combination can be made. This can make the positioning solution stronger because of having higher reliability in the solved ambiguity.

One of the most problematic error components in high precision GNSS positioning, however, happens from the non-dispersive medium. For this reason, even if multiple frequencies are available, they are not very helpful in mitigating the error due to the non-dispersive characteristics. One of the benefits of having more signals is that all other frequency-dependent errors, such as the ionosphere, can be removed enabling an improvement in the modelling of non-dispersive medium, such as the troposphere, e.g. using 4D tomography. However, in terms of positioning, it may take a long time to evaluate corrections to a receiver′s estimated position for a whole network with recorded atmospheric profiles over a limited time period. In terms of the atmospheric science, Manning et al. [2012] studied GPS tomography to reconstruct spatially and temporally changing 4D wet refractivity every 5 minutes during an extreme convective super cell storm in Australia. They concluded that there is strong correlation between the 4D wet refractivity evolution and the lifecycle of the studied sample, and implied that the tomography research is beneficial in the early detection and

forecasting severe weather systems. The tomography study and radio occultation research is currently an active research field for atmospheric science together with GNSS technology. Recent research includes Jiang et al. [2014] who carried out for a year worth of data processing and comparisons for tomography research and Rieckh et al. [2014] who estimated of the tropopause meteorological parameters from radio occultation techniques.

As described by Mendes et al. [1995], almost 90% of the total delay occurs from the hydrostatic component in the troposphere which varies slowly with time so that it can be easily modelled (with the assumption of hydrostatic equilibrium) to an accuracy at the millimetre level. Unlike the hydrostatic part, the non-hydrostatic part has strong spatial and temporal variations. This makes the problem much more complicated. Typically, the effects of the non-hydrostatic delay in the range direction can reach 10∼40 cm depending on the elevation cutoff angle. If the functional models do not fully account for the non-hydrostatic delay part, the resulting residual errors in modelling can cause significant errors in high precision GNSS positioning solutions. Consequently, a misclosure vector can not be sufficiently minimized.

To reduce or minimize these errors (arising from poor modelling of the wet troposphere), one possibility is to model the tropospheric refraction using a data set of non-GNSS observations. However, this is not always available at a rover receiver. The other approach is to estimate by least-squares over a 1∼2 hour time window the tropospheric parameters directly using the available GNSS data , e.g. as used in Bernese GNSS software. Typically, the highest accuracy can be achieved using least square to estimate the troposphere parameter over a 1∼2 hour time interval with redundant observations with a batch processing approach, such as in the Bernese GNSS software. Kalman filtering needs a certain time window to converge to the

correct solution and thus it may be hard to model the dynamic behaviour of the troposphere. In addition, the solution may unexpectedly be degraded once process noise is artificially estimated in the Kalman filter. The Kalman filter de-noises unwanted signals in a certain time window, and gives very good results only in the situation that its dynamic behaviour can be well approximated, which is not always possible. As the troposphere changes rapidly, it is hard to predict the behaviour of the troposphere, while the filter needs at least a few minutes to converge, depending on the observables used and the environment.

When there is a strong anomaly effect in the lower atmosphere, the approach to resolve or to mitigate the error associated with the atmosphere can be much more complicated and thus the GNSS solution in this situation can no longer be precise with current estimation methodology, especially in the kinematic case. A network-based RTK method is useful and provides a reliable spatial solution [*Raquet*, 1998] but most of the research is still focused on long baselines. When there is a localized effect by the atmosphere, the method still faces a similar challenge to the single baseline case. As the troposphere and resultant height component are highly correlated (as both parameters are zenith and linearly dependent above a 20° elevation angle), it may be almost impossible to distinguish between those parameters. Therefore, the problem often suggested or asked is how to correctly and efficiently de-correlate those two parameters in order to achieve better and reliable height solutions. Once a severe tropospheric effect happens over a short time domain, (e.g. typically less than 30 minutes), the positioning solution is rarely reliable even if the best solution can be achieved by estimating the troposphere every 1$\sim$2 hours, even under a short baseline. Cases of such an anomaly have often been observed around the world. Under normal troposphere conditions, the troposphere errors in GNSS can be substantially minimized in short-baseline situations by the differencing techniques due

to the spatial and temporal correlation characteristics. Even in a short baseline situation, however, the resultant solution can be highly degraded once there is a strong anomaly effect due to the troposphere. The problem can be much more difficult as the troposphere parameters are highly correlated with the height component, thus one may end up with the ill-conditioned case in the normal equations.

In order to have a better positioning solution of a rover in terms of reliability, one can either have a better model for the troposphere that can be applied towards the anomalous cases, or have a different elimination technique for the troposphere. Current mitigation techniques for the tropospheric refraction, such as the theoretical or empirical model, are considered only in the normal troposphere cases. Some studies have focused on independent observables (e.g., water vapour from a water vapour radiometer) to retrieve the absolute atmospheric parameters for other stations. Even if relative GNSS positioning gives better results and faster convergence time compared to those of precise point positioning (PPP), interpretation of parameters can be limited. For example, to estimate the troposphere delay at the rover site one fixes the reference site′s troposphere. This allows us to solve, or avoid, the mathematical correlation between the partial derivatives of the troposphere at two sites, e.g. levering technique [*Rocken et al.*, 1997]. As with positioning estimates, a wrongly estimated troposphere delay at the reference site can be propagated into other sites. Another approach in mitigating the troposphere delay includes a ray-tracer based on a numerical weather prediction (NWP) model. However, currently, the grid spacing adopted in NWP is too large to consider creating a locally anomalous atmospheric condition, as the grid nodes (which need to be integrated) are typically at least 10 km apart.

Due to the high correlation between height and GNSS troposphere parameter,

a suggestion might be the troposphere parameters must be determined whenever possible. For long sessions, the troposphere parameters are usually estimated every 1∼2 hours. However, Rothacher and Beutler [2002] suggested that the estimation of zenith total delay (ZTD) is problematic when a short sessions is observed as the decorrelation of the troposphere and height requires a long session (at least one hour). Within this context, we have also evaluated smaller time intervals than one hour when estimating the troposphere delay, and confirmed that it worsened the entire positioning solution. Based on a number of tests, the troposphere delay parameter estimation is found problematic if kinematic measurement are processed where the receiver coordinates have to be estimated at every epoch.

Previous research by the author (e.g. Ahn et al. [2007]) investigated the use of additional tropospheric parameters such as residual zenith tropospheric delay and horizontal gradient parameters. Although the method was successful in reducing the tropospheric residuals to some extent and thus resulted in an improvement in the solution domain, this approach has two main practical limitations. Firstly, the additional parameters may degrade the entire positioning solution in the estimation process due to redundancy and inter-correlation of parameters. Secondly, an arbitrary choice of the parametric spacing for the residual troposphere or the gradient estimation is not practical in a kinematic scenario. In a kinematic case with a limited observation period, introducing more parameters can make the entire solution worse.

Even for a short baseline, imbalanced atmospheric errors are shown to have a severe impact on rover positioning solutions, resulting in a worsening of the quality of the positioning solutions. A potential explanation is that under extremely inhomogeneous conditions in the lower troposphere, a physical interpretation may be difficult, if not impossible to evaluate, resulting in certain incorrect assumptions

about the parametric model. Therefore, residual analysis of the tropospheric delay can be carried out, but also, if not, a new approach has to be suggested to solve the troposphere mitigation in the kinematic situation especially during an anomalous tropospheric case.

This dissertation thus addresses the issues associated with the troposphere mitigation in GNSS positioning and tests a number of different methods regarding troposphere mitigation for positioning application and troposphere estimation for atmospheric research. To overcome the correlation problem, the dissertation proposes a new approach to decorrelate the height and the troposphere parameter. The associated ill-conditioned problem can be solved after combining two zenith dependent parameters into one common parameter with correct weighting parameters. In order to estimate those parameters separately in the parameter estimation process, a new recursive weighting scheme is also introduced to determine proper weighting to decorrelate the troposphere and the height component which could enable GNSS users to achieve high precision positioning solutions in the parameter estimation process.

1.2 Statement of the Problem

1.2.1 Objectives

The overall aim of this study is to address a number of different methods regarding the troposphere mitigation, and to develop a method to resolve the correlation between the troposphere parameter and the height component. A number of tasks to achieve the goal includes:

- Evaluation of a number of current mitigation methods for the GNSS tropo-

sphere delay and addressing of potential issues in degradation especially the troposphere anomaly in kinematic applications,

- Development of a new methodology to resolve the correlation between the height and troposphere parameters especially under severe troposphere anomaly cases in the lowest atmosphere,
- Development of a post-processed kinematic platform for validating the methodology and evaluating the test results for short baseline processing,
- Performance of the methodology is measured in terms of the reliability of the positioning solution, especially the height component.

1.2.2 Hypothesis

The hypothesis for this study is that by decorrelating the height and the troposphere parameters the height accuracy can be significantly improved. Correlated parameters are difficult to separate unless there are enough satellites available with a low elevation angle to make the correlated parameters distinguishable. The data in lower elevation satellites are, in general, prone to have more noisy data due to larger multipath, uncertainties in the atmospheric model, receiver noise and so on. In addition, the lower elevation satellites are not always available due to obstacles blocking the signal path.

If two correlated parameters can be combined into a single parameter and brought into a least squares estimator, there must exist a value which will minimize the weighted sum of the squared residuals. Previous experience in the analysis of decorrelation based on intermediate data sets from a geodetic software platform support this idea, that height estimates can be dramatically improved once the weight coefficients are properly estimated or found.

1.2.3 Assumption

The main goal of the research is to develop a new methodology which meets the primary objectives to overcome the decorrelation problem between two parameters under severe troposphere anomaly situations and evaluation of the proposed methodology using a number of different baselines. In order to achieve the ultimate goal, assumptions were made to help define the scope of this research.

The research is based on the analysis of baseline processing results where the reference station is assumed to be known and the rover is to be estimated, which is typical in relative positioning. Instead of estimating both sets of coordinates, the reference station's coordinates are assumed to be known to the milimetre level. All of the baselines tested in this research are short (e.g. around 10 km) and dual frequencies are available and usable. Further, epoch-wise kinematic software is developed and validated against other software platforms.

1.3 Significance

The purpose behind this research is to improve the height solution with acceptable accuracy without the help of external measurements of the tropospheric correction. Importantly, the data tested herein for evaluating the methodology include especially anomalous tropospheric conditions. The primary development in this research is that it enables a recursive weighting scheme to provide a proper weighting on each parameter after determining the magnitude of the tropospheric contribution from the residual analysis. The major contributions of this research within the area of the troposphere mitigation and positioning enhancement can be described as follows:

- Evaluation of existing methodologies to mitigate troposphere delay and develop a completely different approach to resolve the correlation issue,

- Development of a methodology to minimize the correlation between the troposphere and height parameter with a new test-bed software platform. To achieve this goal, generalized mathematical descriptions for the software platform are given.

- Development of a method to solve the tropospheric delay on GNSS observables without external aids. The data tested are solely based on GNSS observables. This means that the methodology does not use any external tropospheric measurements to help to determine the weighting. Although the lower troposphere has strong spatial and temporal variation and the test is based on a post-processed scheme, this methodology may be suitable for use in real time with a sufficient accuracy compared to using a predicted model value, if controlled. Based on a series of tests, we have concluded that it is nearly impossible to achieve a meaningful result under the severe troposphere circumstances using current model-based predictions.

1.4 Dissertation Outline

Overall, the dissertation has nine chapters. They are classified in two different categories.

Part I (the first three chapters) presents basic fundamentals relevant to understanding contents of this dissertation.

- Chapter 1 states the background, overall research objectives, hypothesis, and

assumptions made. It provides the motivation of the research. It also includes the contribution of this dissertation.

- Chapter 2 is an overview of GNSS fundamentals. The different error sources that affect GNSS observations are discussed.

- Chapter 3 provides the principles of GNSS signal delays in the troposphere, and some of the current fundamental models for mitigating the troposphere errors. It includes the mathematical background of a few important troposphere mitigation models and precipitable water vapour retrieval based on the troposphere estimates from GNSS observables. It also describes the ray-tracing method using a numerical weather prediction model as well as radiosonde observables. Some of the test results are given in this chapter for addressing the importance of GNSS as a research tool in troposphere research.

Part II describes the new methodology developed to solve the current issue and problem, which enhances the positioning solution.

- Chapter 4 introduces the proposed new methodology. The proposed new combined zenith dependent parameter to decorrelate the height and troposphere parameter is described and the weighting method (named combined zenith-dependent weighting) is discussed in this chapter. It covers the derivation of the algorithm used in this approach and demonstrates how to realize it with an actual data set.

- To test the methodology, an epoch-wise post-processed kinematic software platform was developed. In Chapter 5, fundamental mathematical formulations for relative positioning needed to develop epoch-wise kinematic software are

described. The developed software is mainly used to test the proposed new methodology.

- In Chapter 6, the scenarios selected for this research are processed with the software based on the methodology. To evaluate it, a few short baseline scenarios over a few geographical regions are selected for the test which includes the United States, Canada and the Caribbean. A number of different baselines are processed to evaluate the results. This includes consecutive days which are relatively humid compared to other days. The details of these data sets are also described in this chapter.

- Chapter 7 evaluates important mitigation approaches for the troposphere, evaluates the proposed methodology, and discusses a performance analysis for each scenario defined previously. The temporal behaviour of the errors, in addition to an analysis of the observation domain, is given. An analysis is carried out, with an emphasis on the differences in the performance of reduction of errors. This chapter presents further investigations into the combined zenith-dependent weighting method.

- Chapter 8 provides discussions and conclusions of this research.

- Finally, Chapter 9 includes recommendation for further research avenues.

Chapter 2

GNSS Fundamentals

This chapter addresses the measurement equations, and describes error sources in GNSS, especially clock errors, orbit errors, ionospheric errors, multipath, and system noise. As this research is dealing with dual frequency GPS, fundamental aspects for both signals are described here. The tropospheric errors are described in detail in Chapter 3.

2.1 Observables and Measurement Equations

The pseudorange is a measure of the apparent propagation time from the satellite to the receiver's antenna. This apparent propagation time is determined from the time shift required to align a replica of the GPS code generated in the receiver with the received GPS code. This time shift is the difference between the time of signal reception measured in the receiver time frame, and the time of emission measured in the satellite time frame.

The pseudorange is obtained by multiplying the apparent signal-propagation time by the speed of light, and differs from the actual range by the amount that the satellite and receiver clocks are offset, by propagation delays, and other errors including

those in cables, electronics, etc. Since this measurement is not a true range measurement, it is referred to as the pseudorange [*Wells et al.*, 1987]. The carrier phase refers to an accumulated or integrated measurement, which consists of a fractional part, plus the integer number of wavelengths since signal lock-on. Since a GPS receiver cannot distinguish one cycle from another, the carrier phase measurement is ambiguous.

There is another GPS observable, called the Doppler measurement, which tracks the line of sight velocity between the satellite and antenna. Since Doppler measurements do not have an integer ambiguity, and are in the range of $\pm$ 5 kHz, this method is typically used to detect cycle slips in the carrier phase measurement, or to determine the a receiver′s velocity.

All GPS satellites transmit on the L1 and L2 frequencies. The L1 frequency is 1575.42 MHz, and L2 is 1227.60 MHz. Physically, GPS sends just a very complicated digital code. As the coded signal looks random electrical noise, it is called Pseudorandom noise code (PRN). Two types of PRN are sent by a satellite; C/A (Coarse/Acquisition) code which is for civilian users and modulated on L1 carriers at a rate of 1.023 MHz, the other the P (Precise) code which is for military users and is modulated on both the L1 and L2 carriers at a rate of 10.23 MHz.

Since the P code is encrypted, which is then called Y code, the measurements are not directly available to civilian users, unless a special so-called 'code-less' technique is used. For this reason, the signal strength is decreased by 14 to 31 dB, and L2 measurements cannot be made with the same quality as those on the L1 frequency.

Recent advancement includes testing a few modernized signals including L2C (pre-

operational), L5 (pre-operational), and L1C (which is scheduled for test in 2017) (http://www.gps.gov/systems/gps/modernization/civilsignals/). The L2C signal is the 2nd civilian signal and, as of Feb. 5, 2016, 18 satellites are transmitting the signal. The most beneficial effect of having another civilian signal is that when it is combined with existing L1 C/A signal, it will make position determinations much more resistant to ionospheric errors. The L5 frequency of 1176.45 MHz also has pre-operation status. Eleven satellites are transmitting the signal and it will be available fully operational around 2021. The main advantages that would arise from L5 availability include: robustness via signal redundancy, improved accuracy via ionospheric correction, improved interference resistance, higher transmitted power than L1 C/A or L2C, improved data message quality, and higher chipping rate (which would improve the multipath performance). The L5 signal is mainly designed for safety-related transportation as it uses the highly protected Aeronautical Radio Navigation Services (ARNS) radio band. The fourth civil signal scheduled is L1C. The first satellite for the L1C signal test will be launched in 2017.

There are a few GNSS. These are GPS (USA), GLONASS (Russia), Galileo (Europe), QZSS (Japan) and Beidou (China). As the individual system broadcasts its own different signal, there is a demand to have a common signal for civilian user. Enabling interoperability between GPS and other compatible navigation systems can dramatically improve many civilian navigation applications in challenging environments. This is one of the main reasons to develop the common L1C signal. For carrier-phase-based differential GPS (DGPS) users, over long baselines, this modernization will further compensate for ionospheric errors, minimize the time required for ambiguity resolution and reacquisition, maximize the probability of correct ambiguity resolution over short time spans, etc., and help to achieve centimetre-level accuracies, or better, in the future.

The GPS observation equation for phase measurement of either the L1 or L2 frequency, in units of metres between the receiver and satellite, can be written, in a general form as follows [*Rothacher and Beutler*, 2002]:

$$\Phi_r^s = \rho_r^s + c\cdot\delta t_r + c\cdot\delta t_{r,sys} - c\cdot\delta t^s - c\cdot\delta t_{sys}^s + \delta T - \delta I + \delta\rho_{rel} + \delta\rho_{mul} + \lambda\cdot N_r^s + \varepsilon_{err} \quad (2.1)$$

where,

ρ_r^s : geometrical distance between a satellite and a receiver,

c : speed of light in vacuum,

δt_r : station clock correction,

$\delta t_{r,sys}$: delays in receiver and its antenna,

δt^s : satellite clock correction due to satellite clock error,

δt_{sys}^s : delays in satellite and its antenna,

δT : tropospheric delay,

δI : ionospheric delay,

$\delta\rho_{rel}$: relativistic corrections due to special and general relativity,

$\delta\rho_{mul}$: multipath,

λ : wavelength of the GPS signal (L1 or L2),

N_r^s : integer ambiguity,

ε_{err} : other remaining measurement and model errors.

The corresponding observation equation for pseudoranges only differs in two ways. The ionospheric refraction correction δI has the opposite sign for pseudoranges. The speed of the carrier wave (the "phase velocity") is actually increased, or "advanced", hence the phase refractive index is less than unity. However, the speed of the pseudorange is decreased (the so-called "group velocity"), and therefore the pseudorange is considered "delayed", and hence the range (or group) refractive index is greater

than unity [*Hofmann-Wellenhof et al.*, 2008]. In addition, there is no ambiguity term.

Using Equation 2.1, the geometric distance term, ρ_r^s can be written as follows [*Rothacher and Beutler*, 2002]:

$$\rho_r^s = |\vec{r}_i^s(t^s) - \vec{r}_{r,i}(t_r)| = |\vec{r}_i^s(t_r - \tau_r^s) - \vec{R}(t_r) \cdot \vec{r}_{r,e}(t_r)| \tag{2.2}$$

where,

$\vec{r}_i^s(t^s)$: satellite position at emission time $t_s = t_r - \tau_r^s$ in inertial system,

$\tau_r^s (= \rho_r^s / c)$: light travel time,

$\vec{r}_{r,i}(t_r)$: receiver position at reception time t_r in inertial system,

$\vec{r}_{r,e}(t_r)$: receiver position at time t_r in Earth-fixed system (e.g., International Earth Rotation and Reference System Service (IERS) International Terrestrial Reference Frame (ITRF)) with

$$\vec{r}_{r,i}(t_r) = \vec{R}(t_r) \cdot \vec{r}_{r,e}(t_r) \tag{2.3}$$

which refers to the relation between inertial frame and Earth-fixed frame, and $\vec{R}(t_r)$ is the transformation matrix from Earth-fixed to inertial system with

$$\vec{R}(t_r) = \vec{P}\vec{N}\vec{U}\vec{X}\vec{Y}. \tag{2.4}$$

Equation 2.4 contains the Earth rotation parameters such as polar coordinate x_p and y_p in $\vec{X}$ and $\vec{Y}$ due to the polar motion, UT1-UTC in the sidereal rotation matrix $\vec{U}$ and nutation parameter in obliquity $\Delta\epsilon$ and longitude $\Delta\lambda$ in $\vec{N}$. More details of the transformation matrix can be found in Cappellari et al. [1976] or Leick [2004].

In an inertial reference frame, the satellite position $\vec{r}_i^s(t^s)$ can be written as follows:

$$\vec{r}_i^s(t^s) = \vec{r}_{i,o}^s(t^s; a_{sat}, e_{sat}, i_{sat}, \Omega_{sat}, \omega_{sat}, t_p; p_1, p_2, p_3, \cdots, p_d) + \delta r_{ant}^s(t^s) \qquad (2.5)$$

where,

$\vec{r}_{i,o}^s$: position vector at the centre of mass,

δr_{ant}^s : antenna phase centre offset and variations,

$a_{sat}, e_{sat}, i_{sat}, \Omega_{sat}, \omega_{sat}, t_p$: six orbital elements,

$p_1, p_2, p_3, \cdots, p_d$: gravity field coefficients, air drag and radiation pressure parameters, etc.

In Equation 2.5, the semi-major axis a is used to define the size of the orbit, and the eccentricity e defines the shape of this orbit. The inclination angle i is the angle between the z-axis and the angular momentum vector, which is perpendicular to the orbit plane. If $i < 90°$, the orbital motion is counterclockwise when viewed from the north side of the fundamental plane (i.e. direct motion). If $i > 90°$, the satellite is in retrograde motion. The longitude of the ascending node Ω is the angle between the x-axis and a line from the dynamical centre to the point where the satellite crosses through the fundamental plane, from south to north, measured counterclockwise from 0° to 360°. If $i = 0°$, then the orbit cannot be defined. The argument of the perigee ω is the angle between the line of the ascending node and the line from the dynamical centre to the perigee. If $e = 0, i = 0°$, the argument of perigee cannot be defined. The time of perigee passage t_p is normally used to relate position along the orbit to the elapsed time, by means of the Kepler equations. If $e = 0$, t_p cannot be defined [*Escobal*, 1976; *Taff*, 1985; *Cappellari et al.*, 1976; *Montenbruck and Gill*, 2000].

In a similar way, the station position $\vec{r}_{r,e}(t_r)$ can be written in Earth-fixed frame

as follows:

$$\vec{r}_{r,e}(t_r) = \vec{r}_{r,e}(t_o) + \vec{v}_{r,e}(t_r - t_o) + \delta\vec{r}_{r,sol} + \delta\vec{r}_{r,pol} + \delta\vec{r}_{r,ocn} + \delta\vec{r}_{r,atm} + \delta\vec{r}_{r,ant} \quad (2.6)$$

where,

$\vec{r}_{r,e}(t_o)$: coordinates of the station,

$\vec{v}_{r,e}$: velocities of the station,

$\delta\vec{r}_{r,sol}$: solid Earth tides which are caused by the gravitational forces of Sun and Moon,

$\delta\vec{r}_{r,pol}$: pole tides which are caused by the reaction of the elastic Earth to the change of the rotation axis due to polar motion,

$\delta\vec{r}_{r,sol}$: ocean loading which is due to the weight of the water on the continental plate during tides,

$\delta\vec{r}_{r,atm}$: atmospheric loading which is due to the weight of the atmosphere on the continental plate,

$\delta\vec{r}_{r,ant}$: antenna phase center offset and variations.

Since all these errors are combined together in the measurement, they should be modelled for applications requiring sub-centimetre precision in high-accuracy global reference or high-accuracy geodetic surveys.

Generally, there are two different methods when process GPS data (unless assisted GPS (A-GPS) is used); one is precise point positioning (PPP) and the other is the relative positioning method. The general data processing procedure for the relative positioning method is as follows:

• The pseudorange or carrier phase measurements made simultaneously by two GPS receivers are combined so that, for any measurement epoch, the observations

from one receiver to two satellites are subtracted from each other to remove the receiver's clock error or common bias.

• The two single-differences are subtracted so as to eliminate the satellite clock errors, as well as to reduce significantly the effect of unmodelled atmospheric biases and orbit errors.

• The resulting set of double-differenced observables, which are independent combinations of two-satellite-two-receiver combinations, can be processed to solve for the baseline components, and, in the case of ambiguous carrier phase measurements, for the integer ambiguity parameters.

Although the PPP method is getting more popular due to its benefit of absolute positioning and is based on a direct measurement observation equation, many high-precision positioning techniques still use a form of the double-difference processing technique. More details on PPP and the relative positioning method are given in Chapter 4.

2.2 Error Sources

The carrier phase measurements and pseudoranges are affected by the systematic and random errors. There are many sources of systematic errors, such as: satellite orbits, clocks, the propagation medium such as through the ionosphere as well as the troposphere, receiver clocks, relativistic effects, antenna phase centre variations, multipath, phase wind-up, and other systematic errors, e.g. errors due to cable noises. Using the double difference technique, most of these systematic errors can

be eliminated or much reduced. For high-accuracy GPS real-time kinematic (RTK) positioning, the double difference technique is a common approach as it dramatically reduces the errors in GPS signals. Santerre [1989], as discussed on Beutler et al. [1988], studied about a few important systematic errors in relative positioning for different satellite configurations and quantified the effects in a different scenarios from simulation work. Based on their research, two classes of biases are found when looking at GPS error sources: those mainly influencing the height (vertical direction), and those influencing the scale of a baseline or a network, in the horizontal direction. The effect on baseline length can occur due to a bias in the absolute tropospheric delay, to neglecting the ionospheric delay, or to incorrect heights of fixed reference stations, for example.

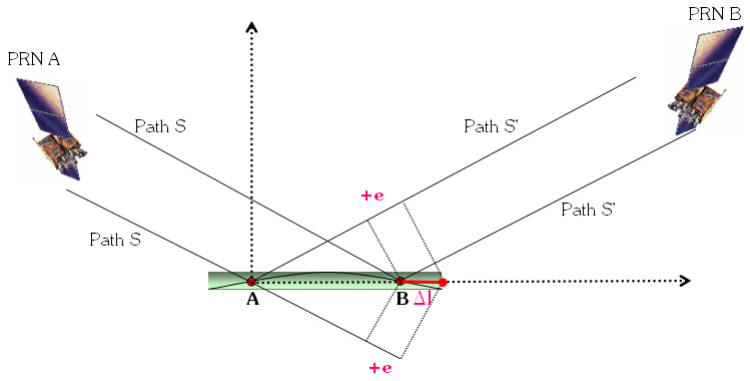

Figure 2.1: Effect of GPS errors on baseline length

For example, if there is a bias in the absolute tropospheric delay, the baseline length between the point A and B can be affected by an amount of the same magnitude of $|e|$ as shown in Figure 2.1, for the signals transmitted on pseudorandom noise code (PRN) A and PRN B satellite. Consequently, the estimated baseline length can be either extended (if e is positive) or contracted (if e is negative in magnitude) compared to the true position due to this error.

However, the second class of biases can affect the relative station heights. This can occur due to a different bias at each endpoint of a baseline. Such cases happen when there is a bias in the relative tropospheric delay, in the horizontal positions for fixed reference stations, in the satellite orbit, in the antenna phase centre differences, and in the multipath, for example.

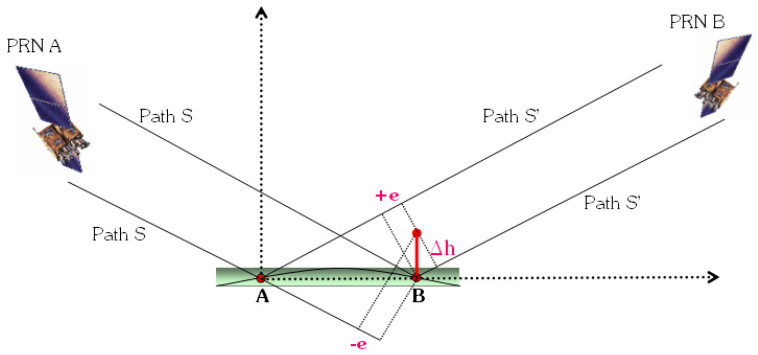

Figure 2.2: Effect of GPS errors on station height

Similarly, for example, if there is a bias in the relative tropospheric delay, it can have an effect of the same magnitude, but in a different direction, on the signals transmitted on PRN A and PRN B to the point of either A or B. Consequently, the estimated station height could be higher or lower than the true position due to the effect, as shown in Figure 2.2. The remainder of section 2.2 briefly describes error sources apart from errors due to the troposphere which is discussed in detail in Chapter 3.

2.2.1 Clock Errors

Let $c \cdot \delta_r \equiv c \cdot \delta t_r + c \cdot \delta t_{r,sys}$ in Equation 2.1 so that $\delta_r = \delta t_r + \delta t_{r,sys}$ which is the error of the receiver clock at time t with respect to GPS time. Similarly, $\delta^i = \delta t^s + \delta t^s_{sys}$ is for the satellite. If so, the signal reception time can be written as $t = t_r - \delta_r$ where

t is the signal reception time and t_r is the reading of the receiver clock in the signal reception time. The term, $c \cdot \delta_r - c \cdot \delta^i$ or $c \cdot \delta t_r + c \cdot \delta t_{r,sys} - c \cdot \delta t^s - c \cdot \delta t^s_{sys}$ in Equation 2.1, can be eliminated by implementing the double difference of the measurements (see Chapter 4).

However, this does not mean that the receiver clock error δ_r is completely eliminated in the differencing technique. In order to compute the geometric distance ρ^s_r between the satellite and the receiver at time t, we still need to linearize the measurements, so the receiver clock error δ_r must be known in order to correct the reading of the receiver clock t_r. Now, the geometric distance ρ^s_r can be written in a simpler way, and its derivative can be obtained as follows:

$$\rho^s_r(t) = \rho^s_r(t_r - \delta_r) \qquad \text{or} \qquad d\rho^s_r(t) = -\dot{\rho}^s_r d\delta_r \tag{2.7}$$

where $\dot{\rho}^s_r$ can be interpreted as the radial velocity of a GPS satellite with respect to the receiver. Obviously, this radial velocity can be minimized when the satellite just passes the zenith direction. However, the velocity can reach up to 900 m/s ($\sim 10^\circ$ elevation angle) near the horizon.

Hugentobler et al. [2005] mentioned that if $|d\delta_r|$ is smaller than $1\mu s$, the error $|d\rho^s_r(t)|$ due to $|-d\delta_r|$, which can be interpreted as the receiver clock synchronization error, can be as small as 1 mm.

2.2.2 Orbit Errors

There are four different kinds of GPS orbits: broadcast, ultra-rapid, rapid and precise orbit. The broadcast orbit is based on pseudoranges, which have uncertainties of approximately 1 m, while the final precise orbit is based on phase observables

Table 2.1: Four different kinds of GPS orbit [1]

Type		**Accuracy**	**Latency**	**Update**	**Sample Int.**
Broadcast	Orbits	∼100 cm	realtime	–	daily
	Sat. clocks	∼5 ns rms ∼2.5 ns std			
Ultra-Rapid (predicted half)	Orbits	∼5 cm	realtime	03,09, 15,21 UTC	15 m
	Sat. clocks	∼3 ns rms ∼1.5 ns std			
Ultra-Rapid (observed half)	Orbits	∼3 cm	3 ∼ 9 h	03,09, 15,21 UTC	15 m
	Sat. clocks	∼150 ns rms ∼50 ps std			
Rapid	Orbits	∼2.5 cm	17 ∼ 41 h	17 UTC daily	15 m
	Sat. & Sta. clocks	∼75 ps rms ∼25 ps std			5 m
Final	Orbits	∼2.5 cm	12 ∼ 18 d	every Thur.	15 m
	Sat. & Sta. clocks	∼75 ps rms ∼20 ps std			Sat.: 30 s Stn.: 5 m

that have currently uncertainties of about 2.5 cm. For the broadcast orbit, there is no latency which means the orbit can be retrieved in real time. There are three different types of precise orbit products produced by the International GNSS Service (IGS), which are generated based on estimates of orbits at twelve different IGS analysis centres (ACs), with individual weights used in a sum, to get a weighted combination, resulting in: the ultra-rapid, rapid, and final orbit products. The twelve different ACs use different software packages, e.g., GIPSY-OASIS, Bernese GNSS S/W, GAMIT, and apply different strategies, parameterizations, and models.

Table 2.1 represents each of the orbit′s quality. The three precise orbits are based on phase measurements using the data from a global GNSS network, and the orbit information is available in the Standard Product #3 ASCII (SP3) format, which is a geocentric earth-fixed satellite position in ITRF, reported at intervals of every 15 minutes or less.

[1]https://www.igs.org/products, accessed March 2016

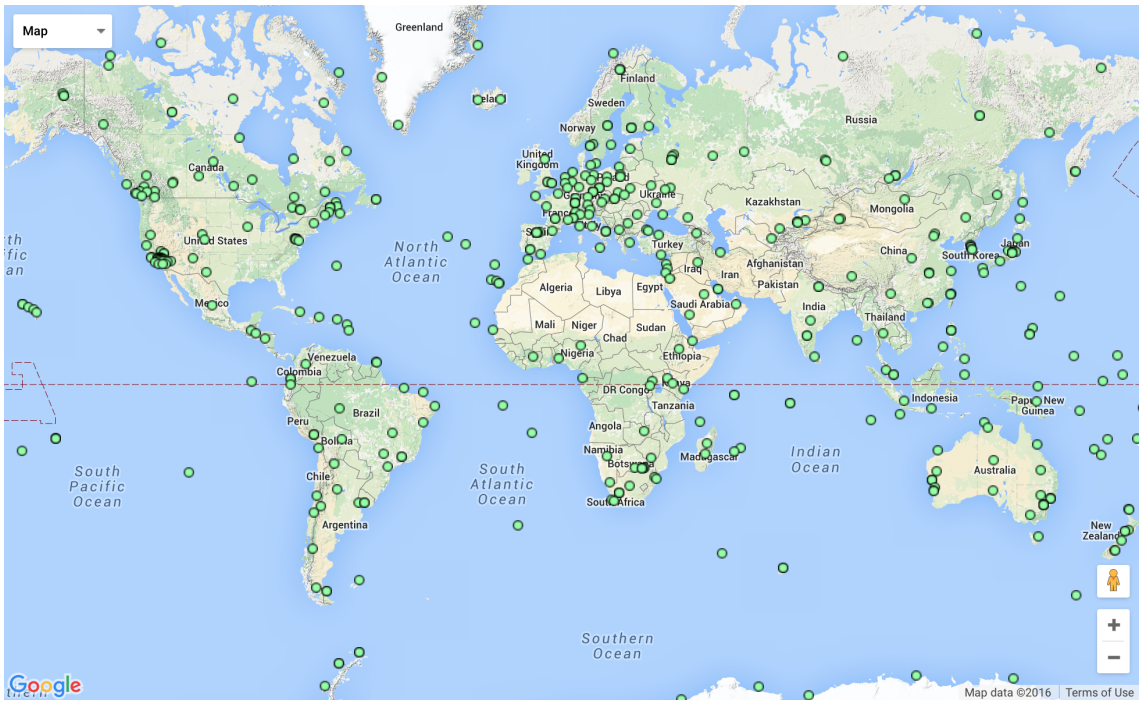

Figure 2.3: IGS Tracking Network (from IGS 2016) [3]

In addition to GNSS satellite ephemerides, the IGS also provides Earth rotation parameters (ERPs), global tracking station coordinates and velocities, satellite and tracking station clock information, global ionosphere maps, and zenith tropospheric delay estimates. Figure 2.3 illustrates the distribution of the global GNSS network. The ITRF coordinates are positioned relative to the geo-centre using a variety of space geodetic techniques, such as Satellite Laser Ranging (SLR), Very Long Baseline Interferometry (VLBI), and GNSS. Therefore, ITRF is considered to be a more reliable datum than World Geodetic System 84 (WGS84). The discrepancy between ITRF2008 and WGS84 is approximately 10 cm.[2] The most recent realization of ITRF is ITRF2014 and the details can be found Altamimi et al. [2016].

With respect to the influence of the orbit errors on station coordinates, for different

[2]More details can be found on: ftp://itrf.ensg.ign.fr/pub/itrf/wgs84.txt
[3]More details on each station can be found on: http://igs.org/network

baseline lengths, Bauersima [1983] estimates and quantifies the approximate baseline errors as a function of orbit errors, as follows:

$$|\Delta r| = \frac{l}{\rho} \cdot |\Delta R| \approx \frac{l(km)}{25,000(km)} \cdot |\Delta R| \tag{2.8}$$

where,

Δr : error of a baseline length l,

ΔR : orbital errors.

Equation 2.8 means that broadcast orbits may be sufficient to achieve an accuracy of 0.4 mm in the baseline, for a 10 km baseline length. Due to the high orbit quality provided by the IGS, orbit errors are usually ignored in the post-processing. However, this does not mean that this quality is sufficiently good for all applications, such as PPP and GPS RTK positioning for long baselines, or for use by the atmospheric community.

Especially in the case of retrieving the integrated precipitable water vapour (IPW), or slant wet delay of the troposphere, Rocken et al. [1997], Dousa [2001] and Kruse et al. [1999] address the importance of the orbit quality, since accurate near-real-time GPS IPW estimation depends on the accuracy of the satellite orbits. Baltink et al. [2002], Rocken et al. [1997] and Kruse et al. [1999] tested whether orbit relaxation, (i.e., the simultaneous adjustment of orbit parameters during the processing of GPS data), could increase the accuracy of the IPW estimates. They compared their results by orbit relaxation to the IPW estimates based on the final IGS orbits, and found an improvement of 20% in the rms error, compared with other methods which use the quality index to remove bad satellites, or wrongly predicted satellites. However, Baltink et al. [2002] suggested that an orbit improvement procedure, using an ultra-rapid orbit, would still be necessary for securing better IPW estimates.

2.2.3 Ionosphere Errors

An electromagnetic wave, especially at GNSS frequencies, is affected by the propagation media. This creates a bending of the signal path, time delays, advancement of carrier phases, and scintillation [*Leick*, 2004]. The ionosphere extends from about 60 km to beyond 1000 km and consists of ionized particles associated with (negatively charged) free electrons, which delay the signals coming from space [*Klobuchar*, 1996]. As the ionosphere is a dispersive medium, which means that the refraction due to the ionosphere is dependent on the frequency, a combination of different frequencies, (e.g. dual frequency user), can dramatically reduce the effect. With the help of augmented systems, like WAAS (Wide Area Augmented System), the error of the ionosphere can be also reduced. In terms of the error budget, the effect of the ionosphere on GNSS signals still remains a major contributor.

A single electromagnetic wave propagating with wavelength λ and frequency f travels in space with the velocity of its phase. This phase velocity, e.g. carrier phase waves for GNSS, can be written as follows [*Hofmann-Wellenhof et al.*, 2008]:

$$v_{ph} = \lambda f \tag{2.9}$$

For a group of waves with slightly different frequencies, the propagation of the resultant energy is defined by the group velocity, e.g. code measurement for GNSS, as follows:

$$v_{gr} = -\frac{df}{d\lambda}\lambda^2 \tag{2.10}$$

Based on the Rayleigh equation [*Hofmann-Wellenhof et al.*, 2008], both phase and group velocity can be related by the following equation:

$$v_{gr} = v_{ph} - \lambda \frac{dv_{ph}}{d\lambda} \tag{2.11}$$

To associate the wave propagation with a medium, the refractive index n must be introduced. The propagation velocity for the corresponding refractive indices n_{ph} and n_{gr} can be written, in general, as follows:

$$v_{ph} = \frac{c}{n_{ph}} \qquad \text{or} \qquad v_{gr} = \frac{c}{n_{gr}} \tag{2.12}$$

These two equations have a very important physical connotation within atmospheric propagation, i.e., the larger the refractive index the smaller the velocity, therefore resulting in proportional signal-path magnitude changes (with longer lengths for the group and smaller for the phase signal-path). As $d\lambda/\lambda = -df/f$, Equation 2.11 can be rewritten, using the refractive index, as follows:

$$n_{gr} = n_{ph} + f \frac{n_{ph}}{df} \tag{2.13}$$

The phase refractive index, n_{ph}, can be approximated by the series given by Seeber [1993] with the coefficients c_2, c_3, c_4 as follows:

$$n_{ph} = 1 + \frac{c_2}{f^2} + \frac{c_3}{f^3} + \frac{c_4}{f^4} + \cdots \tag{2.14}$$

Considering the 2nd order, the phase refractive index and the group refractive index can be approximated as follows:

$$n_{ph} = 1 + \frac{c_2}{f^2} \qquad \text{and} \qquad n_{gr} = 1 - \frac{c_2}{f^2} \tag{2.15}$$

These coefficients do not depend on frequency but on the quantity N_e which represents the density of the electrons along the propagation path [*Hofmann-Wellenhof et al.*, 2008]. The coefficient c_2 can be approximated with a value of [*Seeber*, 1993] :

$$c_2[\mathrm{Hz}^2] = -40.3 \cdot N_e \tag{2.16}$$

Equation 2.16 suggests that $n_{gr} > n_{ph}$, thus, $v_{gr} < v_{ph}$. Therefore, as a consequence of the different velocities, signal measurements are delayed when represented by code pseudo-range observables, and are advanced when represented by carrier-phases. The magnitude of these signal-path changes can be quantitatively obtained by only using up to the second-order term of Equation 2.14, and by using the c_2 value, i.e.:

$$n_{ph} = 1 - \frac{40.3 N_e}{f^2} \tag{2.17}$$

Based on Fermat's principle [Born and Wolf, 1964], the measured range s along the signal propagation path through the ionosphere between a satellite and a receiver, and the corresponding geometric distance $s_\circ$, can be written as follows:

$$s = \int_{path} n ds \qquad \text{and} \qquad s_\circ = \int_{path} ds_\circ \tag{2.18}$$

The difference between the measured range s and the geometric distance $s_\circ$ tells us the effect on the ionosphere path delay. Simply,

$$\delta I = \int n ds - \int ds_\circ \tag{2.19}$$

From Equation 2.15 and Equation 2.19, the following phase (δI_{ph}) and group (δI_{gr}) ionosphere delay can be obtained if the coefficient c_2 is replaced by $-40.3N_e$:

$$\delta I_{ph} = -\frac{40.3}{f^2}\int N_e ds \qquad \text{and} \qquad \delta I_{gr} = \frac{40.3}{f^2}\int N_e ds \tag{2.20}$$

Total Electron Content (TEC) is defined by:

$$\text{TEC} \equiv \int N_e ds \tag{2.21}$$

and substituting into Equation 2.20, we obtain:

$$\delta I_{ph} = -\frac{40.3}{f^2}\text{TEC} \quad \text{and} \quad \delta I_{gr} = \frac{40.3}{f^2}\text{TEC} \tag{2.22}$$

TEC is given in TEC units (TECU), where 1 TECU = 10^{16} electrons per m^2. Due to the dispersive nature of the ionosphere, GNSS users with dual-frequency receivers can mitigate the ionospheric range error (at least the first-order effect) through an appropriate combination of measurements observed on L1 and L2.

For arbitrary lines of sight, the Equation 2.22 can be rewritten with an elevation dependent function as follows:

$$\delta I_{ph} = -\frac{1}{\cos z'}\frac{40.3}{f^2}\text{TEC} \quad \text{and} \quad \delta I_{gr} = \frac{1}{\cos z'}\frac{40.3}{f^2}\text{TEC} \tag{2.23}$$

where, the z' can be defined from the Figure 2.5 as follows:

$$\sin z' = \frac{R_E}{R_E + h_m}\sin z_\circ \tag{2.24}$$

where,

$z_\circ$ or z' : zenith angle either at observing station or at ionospheric point (IP),

R_E : mean radius of the Earth,

h_m : mean value for the height of the ionosphere.

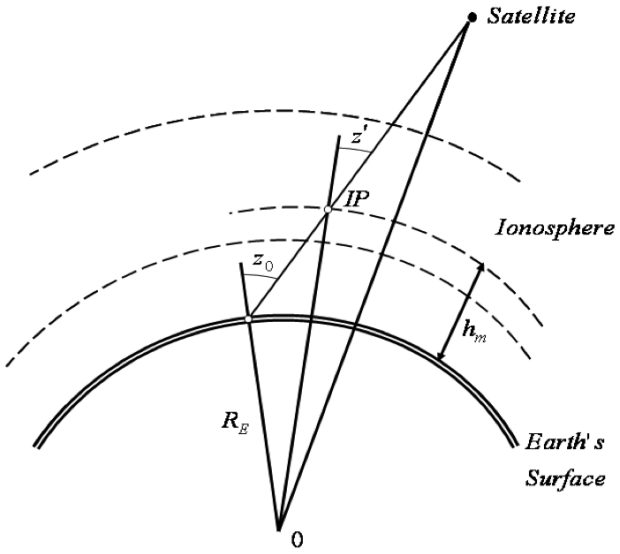

Figure 2.4: Geometry for the ionospheric path delay assuming a single-layer model [*Hofmann-Wellenhof et al.*, 2008]

This ionospheric delay can be modelled by estimating TEC in a column of the atmosphere, alternatively eliminated as a first order effect, based on its dispersive char-

acteristic, by using dual frequency measurements. Ionospheric disturbances mainly show up close to the equator, due to the high TEC there, and over the polar regions, due to short-term variations. The ionosphere is, however, quiet in mid-latitude regions, except in areas where Traveling Ionospheric Disturbances (TIDs) and storm enhanced density (SED) exist. The ionospheric storms, with enormous variations, are correlated with solar flares. When the GNSS signal travels high concentration of irregular plasma during a storm period, the ionosphere creates a rapid change in the phase and amplitude of the GNSS signal, called ionospheric scintillation. This scintillation is fast changing phenomena, and is difficult to predict, so that many receivers experiences a loss of lock, lose accuracy during the period, or even experience in failure in the positioning service. However, due to the dispersive nature of the ionosphere, the error caused by ionosphere can be significantly reduced if using more than one signal frequency in the majority of circumstances.

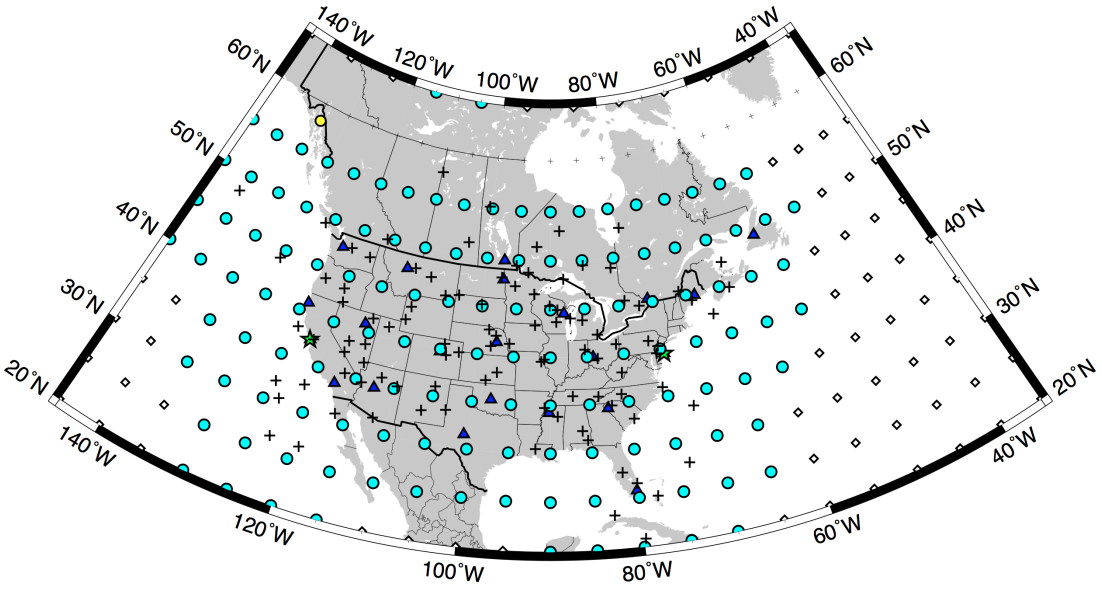

Figure 2.5: Ionospheric model broadcast by WAAS. It consists of a thin shell at 350 Km altitude which is discretized into a geodetically rectangular grid. A vertical delay estimate and a confidence bound on that estimate are calculated at each grid vertex [*Hansen et al.*, 2000]

There are many ionospheric models which have been proposed over a number of decades. Having the proper model, a user can mitigate the error in order to achieve a higher precision positioning solution. One common type for mitigating the error is based on the augmentation system, e.g. WAAS. The Federal Aviation Administration (FAA) and the Department of Transportation (DOT) in US developed WAAS to meet the FAA's navigation requirement. This includes accuracy, integrity and availability. WASS consists of a number of ground reference stations which collect and create a correction message. The uploaded correction message (which includes satellite orbit, clock drift and signal path delay) are then transmitted over North America via geostationary satellites. A WAAS enabled receiver can directly correct the errors on the observables without the help of any other secondary devices. Due to the benefit of the system, a few countries are trying to develop their own augmentation system which includes MSAS (Japanese Multi-Functional Satellite Augmentation System), EGNOS (European Geostationary Navigation Overlay Service), and GAGAN (GPS Aided Geo Augmented Navigation by India). Figure 2.5 represents WAAS with a thin-shell (like a planar fit) approximation.

For a single frequency user, the ionospheric correction model such as the Klobuchar model can be used [*Klobuchar*, 1996]. The model coefficients are transmitted as a part of GPS satellite message. The model is described by a total of eight coefficients. Using the model, the ionospheric delay at mid latitude can be reduced by 50%. For a dual frequency user, it is possible to derive the ionospheric-free (IF) linear combination, which can be used to eliminate the first order ionospheric effects using the L1 and L2 phase measurements. In this case, the combination looks like:

$$\Phi_{IF} = \frac{f_{L1}^2}{f_{L1}^2 - f_{L2}^2}\Phi_{L1} - \frac{f_{L2}^2}{f_{L1}^2 - f_{L2}^2}\Phi_{L2} \tag{2.25}$$

where,

Φ_{IF} : IF observables,

f_{L1} : L1 frequency,

f_{L2} : L2 frequency,

Φ_{L1}, Φ_{L2} : Phase observables for L1 frequency, L2 frequency.

This IF linear combination significantly reduces the ionospheric error, but it cannot completely remove the errors[4], as it neglects the higher-order terms which remain in the series expansion of the refractive index (see Equation 2.14 and Equation 2.15), which represent the effect of the geomagnetic field, and the bending effect of the wave paths. Due to the combination, the ambiguity is no longer an integer property in Equation 2.1.

Bassiri and Hajj [1993] developed an approximate method to describe the higher ionospheric effects, for average conditions, and showed that the level of the error of the second order effects S_{ion}^{2nd} is in the range of 1 cm, with a maximum of less than 3cm, using the IF combination.

$$S_{ion}^{2nd} \approx \left(1.377 \times 10^{-6} \varphi \frac{r_E}{r_E + h_{ion}}\right)^3 |\sin\theta'_M \cos\epsilon_E \cos\alpha_M - 2\cos\theta'_M \sin\epsilon_M| \times m_{ion}(z_{IP}^i)\mathrm{VTEC} \tag{2.26}$$

$$\theta'_M \approx \theta_M - \frac{h_{ion}}{r_E}\frac{\cos\alpha_M}{\tan\epsilon_M}$$

where,

[4]The higher order contribute less than 0.1% but it can be reached up to a few cm level under the worst conditions [*Brunner and Gu*, 1991].

φ : geodetic latitude,

α_M : geomagnetic azimuth,

θ'_M : pole distance,

θ_M : geomagnetic pole distance,

ϵ_M : geomagnetic elevation angle,

VTEC : vertical TEC.

Table 2.2 shows the maximum range errors in the vertical direction that can be expected for the dual frequency observations and IF combination as quantified by Wübbena [1991].

Table 2.2: Maximum vertical ionosphere range error (m)

Frequency	1^{st}order effect($1/f^2$)	2^{nd}order effect($1/f^3$)	3^{rd}order effect($1/f^4$)
L_1	32.5	0.036	0.002
L_2	53.5	0.076	0.007
IF	0.0	0.026	0.006

Although the IF combination eliminates the ionospheric effects to a considerable degree, this does not mean that this combination can give us the best solution for all networks. For example, in a small network, even if the combination reduces the ionopheric errors, the noise of the combination is almost three times higher, resulting in accuracies that are three times worse for the stations' coordinates. This is one of the limitations in using this combination in a small network. Higher accuracy using fixed ambiguities of L1 and L2 could be possible, but it also needs an additional combination to resolve the individual ambiguities first. For a smaller network or baseline which is less than 10 km, the best approach to achieve a highest positioning precision result might be still from a single L1 phase observables, provided the integer ambiguities are correctly resolved.

Except in the case of the IF linear combination, ionospheric refraction represents the largest of the error sources for all other linear combinations, including: wide-lane, narrow-lane, geometry-free, and Melbourne-Wübbena (see Hugentobler et al. [2005]), as well as for the original L1 and L2 measurements. In differential positioning, the ionosphere can cause delays in excess of 20 ppm, in the code measurements, and also the signals may be advanced by about the same amount, in the phase measurements. Therefore, the code minus phase measurement is a good indicator in estimating the ionospheric effects.

The ionosphere changes very fast, especially during scintillation at high or low latitudes, and trough phenomena below the auroral oval, which has 10 $\sim$15 ppm gradients at $35^\circ \sim 45^\circ$ latitudes, and storm-enhanced density generated when the plasma goes into the sub-auroral region, which has up to 75 ppm gradients [*Skone*, 2003]. In this case, it would be better to estimate these ionospheric effects using stochastic ionosphere parameters (SIPs). Unlike the deterministic component of the ionosphere, which may be modelled by mathematical functions, the stochastic part of the TEC represents the residuals of the modelling that are due to the magnitude of short term fluctuations in the TEC. Using fixed double difference ambiguities, these SIPs for the ionosphere can be computed at the double difference level, either by analyzing the L1-L2 linear combinations, or by simultaneously analyzing the original L1 and L2 measurements [*Schaer*, 1999]. The main procedure for the stochastic ionospheric estimation is that, at the beginning, the L1 and L2 observations are processed simultaneously, and for each satellite and each epoch, one ionosphere parameter is set up, and then the ionosphere parameters are constrained with a priori weights, or a process noise in a filter. Stochastic ionosphere modeling and parameterization is necessary in many cases, because short-period variations cannot be

taken into account in global, regional, or even local ionosphere models [*Hugentobler et al.*, 2005]. In addition, Skone [2008] showed that the temporal stability of the ionospheric error was degraded under active ionospheric conditions. One of the good indicators of the storm activity is based on the K_p index. If K_p values exceeds 5, this means relatively quiet to moderate ionospheric activity. A 3 hour K_p index over three days with actual and predicted values can be found on the following link: *http://www.swpc.noaa.gov/products/planetary-k-index.*

2.2.4 Multipath

Multipath is also considered as one of the major error sources in GNSS. The effect happens when a transmitted signal arrives at the receiver via multiple paths due to unwanted reflection and diffraction. Technically, the multipath is similar to a ring or ghosting effect. When multipath is present and compared to the light-of-sight signal path, this distortion are always delayed as the wave will take longer paths due to the reflected surfaces. A satellite itself may also experience multipath during the signal transmission but the effect of the satellite is minimal on a short baseline in a single-difference observables [*Leick*, 2004]. Most prominent multipath happens in the surroundings of the receiver, e.g. from buildings, streets, waterways, and vehicles. The reflected signal is always weaker because of the attenuation of the reflector which is dependent on the material itself, incident angle and the polarization of the reflector. The signal attenuation due to reflection of a wave signal causes trouble not only on GNSS surveyor but also for a conventional surveyor, especially a reflectorless EDM (Electronic Distance Measurement) user. In general, a higher incident angle tend to generate more multipath interference and therefore a satellite on a lower elevation angle tends to have more interference. The multipath signature for consecutive days shows a very similar pattern as the geometry of the satellite and receiver repeats every sidereal day (see Figure 2.6). In static surveying, this is a useful

feature of the multipath effect; by experiencing multipath over a number of days at the same location. This eventually enables a spatial and temporal mitigation model at the specific location to be created. The receiver receives many different satellite signals from many direction and the intensity should be all different. By having a better antenna, e.g. choke ring, (specifically resistant to the multipath effect) or a better cable, one can mitigate much of the multipath effect.

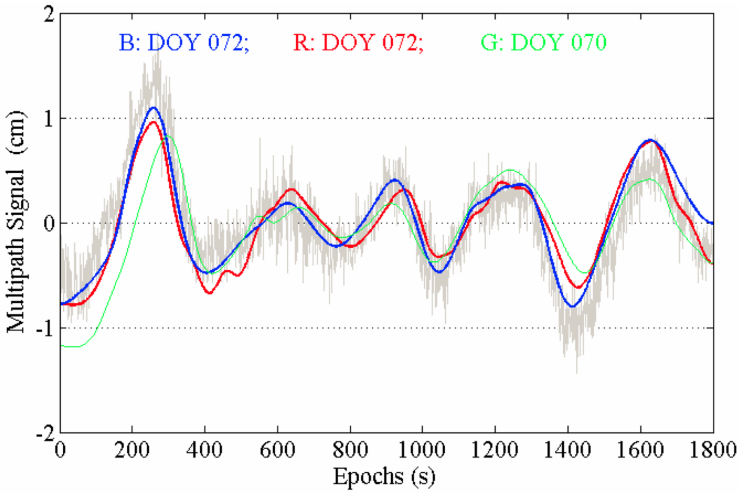

Figure 2.6: Multipath daily repeatability in a short baseline [*Hsieha and Wu*, 2008] [5]

Reflection and scattering of an electro-magnetic (EM) wave from a surface has two components; specular and diffused. Diffused scattering is irregular, non-coherent and non-deterministic and occurs on rough surface. Diffraction, however, occurs when the signal hits the sharp edge or a rounded object. In Figure 2.7, specular reflections and diffracted paths are depicted. The choke ring antenna especially prevents these kind of diffracted signals. As the multipath error is affected by correlator spacing and bandwidth, the use of the narrow correlator can reduce the amount of the multipath error. Even with the use of narrow-correlator, the error due to the multipath

[5]The baseline length of the processed data is 23122.72 m collected in 2006. It shows temporal variations of the double-differenced multipath signal.

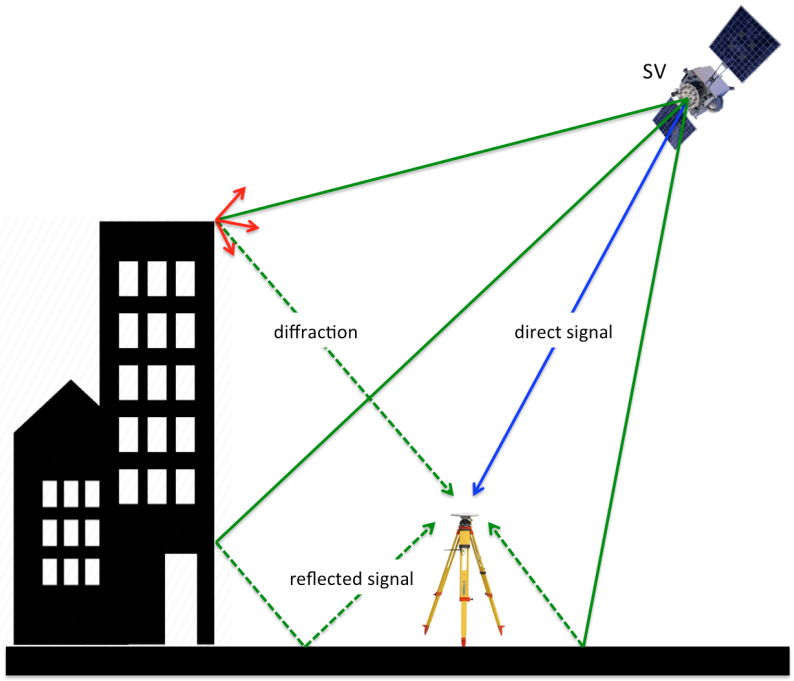

Figure 2.7: Geometry of multiple multipath specular reflections upon a static GNSS receiver

can have a magnitude of a few metres, and a few centimetres for code and carrier phase observables, respectively. The effect is more complicated in a moving platform as the dynamics and reflection condition change continuously.

In brief, the direct and the reflected signals at the antenna phase centre can be written as follows [*Seeber*, 1993]:

$$A_D = A\cos\Phi_D \qquad \text{and} \qquad A_R = \alpha_{mul} A\cos(\Phi_D + \Phi_R) \tag{2.27}$$

where,

A_D : amplitude of the direct signal,

A_R : amplitude of the reflected signal,

α_{mul} : damping factor ($0 \leq \alpha_{mul} \leq 1$),

0 : no reflection

1 : reflected signal as strong as direct signal

Φ_D : phase position of the direct signal,

Φ_R : phase shift of the reflected signal with respect to the phase of the direct signal.

The amplitude of the indirect signal is reduced by the damping factor α_{mul} which is dependent on the characteristics of the reflection at the surface. The phase of the indirect signal Φ_D is delayed by the phase shift Φ_R which is a function of the geometry between a satellite, receiver, and reflector. The superposition of two sinusoidal terms gives:

$$A_\Sigma = A_D + A_R = A\cos\Phi_D + \alpha_{mul}A\cos(\Phi_D + \Phi_R) = \beta A\cos(\Phi_D + \Theta) \tag{2.28}$$

With $A_{D,max} = A$ and $A_{R,max} = \alpha_{mul}A$, the equation for the resultant multipath error in the observed carrier phase can be written as follows:

$$\Theta = \arctan\left(\frac{\sin\Phi_R}{\alpha_{mul}^{-1} + \cos\Phi_R}\right) \tag{2.29}$$

The signal amplitude is

$$B = \beta A = A\sqrt{1 + \alpha_{mul}^2 + 2\alpha_{mul}\cos\Phi_R} \tag{2.30}$$

Equations 2.29 and 2.30 tells that as $\alpha_{mul} \to 1$, $\Theta \to 90°$. Therefore, the theoretical maximum effect of multipath on carrier phase measurements would be about 5 cm in the L1 signal ($\lambda = 19.05$ cm) as $\Phi_R = 90° = 1/4$ cycle. In addition, Georgiadou and Kleusberg [1988] demonstrated that a height error due to the multipath can reach $\pm$15 cm. Depending on a damping factor, carrier phase multipath behaviour reveals

a completely different signature.

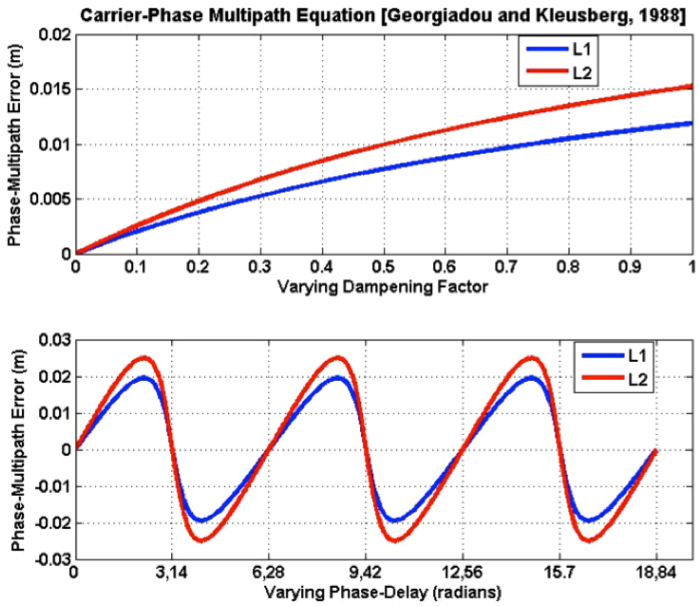

Figure 2.8: Example of carrier-phase multipath behavior [*Georgiadou and Kleusberg*, 1988]

Figure 2.8 is an example plot for varying damping-factor versus phase multipath error at $\Phi_R = 45°$ (top panel). The lower panel is for varying the phase-delay error when the damping-factor is set to 0.6.

The multipath effects on code and carrier phases have been thoroughly studied from early 1980s. These includes detailed physical understanding of the phenomena, mathematical interpretation, new technological advancement of the receiver and antenna design, and modelling of the surroundings at the receiver. Some of modelling and simulation results of GPS multipath propagation on a different terrestrial environment are described on Hannah [2001]. Due to the complexity, much of the research have been focused on a static scenario. A recent approach, however, is to deal with kinematic applications, e.g. RTK-based dual antenna system for multipath error mitigation [*Serrano*, 2013].

2.2.5 System noise

There are many different error sources affecting on GNSS observables. Some of the important error sources are described in earlier section. The errors associated with the receiving system includes receiver noise, phase delay, oscillator's stability, phase centre offset & variations, phase delay variation, interchannel bias, and cables. One of the common mistakes, however, happens when the user may under-estimate the impact on the overall system noise effect, for example, by a cable. This is a simpler example to deal with compared to other system noise effects. The precision of the code and phase measurement is largely dependent on how much noise accompanies the signal in the receiver's tracking loops. The noise may be coming from the receiver electronics itself or from receiver's antenna [*Langley*, 1997].

The antenna noise temperature is one of two components contributing to the overall system noise performance of a GNSS receiver. The other component is the receiver's equivalent noise temperature, which is a combination of cable losses and the noise internally generated in the receiver. If the source of temperature T does not extend over the entire antenna reception pattern, the detected noise power, and hence temperature, will be less. This detected temperature is called the antenna temperature. If the antenna is a hypothetical isotropic type, with unit gain in all directions, then the antenna temperature is given by Langley [1997]:

$$T_a = \frac{\Omega_s}{4\pi} T_{avg} \tag{2.31}$$

where,

Ω_s : solid angular extent of the noise source,

T_{avg} : average noise temperature of the source across the antenna reception pattern.

The antenna noise temperature, T_a, must be corrected for the contribution by the cable between the antenna and the receiver or antenna preamplifier input. As there is no perfect cable, a signal traveling through the cable is attenuated. But not only does the cable component reduce the signal level, it also adds to the noise. If L_{sn} is the total loss in the cable (power in divided by power out; $L_{sn} > 1$), then the total antenna temperature is given by

$$T_{ant} = \frac{T_a}{L_{sn}} + \frac{L_{sn} - 1}{L_{sn}} T_\circ \tag{2.32}$$

where $T_\circ$ is the cable's ambient temperature. Alternatively, this could be written as follows:

$$T_{ant} = \alpha_{sn} T_a + (1 - \alpha_{sn}) T_\circ \tag{2.33}$$

where,

$\alpha_{sn} (= 1/L_{sn})$: fractional attenuation $(0 \leq \alpha_{sn} \leq 1)$.

This equation is of the same form as the equation of radiative transfer found in physics. In fact, the physics of emission and absorption of electromagnetic radiation by a cloud of matter is similar to the emission and absorption taking place in an antenna cable [*Langley*, 1997]. We now have a measure of the noise level that can contaminate a GPS observation and we can compare it with the power of a GPS signal. In the absence of any GPS signal, the receiver and its associated antenna and preamplifier will detect a certain noise power, N. We can use the ratio of the power of a received signal S, and the noise power N, measured at the same time and place in a circuit as a measure of signal strength. Obviously, the larger the S/N value, the stronger the signal. We usually make signal-to-noise measurements of signal at

baseband (the band occupied by a signal after demodulation). At radio and intermediate frequencies (RF and IF), we commonly describe the signal level with respect to the noise level using the carrier-to-noise-power-density ratio, $C/N_{\circ}$. This is the ratio of the power level of the signal carrier to the noise power in a 1-Hz bandwidth. It is a key parameter in analyzing GNSS receiver performance and directly affects the precision of the receiver's pseudoranges and carrier phase observations.

To see and test the effect of the different cables, I used the SPIRENT^{TM} STR4760 GNSS simulator was used. All of the cables have often been used for GPS surveys. For the test, the NovAtel^{TM} Propak-V3 receiver was used.

Table 2.3: Specification of each cable tested

	Manufacturer	Model	Length	Recom. Use	nominal attenuation
No.1	Huber & Suhner	RG303U	14 m	<1 GHz	0.46 dB/m (1 GHz at 25°)
No.2	Trimble	41300-10	10 m	N/A	N/A
No.3	Huber & Suhner	RG223U	5 m	<6 GHz	0.57 dB/m (1.5 GHz at 25°)
No.4	LMR	LMR400	10 m	<16.2 GHz	16.8 dB / 100 m (1.5 GHz at 25°)
No.5	Trimble	41299	1 m	N/A	N/A

Each simulation test was controlled by SimGEN^{TM} control software with exactly the same scenario. Each test period was about 30 minutes. After each test was finished, the data were collected for the further analysis. Table 2.3 shows some details of each cable which was used for the test. Some specifications could not be found which are denoted by N/A in the Table.

Figure 2.9 provides an insight of the importance of the cable selection depending on the engineering survey needs. The figure shows each SNR for a different cable for

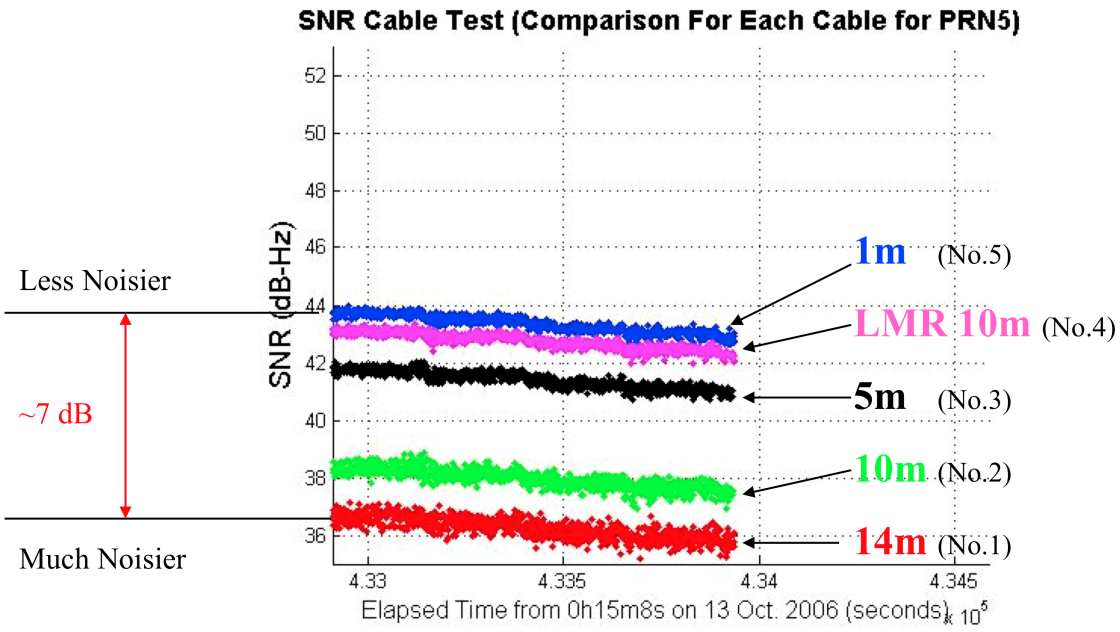

Figure 2.9: Noise test for five different cables using a SPIRENT simulator

the same PRN5 satellite as an example. As clearly seen from the figure, comparing for 10m cables, the high-end LMR 10 m thick antenna cable shows much better performance than the thin 10 m Trimble cable. From the test, we found that the difference of SNR between cables can reach up to 7 dB. From this test, we could also confirm that as a satellite sets to the horizon, the tracked signals are prone to be nosier than a higher elevation angle.

Without considering the antenna cable effect, as a rule of thumb, the observation resolution for the traditional GPS receiver is about 1% of the signal wavelength and the modern receiver be even lower. Table 2.4 shows typical GPS range noises [*Hofmann-Wellenhof et al.*, 2008].

Table 2.4: Typical GPS range noise figures

	wavelength	noise
C/A-code	$\lambda \approx 300m$	$10 \sim 300cm$
P-code	$\lambda \approx 30m$	$10 \sim 30cm$
Carrier	$\lambda \approx 20cm$	$0.2 \sim 5mm$

2.3 Summary

In this chapter, the theoretical background of GNSS has been discussed, and the errors affecting GNSS signals have been distinguished into two different groups. Especially, the orbit errors, ionosphere errors, multipath, and system noise from antenna cables have been reviewed. In Chapter 3, the error mitigation for the troposphere will be discussed in detail. This includes the general theory, a few important tropospheric error mitigation strategy based on theoretical and empirical models, the background of raytracing based on NWP, and radiosondes. Chapter 3 also includes some experimental results that show the importance of GNSS technology in neutral atmosphere research.

Chapter 3

Troposphere Error Mitigation

3.1 Troposphere

The troposphere is part of the neutral atmosphere, ranging from sea level to a height of about 12 km. The tropopause is a small boundary region between 12 km and 16 km where the temperature remains approximately constant at a level of $-60°$C to $-80°$C [*Schuler*, 2001]. The upper part above the tropopause is referred to as the stratosphere, up to an altitude of 40 km with a slow temperature increase. In GNSS, the "troposphere" generally refers to the neutral atmosphere at altitudes 0 to 40 km [*Skone*, 1998]. At the GNSS signal frequencies, the troposphere is a non-dispersive medium (i.e., no frequency dependence in signal transmissions), and hence it affects the L1 and L2 signals by the same amount, unlike the effect of the ionosphere.

The tropospheric effect on GNSS signals can be divided into two different components: the hydrostatic (or $'$dry$'$) part, and the non-hydrostatic (or $'$wet$'$) part. The hydrostatic and non-hydrostatic refractivity of the troposphere cause delays in the signals. Most of the total delay is due to the hydrostatic component, while the

non-hydrostatic component is responsible for approximately 10% of the total delay. Various tropospheric delay models have been developed to estimate these delays, as a function of the satellite elevation angle, receiver height, and meteorological parameters, such as temperature, pressure, and humidity. The range delay in the zenith direction is approximately 2.5 m which corresponds to about $8ns$; however, for an elevation of 5°, it increases to about 25 m. This dependence on elevation angle is described by a mapping function, so that the delay near the horizon is three to five times higher than in the zenith direction. Most of the delay is mitigated in differential positioning; however the residual tropospheric delay increases as the baseline length increases.

Unlike the ionospheric errors and orbital errors, which can be reduced to sufficiently low manageable levels, errors in the tropospheric delay, which mostly contribute to errors in the height component in the station′s coordinate estimates, are known to be one of the largest limiting factors for high accuracy GNSS positioning, at the current time.

3.2 Principles of GNSS Signal Delay

The neutral atmosphere can be divided into the troposphere, the tropopause and the stratosphere. The tropospheric delay of GNSS signals depends on the index of refraction n along the signal path. For radio waves up to 15 GHz propagating through the atmosphere along a path s, the length L_e of the signal path can be calculated by Fermat′s principle (similar to Equation 2.18):

$$L_e = \int_{path} n(s)ds \tag{3.1}$$

where,

$n(s)$: index of refraction as function of the distance s

The geometrical distance is different from the actual path due to the difference between the path delays in the troposphere versus a vacuum, and in reality is given as follows:

$$\delta T = \int_{path} n(s)ds - \int_{vacuum} ds = \int_{path} (n(s) - 1)ds + \text{bending effect} \tag{3.2}$$

which is also called total or neutral slant path delay.

For elevation angles above 15°, the bending effect is less than 1 cm; however, for smaller elevations, the effect can be as larger as $2 \sim 3$ cm. This total delay can be divided into a hydrostatic component ($\delta\rho_h$) and a non-hydrostatic component ($\delta\rho_w$) as follows:

$$\delta T = \delta T_h + \delta T_w \tag{3.3}$$

However, this can be expanded to further distinguish between the azimuthally symmetric delay and asymmetric parts [*Schuler*, 2001].

$$\delta T = \delta T_{h,sym} + \delta T_{h,asym} + \delta T_{w,sym} + \delta T_{w,asym} \tag{3.4}$$

where,

$\delta T_{h,sym}$: hydrostatic delay term under the assumption of symmetry in azimuth,

$\delta T_{w,sym}$: non-hydrostatic delay term under the assumption of symmetry in azimuth,

$\delta T_{h,asym}$: hydrostatic correction term taking asymmetry into account,

$\delta T_{w,asym}$: non-hydrostatic correction term taking asymmetry into account.

Equation 3.4 can be further expanded when the horizontal tropospheric gradient model is applied to the above asymmetric components as follows:

$$\delta T = m(\epsilon)_h \cdot \mathrm{ZHD} + m(\epsilon)_w \cdot \mathrm{ZWD} + m(\epsilon)_{azi} \cdot [G_{north} \cdot \cos\alpha_{azi} + G_{east} \cdot \sin\alpha_{azi}] \quad (3.5)$$

where,

$m(\epsilon)$: mapping function,

ZHD : zenith hydrostatic delay,

ZWD : zenith wet delay,

G_{north} : gradient in northward direction,

G_{east} : gradient in eastward direction,

α_{azi} : azimuth,

h, w : subscript for hydrostatic or non-hydrostatic component.

The tropospheric delay model most widely used is the one without the gradient components. The zenith delay model as well as the mapping function is further explained in section 3.3.

In Equation 3.1, the index of the refraction, n (ratio of the speed of the propagation of electromagnetic wave in vacuum to the speed of the propagation of the medium), can be expressed in term of the refractivity index N_t as follows:

$$N_t = 10^6(n-1) \quad (3.6)$$

The refractivity of humid air in the frequency band between 100 MHz and 20 GHz is given by Thayer [1974] as follows:

$$N_t = k_1 \frac{p_d}{T} Z_d^{-1} + k_2 \frac{e_w}{T} Z_w^{-1} + k_3 \frac{e_w}{T^2} Z_w^{-1} \tag{3.7}$$

where,

p_d : partial pressure of dry air $(mbar)$; $p_d = p_t - e_w$ with p_t being the total pressure,

e_w : partial pressure of water vapour $(mbar)$,

T : temperature $(^\circ K)$,

k_1, k_2, k_3 : refraction constants $(^\circ K/mbar, ^\circ K/mbar, ^\circ K/mbar^2)$,

Z_d^{-1}, Z_w^{-1} : inverse compressibility factors for dry and wet air which are empirical factors.

Atmospheric refractivity relies on pressure and compressibility of the gases, but also depends on the electric properties of the molecules. The molecules act like tiny dipoles and cause a dipole moment affecting the radio wave. In case of O_2 or N_2, there exists only an induced dipole moment, but there is a permanent dipole moment in water vapour.

The first term in Equation 3.7 is the hydrostatic component and represents the effect of the induced dipole moment of the dry component, while the second term is related to the dipole moment of water vapour and the last term represents the dipole orientation effects of the permanent dipole moment of water vapour molecules. The last two terms in Equation 3.7 constitutes to the wet component of the refractivity. The refraction constants k_1, k_2, k_3 are determined empirically. The inverse compressibility accounts for the difference between ideal gas assumptions and non-ideal gas behaviour. These values and the pressure of water vapour are found on Schuler

[2001], Thayer [1974] and Hugentobler et al. [2005] as follows:

$$
\begin{aligned}
Z_d^{-1} &= 1 + p_d\left(57.97 \cdot 10^{-8} \cdot \left(1 + \frac{0.52}{T}\right) - 9.4611 \cdot 10^{-4} \cdot \frac{T_c}{T^2}\right) \\
Z_w^{-1} &= 1 + 1650\frac{e_w}{T^3}\left(1 - 0.01317 \cdot T_c + 1.75 \cdot 10^{-4} \cdot T_c^{-2} + 1.44 \cdot 10^{-6} \cdot T_c^{-3}\right) \\
e_w &= \frac{H_{rh}}{100} e^{-37.2465 + 0.213166T - 0.000256908T^2}
\end{aligned}
\tag{3.8}
$$

where,

T_c : temperature (°C),

T : temperature (°K),

H_{rh} : relative humidity (%).

These inverse compressibility factors, i.e. Z_d^{-1} and Z_w^{-1}, for dry and wet air are empirical factors and can be modeled as a function of pressure and temperature as shown in Equation 3.8.

In order to define the zenith delay, it is necessary to express the refractivity in Equation 3.7 in terms of its hydrostatic and non-hydrostatic components. With the assumption of the hydrostatic equilibrium, the following relationship can be made:

$$
\begin{aligned}
k_1 \frac{p_d}{T} Z_d^{-1} &= k_1 \frac{\rho_d R_d T Z_d}{T} Z_d^{-1} = k_1 \rho_d R_d \\
&= k_1 \frac{\rho_d R_o}{M_d} = k_1 \left(\frac{\rho_t R_o}{M_d} - \frac{e_w}{T} Z_w^{-1} \frac{M_w}{M_d}\right)
\end{aligned}
\tag{3.9}
$$

where,

R_o : universal gas constant ($= 8.31434 J\ mol^{-1}\ {}^\circ K^{-1}$),

R_d : specific gas constant for dry air ($= 287.054 J\ mol^{-1}\ {}^\circ K^{-1}$),

M_w : molar weight of wet air ($= 18.0152 kg\ kmol^{-1}$),

M_d : molar weight of dry air ($= 28.9644 kg\ kmol^{-1}$),

ρ_d : density of dry air ($kg\ m^{-3}$), [6]

ρ_t : total density for dry and wet air ($kg\ m^{-3}$).

Substituting Equation 3.9 into Equation 3.7, the refractivity can be rewritten as follows:

$$\begin{aligned} N_t &= k_1 \left(\frac{\rho_t R_o}{M_d} - \frac{e_w}{T} Z_w^{-1} \frac{M_w}{M_d} \right) + k_2 \frac{e_w}{T} Z_w^{-1} + k_3 \frac{e_w}{T^2} Z_w^{-1} \\ &= k_1 \frac{\rho_t R_o}{M_d} + k_2' \frac{e_w}{T} Z_w^{-1} + k_3 \frac{e_w}{T^2} Z_w^{-1} \end{aligned} \tag{3.10}$$

$$k_2' = \left(k_2 - k_1 \frac{M_w}{M_d} \right) \tag{3.11}$$

where,

$k_1 = 77.60 \pm 0.09\ ^\circ K/hPa$,

$k_2 = 69.4 \pm 2.2\ ^\circ K/hPa$,

$k_2' = 22.1 \pm 2.2\ ^\circ K/hPa$,

$k_3 = (3.701 \pm 0.012)\ 10^5\ ^\circ K^2/hPa$.

Equation 3.10 is useful, as it allows a strict separation between the hydrostatic and non-hydrostatic components. The hydrostatic component, from Equation 3.10 is

$$N_d = k_1 \frac{\rho_d R_o}{M_d} \tag{3.12}$$

and the non-hydrostatic component is

[6] Standard values can be found on International Standard Atmosphere

$$N_w = \left(k_2' \frac{e_w}{T} + k_3 \frac{e_w}{T^2} Z_w^{-1} \right) \tag{3.13}$$

The zenith hydrostatic delay and the zenith non-hydrostatic ('wet') delay can be defined as follows:

$$\text{ZHD} = 10^{-6} \int_{h_s}^{\infty} N_d dh \tag{3.14}$$

$$\text{ZWD} = 10^{-6} \int_{h_s}^{\infty} N_w dh \tag{3.15}$$

where,

h_s : surface height,

dh : differential increment in height.

Almost 90% of the total delay occurs in the hydrostatic part, which varies slowly with time. This hydrostatic delay can be easily modelled by the assumption of hydrostatic equilibrium with an accuracy at the millimetre level [*Mendes et al.*, 1995]. However, unlike the hydrostatic part, the non-hydrostatic part (which amounts for approximately $10 \sim 40$ cm of range delay) is much more difficult to model than the hydrostatic part, due to its strong spatial and temporal variations. The assumption of hydrostatic equilibrium does not hold for this portion of the air and relative errors of empirical, theoretical models are on the order of 10%.

This uncertainty in the modelling (which leaves large residual errors) can cause significant errors in high-precision GNSS RTK applications. Since these variations

can generate relative and absolute tropospheric errors, the error in the estimation of tropospheric corrections for one station with respect to another in a network can cause relative tropospheric errors, which mostly results in incorrect estimates of the station′s height.

To reduce or minimize these errors arising from poor modelling of the wet troposphere, one possibility is to model the tropospheric refraction without the benefit of GNSS observations using independent datasets; and the other is to estimate the tropospheric parameters directly using available GNSS data. Existing theoretical models are described in the next section.

3.3 Mitigation Models

To model the troposphere hydrostatic delay, many models use information about the surface pressure, temperature, and relative humidity to derive zenith or slant delay estimates. However, almost all models require certain conditions in, or make assumptions about, the atmosphere above the station. Some commonly-used models for the tropospheric delay are, e.g., Modified Hopfield (from Goad and Goodman[1974]), Saastamoinen [1972], Hopfield [1969], Essen and Froome [1971], Lanyi [1984], Davis et al. [1985], Herring [1992] and Niell [1996].

The most commonly used approach uses the Saastamoinen model with the Neill mapping function and the troposphere model, i.e. UNB3 model which is discussed in section 3.3.1 and 3.3.3.

3.3.1 Saastamoinen Model

This model also assumes that the atmosphere is in hydrostatic equilibrium which follows from the ideal gas law. While the Hopfield model assumes the gravity acceleration is not changed with height, it is treated as a function of height in the Saastamoinen model. In more detail here, under hydrostatic equilibrium, the local pressure, which is assumed to be isotropic, provides the balancing force against the atmospheric weight per unit area. The equation of the state of the hydrostatic equilibrium can be written as follows:

$$dp = -g \cdot \rho \cdot \ dH \tag{3.16}$$

where,

dp : differential change in pressure $(mbar)$,

g : gravity change with height (m/s^2),

ρ : density (kg/m^3),

dH : differential change in height (m).

With the introduction of the weighted mean gravity acceleration g_m, the above equation can be rewritten as follows:

$$\rho = -\frac{1}{g_m}\frac{dp}{dH} \tag{3.17}$$

Equation 3.12 can be then rewritten using the introduction of the mean gravity acceleration as follows:

$$N_d = k_1\frac{\rho_d R_o}{M_d} = k_1 R_d \rho = -k_1 R_d \frac{1}{g_m}\frac{dp}{dH} \tag{3.18}$$

When the above equation is substituted to the Equation 3.14, we get,

$$\begin{aligned} \text{ZHD} &= 10^{-6} \int_{H_s}^{\infty} N_d dh = -10^{-6} k_1 R_d \frac{1}{g_m} \int_{p_s}^{\infty} dp \\ &= 10^{-6} k_1 R_d \frac{p_s}{g_m} = 0.022275 \frac{p_s}{g_m} \end{aligned} \tag{3.19}$$

where,

g_m : the weighted mean gravity acceleration,

p_s : surface pressure.

g_m is defined as the gravity acceleration at the centre of mass of the vertical atmospheric column directly above the station and can be approximated by the Saastamoinen equation as follows [*Davis et al.*, 1985]:

$$\begin{aligned} g_m &= 9.784 \ (1 - 0.00266 \cos 2\varphi_{lat} - 0.00028 H_{hgt}) \\ &= 9.784 \ f(\varphi_{lat}, H_{hgt}) \end{aligned} \tag{3.20}$$

where φ and $H(km)$ are the latitude and height of the station, respectively.

Therefore, the ZHD can be written as follows:

$$\text{ZHD} = \frac{0.0022767 p_s}{1 - 0.00266 \cos 2\varphi_{lat} - 0.00028 H_{hgt}} \tag{3.21}$$

For the ZWD, Saastamoinen [1972] assumed that the water vapour pressure and temperature decrease with height as follows:

$$e_w = e_s \left(\frac{T}{T_s} \right)^{\frac{vg}{R_d \alpha_{lr}}} \tag{3.22}$$

where,

e_s : water vapour pressure at the surface ($mbar$),

v : numerical coefficient to be determined from local observations,

α_{lr} : temperature lapse rate ($^\circ K/km$),

T_s : temperature at surface (or antenna) height ($^\circ K$).

The final expression for the zenith wet delay according to Saastamoinen [1972] is:

$$\text{ZWD} = 0.002277 \left(\frac{1255}{T_s} + 0.05 \right) e_s \tag{3.23}$$

The Saastamoinen ZHD and ZWD model is generally used for the tropospheric delay model due to its model accuracy. Mendes and Langley [1995] showed that the root mean squared (rms) error of the ZHD of this model is less than 1 millimetre and that of the ZWD reaches from 8 to 46 mm with respect to ray-tracing values from radiosonde data in selected areas. A ray-tracing technique is described in Section 3.4.

3.3.2 Mapping Functions

The tropospheric delay is the shortest in the zenith direction, and becomes larger with increasing zenith angle. Using a mapping function, the zenith path delay can be projected onto a slant direction. Similar to the tropospheric models, there are many mapping functions that have been proposed, such as: cosecant, Hopfield [1969], Chao [1972], Black [1978], Davis et al. [1985], Baby et al. [1988], Herring [1992], Niell [1996].

The mapping functions are approximately equal to the cosecant of elevation angle, but there are significant deviations from this "cosecant law" due both to the curvature of the earth and the curvature of the path of the GNSS signal propagating through the atmosphere. The cosecant mapping function is $1/\cos(\epsilon)$ where the ϵ is the elevation angle . Due to the large deviations for lower elevation angles, however, this function is limited to use below about 60 degrees elevation.

The Hopfield mapping function is based on the quartic refractivity profiles [*Hopfield*, 1969]. While a constant temperature lapse rate is used to derive the Hopfield mapping function, the Chao [1972] model, which is an expansion of the Marini [1972] model, uses the elevation angle in his mapping function, and defines the coefficients as global constants within a fractional expansion truncated to the second order terms. Despite its simplicity, the Chao mapping function proved to be unexpectedly precise [*Schuler*, 2001]. The Black [1978] model depends slightly on the surface temperature and is based on the quartic profiles by Hopfield [1969]. Davis et al. [1985] requires surface meteorological data, e.g. temperature, pressure and water vapour pressure. This mapping function depends on the surface pressure, temperature, temperature lapse rate, and tropopause height. Herring [1992] calculates the coefficients of his function based on ray-tracing of radiosonde data for 10 sites in North America from 27°N to 65°N, for elevation angles down to 3°, and these coefficients are dependent on the surface pressure, site latitude and height above sea level.

Typical accuracies of the existing mapping functions are similar for higher elevation angles. At about 15° elevation, most of the mapping functions show sub-centimetre accuracies [*Mendes and Langley*, 1994]. However, they start to exhibit very important differences for lower elevation angles, due to the drastic increase in tropospheric

model errors as the atmospheric depth increases. Therefore, the user should select the mapping function very carefully. Even if a mapping function is performing very well in the polar regions, it should not be used in the same way in the equatorial regions, or near coastal regions, due to the uncertainties of the model in these regions.

The mapping functions of Arthur Niell, developed using radiosonde data over a wide range of latitudes, are the most widely used, and are known to be the most accurate and easily-implemented functions. In detail, Niell [1996] uses the continued fraction form as follows:

$$m_{niell}(\epsilon) = \frac{\dfrac{1}{1+\dfrac{a}{1+\dfrac{b}{1+c}}}}{\sin(\epsilon)+\dfrac{a}{\sin(\epsilon)+\dfrac{b}{\sin(\epsilon)+c}}} \tag{3.24}$$

The coefficients a, b, and c are evaluated by using standard meteorological data which is dependent on the latitude, and takes seasonal variations into account. To realize the mapping function, those coefficients must be determined. The atmospheric model chosen affects to the model coefficients, and so different mapping function result. A typical case is the differences between Neill mapping function and Vienna mapping function (VMF). They use the same mapping model like Equation 3.24, but different atmospheric models. The VMF is based on direct raytracing technique through a numerical weather prediction model. Both Neill and VMF models take into account the temporal and spatial behaviour. For the hydrostatic part, these

coefficients are determined based on the height, latitude and day of year (DOY). However, the wet mapping function only depends on latitude. The coefficients of the Neill mapping function are calculated by the equation:

$$a(\varphi_i, t) = a_{avg}(\varphi_i) - a_{amp}(\varphi_i) \cos\left(2\pi \frac{t - t_{mw}}{365.25}\right) \tag{3.25}$$

where,

φ_i : site latitude,

a : mapping function coefficient, separated into average value and amplitude,

t : time (day of year),

t_{mw} : day of year for maximum winter which is set to 28 days for the northern hemisphere and 211 for the southern hemisphere.

The coefficients of a, b, c in Equation 3.24 for latitude are calculated by linear interpolation for both the hydrostatic part and non-hydrostatic part; however, the seasonal variations are subtracted from the average values. The coefficients for the Neill hydrostatic and non-hydrostatic mapping functions are given in Tables 3.1 and Table 3.2.

Table 3.1: The coefficients for Neill hydrostatic mapping function

	$\varphi_i = 15°$	$\varphi_i = 30°$	$\varphi_i = 45°$	$\varphi_i = 60°$	$\varphi_i = 75°$
$a_{avg} \cdot 10^3$	1.2769934	1.2683230	1.2465397	1.2196049	1.2045996
$b_{avg} \cdot 10^3$	2.9153695	2.9152299	2.9288445	2.9022565	2.9024912
$c_{avg} \cdot 10^3$	62.610505	62.837393	63.721774	63.824265	62.258455
$a_{amp} \cdot 10^5$	0	1.2709626	2.6523662	3.4000452	4.1202191
$b_{amp} \cdot 10^5$	0	2.1414979	3.0160779	7.2562722	11.723375
$c_{amp} \cdot 10^5$	0	9.0128400	4.3497037	84.795348	170.37206
a_{height}	$2.53 \cdot 10^{-5}$				
b_{height}	$5.49 \cdot 10^{-3}$				
c_{height}	$1.14 \cdot 10^{-3}$				

Table 3.2: The coefficients for Neill non-hydrostatic mapping function

	$\varphi_i = 15°$	$\varphi_i = 30°$	$\varphi_i = 45°$	$\varphi_i = 60°$	$\varphi_i = 75°$
$a_{avg} \cdot 10^4$	5.8021897	5.6794847	5.8118019	5.9727542	6.1641693
$b_{avg} \cdot 10^3$	1.4275268	1.5138625	1.4572752	1.5007428	1.7599082
$c_{avg} \cdot 10^2$	4.3472961	4.6729510	4.3908931	4.4626982	5.4736038

As the numerical weather model represents a better physical condition for the atmosphere, it enables to a better and more accurate coefficients to be determined. The Neill model uses the seasonal fluctuations, and the VMF uses the daily and sub-daily fluctuations. To validate VMF, Boehm and Schuh [2004] compared it with the Niell mapping function (NMF) and Isobaric mapping function (IMF). They used the baseline length repeatability as a measure and found that there is a significant difference between the models based on different NWP models used, e.g. VMF & IMF, and NMF, especially for baseline of 4000 km length and over (see Figure 3.1).

McAdam [2013] created a robust operational mapping function service based on VMF and made an online interface for the product UNB-VMF1 from the link: *http://unb-vmf1.gge.unb.ca* based on an independent ray-tracing scheme. This provides more flexible opportunity to users to choose different mapping functions for their scientific and geodetic research.

Generally, for low elevations, the errors in the GNSS range observations arise mainly due to multipath and troposphere delays, and these unmodeled systematic errors decrease the quality of results. Hugentobler et al. [2005] mentioned that these effects are marginally reduced by choosing an elevation-dependent weighting scheme.

Most of the global water vapour usually exists near the equatorial or coastal regions. Therefore, even if a mapping function performs very well at polar or mid-

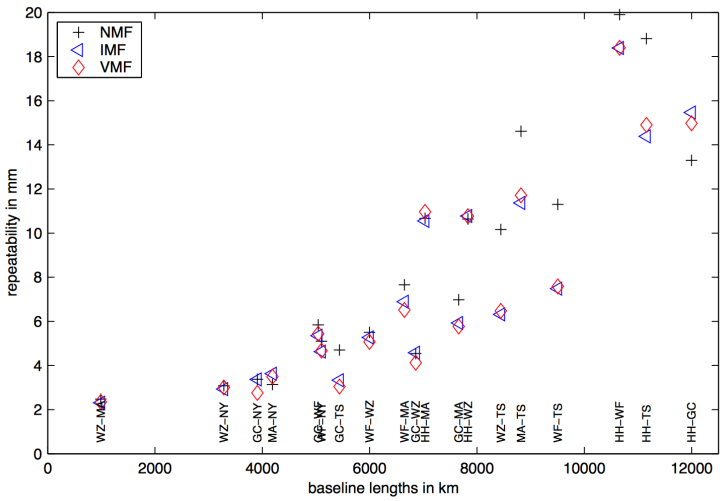

Figure 3.1: Baseline length repeatabilities for several baselines [*Boehm and Schuh*, 2004]

latitude regions, it should not be used in a similar manner in the equatorial region or near coastal regions, since the uncertainties of the model at this region increase. Skone [2003] suggested that the range delays for the wet delay can be as low as centimetres near the pole, but up to 40 cm in the tropics. In this case, a ray-tracing technique may be a promising approach or the use of UNB-VMF1 can be a good alternative to further reduce the uncertainties of the model.

3.3.3 UNB3 Model

The UNB3 model for neutral atmosphere signal propagation delay was originally developed by the University of New Brunswick (UNB) to mitigate the error of the delay especially for WAAS enabled receivers. WAAS/SBAS MOPS model was derived from original UNB3 model. The model is a combination of the Saastamoinen model and the Neill mapping functions with parameters. The associated parameters are the five meteorological parameters which were derived in using the temperature and humidity profiles contained in the 1966 U.S. Standard Atmosphere Supplements. They are: total pressure p_s, temperature T_s, water vapour pressure e_s at the surface,

the temperature lapse rate β and a parameter that represents the average decrease of water vapour λ_s.

There have been a few different UNB tropospheric models, e.g. UNB1, UNB2. Before the introduction of UNB3, temporal variation of the station had not been considered. The UNB3 delay model is an improvement gained by introducing a temporal variation. The Niell mapping functions for a troposphere model represent the annual variation of the atmosphere as a sinusoidal function of the day-of-year. Given the proven performance of the Niell mapping functions, it was thought that a troposphere model derived from the same data would be useful [*Collins and Langley*, 1996]. The model was validated by comparing it to to the ray-traced radiosonde measurements of the signal delay obtained from 173 stations in North America between 1987 and 1996.

The model input parameters are day-of-year, elevation angle, height and latitude. The UNB3 model provides a look-up table of surface meteorological parameter values, and models to propagate these surface values to any arbitrary station height. For each latitude in the 1966 U.S. Standard Atmosphere Supplements, the mean and the amplitude of the five parameters were calculated from the January and June profiles. Between latitudes, linear interpolation is applied for a required parameter ξ at latitude φ and time t [*Collins and Langley*, 1996].

The UNB3 model parameters are tabulated in Table 3.3 and Table 3.4. Each five parameters can be calculated based on the Equation (3.26), i.e. ξ based on Table 3.3 and Table 3.4. The subscripts refer to the nearest latitudes specified in the table to the required one:

$$\begin{aligned}\xi(\varphi,t) =& \xi_{avg}(\varphi_i) + [\xi_{avg}(\varphi_{i+1}) - \xi_{avg}(\varphi_i)m] \\ & - (\xi_{amp}(\varphi_i) + [\xi_{amp}(\varphi_{i+1}) - \xi_{amp}(\varphi_i)]\, m) \cos\left(\frac{2\pi(t-28)}{265.25}\right)\end{aligned} \tag{3.26}$$

where,

$\xi(\varphi,t)$: five different parameters - p_s, T_s, e_s, β, λ_s,

$m = (\varphi - \varphi_i)/(\varphi_{i+1} - \varphi_i)$,

φ : latitude.

For consistency with the Niell functions, day-of year 28 is used for the phase of the temporal variation.

Table 3.3: Parameters for UNB3 model - $\xi_{avg}(\varphi_i)$

average	p_s	T_s	e_s	β	λ_s
15°	1013.25	299.65	26.31	6.03	2.77
30°	1017.25	294.15	21.79	6.05	3.15
45°	1015.75	283.15	11.66	5.58	2.57
60°	1011.75	272.15	6.78	5.39	1.81
75°	1013.00	263.65	4.11	4.53	1.55

Table 3.4: Parameters for UNB3 model - $\xi_{amp}(\varphi_i)$

amp.	p_s	T_s	e_s	β	λ_s
15°	0.99	0.00	0.00	0.00	0.00
30°	-3.75	7.00	8.85	0.25	0.33
45°	-2.25	11.00	7.24	0.32	0.46
60°	-1.75	15.00	5.36	0.81	0.74
75°	-0.50	14.50	3.39	0.62	0.30

For a given latitude and day of year, the zenith delay can be computed from the

following equation:

$$\text{ZHD} = \frac{10^{-6} k_1 R_d}{g_m} \left(1 - \frac{\beta H_{hgt}}{T_s}\right)^{\frac{g_\circ}{R_d \beta}} p_s \tag{3.27}$$

$$\text{ZWD} = \frac{10^{-6} \left(T_m k_2^{'} + k_3\right) R_d}{g_m \lambda_s^{'} - \beta R_d} \left(1 - \frac{\beta H_{hgt}}{T_s}\right)^{\frac{\lambda_s^{'} g_\circ}{R_d \beta} - 1} \frac{e_s}{T_s} \tag{3.28}$$

where,

$T_s, p_s, e_s, \beta, \lambda_s$: for a certain latitude and time, each parameter can be calculated from Equation (3.26),

H_{hgt} : orthometric height (m),

R_d : gas constant for dry air,

g_m : from Equation (3.20),

$g_\circ$: surface gravity,

T_m : mean temperature of water vapour in °K,

$$T_m = T \left(1 - \frac{\beta R_d}{g_m \lambda_s^{'}}\right) \tag{3.29}$$

where $\lambda_s^{'} = \lambda_s + 1$ (unitless).

The total slant delay then can be calculated by:

$$\text{ZTD} = m_{dn}\text{ZHD} + m_{wn}\text{ZWD} \tag{3.30}$$

where, the m_{dn} and m_{wn} represents the Niell′s hydrostatic and non-hydrostatic mapping functions, respectively.

Based on Collins and Langley [1998], the model is able to predict the total zenith delay with average uncertainties of 5 cm (2σ) under normal, non-severe tropospheric conditions.

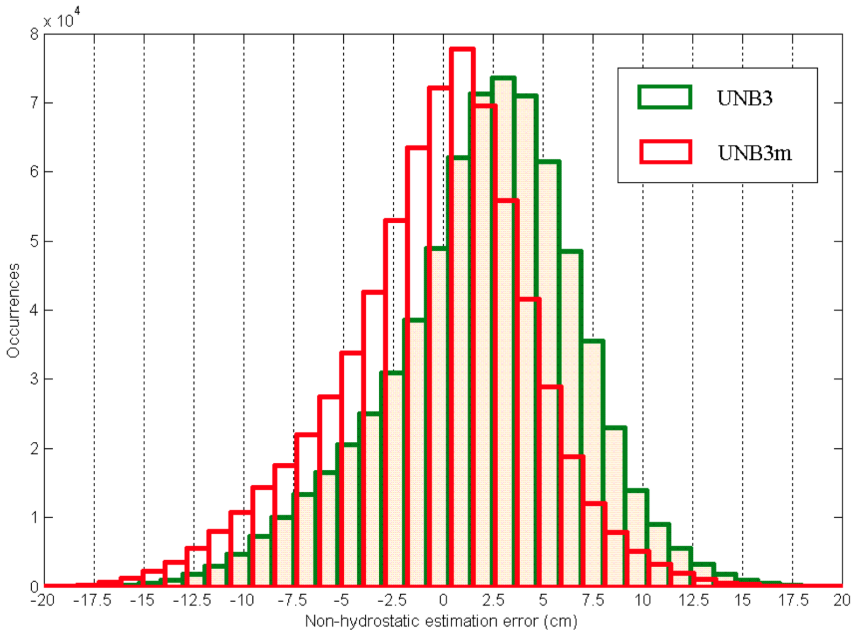

Figure 3.2: Non-hydrostatic estimation error between UNB3 and UNB3m [*Leandro et al.*, 2006]

A modification for UNB3, called UNB3m, has been also developed due to the following stated limitation. In some cases, computed water vapour pressure values based on the relative humidity were found to be not realistic. As the water vapour pressure is affected only by the non-hydrostatic delay component, the UNB3m is a modification of UNB3 model only in the non-hydrostatic part. To develop a newer model, Leandro et al. [2006] processed a total of 223 stations through the years from 1990 to 1996. That analysis showed that UNB3 has a consistent bias of 2 cm with an rms close to 5 cm. Whereas, the bias in the UNB3m is about -0.5 cm.

Table 3.5: Average and amplitude values for relative humidity used in UNB3m

Relative Humidity (%)		
Latitude	Average	Amplitude
15°	75.0	0.0
30°	80.0	0.0
45°	76.0	-1.0
60°	77.5	-2.5
75°	82.5	2.5

Table 3.5 represents the relative humidity correction in the UNB3 model. UNB3m models is achieved by the replacement of the columns of the water vapour pressure e_s in Table 3.3 by this corrected relative humidity values. Figure 3.2 represents the histogram for non-hydrostatic delay estimation error for both UNB3 and UNB3m. The error caused by the different relative humidity values is significantly reduced in UNB3m. More details about the UNB3m model and parameter conversions can be found on Leandro et al. [2006] and the Matlab source code is accessible at: *http://www2.unb.ca/gge/Resources/unb3m/unb3m.html*.

3.4 Ray-Tracing Technique

Ray-tracing techniques are often used in computer graphics to make more realistic 3 dimensional (3D) scenes. From the geometrical point of view, ray-tracing for the atmosphere gives much more realistic results than the empirical or mathematical models for the troposphere. This is because large vertical and horizontal gradients exist in the atmosphere, and these are much more significant for the lowest elevations, due to the irregularity in the water vapour content, or due to other uncertainties. Ray-tracing is known as one of the most reliable and realistic approaches for calculating the tropospheric delay [*Boehm and Schuh*, 2003]. When both GNSS information and 3D numerical weather fields are made available, the path of a satel-

lite signal can be calculated by using a ray-tracing technique, which will give more reliable estimates of the tropospheric delay for low elevation angles. However, in order to maximize its usage, tropospheric delays for all incoming signals from a given satellite should be respectively calculated in real-time for the given sampling rate. This would take much more time than using the mathematical models. Therefore, the direct application of the ray-tracer, using 3D numerical weather fields, to GNSS real-time applications, has some limitations; but, if the 3D numerical weather fields are available, then ray-tracing techniques (with a few simplifying approximations) can be used to directly integrate slant path refractivity profiles and derive slant delay estimates as well.

3.4.1 Numerical Weather Prediction Model

A numerical weather prediction model incorporates a series of weather data which, where applied to mathematical models of the atmosphere, can be used to predict the weather based on previous and current weather conditions. The ultimate goal of NWP is to find the exact state of the atmosphere so that it enables it to accurately predict the weather at a future time. The system is associated with an initial value problem: given an estimate of the present state of the atmosphere, the model forecasts its evolution. Therefore, the primary data source plays a crucial role in obtaining a reliable result.

One of these ray-tracing techniques in NWP for geodetic usage uses the topocentric coordinates of virtual satellites, in terms of the azimuth and zenith angle to each satellite, and necessary information regarding the total pressure, temperature, and partial water vapour pressure or relative humidity [*Schuler*, 2001]. Another method is based on Snell′s law [*Boehm and Schuh*, 2003]. Figure 3.3 illustrates a ray-tracing technique based on the geometrical viewpoint of the method.

NWP has an individual level which is denoted by k level. For each $k(\sim 1000)$ level, the hydrostatic and non-hydrostatic refractivity from the bottom level to k level can be evaluated and calculated. Then the refractivity index can be estimated; these values are used to determine the $(k-1)$ refractivity for both the hydrostatic and non-hydrostatic component, as well as for the refractivity index between the levels. One of the calculated results is Figure 7.40 and Figure 7.41 in Chapter 6. Using the relationship between the height of the levels and the distance to the centre of the Earth, the corresponding distance is calculated:

$$r_i = r_o + h_i \tag{3.31}$$

where subscript i represents the corresponding level.

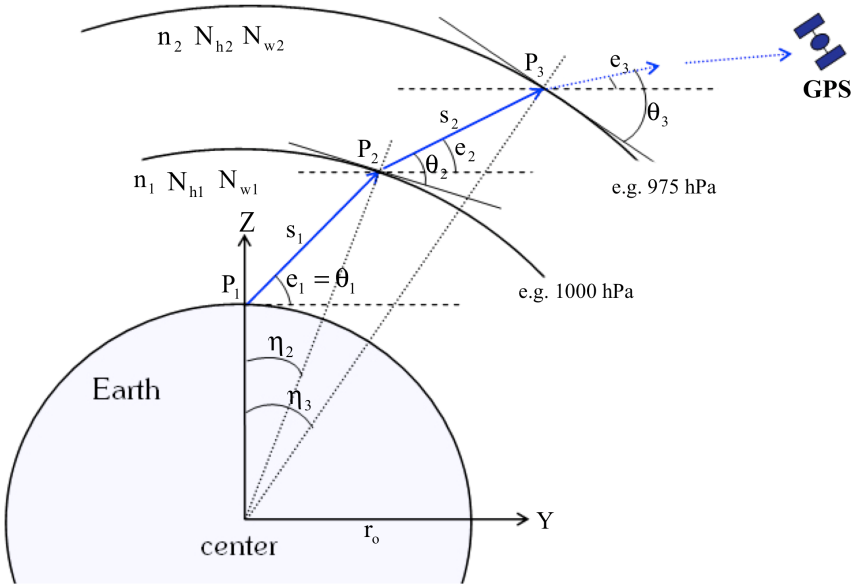

Figure 3.3: A ray-tracing scheme

When the initial angle is given, the point P_1 can be determined by using the rela-

tion, $\theta_1 = e_1$. After this calculation, the second point P_2 and geocentric coordinates of P_1 and P_2 can be determined by the following equations [*Boehm and Schuh*, 2003]:

$$\begin{aligned} s_1 &= -r_1 \sin\theta_1 + \sqrt{r_2^2 - r_1^2 \cos^2\theta_1} \\ z_1 &= r_1 \\ z_2 &= z_1 + s_1 \sin e_1 \\ y_1 &= 0 \\ y_2 &= y_1 + s_1 \cos e_1 \end{aligned} \tag{3.32}$$

The corresponding angles at the centre of the Earth can be determined by the following:

$$\begin{aligned} \eta_1 &= 0 \\ \eta_2 &= \arctan\left(\frac{y_2}{z_2}\right) \end{aligned} \tag{3.33}$$

Now, the angles θ_2 and e_2 at the point P_2 can be determined based on Snell′s law, as follows:

$$\begin{aligned} \theta_2 &= \arccos\left(\frac{n_1}{n_2}\cos(\theta_1 + \eta_2)\right) \\ e_2 &= \theta_2 - \eta_2 \end{aligned} \tag{3.34}$$

Thereafter, the same strategies are used to calculate all other shells from 2 to $(k-1)$ levels as follows:

$$
\begin{aligned}
s_i &= -r_i \sin\theta_i + \sqrt{r_{i+1}^2 - r_i^2 \cos^2\theta_i} \\
z_{i+1} &= z_i + s_i \sin e_i \\
y_{i+1} &= y_i + s_i \cos e_i \\
\eta_{i+1} &= \arctan\left(\frac{y_{i+1}}{z_{i+1}}\right) \\
\theta_{i+1} &= \arccos\left(\frac{n_i}{n_{i+1}} \cos(\theta_i + (\eta_{i+1} - \eta_i)\right) \\
e_{i+1} &= \theta_{i+1} - \eta_{i+1}
\end{aligned}
\tag{3.35}
$$

Finally, one can estimate the slant hydrostatic delay (SHD) and the slant non-hydrostatic delays (SWD) using the discrete ray-tracing technique as follows:

$$
\text{SHD} = \sum_{i=1}^{k-1} s_i N_{h_i} \qquad \text{and} \qquad \text{SWD} = \sum_{i=1}^{k-1} s_i N_{w_i} \tag{3.36}
$$

There are many NWP models available. In Canada, the Canadian Meteorological Centre (CMC) is a major organization for operation and research in NWP. In the USA, computer weather forecasts issued by the National Center for Environmental Prediction (NCEP) in Washington DC, guide forecasts from the US National Weather Service (NWS). NCEP has operated since 1950s [*Kalnay*, 2003]. NWP research takes place in several research centres in USA such as National Oceanic and Atmospheric Administration (NOAA), National Centre for Atmospheric Research (NCAR), National Aeronautics and Space Administration (NASA), etc. Internationally, a research centre such as the European Centre for Medium Range Weather Forecast (ECMWF) has a major role in global scale NWP research through international cooperation. Significantly, the GPS-Met Observing Systems Branch (GPS-Met) within the Forecast Systems Laboratory (FSL) in NOAA had used Rapid Update

Cycle (RUC) until the next generation of NCEP′s Rapid Refresh (RAP) model was introduced in May 2012. Currently, the RAP which is a 1 hr cycle system replaced the operational RUC at NCEP. This is an operational atmospheric prediction system comprised primarily of a numerical forecast model, and an analysis system to initialize that model. A sample data processing with NWP is based on RUC. RUC covers the lower 48 states of the USA, and adjacent areas of Canada, Mexico, and oceanic areas. There are four types of RUC models: RUC60, RUC40, RUC20 and RUC13. The detailed output contents of the RUC models can be found on the following link under the Climate Research Facility (ARM): *http://www.arm.gov/instruments/ruc*.

The key features of RUC model are:

• High-frequency (every 1h) 3-d objective analyses over the contiguous United States

• High-frequency (every 1h) short-range weather model forecasts (out to 12 h) in support of aviation and other mesoscale weather forecast users, i.e. in size from several kilometers to around 100 kilometres.

• Assimilation of data from Commercial aircraft (relayed through ACARS - Aircraft Communications, Addressing, and Reporting System)

• Wind profilers (404 and boundary-layer 915 MHz)

• Rawinsondes and special dropwinsondes

• Surface reporting stations and buoys

• Radio Acoustic Sounding System (RASS) which is experimental

• Velocity-azimuth display (VAD) winds from National Weather Service (NWS) WSR-88D radars

• Geostationary Operational Environmental Satellite (GOES) total precipitable water vapour estimates

• Special Sensor Microwave Imager (SSM/I) total precipitable water vapour esti-

mates

- GPS total precipitable water vapour estimates
- GOES high-density visible and IR cloud drift winds

In Chapter 6, RUC20 NWP was used to calculate the slant tropospheric delay for a baseline, CGSJ and DRHS station, as an example for mitigating the tropospheric delay and for examining the positioning solution. RUC20 has a horizontal grid of 301 by 225 points, and is based on a 20 km by 20 km grid. Currently, the raw data of RUC20, which covers the entire RUC domain, are available only from the ARM archive on request, in GRIB format which can be decoded by such as the Grid Analysis and Display System (GrADS) or read_grib for Matlab. More detailed information on GrADS and read_grib can be found at the following link: *https://www.ncdc.noaa.gov/data-access/model-data/model-datasets /rapid-update-cycle-ruc.*

3.4.2 Radiosonde

A radiosonde is a balloon-borne instrument with radio transmitting capabilities. Typically, weather offices launch balloons twice each day at the same time to obtain basic weather information about the atmosphere. The instruments carried by the balloon measure different weather parameters such as air temperature, humidity and pressure, typically to altitudes of approximately 30 km, and their data are transmitted immediately to the ground station by a radio transmitter. Radiosonde observations, also called RAOB, have been the main source of upper air measurements for over 70 years and still are an important source of data for neutral-atmosphere studies. RAOB data can still be an option for research and validation studies. Figure 3.4 shows the location of RAOB launch sites (∼1500 sites worldwide), whose data are accessible through the NOAA database

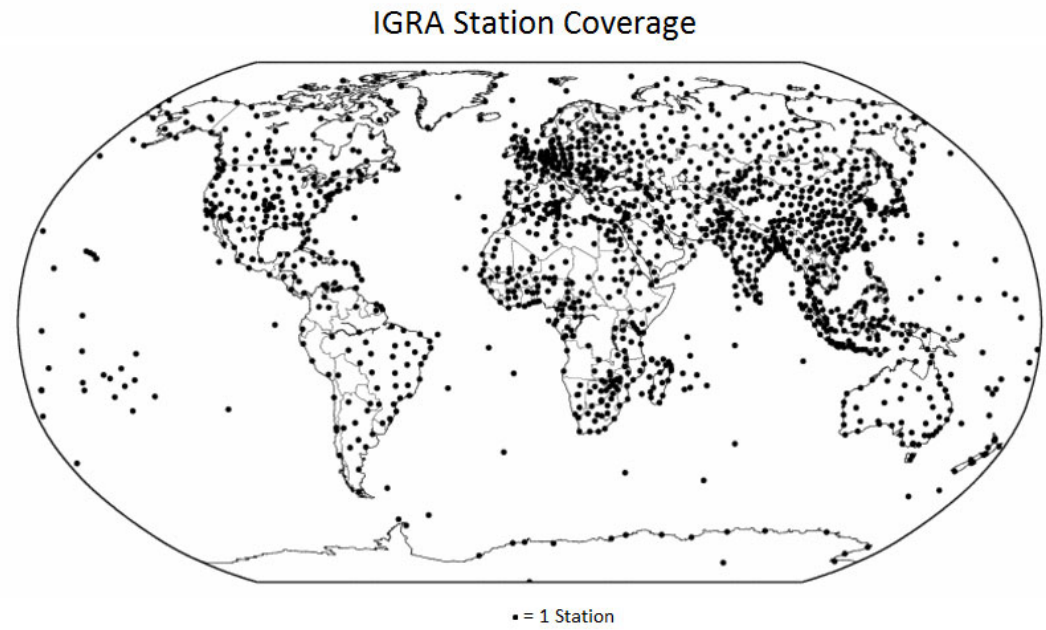

Figure 3.4: Location of 1500 Integrated Global Radiosonde Archive (IGRA) stations around the world (from NOAA) [7]

Typically, ray-tracing is performed using radiosonde data to generate an absolute or true value for validating the zenith wet delay. Although radiosonde data provides a good vertical resolution, they are not typically used due to their poor horizontal resolution and cost. As described earlier, the radiosonde measurements include air temperature, humidity and pressure with varying height.

If we know dew point and temperature at a certain elevation, we can get the relative humidity based on Clausius-Clapeyron equation:

$$T - T_d = 4 \times 10^{-4} T \cdot T_d \cdot (-\log U_w) \tag{3.37}$$

where,

[7]IGRA stations and details can be found on https://www.ncdc.noaa.gov/data-access/weather-balloon/integrated-global-radiosonde-archive, accessed May 2016

T : temperature (°K),

T_d : dew point temperature (°K),

U_w : relative humidity (%).

Based on the Magnus′s formula, the saturated water vapour pressure can be calculated as:

$$\log e_w = \frac{-2973.4}{T} - 4.9283 \log T + 23.5470 \tag{3.38}$$

where,

e_w : saturated water vapour pressure.

The humidity ratio can be expressed by mass of water (or by the partial vapour pressure of the specific moist air). It can be formulated as the ratio between the actual mass of water vapour present in specific moist air - to the mass of the dry air. Its unit is kilogram of waster vapour per kilogram of dry air.

$$q = \frac{m_{wv}}{m_{da}} \tag{3.39}$$

where,

q : humidity ratio (kg_{water}/kg_{dryair}),

m_{wv} : mass of water vapour (kg),

m_{da} : mass of dry air (kg).

There is another term regarding humidity, called the ′mixing ratio′:

$$r = \frac{m_{wv}}{m_d} \tag{3.40}$$

where,

r : humidity ratio (kg_{water}/kg_{dryair}),

m_{wv} : mass of water vapour (kg),

m_d : mass of dry air (kg).

So, based on Equation (3.39) and Equation (3.40), the following ratio q can be derived.

$$q = \frac{r}{1+r} \tag{3.41}$$

The partial pressure for dry air and vapour can be expressed as:

$$\begin{aligned} P_d V &= M_d R_d T \\ eV &= \frac{1}{\epsilon} m_v R_d T \end{aligned} \tag{3.42}$$

where,

R_d : gas constant for dry air,

ϵ : constant.

Therefore, we can arrive at the following equation.

$$r = \frac{\epsilon \cdot e}{P - e} \tag{3.43}$$

where $P = P_d + e$.

Once the air is saturated for the water vapour, Equation (3.43) can be rewritten by:

$$r = \frac{\epsilon \cdot e_w}{P - e_w} \tag{3.44}$$

where, superscript w represents water vapour.

Therefore, using Equation 3.43 and Equation 3.44 with $U_w = e/e_w$, the saturated mixing ratio(r) can be derived:

$$r_w = \frac{U_w r_w}{1 + \frac{(1 - U_w) r_w}{\epsilon}} \tag{3.45}$$

where,

r_w : $\epsilon \cdot e_w/(P - e_w)$,

ϵ : constant.

Once $U_w = e/e_w$ is calculated based on Equation (3.38), the mixing ratio r_w can be determined from Equation (3.45). Finally, Equation (3.41) can be estimated.

Integrated Water Vapour (IWV) gives the total amount of water vapour that a signal from the zenith direction would encounter. Precipitable Water Vapour (PWV) is the IWV scaled by the density of water. IWV can be formulated as follows [*Glowacki*, 2006]:

$$\text{IWV} = \int_0^H \rho_w dh = \int_0^H \rho q dh \tag{3.46}$$

where,

ρ : density,

q : $r/(1+r)$,

r : mixing ratio.

As $-dP = \rho g dh$, IWV becomes

$$\text{IWV} = \frac{1}{g}\int_{P_\circ}^{P_H} q dP \tag{3.47}$$

where,

g : gravitational constant on Earth surface,

$P_\circ$: pressure at the surface $h = 0$,

P_H : pressure at the surface $h = H$.

In the discrete case, IWV can be specifically summarized as follows:

$$\text{IWV} = 0.0102 \sum_{k=1}^{N} \bar{q}_k \Delta P_k \tag{3.48}$$

where,

$$\bar{q}_k = \frac{q_k + q_{k-1}}{2}, \qquad \Delta P_k = P_k - P_{k-1} \tag{3.49}$$

Finally, the precipitable water vapour (PW) can be calculated based on the following formula.

$$\mathrm{PW} = \frac{\mathrm{IWV}}{\rho_w} \tag{3.50}$$

One of the examples in PW estimation based on radiosonde data and GNSS data can be found on the following section.

3.5 GNSS-derived Tropospheric Delay

If the ZWD is estimated from such GNSS, the PW (precipitable water vapour) can be calculated Schuler [2001] from the following relationship:

$$\begin{aligned} \mathrm{Q} = \frac{\mathrm{ZWD}}{\mathrm{PW}} &= 0.10200 + \frac{1708.08}{T_m} \\ T_m &= 70.29 + 0.72 T_\circ \end{aligned} \tag{3.51}$$

where,

T_m : mean temperature of the atmosphere (°K),

$T_\circ$: surface temperature (°K).

As seen in Equation (3.51), the mean temperature is necessary to retrieve the corresponding PW.

One example described here is retrieval of PW from GPS and radiosonde during the passage of a typhoon in Korea peninsula, to see how well both estimates agreed. The example also uses an actual precipitation record. We used the empirical values of Brevis et al. [1992] in Equation 3.51 as the mean value for the region was not available for analysis. Mendes et al. [2000] also evaluated the weighted mean tem-

perature for the global application.

Even if the radiosonde has a poor horizontal resolution compared to the water vapour radiometer (WVR) in a clear sky, it still provides good vertical atmospheric reference parameters during severe weather conditions. The total amount of the PW can be defined by integral of $\rho_v(z)dz$, where ρ_v is the mass density of the water vapour at altitude z.

To evaluate different tropospheric delays, we analyzed a severe weather event. Figure 3.5 illustrates a typhoon, RUSA, passing over the South Korea peninsular in summer 2002. The typhoon was one of the worst in Korean history as it took 184 lives and destroyed 9900 buildings with resulting damage estimated at a value at 6.8 billion Canadian dollars. The image is a GMS infrared satellite image. The data sets are taken from 18 different permanent GNSS stations in Korea from August 25 to September 02. The processing is based on double differences. To get the best possible absolute ZTDs, and to decorrelate the zenith delay and height component, one distant station, TSKB in Japan, is incorporated into the data analysis.

Figure 3.6 illustrates the detailed track of the typhoon and approximate station coordinates used in this research. The time of the track is referenced to UTC. Green dots in Figure 3.6 represent the sites for radiosondes which are processed for evaluating the calculated PW validation.

Figure 3.7 represents the reflectivity composite image at 15.00 hrs on August 31, 2002 local time. This image is from a few of radar observatories across Korea peninsula. They are: near CHJU (named DWSR90C), near TEGN (named DWSR90), near JINJ, MKPO (DWSR90C), near SKMA (DWSR -8) and JINJ (DWSR90C).

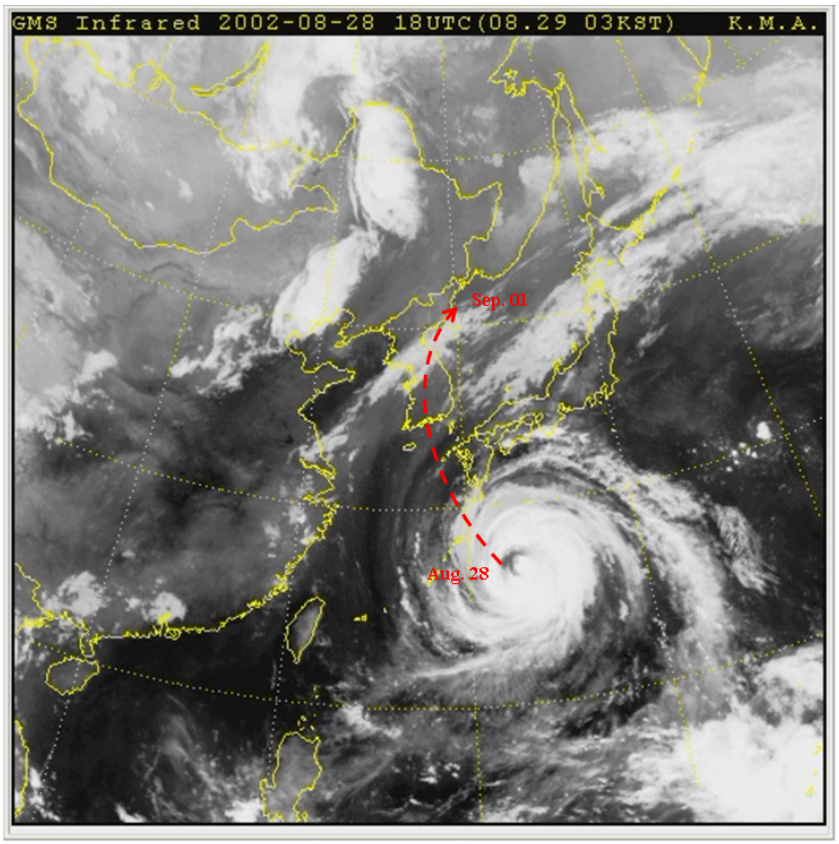

Figure 3.5: Infrared image taken by GMS at 18 UTC on 28 August 2002 (Courtesy: Korea Meteorological Administration)

All of the GPS data sets which was processed are recorded based on Trimble′s SSI GPS receivers with a data rate of 30 seconds.

Some details about the GPS processing for the retrieval of ZTD are given here. For processing the GPS data, Bernese GNSS software was used with Bernese Processing Engine(BPE). Once all of the station networks to be processed were formed and cycle slips were correctly detected and repaired, the L1 and L2 ambiguities were resolved using a stochastic ionosphere approach (namely, the quasi-ionosphere approach). After all possible ambiguities were resolved, these ambiguities were fixed to get the final positioning solutions. Subsequently, troposphere parameters were

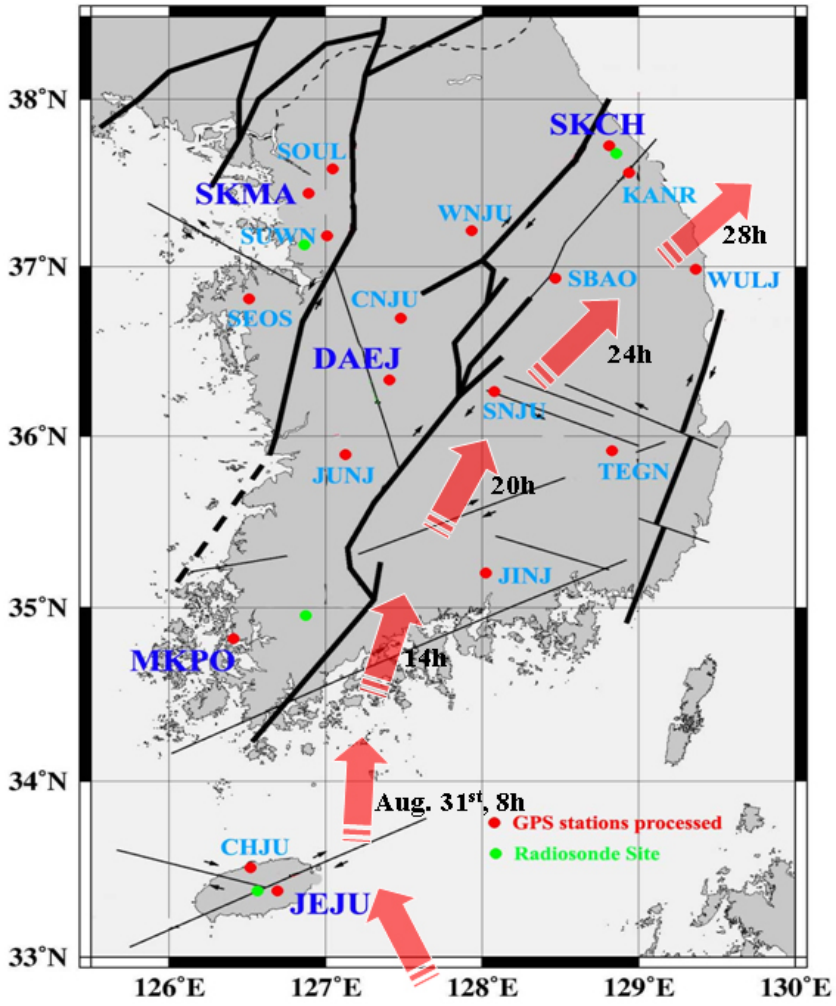

Figure 3.6: The track of the typhoon, RUSA, and the GNSS stations

estimated. To evaluate and try to mitigate the imbalanced network error, a gradient model as Equation (3.5) was set up as an additional parameter in the processing. During data processing, IGS final SP3 orbit products were used. The tropospheric estimation described earlier with elevation-dependent weighting was also used in the processing.

For the processing, the recorded pressure, temperature, and radiosonde data from the Korea Meteorological Administration (KMA) were used. Figure 3.8 represents the pressure curves recorded at some of the GNSS stations.

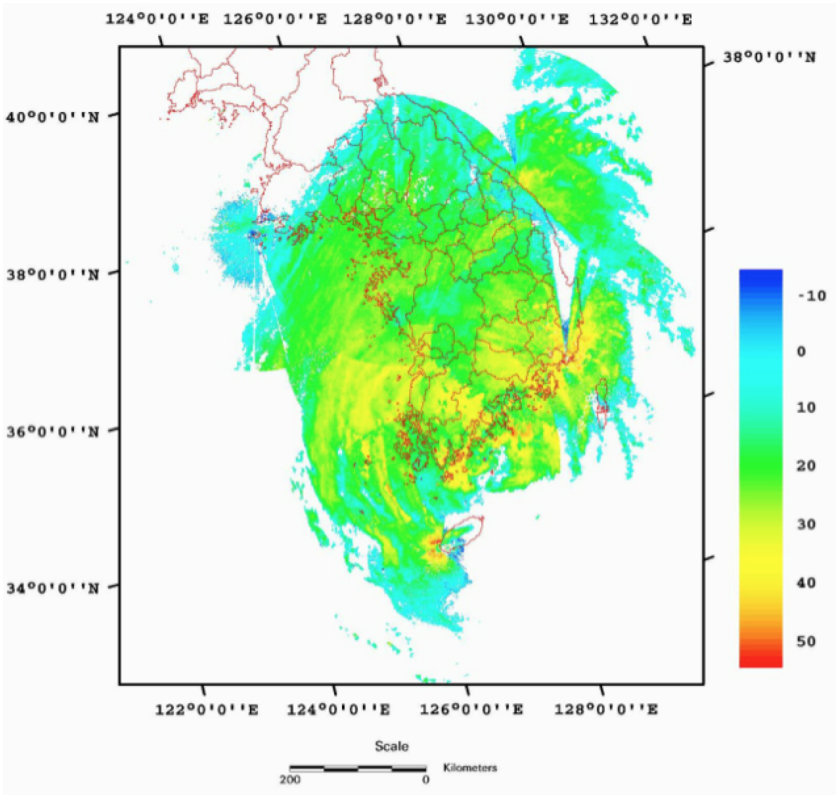

Figure 3.7: Composite reflectivity (dBZ) at 06:00 hrs on August 31, 2002 UTC [*Tachikawa et al.*, 2003]

Based on the above pressure curve, it is evident that the typhoon was crossing the nation during August 31st and September 1st. From Figure 3.8, it is evident that the track across Korea was from south to north as illustrated in Figure 3.6. During the same period of time, torrential rain occurred.

Figure 3.9 shows the estimated PW values for station SKCH over 9 days. This area had the heaviest rainfall during the day. It can be validated based on the actual precipitation and the satellite image. The pink bar is the actual precipitation water amount per hour recorded by the Korea Meteorological Agency (KMA) during that time. The bottom panel shows the pressure in hPa. As seen in the plots, both PW and the precipitation show strong correlation with the pressure. The observed

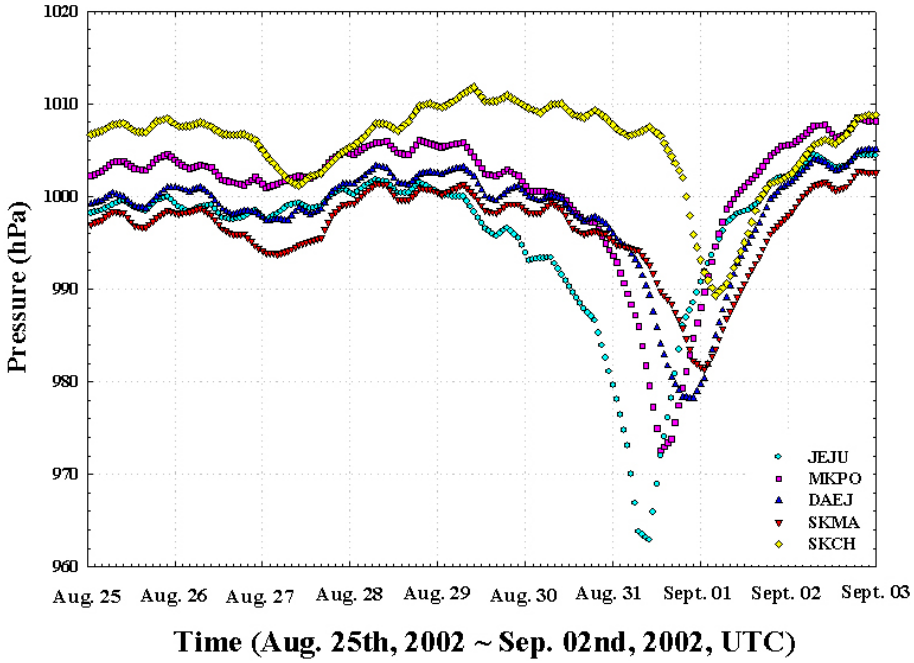

Figure 3.8: Pressure profiles when the typhoon was crossing the nation

PW in Figure 3.9 is high before and during the passage of the typhoon, and then decreases rapidly straight after its passage. During the passage of the typhoon, some of the GPS and radiosonde data were missing and they are indicated by gaps in the plot. The red dashed line represents when the typhoon was close to the station. Figure 3.10 to Figure 3.14 illustrates the estimated PW values for all other stations.

As most of the radiosonde stations are not at exactly the same location as the GNSS station, differences can be seen. Especially, for this JEJU station, the height difference for radiosonde and GNSS is around 350 m and so the corresponding pressure and temperature need to be corrected. In this case, an exponential decay function for pressure and constant lapse rate for temperature for the atmosphere are applied for minimizing the height differences. After corrected, as is expected, those three values are generally well agreed as seen from Figure 3.12.

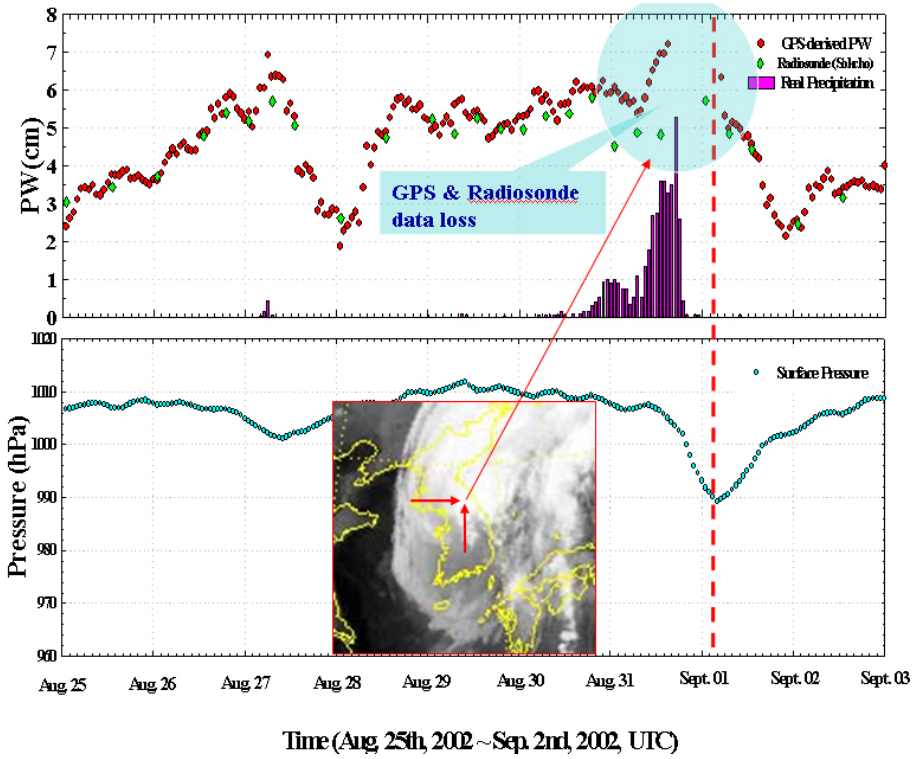

Figure 3.9: PW from GPS and radiosonde, real precipitation, pressure profile (upper plot), and horizontal gradients (lower plot) for station SKCH

The atmosphere is extremely inhomogeneous when the typhoon is close. We hourly estimated the gradient for the period from August 25th to September 2nd during the GPS processing. Figure 3.15 and Figure 3.16 expresses those estimated total gradients for stations JEJU and DAEJ. Black dots and red triangles represent the estimated gradient values. Specifically, the red triangles are the estimated gradients from August 31 to September 1 during the passage of the typhoon. As is shown, the red triangles are slightly biased in the south eastern direction which agrees with the location of the typhoon from the satellite image. As is proven, GNSS is very useful and powerful tool for atmosphere science and research.

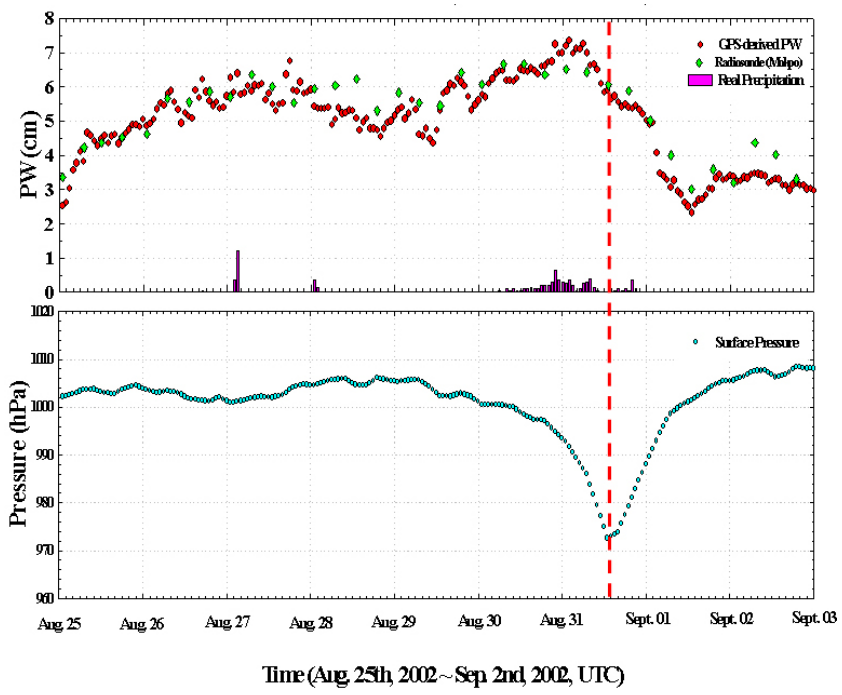

Figure 3.10: PW from GPS and radiosonde, real precipitation, pressure profile (upper plot), and horizontal gradients (lower plot) for station MKPO

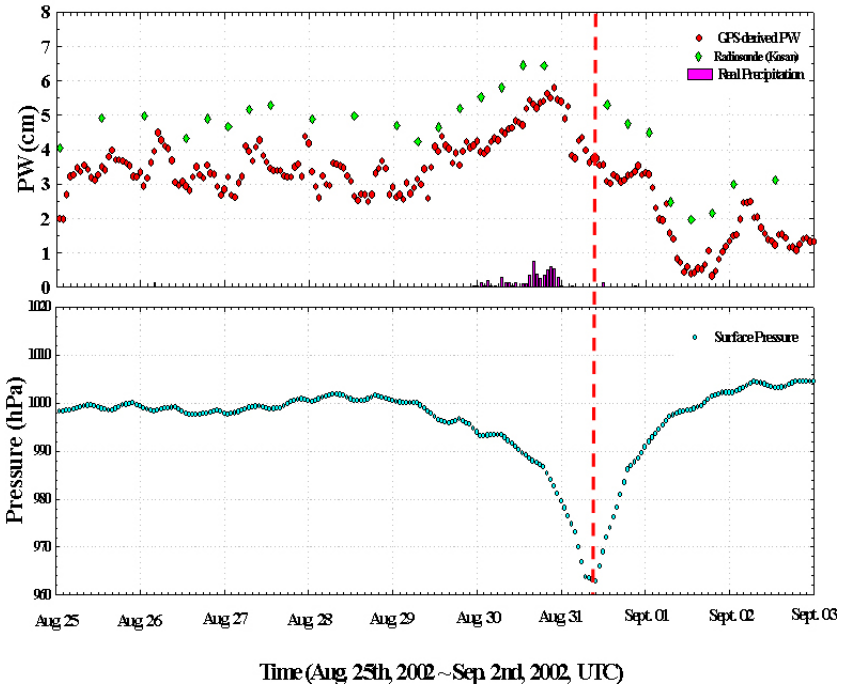

Figure 3.11: PW from GPS and radiosonde, real precipitation, pressure profile (upper plot), and horizontal gradients (lower plot) for station JEJU

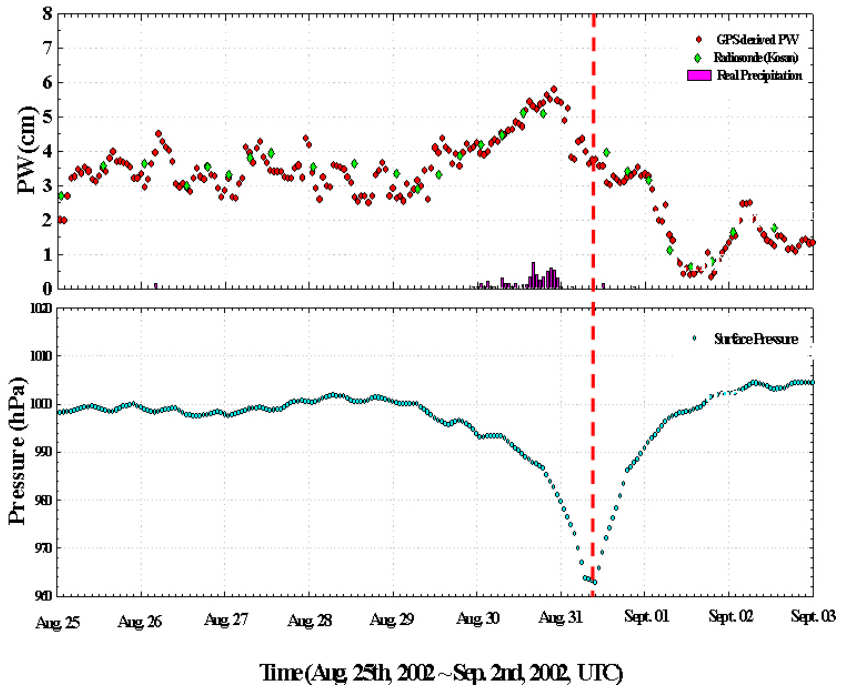

Figure 3.12: Height corrected for JEJU

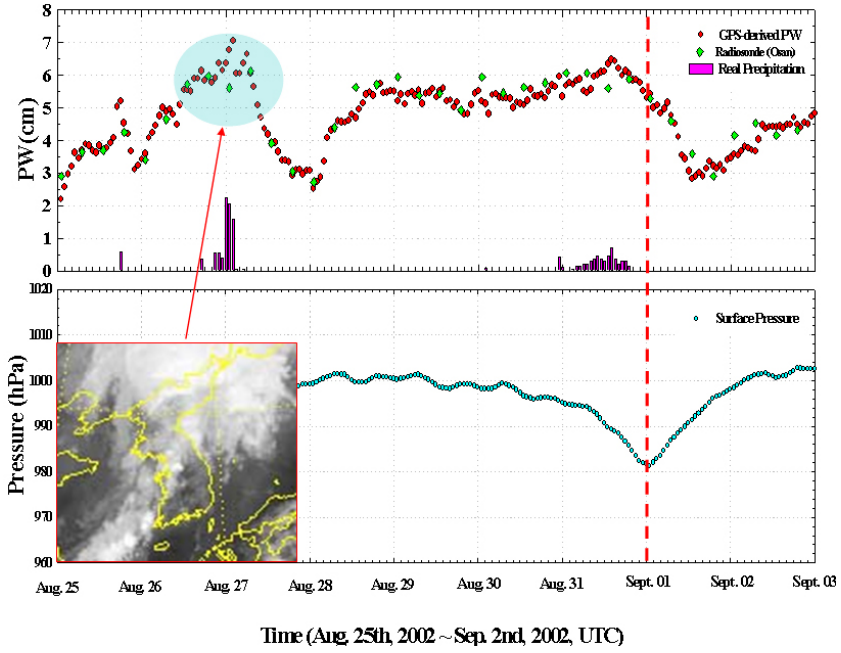

Figure 3.13: PW from GPS and radiosonde, real precipitation, pressure profile (upper plot), and horizontal gradients (lower plot) for station SKMA

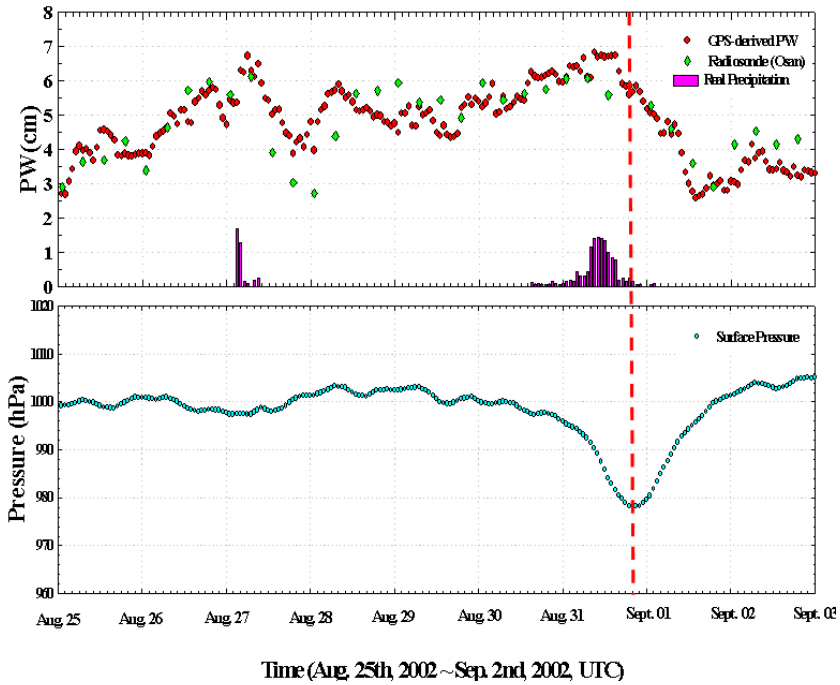

Figure 3.14: PW from GPS and radiosonde, real precipitation, pressure profile (upper plot), and horizontal gradients (lower plot) for station DAEJ

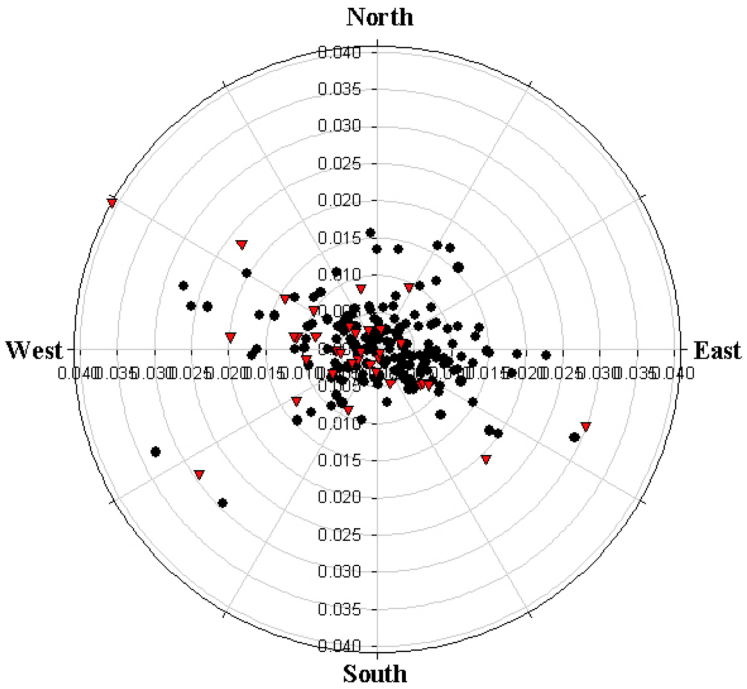

Figure 3.15: Horizontal gradients estimated for station JEJU

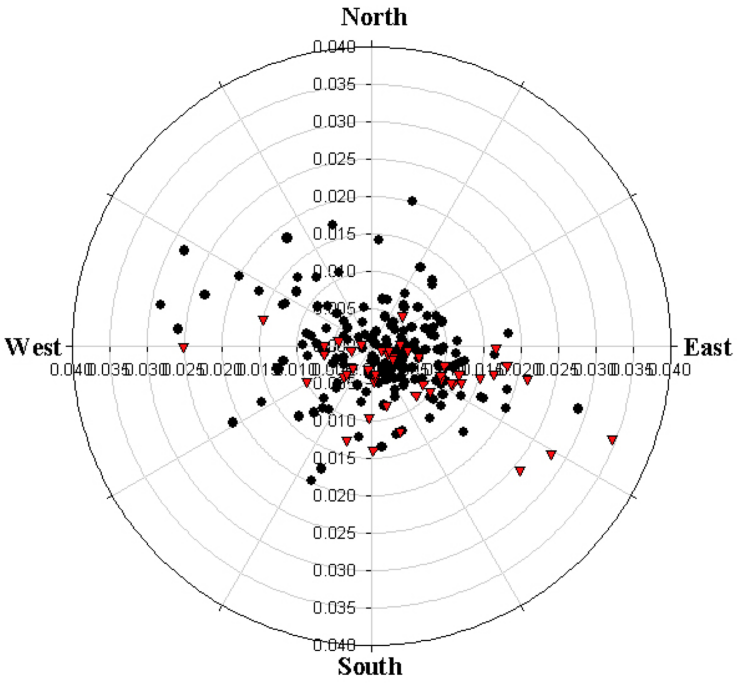

Figure 3.16: Horizontal gradients estimated for station DAEJ

3.6 Summary

In this chapter, the existing troposphere error mitigation models for GNSS and a comparison between GPS-derived PW, radiosonde, PW estimates, and real precipitation, was carried out to show the importance of post-processed GNSS observables in the atmospheric research. In the next chapter, Chapter 4, the limitation of the current troposphere mitigation approachs will be discussed and the proposed new methodology to overcome the limitations will be discussed in detail. This new methodology will be evaluated later in this dissertation both with post-processed intermediate data sets from the Bernese GNSS software and with the developed epoch-wise kinematic software platform.

Chapter 4

Developed Methodology

This chapter describes the background of the developed combined approach for decorrelating height and troposphere parameters in the positioning domain. Section 4.1 discusses the motivation of this method while Section 4.2 discusses the correlation between the two parameters. Section 4.4 addresses details of the combined approach. Especially, this chapter is closely linked to Chapter 5 where the detailed mathematical background of the developed software is discussed.

4.1 Background of the Combined Approach

Atmospheric effects, including the ionosphere and the troposphere, are one of the most significant error sources in GNSS RTK positioning and navigation. As discussed in Chapter 3, almost 90% of the total delay for the troposphere occurs in the hydrostatic component, which varies slowly with time. This hydrostatic delay can be easily modeled with the assumption of hydrostatic equilibrium to an accuracy at the millimetre level [*Mendes and Langley*, 1995]. Unlike the hydrostatic part, the non-hydrostatic (or wet) part has strong spatial and temporal variations. The effects of the wet delay to the range can reach 10∼40 cm in the zenith direction. Large residual errors in modeling can cause significant errors (additional 5 cm and

more) in high-precision GNSS positioning applications even for a short baseline.

The different parameterizations typically recommended when estimating the troposphere delay include [*Rothacher and Beutler*, 2002]:

- Estimation of ZTD for each station and time interval, e.g. 1∼2 hours,
- Estimation of ZTD as a stochastic parameter, e.g. as a random walk or Guass-Markov process,
- For small networks with large height differences, representation of the ZTD correction as a function of station height as a polynomial of low degree.

The above recommended strategy is a typical method for estimating the troposphere delay for the atmospheric research and static positioning scenario. In a kinematic scenario, however, the above strategy has many limitations. To reduce or minimize these errors arising from poor modeling of the wet troposphere, one possibility is to model the tropospheric refraction using a purely independent data set without GNSS observations. Most studies on the troposphere have been focused mainly on tropospheric delay estimation for the atmospheric sciences. These include the atmosphere tomography for modeling the atmosphere. Meanwhile, the GNSS positioning community has been concerned about how well the tropospheric delay can be modeled for high-precision positioning. Some studies have focused on independent observables (e.g., water vapour from a water vapour radiometer) to retrieve the absolute atmospheric parameters for other stations. Another approach in mitigating the troposphere delay includes a ray-tracer based on a numerical weather prediction (NWP) mode (e.g., Rapid Update Cycle 13 km (RUC13) by National Oceanic and Atmospheric Administration (NOAA) in USA, and Global Environmental Multiscale (GEM) NWP model from the Canadian Meteorological Centre of

Environment Canada) [*Cove et al.*, 2004; *Ahn et al.*, 2005; *Cove*, 2005; *Santos et al.*, 2005]. For sparse areas, it gives an independent measurement of the tropospheric delays. From a practical point of view, however, the ray-tracer has its limitations such as its latency and real-time data reception. In addition, the grid spacing currently adopted is too large to consider in a locally anomalous atmospheric condition.

The other approach is to estimate the tropospheric parameters directly using the available GNSS data. Due to their spatial and temporal correlation characteristics, these errors can be substantially minimized under short-baseline situations by differential techniques. However, the main issue when estimating troposphere parameters includes that estimation of additional parameters in general weaken the solution. In addition, the troposphere parameters are highly correlated with other parameters such as station heights (which is discussed in the following section 4.2), receiver and satellite clocks, and phase ambiguities.

When a strong tropospheric anomaly exists within a network, however, the differential errors cannot be reduced to a negligible level even under short-baseline situations. These errors can adversely affect the rover positioning solution (5 cm or more additional errors especially on height component) and this can make the entire network solutions unreliable. One of the localized anomalies could be observed at Stennis Continuously Operating Reference Stations (CORS) in Texas, USA. The baseline length is about 2.1 km which is short enough to eliminate the correlated errors in the atmosphere in double difference technique. During the time when there was a localized troposphere anomaly at 20 hours UTC (see Figure 4.1), the residuals reached over a half cycle, thus causing a failure to resolve ambiguities successfully.

Similar weather could be observed near San Marcos CORS stations, CSM1 and

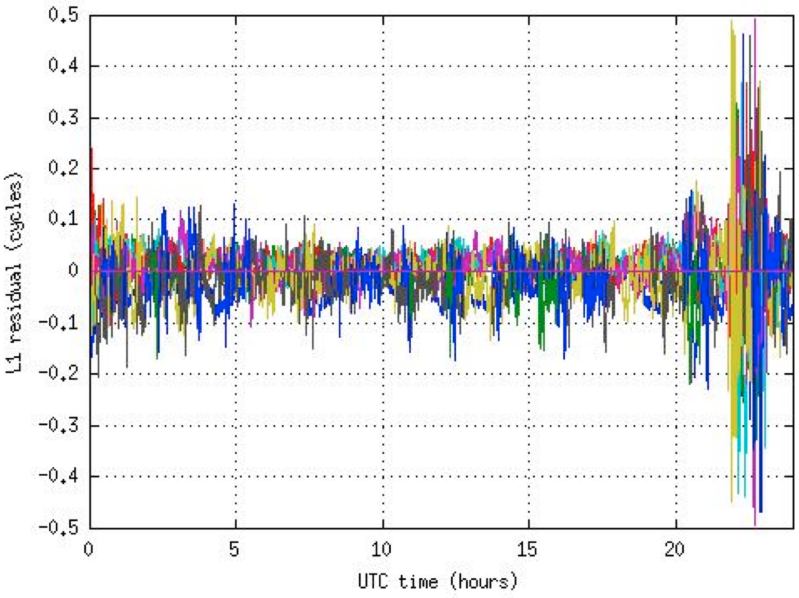

Figure 4.1: L1 DD residuals on Stennis CORS Stations in Texas on 21st August in 2005. The baseline length is 2.1 km [*Lawrence et al.*, 2006]

TXSM in Texas on 11th October 2005 over a 2.7 km length baseline. During passage of the localized storm, the GNSS RTK performance were much degraded mainly due to wrongly fixed ambiguities, resulting in corrupting the positioning performance. Figure 4.2 shows the L1, L2, and wide-lane DD residual for the satellite pair PRN20 and PRN25 as determined by UNB-RTK software.

A very strong localized tropospheric anomaly was also observed in Southern Texas on August 21, 2005. Over a baseline length of around 7.8 km, the atmospheric effects should be highly correlated and thus easily eliminated in double-differencing (DD). However, the DD residuals of the carrier-phase measurements reached over 50 ppm and most of the carrier-phase ambiguity resolutions on those specific periods failed even in Bernese GNSS software (even with preprocessed and cleaned data) and current conventional RTK platforms. We found that the errors created by mis-modeling the troposphere are propagated into the vertical component. During this process, we also introduced the residual zenith tropospheric delay and the horizontal gradient

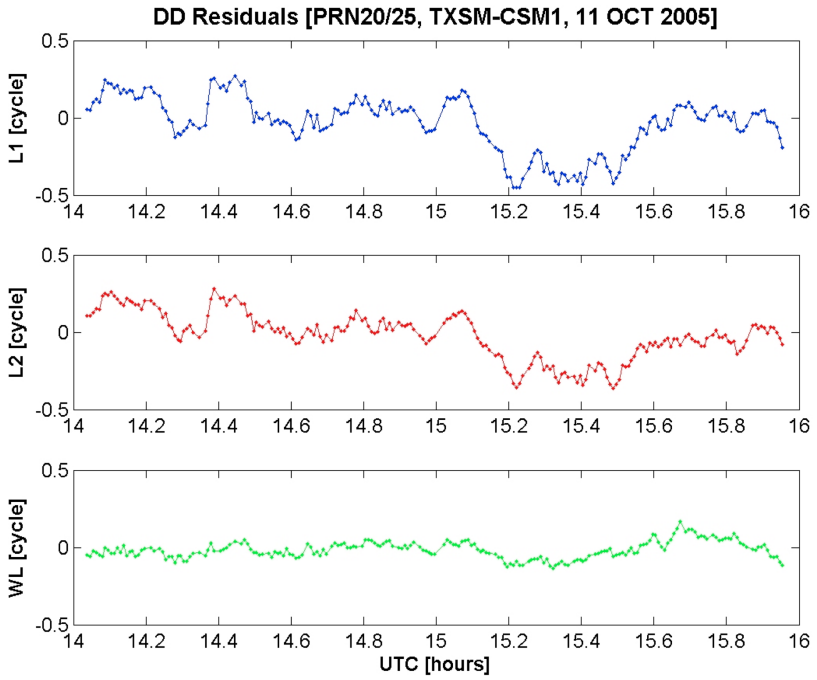

Figure 4.2: L1, L2, and wide-lane residuals on San Marcos CORS stations, TXSM and CSM1, in Texas, observed on 11th October 2005. The baseline length is 2.7 km

parameters to estimate the rover position. We concluded that additional parameters to decorrelate the troposphere and height could be marginally seen, e.g. Ahn et al. [2007], but this result was from a batch solution. In a kinematic scenario where position needs to be estimated at each epoch without preprocessing or cleaning data, estimating more unknown parameters is not helpful in reducing the errors. The data set for the baseline of 7.8 km with a troposphere anomaly is discussed in more detail in Chapter 6 and Chapter 7.

The possibility of other error sources combining with the water droplets (e.g. sand and hydrometeors) has been also examined. For example, to evaluate the sand and dust effect on GNSS positioning, various sparse network data from a CORS network in Texas on 24th February 2007 has been reprocessed using Bernese GNSS software v5.0. A large dense blowing dust storm was observed across the middle of Texas mov-

ing into southwestern Oklahoma on that day. This phenomenon was also observed by a Moderate Resolution Imaging Spectroradiometer (MODIS) instrument and an image was provided by National Aeronautics and Space Administration (NASA). However, in summary, based on our result, we concluded that the effect of sand and dust (combined with the water droplets) could only be marginally observed for those specific GNSS frequencies even for the very strong sand storm. One of the analysis results for this sand storm effect is included in Figure 4.15 and Figure 4.16.

Depending on weather conditions, use of a stochastic modeling approach or parametric estimation approach to decorrelate or mitigate the tropospheric error for medium length baselines has been possible. However, the case will be substantially different when a local tropospheric anomaly exists in a network. As the residual zenith delay of the troposphere and the height component of the positioning solutions are highly dependent on the zenith angle, the problem is very challenging to solve. In the next section, the correlation between two parameters is discussed.

4.2 Correlation between Height and Troposphere

Under extremely inhomogeneous conditions in the lower troposphere, a physical interpretation of the troposphere may be difficult, if not impossible to determine, resulting in certain misassumption about the parametric model. Therefore, not only was a residual analysis of the tropospheric delay carried out, but also a new approach to combine the zenith dependent parameters into one common parameter was developed.

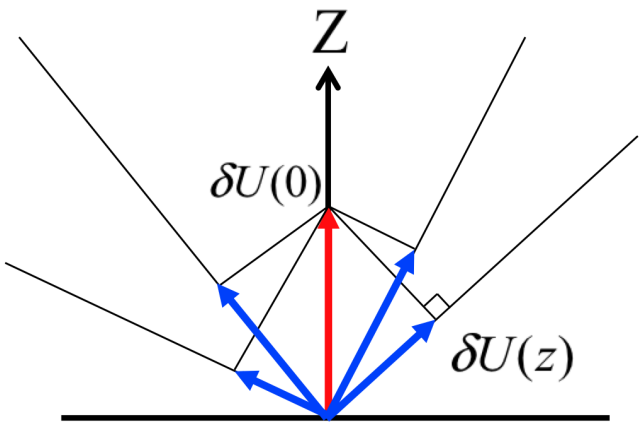

Figure 4.3: Zenith dependency for the height component

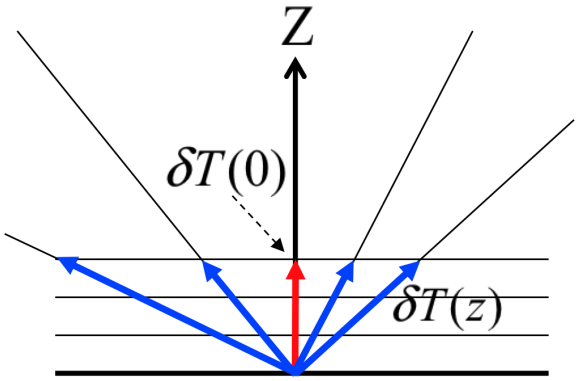

Figure 4.4: Zenith dependency for the troposphere component

Figure 4.3 and Figure 4.4 illustrate the dependency on the zenith angle for both the height component and the residual tropospheric component [*Rothacher and Beutler*, 2002]. Numerically, these dependencies can be written as:

$$\begin{aligned} \delta U(z) &= \cos(z) \cdot \delta U(0) \\ \delta T(z) &= \frac{1}{\cos(z)} \cdot \delta T(0) \end{aligned} \tag{4.1}$$

From Equation (4.1), the correlation between a zenith troposphere parameter and

station height can be numerically evaluated [*Rothacher and Beutler*, 2002]. To make it simple, it is assumed that one parameter for station height and troposphere parameter and/or station clock parameters for entire session is to be estimated. The simplified zero-difference observation equation can be written like:

$$v = -\cos(z) \cdot \delta U(0) + \frac{1}{\cos(z)} \cdot \delta T(0) - c \cdot \delta t_r - (\rho - \rho_\circ) \tag{4.2}$$

where,

v : residuals,

$\delta U(0)$: station height component,

$\delta T(0)$: troposphere parameter in zenith direction,

ρ : geometric distance between satellite and receiver,

$\rho_\circ$: a priori value for geometric distance between satellite and receiver.

With n observations in the zenith directions $z_i (i = 1, \ldots, n)$, a normal equation matrix for Equation (4.2) can be written as:

$$\begin{aligned} N &= H^T P H \\ &= \begin{pmatrix} \sum_i^n \cos^2 z_i & -\sum_i^n 1 & \sum_i^n \cos z_i \\ -\sum_i^n 1 & \sum_i^n \cos^{-2} z_i & \sum_i^n \cos^{-1} z_i \\ \sum_i^n \cos z_i & -\sum_i^n \cos^{-1} z_i & 1 \end{pmatrix} \end{aligned} \tag{4.3}$$

where,

N : normal equation matrix,

H : Jacobi matrix,

P : weight matrix.

With the assumption of a homogeneous distribution of the satellites in the sky between a minimal zenith angle z_{min} and a maximal zenith angle z_{max}, the sum $\sum_i^n$ can be replaced by integrals in Equation (4.3). In addition, as the number of observations is less at smaller zenith angles, the diagonal weight matrix P with $P_{ii} = \sin^2 z_i$ is introduced to correct this effect. Therefore, the final (but not yet simplified) normal equation matrix can be written as:

$$N = \begin{pmatrix} \int_{z_{min}}^{z_{max}} \sin^2 z \cos^2 z dz & -\int_{z_{min}}^{z_{max}} \sin^2 z dz & \int_{z_{min}}^{z_{max}} \sin^2 \cos z dz \\ -\int_{z_{min}}^{z_{max}} \sin^2 z dz & \int_{z_{min}}^{z_{max}} \sin^2 z \cos^{-2} z dz & \int_{z_{min}}^{z_{max}} \sin^2 z \cos^{-1} z dz \\ \int_{z_{min}}^{z_{max}} \sin^2 z \cos z dz & -\int_{z_{min}}^{z_{max}} \sin^2 z \cos^{-1} z dz & \int_{z_{min}}^{z_{max}} \sin^2 z dz \end{pmatrix} \tag{4.4}$$

In Equation (4.4), when the station height is only estimated, the normal equation matrix is reduced to a 1×1 matrix (N_{11}). If both the station height and the troposphere parameter are to be estimated, it is reduced to a 2×2 matrix ($N_{11}, N_{12}, N_{21}, N_{22}$). For the correlation parameter, we can simply invert the normal equation matrix to obtain the variance-covariance matrix $N^{-1} = Q$. Equation (4.4) can be evaluated easily from $z_{min} = 0°$ to $z_{max} = 85°$. Let Q be a variance-covariance matrix for the two parameters for the height and the troposphere parameter. Then the correlation between the height and the troposphere parameter can be written as:

$$corr(\delta H, \delta T) = \frac{Q_{12}}{\sqrt{Q_{11}}\sqrt{Q_{22}}} \tag{4.5}$$

Table 4.1 represents the correlation value calculated for an equatorial station and

polar station based on Equation (4.5).

Table 4.1: Correlation between height and troposphere delay parameter

0° latitude (equatorial stn.)			90° latitude (polar stn.)		
z_{min}	z_{max}	$corr.$	z_{min}	z_{max}	$corr.$
0°	60°	+0.93	45°	60°	+0.98
0°	65°	+0.90	45°	65°	+0.96
0°	70°	+0.85	45°	70°	+0.92
0°	75°	+0.78	45°	75°	+0.86
0°	80°	+0.67	45°	80°	+0.75
0°	85°	+0.50	45°	85°	+0.57

For equatorial stations, a homogenous satellite distribution from the horizon to the zenith was assumed. For the polar station, satellites may only be observed below about $z_{min} = 45°$ because of the inclination of 55° of GPS satellites. As seen from Table 4.1, a strong correlation between the station height and troposphere parameter is evident. When the elevation mask angle is decreased, significant decorrelation occurs which can lead to an improved solution. However, increased multipath effect may occur and additionally larger phase centre variations may occur that can corrupt the positioning solution. Once the receiver clock parameters are included in the estimates, the correlation gets worse.

Regarding the troposphere on GNSS, as described in chapter 1, the troposphere parameters must be determined whenever possible, and for long observation sessions, the troposphere parameters are usually estimated every 1∼2 hours [*Hugentobler*, 2005]. To achieve reliable troposphere delay estimates, a continuous piece-wise linear function (CPLF) has been typically used.

4.3 Piece-Wise Linear Parameters for the Troposphere Delay

For the troposphere delay estimation, a continuous piece-wise linear function (CPLF) which represents a polygon in time is typically used, e.g. Bernese GNSS software [*Hugentobler et al.*, 2005]. This parameterization is also used in other geodetic software including OCCAM, VieVS (Vienna VLBI software) [*Boehm and Schuh*, 2004; *Titov et al.*, 2004; *Teke*, 2011].

A piece-wise linear parameter x is modelled in each particular interval $[t_1, t_2]$ by a linear function. Figure 4.5 represents modelling of time dependent CPLF.

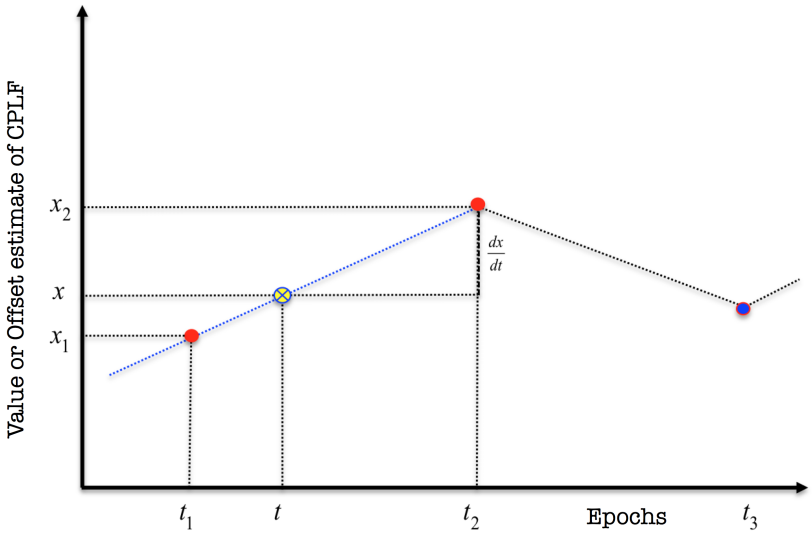

Figure 4.5: Modelling of the time-dependent CPLF

Any parameter offset with the CPLF can be formulated as:

$$x = x_1 + \frac{t - t_1}{t_2 - t_1}(x_2 - x_1) \tag{4.6}$$

where x_1 and x_2 are offsets estimated in integer hour or fractions of integer hours. The tropospheric delay estimates are based on the offset function as:

$$\tau(t) = m_w(t)\left[x_1 + \frac{t - t_1}{t_2 - t_1}(x_2 - x_1)\right] \tag{4.7}$$

where,

$\tau(t)$: zenith wet delay,

$m_w(t)$: wet mapping function at epoch t which is between epoch t_1 and t_2.

The partial derivatives of Equation (4.7) with respect to x_1 and x_2 (zenith wet delay) are:

$$\begin{aligned} \frac{\delta\tau(t)}{\delta x_1} &= m_w(t)\left[1 - \frac{t - t_1}{t_2 - t_1}(x_2 - x_1)\right] \\ \frac{\delta\tau(t)}{\delta x_2} &= m_w(t)\left(\frac{t - t_1}{t_2 - t_1}\right) \end{aligned} \tag{4.8}$$

Equation (4.8) provides the optimal solution in estimating the troposphere delay only if sufficient time intervals such as at least 1∼2 hours are given. Parameters such as the Earth Orientation Parameters, clock offsets etc. can be also estimated using this CPLF in a similar way. The troposphere estimates from GPS data illustrated in Figure 3.9 to Figure 3.16 are based on this CPLF.

For this research, smaller time interval than one hour have also evaluated when estimating the troposphere delay with the CPLF in Bernese GNSS software, and that confirmed that it has worsened the entire positioning solution. Based on a number of tests, the troposphere delay parameter estimation was found to be problematic

if kinematic measurements are processed where the receiver coordinates have to be estimated at every epoch. Some experimental results with different intervals are discussed in Section 7.1.1. Different parameterizations can be found from Figure 7.1 to Figure 7.6.

Previous research (e.g. Ahn et al. [2007]) also investigated the use of additional tropospheric parameters such as residual zenith tropospheric delay and horizontal gradient parameters. Although the method was successful in reducing the tropospheric residuals to some extent, and thus resulted in an improvement in the solution domain, this approach has two main limitations for practical aspects. First, the additional parameters may degrade the entire positioning solution in the estimation process due to redundancy and inter-correlation of parameters. Second, an arbitrary choice of the parametric spacing for the residual troposphere or the gradient estimation is not practical in a kinematic scenario. In a kinematic case with limited observation periods, introducing more parameters may make the entire solution worse.

As stated earlier, even for a short baseline, imbalanced atmospheric errors are shown to have a severe impact on rover positioning solutions, resulting in a worsening of the quality of the positioning solutions (5 cm and more coordinate fluctuation on the height component). A potential explanation is that under extremely inhomogeneous conditions in the lower troposphere, a physical interpretation may be difficult, if not impossible to evaluate, resulting in certain mis-assumption about the parametric model. Therefore, not only was a residual analysis of the tropospheric delay carried out, but also, a new approach has to be established to solve the troposphere mitigation in the kinematic situation. This is discussed in detail in next Section 4.4 which is a new approach to combine zenith dependent parameters into

one common parameter.

In order to introduce our new weighting approach, the general mathematical background is discussed in next section. Under short baselines, the residual effects of the ionosphere and troposphere are typically insignificant. As we are dealing with a strong anomaly effect in the lower troposphere, only the residual tropospheric term (without the assumption of atmospheric azimuthal asymmetry and use of gradient estimation) is included. To evaluate the proposed combined method, the epoch-wise kinematic software was developed for testing different baseline datasets and the details of the test-bed software are discussed in Chapter 5.

4.4 Combined De-Correlation Approach

As described in Section 4.2, the troposphere parameter and height are highly correlated. To try to de-correlate those two parameters, the combined de-correlation approach is introduced. Kim and Langley [2008] also described this approach and performed the feasibility test in their RTK platform in terms of compatibility, controllability, singularity, and redundancy with real data and simulated data sets. The methodology is described here.

To make the problem simpler, let assume that the GNSS signals is experiencing the effect of the troposphere only. Then, the single difference (SD) observables in relative positioning which is fully described in Equation (5.6), can be written like:

$$\varphi^{p}_{km}(t) - N^{p}_{km} + f^{p}_{L1}\delta t_{km}(t) = \frac{1}{\lambda_{L1}}\rho^{p}_{km}(t) + \frac{f_{L1}}{c}\delta T^{p}_{km}(t) \tag{4.9}$$

where,

λ_{L1}: L1 wavelength (metres),

φ^p_{km}: SD phase observables (cycles): superscripts p stands for the satellite, and subscripts m and k for the receivers,

N^p_{km}: SD integer carrier phase ambiguities (cycles),

ρ^p_{km}: SD geometric range (metres),

δT^p_{km}: SD slant tropospheric delay (meters).

Once the geometric term is expanded,

$$\begin{aligned}\rho^p_m &= \rho^p_{m0} \\ &- \frac{X^p(t) - X_{m0}(t)}{\rho^p_{m0}}\Delta X_m - \frac{Y^p(t) - Y_{m0}(t)}{\rho^p_{m0}}\Delta Y_m - \frac{Z^p(t) - Z_{m0}(t)}{\rho^p_{m0}}\Delta Z_m\end{aligned} \tag{4.10}$$

$$\begin{aligned}\rho^p_k &= \rho^p_{k0} \\ &- \frac{X^p(t) - X_{k0}(t)}{\rho^p_{k0}}\Delta X_k - \frac{Y^p(t) - Y_{k0}(t)}{\rho^p_{k0}}\Delta Y_k - \frac{Z^p(t) - Z_{k0}(t)}{\rho^p_{k0}}\Delta Z_k\end{aligned} \tag{4.11}$$

where,

ρ^p_k : geometrical distance between satellite(p) and a receiver(k),

X^p,Y^p,Z^p: satellite (p) positions in Earth-centered Earth-fixed (ECEF) coordinate system (metres),

X_{k0},Y_{k0},Z_{k0}: approximate receiver (k) positions in ECEF coordinate system (metres),

ΔX_k,ΔY_k,ΔZ_k: receiver (k) position increments (metres).

Therefore, the SD geometric range can be written as:

$$\begin{aligned}\rho_k^p - \rho_m^p = \rho_{k0}^p - \rho_{m0}^p \\ - \frac{X^p(t) - X_{k0}(t)}{\rho_{k0}^p}\Delta X_k + \frac{X^p(t) - X_{m0}(t)}{\rho_{m0}^p}\Delta X_m \\ - \frac{Y^p(t) - Y_{k0}(t)}{\rho_{k0}^p}\Delta Y_k + \frac{Y^p(t) - Y_{m0}(t)}{\rho_{m0}^p}\Delta Y_m \\ - \frac{Z^p(t) - Z_{k0}(t)}{\rho_{k0}^p}\Delta Z_k + \frac{Z^p(t) - Z_{m0}(t)}{\rho_{m0}^p}\Delta Z_m\end{aligned} \tag{4.12}$$

If the base station coordinates are known precisely, $\Delta X_m = \Delta Y_m = \Delta Z_m \equiv 0$, then

$$\begin{aligned}\rho_k^p - \rho_m^p = \\ + \rho_{k0}^p - \rho_{m0}^p \\ - \frac{X^p(t) - X_{k0}(t)}{\rho_{k0}^p}\Delta X_k - \frac{Y^p(t) - Y_{k0}(t)}{\rho_{k0}^p}\Delta Y_k - \frac{Z^p(t) - Z_{k0}(t)}{\rho_{k0}^p}\Delta Z_k\end{aligned} \tag{4.13}$$

Therefore, Equation (4.9) can be written as follows:

$$\begin{aligned}\lambda_{L1}\varphi_{km}^p(t) - \lambda_{L1}N_{km}^p + \lambda_{L1}f_{L1}^p\delta t_{km}(t) - \rho_{k0}^p - \rho_{m0}^p - \delta T_{dry,km}^p(t) = \\ - \frac{X^p(t) - X_{k0}(t)}{\rho_{k0}^p}\Delta X_k - \frac{Y^p(t) - Y_{k0}(t)}{\rho_{k0}^p}\Delta Y_k - \frac{Z^p(t) - Z_{k0}(t)}{\rho_{k0}^p}\Delta Z_k \\ + m_{km}^p\tau_{km}(t)\end{aligned} \tag{4.14}$$

where,

$\delta T_{km}^p(t) = \delta T_{dry,km}^p(t) + m_{km}^p\tau_{km}(t)$,

$\delta T^{p}_{dry,km}(t)$: SD slant hydrostatic delay,

$\tau_{km}(t)$: SD wet zenith delay.

Assuming that the carrier phase ambiguities are correctly resolved and accurate meteorological data are available at a reference station and a rover, we will have a reduced DD carrier-phase observation model for short-baseline applications as:

$$\begin{aligned}\lambda_{L1}\varphi^{pq}_{km}(t) - \lambda_{L1}N^{pq}_{km} - \rho^{pq}_{km} - \delta T^{pq}_{dry,km} \\ = h^{pq}_{x}\Delta X_k + h^{pq}_{y}\Delta Y_k + h^{pq}_{z}\Delta Z_k + m^{pq}_{k}(t)\tau_{km}(t) + \varepsilon^{pq}_{km,err}\end{aligned} \tag{4.15}$$

where,

$$\begin{aligned} h^{pq}_{x} &= -\frac{X^q(t) - X_{k_0}}{\rho^q_{k_0}(t)} + \frac{X^p(t) - X_{k_0}}{\rho^p_{k_0}(t)} \\ h^{pq}_{y} &= -\frac{Y^q(t) - Y_{k_0}}{\rho^q_{k_0}(t)} + \frac{Y^p(t) - Y_{k_0}}{\rho^p_{k_0}(t)} \\ h^{pq}_{z} &= -\frac{Z^q(t) - Z_{k_0}}{\rho^q_{k_0}(t)} + \frac{Z^p(t) - Z_{k_0}}{\rho^p_{k_0}(t)} \end{aligned} \tag{4.16}$$

where,

λ_{L1}: L1 wavelength (metres),

φ^{pq}_{km}: DD phase observables (cycles): superscripts p and q stands for the satellites, and subscripts m and k for the receivers,

N^{pq}_{km}: DD integer carrier phase ambiguities (cycles),

ρ^{pq}_{km}: DD geometric range (metres),

$\delta T^{pq}_{dry,km}$: DD slant hydrostatic (or dry) delay (meters),

X^q,Y^q,Z^q: satellite positions in Earth-centered Earth-fixed (ECEF) coordinate system (metres),

X_{k0},Y_{k0},Z_{k0}: approximate receiver positions in ECEF coordinate system (metres),

ΔX_k,ΔY_k,ΔZ_k: receiver position increments (metres),

m_{km}^{pq}: DD non-hydrostatic (or wet) mapping coefficient at the receiver k (unitless),

τ_{km}: relative wet zenith delay (metres),

$\varepsilon_{mk,err}^{pq}$: residual errors (e.g., receiver system noise).

Under short baselines, the residual effects of the ionosphere and troposphere are typically insignificant. As we are dealing with a strong anomaly effect in the lower troposphere, the residual tropspheric term (without the assumption of atmospheric azimuthal asymmetry and use of gradient estimation) is included in order to have a more representative equation. Equation (4.15) can be expressed as follows:

$$L = Hx + m\tau + e \qquad e = N(0, Q_L) \tag{4.17}$$

$$\begin{aligned} L &= \lambda_{L1}\varphi_{km}^{pq}(t) - \lambda_{L1}N_{km}^{pq} - \rho_{km}^{pq} - \delta T_{dry,km}^{pq} \\ H &= [h_x \quad h_y \quad h_z] \\ x &= [\Delta X_k \quad \Delta Y_k \quad \Delta Z_k]^T \end{aligned} \tag{4.18}$$

Note that e is a normally distributed random vector with expected value of 0 and variance-covariance Q_L.

In order to analyze the common zenith dependent parameters (that is, the vertical component of the receiver′s position and the wet zenith delay), the local geodetic coordinate system is introduced. The axes n and e span the local geodetic horizon which is perpendicular to the ellipsoidal normal through the surface of point P as illustrated in Figure 4.6. In Figure 4.6, n and e point north and east, and u coincides

with the ellipsoidal normal with the positive end upward of the ellipsoid [*Leick*, 2004].

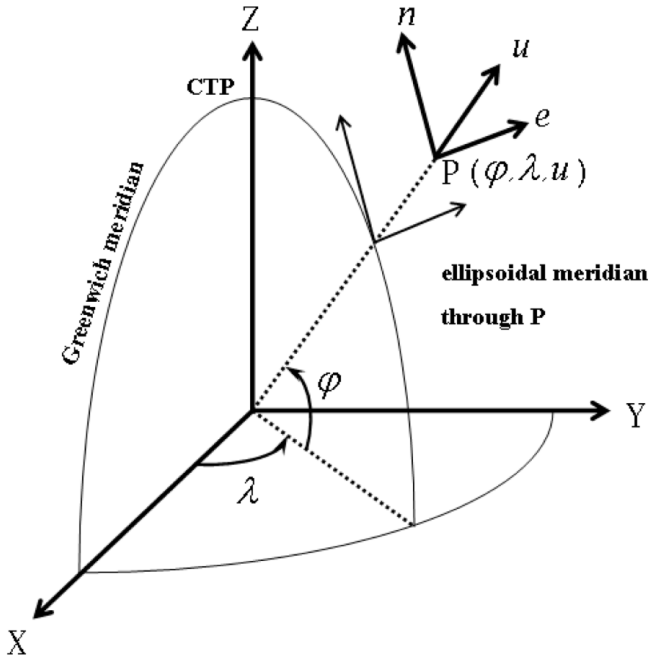

Figure 4.6: Local geodetic coordinate system

The relationship between the local geodetic coordinate system and the geocentric system is as follows:

$$
\begin{aligned}
x &= R^{-1}n \\
R &= \begin{bmatrix} -\sin\varphi\cos\lambda & -\sin\varphi\sin\lambda & \cos\varphi \\ -\sin\lambda & \cos\lambda & 0 \\ \cos\varphi\cos\lambda & \cos\varphi\sin\lambda & \sin\varphi \end{bmatrix} \\
n &= [\Delta n \quad \Delta e \quad \Delta u]^T
\end{aligned}
\tag{4.19}
$$

where R is the rotation matrix and n is a vector of the position component incre-

ments in local geodetic system. Given the latitude and longitude of the receiver, the geocentric coordinate system can be easily transformed to the local geodetic system based on Equation (4.19). Equation (4.17) can be now rewritten as a sub-matrix forms as follows:

$$\begin{aligned} L &= Gn + m\tau + e \\ &= \begin{bmatrix} g_n & g_e \end{bmatrix} \begin{bmatrix} \Delta n \\ \Delta e \end{bmatrix} + \begin{bmatrix} g_u & m \end{bmatrix} \begin{bmatrix} \Delta u \\ \tau \end{bmatrix} + e \\ G &= HR^{-1} \end{aligned} \tag{4.20}$$

Equation (4.20) gives a straightforward interpretation of the vertical increment Δu and the wet zenith delay τ. Figure 4.7 shows the relationship between the vertical component of the design matrix g_u and the Niell′s wet mapping function coefficient m for each satellite. As illustrated in Figure 4.7, they are correlated with each other, especially at high elevation angles. For comparison purpose, we used negative Niell′ wet mapping coefficients at the right-side y-axis in Figure 4.7. The functional relationship between the two coefficients is illustrated in Figure 4.8. As implied in Figure 4.8, the two parameters (the vertical increment and the wet zenith delay) will have strong correlation at high elevation angles. On the other hand, their correlation becomes weaker at lower elevation angles.

The challenge to be overcome in this dissertation is to break-up the correlation between the two parameters (the vertical increment and the wet zenith delay). Even if they have a functional relationship with each other, the two parameters cannot be easily combined into one single parameter and it is probably impossible to have a linearized form. Therefore, we follow a numerical approach to solve the correlation

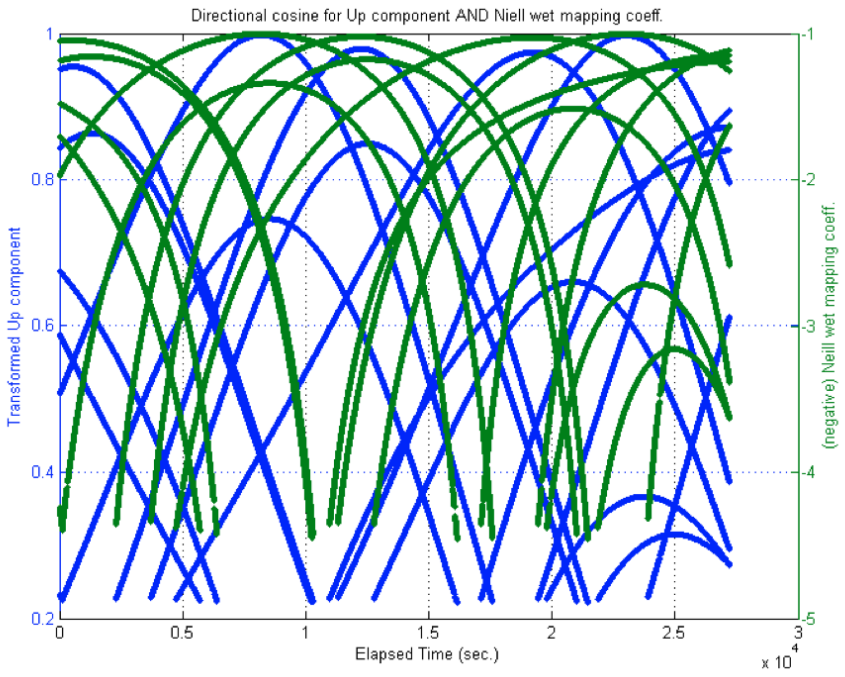

Figure 4.7: Relationship between the vertical component g_u and the Niell′s wet mapping coefficient m

problem. By introducing the new parameters, α and ζ as illustrated in Figure 4.9, the two parameters can be combined as follows:

$$g_u \Delta u + m\tau = [\alpha g_u + (1-\alpha)m]\,\zeta \tag{4.21}$$

where,

$$\alpha = \frac{\Delta u}{\Delta u + \tau} \qquad \zeta = (\Delta u + \tau) \tag{4.22}$$

The parameter α represents the ratio between the vertical component increment and ζ. Typically, α has the value $0 < \alpha \leq 1$ if controlled. By changing the value of

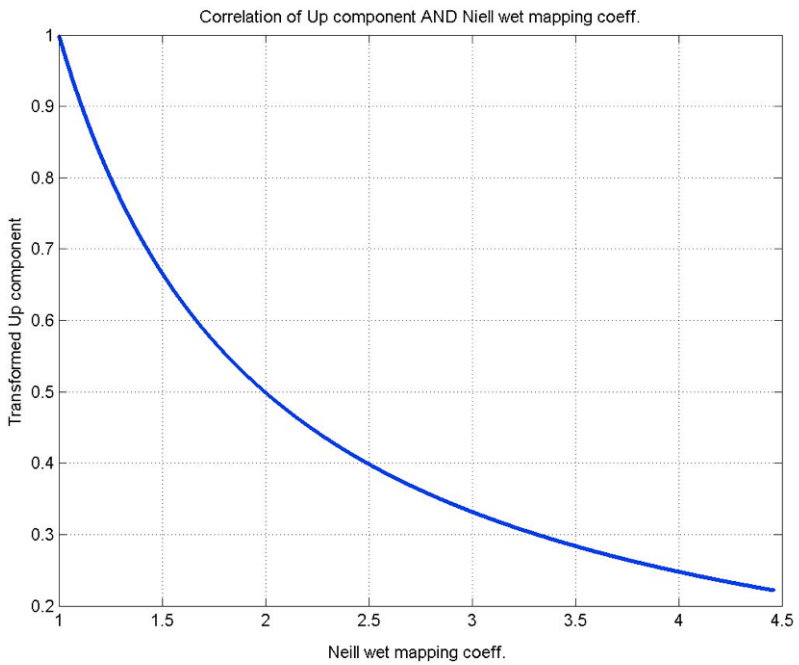

Figure 4.8: Functional relationship between the vertical component g_u and the Niell′s wet mapping coefficient m

α, we can adjust the weight of the two parameters. By changing the α from 0 to 1 with a step size of 0.01, we can find the best positioning solution among 100 different solutions, for example. In Figure 4.10, there is a point which minimizes the weighted sum of the squared residuals. Choosing a different α will give a different solution (e.g. much worse or much better) as they weigh differently the vertical component of the design matrix g_u and the Niell′s wet mapping function coefficient m.

From background research in case of a static scenario, once α, the weighting parameter, is properly selected, the positioning is dramatically enhanced. A different α represents that it is giving a different solution as the vertical component of the design matrix g_u and the Niell′s wet mapping function coefficient m are weighted differently. One difficult issue to be solved, however, is how to determine the weighing parameter, α, in a real practical way in a kinematic situation. The height estimates Δu, can

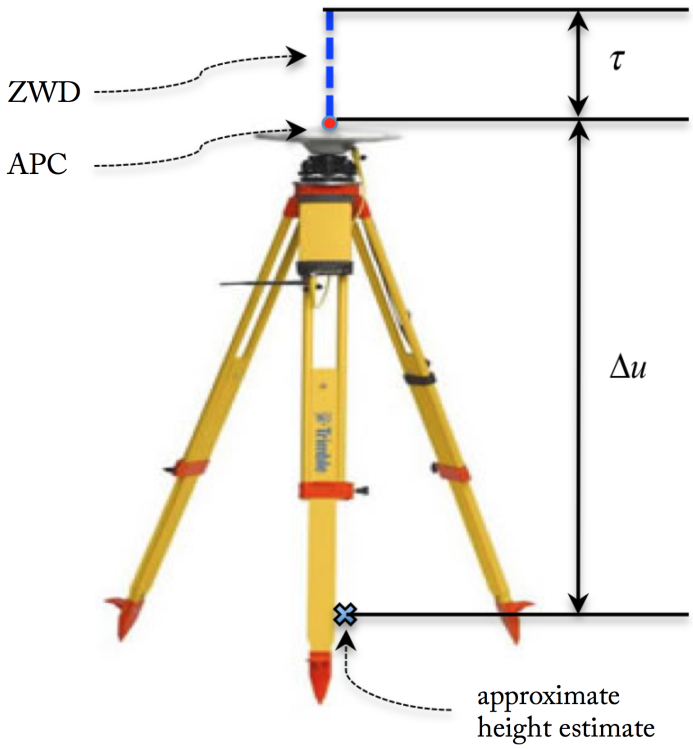

Figure 4.9: Geometric representation for $\zeta = \Delta u + \tau$

be initially estimated in a normal cartesian coordinate system with a certain precision. Once the cartesian position estimates are determined and transformed to local coordinate system, then Δu can be assumed to be known with a certain precision. Thereafter, with a recursive algorithm, subsequent but better Δu can be determined using the proposed weighting scheme when the troposphere is problematic. The level of the contribution for the troposphere $\Delta\tau$ in the weighting parameter can be subsequently identified in the solution domain.

4.5 Residual Analysis

DD residuals can be separated from non-dispersive and dispersive medium and their corresponding magnitudes can be determined. Once the integer or float ambiguities

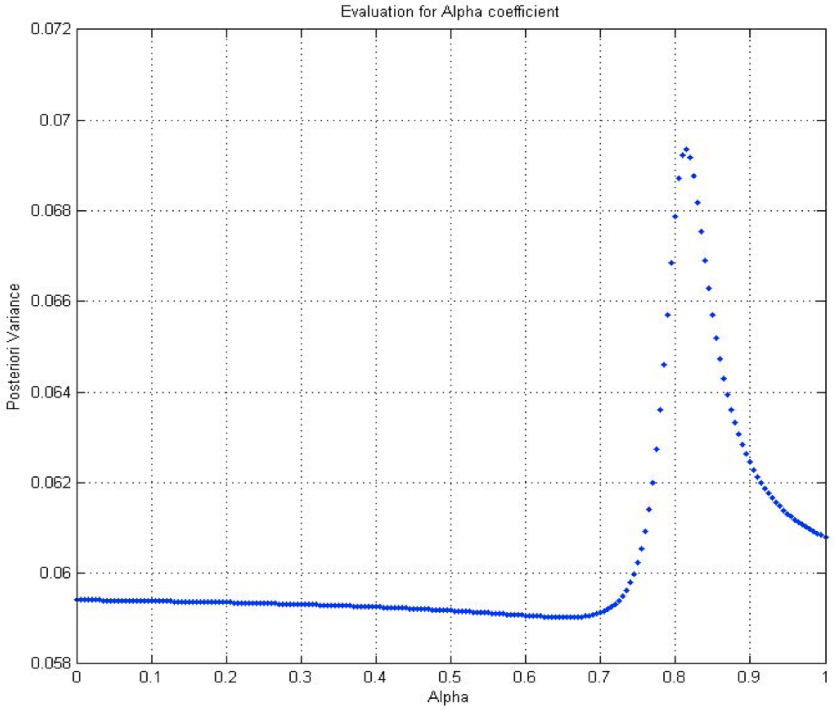

Figure 4.10: Weighted sum of the squared residual corresponding to α from 0 to 1 with a step size of 0.01. This is a single epoch example

are determined, the residuals for L1 or L2 can be generated by the following equations originally proposed by Lawrence et al. [2006]:

$$\gamma^{pq}_{km_\lambda} = \frac{\delta T^p - \delta T^q}{\lambda_{km_\lambda}} - (\delta I^p - \delta I^q)\lambda_{km_\lambda} + \frac{M^{pq}_{km_\lambda} + W^{pq}_{km_\lambda}}{\lambda_{km_\lambda}} \tag{4.23}$$

$$\gamma^{pq}_{km_\lambda} = \Phi^p_{km_\lambda} - \Phi^q_{km_\lambda}$$

$$\Phi^i_{km_\lambda} = \varphi^i_{km_\lambda} - \frac{\Delta r}{\lambda_{km_\lambda}} - N_{km_\lambda}$$

$$M^{pq}_{km_\lambda} = \frac{M^p_{km_\lambda} - M^q_{km_\lambda}}{\lambda_{km_\lambda}}$$

$$W^{pq}_{km_\lambda} = \frac{W^p_{km_\lambda} - W^q_{km_\lambda}}{\lambda_{km_\lambda}}$$

where,

λ : a frequency either $L1$ or $L2$,

$N^i_{km_\lambda}$: the double-difference cycle ambiguity for satellite i and frequency k relative to the reference satellite r for baseline k and m,

$\gamma^{pq}_{km_\lambda}$: the double-difference phase residual between satellites p and q,

$\varphi^i_{km_\lambda}$: the single-difference carrier-phase measurement for satellite i on frequency λ (in units of cycles),

λ_{km_λ} : the wavelength of frequency λ,

Δr : the differential distance to the satellite,

δT^i : the differential troposphere delay for satellite i,

$\delta I^i \lambda_{km_\lambda}$: the differential ionosphere group delay at frequency k,

$M^i_{km_\lambda}$: the differential carrier multipath error for satellite i and frequency k,

$W^i_{km_\lambda}$: the differential receiver noise error for satellite i and frequency k.

Equation (4.23) shows that there is a fixed ratio between the contribution of the troposphere to the $\gamma^{pq}_{km_2}$ and $\gamma^{pq}_{km_1}$ residuals. Also, there is a fixed ratio between the contributions of the ionosphere to those residuals. When we choose $\gamma^{pq}_{km_2}$ as the y-axis and $\gamma^{pq}_{km_1}$ as the x-axis, then the troposphere contribution is given by the slope of λ_1/λ_2. Also, in a similar way, the ionosphere can be given by λ_2/λ_1. The DD residuals for both L1 and L2 which can separate the contribution of DD troposphere into the DD ionosphere delay. An example can be seen from Figure 4.16. The only assumption behind this identification method is that the slope of λ_1/λ_2 purely follows the troposphere signature which may not be true under all actual environments due to many other effects, such as multipath, and phase centre offset variations. Figure 4.11 represents the geometry of the residuals of L1 and L2.

Once the DD residual is determined at each epoch, it can be either within the

identification boundary for the troposphere, $\theta_2 - 7° < P < \theta_2 + 7°$ and $\pi + (\theta_2 - 7°) < P < \pi + (\theta_2 + 7°)$ or outside the boundary limit.

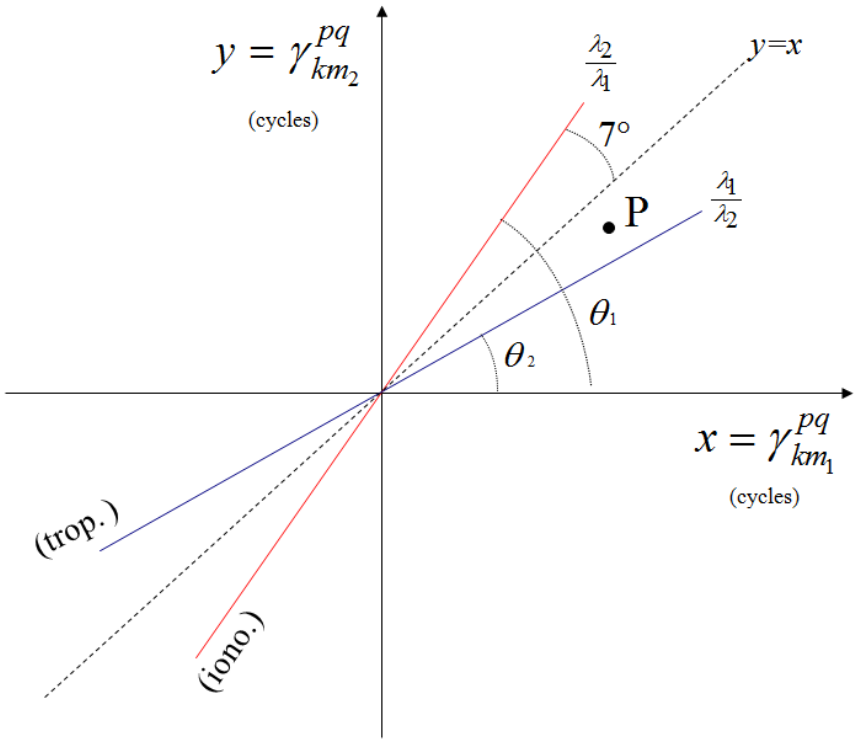

Figure 4.11: Identification of the contribution

The magnitude and the angle can be calculated based on the DD residual from the following relationships:

$$\begin{aligned} \mathrm{P}_{mag} &= \sqrt{\left(\gamma_{km_2}^{pq}\right)^2 + \left(\gamma_{km_1}^{pq}\right)^2} \\ \theta_{\mathrm{P}} &= \arctan\left(\gamma_{km_2}^{pq} / \gamma_{km_1}^{pq}\right) \end{aligned} \tag{4.24}$$

4.5.1 Troposphere Error Signature from Residual Analysis

Figure 4.12 represents the identification and magnitude of a pair of satellites, PRN 19-27, during the tropospheric anomaly based on the residual analysis, as an exam-

ple. Actual troposphere error signature plots for both L1 and L2 frequency such as an identification plot similar to Figure 4.11 can be found in Figure 4.16 or in Chapter 7 from a few baselines evaluated.

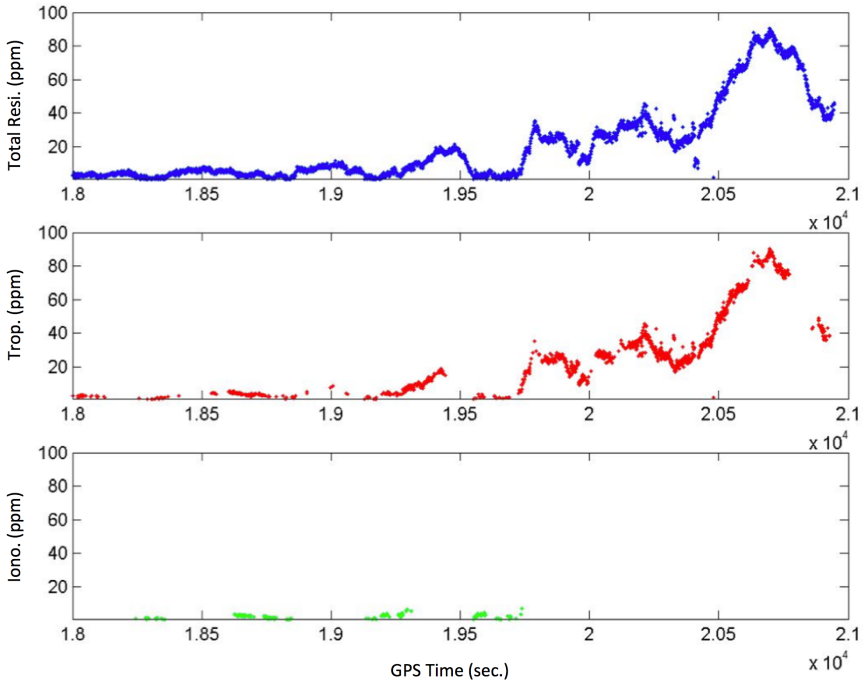

Figure 4.12: Identification of the contribution and magnitude in terms of ppm (in y-axis) for an example pair, PRN19-27

The magnitude of residuals in Equation (4.24) can be transformed in terms of ppm (part per million) of the baseline length. Figure 4.12 represents a transformed magnitude of a tropospheric anomaly as an example. The top panel in Figure 4.12 represents the magnitude of actual residuals of L1 in terms of ppm versus elapsed time in seconds, and the middle panel represents the troposphere signature based on the L1 and L2 residual analysis described above. The lower panel is the ionosphere signature. Some of the missing points are not within the boundary limit (as described in Figure 4.11) which is not from either the troposphere or from the ionosphere. It clearly shows that most of the residuals follow by the tropospheric contribution line

in this case and the magnitude in the slant range reached almost up to 100 ppm levels.

As is expected, the residuals agree well with the DD tropospheric signature. During the anomaly, almost all other satellite pairs also showed similar patterns. At every epoch, the residual analysis can be performed to determine the magnitude of the troposphere. Once the magnitude over the 20 ppm level is found in the slant range and retrieved into the zenith direction, its value has been applied to determine the weighting parameter. The benefit of using this methodology is that, as each satellite pair is examined to determine the weighting parameter in a different direction, it already contains the tropospheric gradient information.

4.5.2 Ionosphere Error Signature from Residual Analysis

In high-accuracy geodetic applications of GNSS, time variable tropospheric propagation delay limits the performance of positioning. Previous research on the troposphere focused mainly on the mitigation of tropospheric delay under long baseline situations. However, a local tropospheric anomaly can also severely degrade the performance of kinematic positioning even under short-baseline situations; this can be a potential major issue for local surveyors.

The propagation of electromagnetic waves were found by Oguchi [1983] to be potentially affected by rain drop and dust (the amount getting a function of their size) in terms of attenuation, de-polarization and noise, including (but may not be limited to) millimetre waves. Many researchers have tried to identify the effect on a scope of applications mostly from the ideal experimental situation such as Comparetto [1993]. To quantify the impact on a GNSS survey associated with signal attenuation through dust, foliage, rain, cable, and other materials in many situation is a

challenging task. One example shown in this section is the verification of the error signature identification method based on the method described in section 4.5.

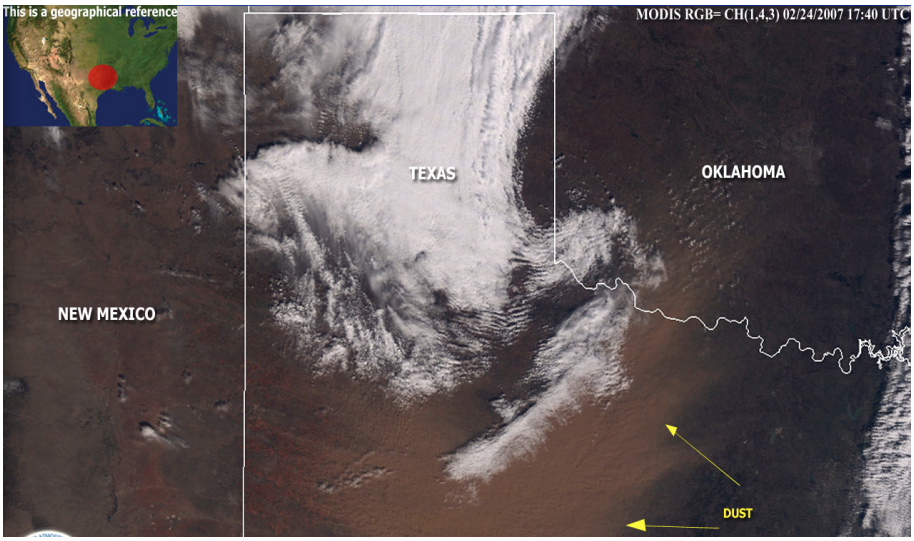

Figure 4.13: MODIS RGB satellite image (Courtesy: NOAA/NASA)

To evaluate the identification method of the residual contribution either troposphere or ionosphere as described in Equation (4.23), data during a sand storm were processed as well. During the sand storm, typically the air is known to become dry and therefore the signature of the troposphere can be more easily differentiated from any other effects. The dust storm data in Texas, USA on Feb. 24, 2007 were processed to investigate this. Figure 4.13 shows the MODIS RGB satellite image. It shows a large dense blowing dust cloud across the middle of Texas and moving into southwestern Oklahoma. The yellow arrows near the bottom right in Figure 4.13 show the area of dust coverage, revealing that the sand storm has covered nearly half of the State of Texas.

Figure 4.14 represents the stations used to obtain the required data. To identify the residual signature, the data were processed with Bernese GNSS software. The

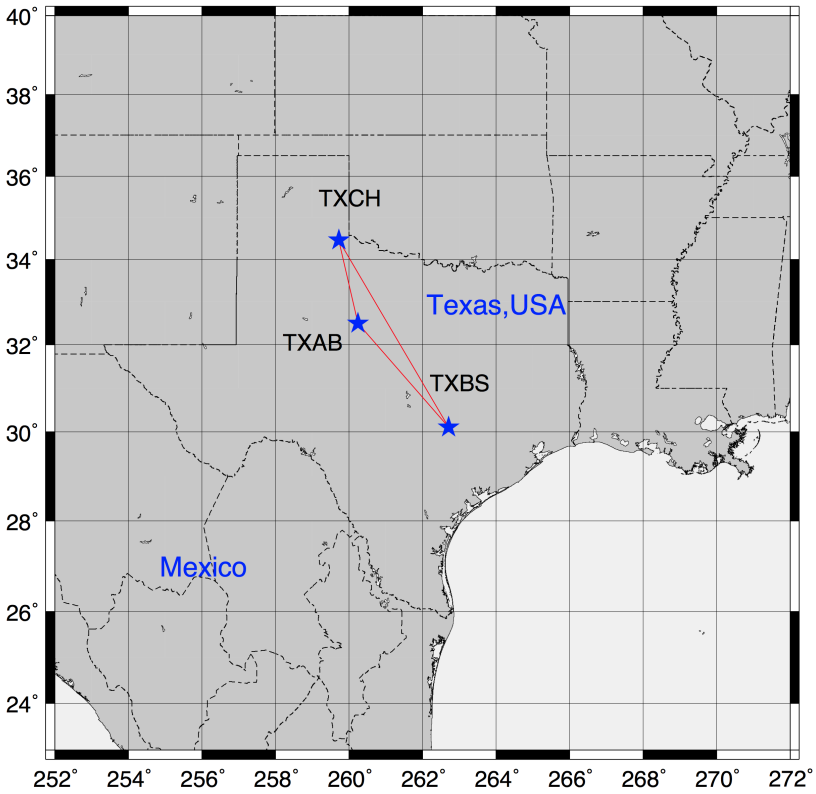

Figure 4.14: Network diagram during sand storm

station IDs are TXAB, TXBS and TXCH. The distance between TXAB and TXCH was 354 km. For the processing, the quasi-ionosphere was chosen as a methodology [*Hugentobler et al.*, 2005]. After pre-processing the data and solving for the ambiguities, the final post-processed kinematic position (PPK) results shown in Figure 4.15 were obtained. As the baseline length was over 300 km, the PPK positioning result obtained was cm level accuracy which is very reasonable.

The corresponding residuals in both L1 and L2 for the baseline TXAB-TXBS was calculated and is illustrated in Figure 4.16. From Figure 4.16, one can clearly see the signature of the troposphere and ionosphere from DD residual analysis. As expected, the residuals are mainly followed by the ionosphere signature line (or any other effect rather than the troposphere signature line) during the sand storm. Compared

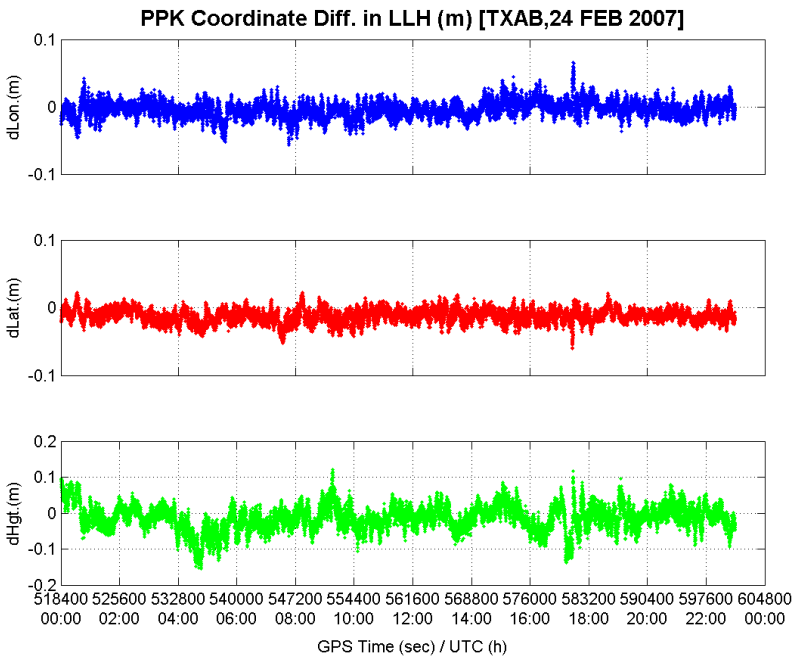

Figure 4.15: PPK solution with Quasi ionospheric-free combination during sand storm

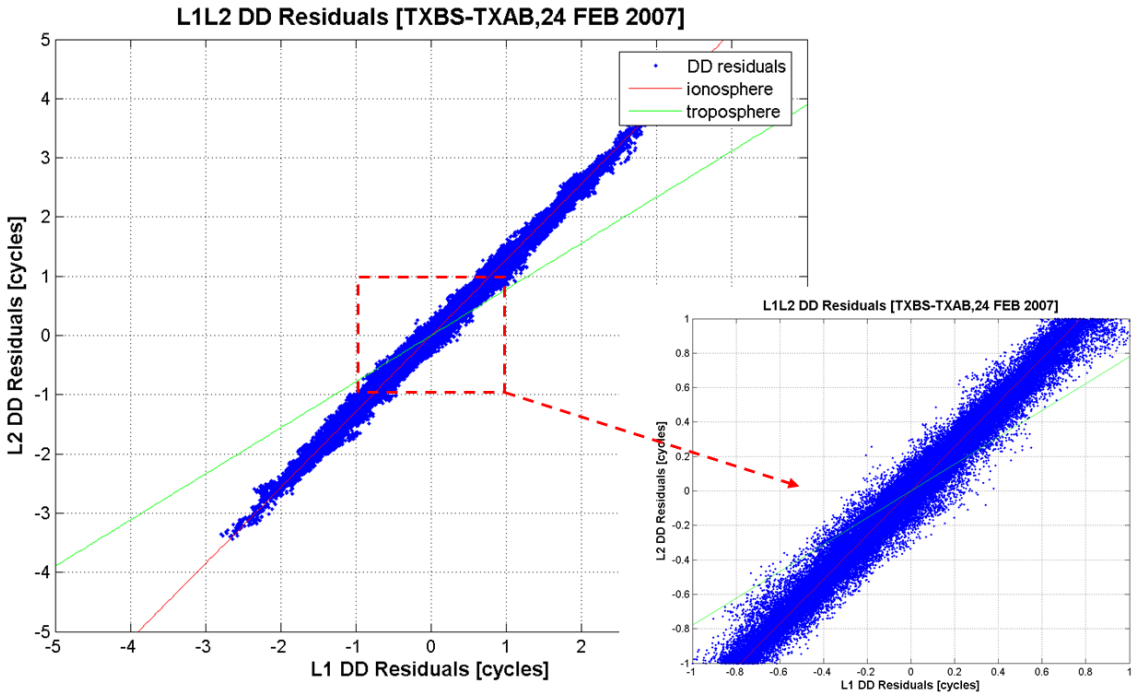

Figure 4.16: Residual plots for L1 and L2 during a sand storm

to the ionosphere line, this strongly suggests that the troposphere model applied to the correction on the data processing were found relatively more precise than other prominent error sources including the ionosphere errors or any other frequency dependent component.

Although it is known that microwave wave bands affects to levels of signal attenuation (e.g. Musa and Bashir [2013]), I could not prove here if this specific sand storm largely affected on GNSS signals or not, and could not quantify the amount of the effect. It needs to be further investigated. However, based on this test and results, in order to improve the solution, it is clear that the elaborated ionosphere model or a different ionosphere model or the frequency dependent effects must be employed rather than using a different troposphere model in this specific case. As the baseline length is extended, the de-correlated errors due to the atmosphere are more difficult to resolve. Figure 4.16 was the best solution for the data that could be obtained from processing using many different options in the Bernese GNSS software.

4.6 Summary

The correlation between the height and the troposphere has been discussed in this chapter. To overcome, the limitation of the current troposphere mitigation approach during the troposphere anomaly even for a short baseline, a new developed methodology has been derived and described in detail in Chapter 4. To evaluate the methodology in a kinematic scenario, a test-bed relative positioning software has been developed. Chapter 5 will discuss the mathematical background of the developed epoch-wise relative positioning software.

Chapter 5

Test-Bed Relative Positioning Software

In order to test the developed combined approach that is described in Chapter 4, a relative positioning software was developed. This chapter describes some details of the software regarding the functional model and epoch-wise least square approach and error handling for the developed positioning system. The combined approach described in Chapter 4 in several baselines is tested with this software platform.

5.1 Observational Equation

As described in Chapter 2, there are two fundamental GNSS observables. One is the pseudorange (or code) and the other is the phase. The phase observables of either L1 or L2 frequency are based on the difference between the received satellite phase and the receiver′s internal phase replica by an oscillator. The only observables in this case are the accumulated phase differences.

In a conventional survey, we use the distance measurement unit (EDM) or total station (TS) unit to determine the mm-level distances between the unit and targets

on nearby control points. It uses the same fundamental principle in a satellite surveying. The observables from the conventional survey units are, however, unambiguous as the EDM it transmits at a number of different wavelengths to the target(s). With this unique method, the EDM or TS can identify the number of integer cycles (or ambiguities) to the object and thus it can accurately determine the total distance.

In a satellite surveying, it is unlikely because the distance between the receiver and the satellite is too large to use numerous signals like the conventional surveying EDM or TS instrument. Therefore, unlike code observables, the phase observables are alway ambiguous, although it is 100 times more precise than the code observables.

The phase equation in Equation (2.1) in the case of L1, in terms of cycles, and code observables, can be rewritten as:

$$\begin{aligned}\varphi^p_{k,L1}(t)^8 = {} & \frac{f_{L1}}{c}\rho^p_{k,L1}(t) - f_{L1}\left[1 - \frac{\dot{\rho}^p_{k,L1}(t)}{c}\right]\delta t_k + f_{L1}\delta t^p \\ & + N^p_{k,L1}(1) + \frac{a^p}{c}\rho^p_{k,L1}(t) - \delta I^p_{k,L1}(t) + \frac{f_{L1}}{c}\delta T^p_k(t) \\ & + (\delta t_{k,sys}(t) + \delta\rho_{mul} + \delta t^p_{sys}(t) + \varepsilon_{err})\end{aligned} \tag{5.1}$$

$$\begin{aligned}P^p_k(t) = {} & \rho^p_k(t) - \left[1 - \frac{\dot{\rho}^p_k(t)}{c}\right]\delta t_k + c\delta t^p \\ & + \delta I^p_k(t) + \delta T^p_k(t) + (\delta t_{k,sys}(t) + \delta\rho_{mul} + \delta t^p_{sys}(t) + \varepsilon_{err})\end{aligned} \tag{5.2}$$

where,

$\varphi^p_{k,L1}(t)$: phase observables between satellite(p) and receiver(k) for L1,

[8]This equation includes all possible error sources that can be considered; similar to Leick [2004]

$\rho^p_{k,L1}(t)$: geometrical distance between satellite(p) and a receiver(k) for L1,

c : speed of light in vacuum,

δt_k : station clock correction,

$\delta t_{k,sys}$: delays in receiver and its antenna,

δt^p : satellite clock correction due to satellite clock error,

δt^p_{sys} : delays in satellite and its antenna,

δT : tropospheric delay,

δI : ionospheric delay,

$\delta \rho_{rel}$: relativistic corrections due to special and general relativity,

$\delta \rho_{mul}$: multipath,

f_{L1} : frequency of the GPS signal ($L1$),

N^p_k : integer ambiguity,

a^p: satellite frequency offset,

$\dot{\rho}^p_{k,L1}(t)$: topocentric range rate,

$L1, k, p$: subscript ($L1$, k) and superscript (p) denote frequency IDs, receiver ID and satellite ID,

ε_{err} : other remaining measurement errors.

As the ionosphere is a dispersive medium (which means that it acts differently at different GNSS frequencies), the following relationship can be made:

$$\begin{aligned} \delta I^p_{k,C/A,m}(t) &= -\delta I^p_{k,L1,m}(t) = -\frac{c}{f_{L1}} \delta I^p_{k,L1,c}(t) \\ \delta I^p_{k,P2,m}(t) &= -\delta I^p_{k,L2,m}(t) = -\frac{c}{f_{L2}} \delta I^p_{k,L2,c}(t) \end{aligned} \tag{5.3}$$

where the subscript m and c represents in the units of metres or cycles. C/A denotes coarse/acquisition code which is transmitted on the L1 carrier frequency. P2

means precision code transmitted on the L2 carrier.

The relationship in Equation (5.3) leads to:

$$\frac{\delta I^p_{k,C/A,m}(t)}{\delta I^p_{k,P2,m}(t)} = \frac{f^2_{L2}}{f^2_{L1}}, \qquad \frac{\delta I^p_{k,L1,c}(t)}{\delta I^p_{k,L2,c}(t)} = \frac{f_{L2}}{f_{L1}} \tag{5.4}$$

Therefore, Equation (5.1) for the L2 frequency can be written as:

$$\begin{aligned}\varphi^p_{k,L2}(t) = {} & \frac{f_{L2}}{c}\rho^p_{k,L2}(t) - f_{L2}\left[1 - \frac{\dot{\rho}^p_{k,L2}(t)}{c}\right]\delta t_k + f_{L2}\delta t^p \\ & + N^p_{k,L2}(1) + \frac{a^p}{c}\rho^p_{k,L2}(t) - \frac{f^2_{L1}}{cf^2_{L2}}\delta I^p_{k,L2}(t) + \frac{f_{L2}}{c}\delta T^p_k(t) \\ & + (\delta t_{k,sys}(t) + \delta\rho_{mul} + \delta t^p_{sys}(t) + \varepsilon_{err})\end{aligned} \tag{5.5}$$

The phase and code equation in Equation (5.1), Equation (5.2) and Equation (5.5) are the basic functional models for each observables.

There have been many different positioning algorithms developed over decades that can generally be divided in two main categories. One is relative positioning and the other is precise point positioning.

In relative positioning, there are the single difference (SD), the double difference (DD) and triple difference (TD) observables that can be formulated from baseline stations. If two receivers k and m receive the observables from a satellite p, one can write the difference between two observables for the same satellite p as follows [*Leick*, 2004]:

$$
\begin{aligned}
\varphi^p_{km}(t) &\equiv \varphi^p_k(t) - \varphi^p_m(t) \\
&= \frac{f}{c}\left[\rho^p_k(t) - \rho^p_m(t)\right] + \frac{a^p}{c}\left[\rho^p_k(t) - \rho^p_m(t)\right] \\
&+ \frac{f}{c}\left[\dot{\rho}^p_k(t)\delta t_k - \dot{\rho}^p_m(t)\delta t_m\right] - f(\delta t_k - \delta t_m) + N^p_{km}(1) \\
&+ \delta I^p_{km,\varphi}(t) + \frac{f}{c}\delta T^p_{km}(t) + \delta t_{km,sys,\varphi}(t) + \delta\rho^p_{km,mul,\varphi}(t) + \varepsilon^p_{km,err,\varphi}
\end{aligned}
\tag{5.6}
$$

where,

$N^p_{km}(1) = N^p_k(1) - N^p_m(1)$,

$\delta I^p_{km,\varphi}(t) = \delta I^p_{k,\varphi}(t) - \delta I^p_{m,\varphi}(t)$,

$\delta T^p_{km}(t) = \delta T^p_k(t) - \delta T^p_m(t)$,

$\delta t_{km,sys,\varphi}(t) = \delta t_{k,sys,\varphi}(t) - \delta t_{m,sys,\varphi}(t)$,

$\delta\rho^p_{km,mul,\varphi}(t) = \delta\rho^p_{k,mul,\varphi}(t) - \delta\rho^p_{m,mul,\varphi}(t)$,

$\varepsilon^p_{km,err,\varphi} = \varepsilon^p_{k,err,\varphi} - \varepsilon^p_{m,err,\varphi}$,

φ: the subscript represents that it is dependent on the frequency used.

$$
\begin{aligned}
\varphi^{pq}_{km}(t) &\equiv \varphi^p_{km}(t) - \varphi^q_{km}(t) \\
&= \frac{f}{c}\left[\rho^p_k(t) - \rho^p_m(t)\right] - \frac{f}{c}\left[\rho^q_k(t) - \rho^q_m(t)\right] \\
&+ \frac{a^p}{c}\left[\rho^p_k(t) - \rho^p_m(t)\right] - \frac{a^p}{c}\left[\rho^q_k(t) - \rho^q_m(t)\right] \\
&+ \frac{f}{c}\left[\dot{\rho}^p_k(t)\delta t_k - \dot{\rho}^p_m(t)\delta t_m\right] - \frac{f}{c}\left[\dot{\rho}^q_k(t)\delta t_m - \dot{\rho}^q_m(t)\delta t_m\right] \\
&+ N^{pq}_{km}(1) + \delta I^{pq}_{km,\varphi}(t) + \frac{f}{c}\delta T^{pq}_{km}(t) + \delta\rho^{pq}_{km,mul,\varphi}(t) + \varepsilon^{pq}_{km,err,\varphi}
\end{aligned}
\tag{5.7}
$$

Figure 5.1 illustrates the details of each differencing technique. For the single difference, reference station m and rover station k is the received signals from the satellite j at time t_1. For the double difference, reference station m and rover sta-

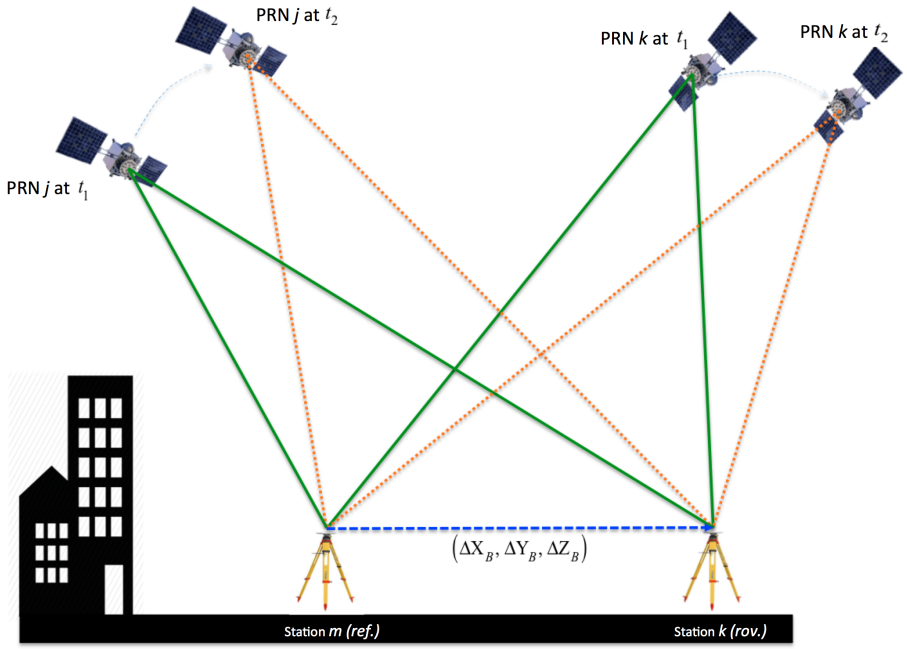

Figure 5.1: Differencing scheme in relative positioning

tion k receives signals from satellites j and k. Two individual single differences are subtracted from each other to obtain the double difference observables as in Equation (5.7). Based on this method, the most problematic common receiver errors are additionally eliminated (or at least minimized), but there is still the double difference ambiguity to consider.

In Equation (5.7),

$$N_{km}^{pq}(1) = N_{km}^{p}(1) - N_{km}^{q}(1),$$

$$\delta I_{km,\varphi}^{pq}(t) = \delta I_{km,\varphi}^{p}(t) - \delta I_{km,\varphi}^{q}(t),$$

$$\delta T_{km}^{pq}(t) = \delta T_{km}^{p}(t) - \delta T_{km}^{q}(t),$$

$$\delta \rho_{km,mul,\varphi}^{pq}(t) = \delta \rho_{km,mul,\varphi}^{p}(t) - \delta \rho_{km,mul,\varphi}^{q}(t),$$

$$\varepsilon_{km,err,\varphi}^{pq} = \varepsilon_{km,err,\varphi}^{p} - \varepsilon_{km,err,\varphi}^{q}$$

The triple difference is an ambiguity free observables. This observable is espe-

cially useful for determining an initial position estimate or evaluating the cycle slip. Two DD observables at different time at t_1 and t_2 can be subtracted to obtain TD observables. TD observable looks like:

$$\begin{aligned}
\varphi_{km}^{pq}(t_2,t_1) &= \varphi_{km}^{pq}(t_2) - \varphi_{km}^{pq}(t_1) \\
&= [\varphi_{km}^{p}(t_2) - \varphi_{km}^{q}(t_2)] - [\varphi_{km}^{p}(t_1) - \varphi_{km}^{q}(t_1)] \\
&= [\varphi_{km}^{p}(t_2) - \varphi_{km}^{p}(t_1)] - [\varphi_{km}^{q}(t_2) - \varphi_{km}^{q}(t_1)] \\
&= [\varphi_{k}^{p}(t_2) - \varphi_{m}^{p}(t_2)] - [\varphi_{k}^{p}(t_1) - \varphi_{m}^{p}(t_1)] \\
&- [\varphi_{k}^{q}(t_2) - \varphi_{m}^{q}(t_2)] - [\varphi_{k}^{q}(t_1) - \varphi_{m}^{q}(t_1)]
\end{aligned} \tag{5.8}$$

There are many linear combinations available between the observables. More signals from GNSS modernization means more possibility to make different combinations, but each has their own strength and weakness. As discussed in Chapter 2, the first order ionosphere can usually be eliminated using ionosphere-free linear combination. Assuming the ambiguity for both the L1 and L2 frequency are correctly solved for two corresponding epochs, when subtracted from each other, there is no ambiguity term. This geometry-free combination provides an excellent tool to detect cycle slips, especially if the Melbourne-Wübbena linear combination is used. The dual frequency linear combination, in general, can be written like:

$$\varphi_{\eta,\gamma} \cong \eta\varphi + \gamma\varphi \tag{5.9}$$

Then, Equation (5.1) and Equation (5.5) can be written like:

$$
\begin{aligned}
\varphi^p_{\eta,\gamma}(t) = & \frac{1}{\lambda_{\eta,\gamma}} \left(\rho^p_{k,L1}(t) - \left[1 - \frac{\dot{\rho}^p_{k,L1}(t)}{c} \right] c\delta t_k + c\delta t^p + \delta T^p_k(t) \right) \\
& + \frac{\eta}{\lambda_{L1}} (\delta t_{k,sys,L1}(t) + \delta \rho_{mul,L1} + \delta t^p_{sys,L1}(t) + \varepsilon_{err,L1}) \\
& + \frac{\gamma}{\lambda_{L2}} (\delta t_{k,sys,L2}(t) + \delta \rho_{mul,L2} + \delta t^p_{sys,L2}(t) + \varepsilon_{err,L2}) \\
& + c\frac{\eta}{\lambda^2_{L1}} a^p \rho^p_{p,L1}(t) + c\frac{\gamma}{\lambda^2_{L2}} a^p \rho^p_{p,L2}(t) \\
& - \frac{\delta I}{c} \left(\frac{\eta f_{L2} + \gamma f_{L1}}{f_{L1} f_{L2}} \right) \\
& + \eta N_{L1} + \gamma N_{L2}
\end{aligned}
\tag{5.10}
$$

where,

$$
\varphi^p_{\eta,\gamma}(t) \equiv \left(\frac{\lambda_{L1}\lambda_{L2}}{\eta\lambda_{L2} + \gamma\lambda_{L1}} \right) \tag{5.11}
$$

Table 5.1: Linear combination (LC) of phase measurements

LC	η	γ	Wavelength	Iono. delay	Error Amp. (by L1)	Error (cm)
L1	1	0	$\frac{c}{f_{L1}}$ ~19cm	1.0	1	0.3
L2	0	1	$\frac{c}{f_{L2}}$ ~24.4cm	$\frac{f_{L1}}{f_{L2}}$ ~1.6	1	0.3
WL	1	-1	$\frac{c}{f_{L1} - f_{L2}}$ ~86.2cm	$\frac{f_{L1} - f_{L2}}{f_{L2}}$ ~1.3	$\sqrt{2}$	1.7
NL	1	1	$\frac{c}{f_{L1} + f_{L2}}$ ~10.7cm	$\frac{f_{L1} + f_{L2}}{f_{L2}}$ ~1.3	$\sqrt{2}$	1.7
IF	1	$-\frac{f_{L2}}{f_{L1}}$	10.7cm	0	1.27	0.9

Table 5.1 represents a number of linear combination which are typically used for resolving the carrier phase integer ambiguity (e.g. WL) and for eliminating the first order ionosphere effect (e.g. IF). The ambiguity resolution is described in section 5.4.

5.2 Linear Least-Squares Approach

All the various parameter types contained in the observation equation in Equation (5.10) can be determined from GNSS (code or phase) using the method of least squares. In a least squares adjustment,

$$\begin{aligned} \hat{l} &= \Psi(\hat{x}) \\ &= L + v \\ &= \Psi(x_\circ) + Hx \end{aligned} \tag{5.12}$$

where,

Ψ : Model function (mathematical relationship between observations and parameters; observation equation),

$\hat{l}$: Column matrix of adjusted observations,

L : Column matrix of observations,

$\hat{x}$: Estimated parameters,

$x_\circ$: A priori values of parameters,

x : Improvements to the a priori parameter values,

v : residuals,

H : Jacobi matrix of partial derivatives.

Therefore,

$$\begin{aligned} v &= Hx - (L - \Psi(x_\circ)) \\ &= Hx - l \end{aligned} \tag{5.13}$$

with

$$\begin{aligned} \hat{x} &= x_\circ + x \\ l &= L - \Psi(x_\circ) \end{aligned} \tag{5.14}$$

where,

l : Column matrix of $'$observed-computed$'$ (O-C),

The Jacobian matrix A is defined by

$$H = \left(\frac{\partial \Psi(\hat{x})}{\partial(\hat{x})} \right) \tag{5.15}$$

The stochastic model of the observation is given by the covariance matrix

$$K_l = \sigma_\circ^2 Q_l = \sigma_\circ^2 P^{-1} \tag{5.16}$$

where,

$\sigma_\circ^2$: A priori variance of the observations,

Q_l : cofactor matrix,

P : weight matrix of the observations.

The solution of the linear system of equations in Equation (5.13) follows from the least square condition:

$$v^T P v = min. \tag{5.17}$$

and we obtain the followings,

$$x = \left(H^T P H\right)^{-1} H^T P l = Q_l b \tag{5.18}$$

where,

$$\begin{aligned} Q_x^{-1} &= N = H^T P H \\ b &= H^T P l \end{aligned} \tag{5.19}$$

where,

Q_x : cofactor matrix of the parameters,

N : normal equations matrix.

The a posteriori rms $m_\circ$ is computed by,

$$m_\circ = \sqrt{\frac{(v^T P v)}{n-u}} = \sqrt{\frac{(l^T P l - x^T b)}{n-u}} \tag{5.20}$$

where,

n : number of observations,

u : number of unknown parameters.

The covariance matrix of the parameter will be

$$K_x = m_\circ Q_x \tag{5.21}$$

5.3 Cycle Slips

Cycle slips occur when the receiver experiences a sudden loss-of-lock in the carrier tracking loop. This could be due to a number of reasons; especially due to obstruction from trees, cars, buildings, or because of a low signal-to-noise ratio. This will result in discontinuities and jumps of the integer of the measured cycles. There are many different ways to detect and repair cycle slips. As the cycle slips are integer jumps, the identification and repair can be performed either from only a single receiver′s data only or a pair of receivers (which is typically achieved by checking residuals from a triple differencing (TD) solution). Even though the software designed here is relative positioning software, the methodology to detect and repair cycle slips is primarily based on a single receiver′s data. After successfully fixing the cycle slips, the continuity of the observation data is checked again with the geometry-free observables to confirm whether the software repaired the cycle slips well or not.

The mathematical background behind the cycle slip detection and repair is based on the methodology proposed by Blewitt [1990]. The methodology was tested and discussed in a few papers, e.g. Witchayangkoon [2000]. This method is based on wide-lane combination and the observables can be written as:

$$\varphi^p_{k,WL} = N^p_{k,WL} - \frac{f_{L1}P^p_{k,L1} + f_{L2}P^p_{k,L2}}{(f_{L1} + f_{L2})\lambda_{WL}} \tag{5.22}$$

where,

$\varphi^p_{k,WL}$: wide-lane observables for receiver k and satellite p,

$N^p_{k,WL}$: wide-lane ambiguities,

λ_{WL} : wide-lane wavelength.

The wide-lane ambiguities are evaluated in a sequential recursive algorithm in each epoch with a priori rms of half a cycle of the wide-lane cycle. The mean value of wide-lane ambiguities and the corresponding standard deviation are given as:

$$\begin{aligned} \bar{N}^p_{k,WL}(t_i) &= \bar{N}^p_{k,WL}(t_{i-1}) + \frac{1}{i}\left[N^p_{k,WL}(t_i) - \bar{N}^p_{k,WL}(t_{i-1})\right] \\ \sigma^2(t_i) &= \sigma^2(t_{i-1}) + \frac{1}{i}\left[\left(N^p_{k,WL}(t_i) - \bar{N}^p_{k,WL}(t_{i-1})\right)^2 - \sigma^2(t_{i-1})\right] \end{aligned} \tag{5.23}$$

where,

$\bar{N}^p_{k,WL}$: mean of $N^p_{k,WL}$,

t_i and t_{i-1} : current and previous epoch.

Equation (5.23) is evaluated at t_i and, at the following epoch, $N^p_{k,WL}(t_{i+1})$ must be within $4\sigma(t_i)$ of the mean $\bar{N}^p_{k,WL}(t_i)$. If the condition is not met, then a cycle slip is assumed to have occurred on the epoch.

The ionosphere-free observables have to be evaluated as well in case both L1 and L2 have equal jumps. Equation (2.25) describes the ionosphere-free observables. If Equation (2.25) is rewritten to include the wide-lane observables, then we get:

$$\Phi^p_{k,IF} = \left(\frac{f^2_{L1}}{f^2_{L2}} - 1\right) I^p_{k,CA} + \lambda_{L1} N^p_{k,WL} - \lambda_{IF} N^p_{k,L2} \tag{5.24}$$

where,

$I^p_{k,CA}$: the ionosphere delay on CA code,

λ_{IF} : wavelength of the ionosphere-free combination $(\lambda_{L1} - \lambda_{L2})$.

Assuming that $\Delta N^p_{k,L1}$ and $\Delta N^p_{k,L2}$ are the cycle slips for L1 and L2, then the

wide-lane slips can be written as:

$$\Delta N^p_{k,WL} = \Delta N^p_{k,L1} - \Delta N^p_{k,L2} \tag{5.25}$$

When the cycle slips are detected, a polynomial fit employed ranging from the previous epochs of the slip to the epochs of the slip and extrapolated to the next epoch which is denoted by $\tilde{\Phi}^p_{k,IF}$.

As $\tilde{\Phi}^p_{k,IF}$ and $\Phi^p_{k,IF}$ can be calculated, these two values can be evaluated at the cycle slip epoch as:

$$\begin{aligned} \Delta\Phi^p_{k,IF} &= \Phi^p_{k,IF} - \tilde{\Phi}^p_{k,IF} \\ &= \lambda_{L1}\Delta N^p_{k,WL} - \lambda_{IF}\Delta N^p_{k,L2} \end{aligned} \tag{5.26}$$

$\Delta N^p_{k,WL}$ can be obtained from the wide-lane slip detection and then $\Delta N^p_{k,L2}$ can be determined from Equation (5.26). Consequently, $\Delta N^p_{k,L1}$ can be retrieved from Equation (5.25). The determined values are fixed to all subsequent data points.

5.4 Ambiguity Resolution

Let us assume in Equation (5.7) that we are free for ionosphere, troposphere delay but has marginal errors only. This may be valid for examine the ambiguity resolution for very short baseline. In addition, the following four observables are available as:

$$
\begin{aligned}
P^{pq}_{km,L1}(t) &= \rho^{pq}_{km}(t) + \varepsilon^{pq}_{km,err,L1} \\
P^{pq}_{km,L2}(t) &= \rho^{pq}_{km}(t) + \varepsilon^{pq}_{km,err,L2} \\
\Phi^{pq}_{km,L1}(t) &= \rho^{pq}_{km}(t) + \lambda_{L1} N^{pq}_{km,L1}(t) + \varepsilon^{pq}_{km,err,L1} \\
\Phi^{pq}_{km,L2}(t) &= \rho^{pq}_{km}(t) + \lambda_{L2} N^{pq}_{km,L2}(t) + \varepsilon^{pq}_{km,err,L2}
\end{aligned}
\tag{5.27}
$$

$$
\begin{bmatrix} P^{pq}_{km,L1}(t) \\ P^{pq}_{km,L2}(t) \\ \Phi^{pq}_{km,L1}(t) \\ \Phi^{pq}_{km,L2}(t) \end{bmatrix} = \begin{bmatrix} 1 & 0 & 0 \\ 1 & 0 & 0 \\ 1 & \lambda_{L1} & 0 \\ 1 & 0 & \lambda_{L2} \end{bmatrix} \begin{bmatrix} \rho^{pq}_{km}(t) \\ N^{pq}_{km,L1}(t) \\ N^{pq}_{km,L2}(t) \end{bmatrix} + \begin{bmatrix} \varepsilon^{pq}_{km,err,L1} \\ \varepsilon^{pq}_{km,err,L2} \\ \varepsilon^{pq}_{km,err,L1} \\ \varepsilon^{pq}_{km,err,L2} \end{bmatrix} \tag{5.28}
$$

The typical approach for resolving ambiguities is that at initially, the ambiguities are estimated with real values with other unknown parameters. Once real-valued ambiguities are obtained, they, together with statistical information (which includes variance-covariance matrix for the estimated ambiguities), are fed to a search algorithm, e.g. LAMBDA method [*Teunissen*, 1993] or MLAMBDA [*Chang et al.*, 2005], to determine the integer ambiguities. Once they are estimated, the ambiguities are introduced as known values to obtain final ambiguity fixed solution.

Expanding Equation (5.13) with the ambiguity terms, it can be written like:

$$
H_1 x_1 + H_2 x_2 = \left(L - \Psi(x_1^\circ, x_2^\circ)\right) (= l) + v \qquad v \sim N(0, Q_l) \tag{5.29}
$$

where,

x_1, x_1° : column vector with all non-ambiguity parameters and column vector with

the a priori values of these parameters,

x_2, x_2° : column vector with all ambiguity parameters and column vector with the a priori values of these parameters,

H_1, H_2 : first design matrix of the parameters x_1 and x_2 involving partial derivatives,

$\Psi(x_1^\circ, x_2^\circ)$: computed observables,

$L - \Psi(x_1^\circ, x_2^\circ) \equiv l$: observed minus computed (O-C) double difference observables,

v : residuals,

L : observables.

Once the geometric distances are linearized in Equation (5.28) around a priori information, the linearized system with real-valued ambiguities can be written like:

$$\begin{bmatrix} H_1 & H_2 \end{bmatrix} \begin{bmatrix} x_1 \\ x_2 \end{bmatrix} - (L - \Psi(x_1^\circ, x_2^\circ)) = v \tag{5.30}$$

The estimated parameters, $\hat{x}_1$ and $\hat{x}_2$ can be determined from the following:

$$\begin{bmatrix} H_1 & H_2 \end{bmatrix}^T Q_l^{-1} \begin{bmatrix} H_1 & H_2 \end{bmatrix} \begin{bmatrix} \hat{x}_1 \\ \hat{x}_2 \end{bmatrix} = \begin{bmatrix} H_1 & H_2 \end{bmatrix}^T Q_l^{-1} (L - \Psi(x_1^\circ, x_2^\circ)) \tag{5.31}$$

where Q_l^{-1} is weight matrix. Or, Equation (5.31) can be written like:

$$\begin{bmatrix} H_1^T Q_l^{-1} H_1 & H_1^T Q_l^{-1} H_2 \\ H_2^T Q_l^{-1} H_1 & H_2^T Q_l^{-1} H_2 \end{bmatrix} \begin{bmatrix} \hat{x}_1 \\ \hat{x}_2 \end{bmatrix} = \begin{bmatrix} H_1^T Q_l^{-1} l \\ H_2^T Q_l^{-1} l \end{bmatrix} \tag{5.32}$$

Therefore,

$$\begin{bmatrix} \hat{x}_1 \\ \hat{x}_2 \end{bmatrix} = \begin{bmatrix} H_1^T Q_l^{-1} H_1 & H_1^T Q_l^{-1} H_2 \\ H_2^T Q_l^{-1} H_1 & H_2^T Q_l^{-1} H_2 \end{bmatrix}^{-1} \begin{bmatrix} H_1^T Q_l^{-1} l \\ H_2^T Q_l^{-1} l \end{bmatrix} \tag{5.33}$$

Assuming,

$$\begin{bmatrix} H_1^T Q_l^{-1} H_1 & H_1^T Q_l^{-1} H_2 \\ H_2^T Q_l^{-1} H_1 & H_2^T Q_l^{-1} H_2 \end{bmatrix} \equiv \begin{bmatrix} N_{11} & N_{12} \\ N_{21} & N_{22} \end{bmatrix} \tag{5.34}$$

then,

$$\begin{bmatrix} N_{11} & N_{12} \\ N_{21} & N_{22} \end{bmatrix}^{-1} = \begin{bmatrix} N_{11}^{-1} + N_{11}^{-1} N_{12} \tilde{N}_{22} - 1 N_{21} N_{11}^{-1} & -N_{11}^{-1} N_{12} \tilde{N}_{22}^{-1} \\ -\tilde{N}_{22}^{-1} N_{21} N_{11}^{-1} & \tilde{N}_{22}^{-1} \end{bmatrix} \tag{5.35}$$

where, $\tilde{N}_{22} = (N_{22} - N_{21} N_{11}^{-1} N_{12})^{-1}$.

Therefore, the parameters $\hat{x}_1$ and $\hat{x}_2$ in Equation (5.33) can be solved like:

$$\begin{aligned} \hat{x}_1 &= \left(N_{11}^{-1} + N_{11}^{-1} N_{12} \tilde{N}_{22}^{-1} N_{21} N_{11}^{-1} \right) \left(N_{12} N_{22}^{-1} H_2^T - H_1^T \right) Q_l^{-1} l \\ \hat{x}_2 &= \tilde{N}_{22}^{-1} \left(N_{21} N_{11}^{-1} H_1^T - H_2^T \right) Q_l^{-1} l \end{aligned} \tag{5.36}$$

The variance-covariance matrix for $\hat{x}_1$ and $\hat{x}_2$ can be given as the followings:

$$\begin{bmatrix} Q_{\hat{x}_1} & Q_{\hat{x}_1\hat{x}_2} \\ Q_{\hat{x}_2\hat{x}_1} & Q_{\hat{x}_2} \end{bmatrix} \equiv \begin{bmatrix} H_1^T Q_l^{-1} H_1 & H_1^T Q_l^{-1} H_2 \\ H_2^T Q_l^{-1} H_1 & H_2^T Q_l^{-1} H_2 \end{bmatrix} \tag{5.37}$$

Integer ambiguities can be determined by minimizing the following objective function which is achieved by least squares estimation.

$$\min_{x_2} \|\hat{x}_2 - x_2\|^2_{Q^{-1}_{\hat{x}_2}} \qquad \text{with} \quad x_2 \in Z^n \tag{5.38}$$

The advantage of the LAMBDA method is that it efficiently finds the integer vectors by minimizing the rms in Equation (5.38). At each epoch, integer ambiguities are solved and fixed by searching around float ambiguities for the vector minimizing the rms error in Equation (5.38). Once the functional model is set like Equation (5.31), the float ambiguities have to be determined first from least square estimation. Integer ambiguities are then determined by, e.g. the LAMBDA method. With these fixed ambiguities, all desired unknown parameters can be re-estimated to obtain an improved solution.

5.5 Summary

This chapter has provided by the author, the mathematical details of the relative positioning software which has been developed to test the new methodology to overcome the correlation issue between the height and the troposphere. Chapter 6 will discuss several example baseline data sets which will be processed by the developed software, and then evaluated, to test the developed methodology. The data sets to be

tested include a troposphere anomaly at certain time epochs. There will also be a discussion about the separation of the residual signatures into the frequency-dependent and frequency-independent components.

Chapter 6

Data Description

This chapter describes the criteria used when choosing baseline data to test the proposed methodology; the data are from various places. Detailed descriptions of various baselines are given in Section 6.1; in each of these, a rover is selected. When using a single reference station for GPS RTK, the baseline length is typically limited to less than ten kilometres to reliably determine ambiguities as integers, and to tens of kilometres for ionospheric-free float or fixed processing to eliminate the most prominent error source; the ionosphere. Fixing ambiguities allows one to obtain the most accurate and reliable GPS positioning solutions.

A major objective of this dissertation is to demonstrate how correlated height and tropospheric errors can be effectively reduced when combined with the proposed combined approach for height and troposphere, especially during a tropospheric anomaly or a humid region. Since the ionosphere is one of the most prominent the error sources in GNSS, the data should be carefully selected, as any improvements in accuracy due to the use of the developed combined model (which is described in Chapter 4) would be masked by the much larger effects, especially if there is an ionosphere storm. Since the latter changes substantially from day to day, especially when there are

severe ionospheric storm events, for example, general indicators which reflect ionospheric activity are very helpful in the selection of data sets. Two main indices for the ionosphere, Kp and Dst, are good indicators of the global geomagnetic activity levels.

In a relative positioning, the differential errors increase if the baseline length is getting larger. This is because the spatial errors are typically decorrelated. Once the decorrelated errors are mixed together, the problem to mitigate each error is more complicated. As we try to investigate the troposphere anomaly, the ideal situation is that the reference stations should be located at short enough intervals to resolve the spatial frequency of the errors. Consequently, the proposed approach can perform very efficiently only when the distance to the reference station is short enough to measure the spatial variation of the differential atmospheric errors which is, in this case, the troposphere. Therefore, to meet these constraints, the baseline used in this dissertation is limited to a short range of about 10 km. The following section describes each of the chosen scenarios, with these requirements in mind.

Typically, in longer baseline, it is more difficult to deal with many errors. The data specifically chosen for this research are mainly from wet regions to test the methodology.

6.1 Field Data During the Anomaly

An inhomogeneous atmospheric phenomenon has been frequently observed in many different networks around the world. These include severe sand, dust storms, volcanic eruptions, ionospheric scintillation effects, and localized or regional tropospheric anomaly effects [*Comparetto*, 1993]. Occasionally, these phenomena are observed

when a strong tropospheric anomaly exists within a network. As stated, even for a short baseline, imbalanced atmospheric errors have been shown to have a severe impact on rover positioning solutions, resulting in a worsening of the quality of the positioning solutions [*Ahn et al.*, 2006; *Lawrence et al.*, 2006; *Zhang and Bartone*, 2006; *Huang and Graas*, 2006; *Kim and Langley*, 2007].

Strong localized tropospheric anomalies have been often observed by communities around the world. One such anomaly where they were operating GNSS receivers was in Southern Texas on August 21, 2005. In summary, over a baseline length of around 7.8 km, from the theoretical point of view, the atmospheric effects should be highly correlated and thus most of the errors are known to be easily eliminated in double-differencing (DD) technique. However, the processing result reveals that it is much different from our expectation.

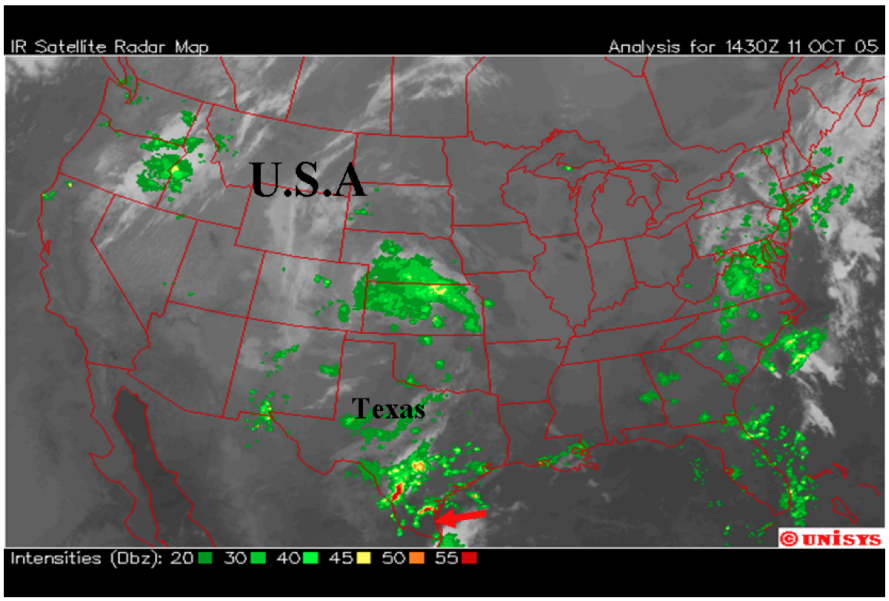

Figure 6.1: Satellite infrared image and radar map (Courtesy: UNISYS)

Figure 6.1 illustrates the infrared image taken by satellite and radar during the

local anomaly in Southern Texas areas (denoted by red arrow). One can clearly see that one could experience a strong atmospheric effect within those regions. The GNSS data sets were recorded and collected by Novariant, Inc., using the NovAtel OEM4 receiver with a data rate of 1 Hz. The observation time was around 7 hours. The observation area is near a desert region in Texas, where there are no buildings or trees that can usually cause multipath, cycle slips, etc. Therefore, we can presume that there are no significant contributions in the data sets from multipath or any other effects rather than the tropospheric effect.

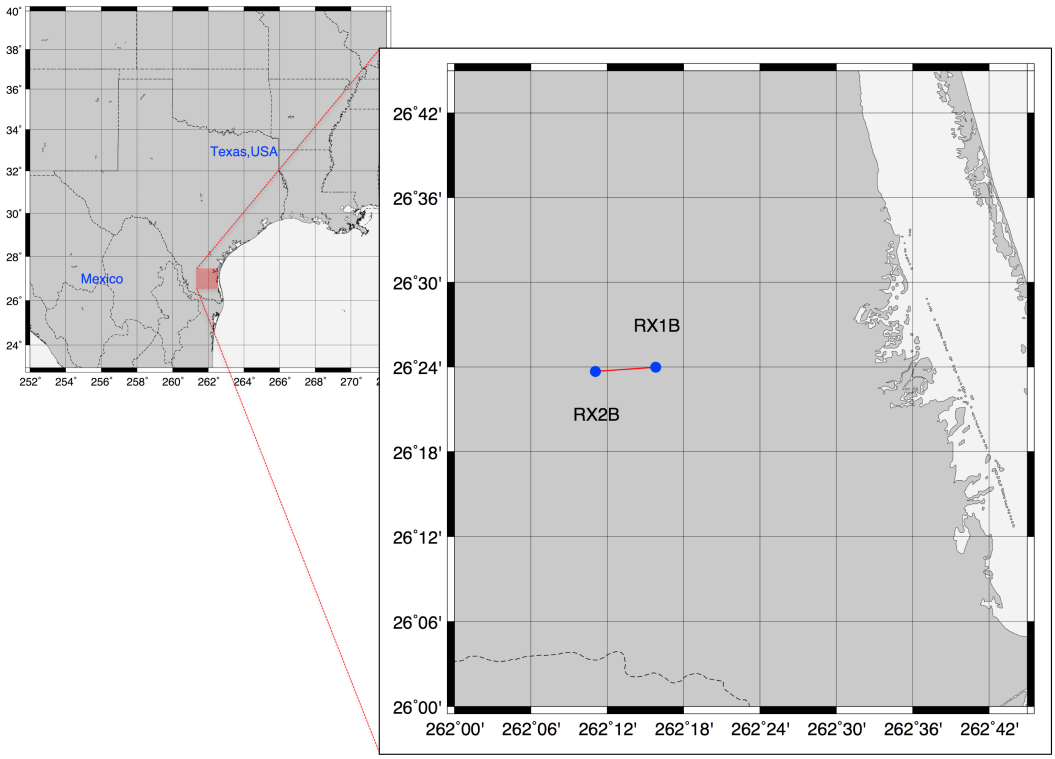

Figure 6.2: Network diagram for RX1B and RX2B [9]

This data has a very strong localized tropospheric anomaly and were tested with UNB-RTK software to see whether this software could obtain a reliable positioning result during the anomaly or not. The software was originally designed for a

[9]The figure is generated with Generic Mapping Tools; see http://gmt.soest.hawaii.edu

real-time gantry crane auto-steering application but had been enhanced for long-baseline applications as well. The software is based on the ambiguity search engine OMEGA (Optimal Method for Estimating GNSS Ambiguities), and quality control algorithms [*Kim and Langley*, 2003; *Kim and Langley*, 2005]. The software uses an optimal inter-frequency carrier-phase linear combination of the L1 and L2 measurements and a receiver system noise estimation routine. The software carries out independent ambiguity resolution for WL, L1 and L2 observations to improve RTK positioning reliability.

The tested baseline with UNB-RTK was RX1B to RX2B and is of around 7.8 km in length and the geographic location is illustrated in Figure 6.2. As the baseline is short, we expected that the atmospheric effects should be highly correlated and thus most of the errors were expected to be eliminated or significantly reduced in the DD process in relative positioning. However, it was found that the DD residuals of the carrier-phase measurements reached around 100 ppm in the slant range in kinematic processing without any pre-processed parameters based on the whole data set. It was found that most of the carrier-phase ambiguity resolutions on those specific periods failed to fix in the UNB-RTK software. As expected, the errors created by mis-modeling the troposphere in the least square adjustment are propagated into the vertical component. Some of the processing results for the Bernese GNSS software can be found in Chapter 7.

Figure 6.3 represents the positioning performance using the UNB-RTK software platform using L1 frequency with fixed ambiguities. As clearly seen from the figure, the anomaly peaked at around 24800 (GPS Time) which is highlighted. Due to the quality control of the software, almost 600 epochs of the data collected during the anomaly were rejected to improve the coordinate estimation.

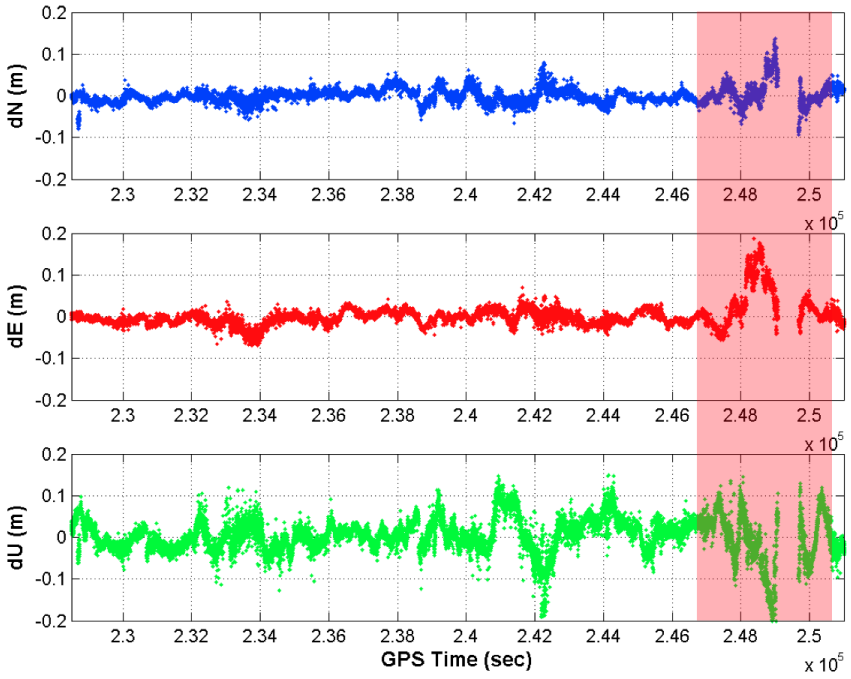

Figure 6.3: Kinematic Positioning Solution by UNB-RTK in a real-time scenario

One of the localized anomalies could also be observed at Stennis Continuously Operating Reference Stations (CORS) in Texas, USA in 2005. The baseline length is about 2.1 km which is short enough to essentially eliminate the correlated errors in the atmosphere. During the time when there was a localized troposphere anomaly, the residuals reached over a half cycle, thus causing a failure to resolve ambiguities successfully. The L1 DD residual result can be seen in Figure 4.1. Similar weather could be observed near San Marcos CORS stations, CSM1 and TXSM in Texas on 11th October 2005 over a 2.7 km baseline length. During the passage of the localized storm, the GNSS RTK performance was much degraded mainly due to wrongly fixed ambiguities, resulting in corrupting the positioning performance as well. The L1, L2 and WL residuals for the processing result can be found in Figure 4.2.

This kind of anomaly phenomenon is not often seen, but can not be ignored due to possible impact on the GNSS community. Due to several reasons mentioned earlier, the data set for baseline RX1B to RX2B is chosen for testing the proposed methodology. This real data set contains not only delays due to the troposphere, but also has errors from many other residual effects. Therefore, if there is any way that the data sets could have only delays from the tropospheric effect, or that the anomaly can be simulated, then it will help in the analysis of the tropospheric effect.

6.2 Field Data in Caribbean

The second data sets tested for this research are from Continuously Operating Caribbean GPS Observational Network (COCONet). The COCONet project is developing large-scale geodetic and atmospheric infrastructure in the Caribbean region that supports the atmospheric research community and geoscience community. It is comprised of a network of over 100 continuous Global Positioning System (cGPS) and meteorology stations in the Caribbean. Figure 6.4 represents the current COCONet stations distributed in Caribbean.

COCONet provides raw GPS data, GPS-PWV, surface meteorology measurements, time series of daily positions, as well as a station velocity field to support a broad range of geoscience investigations. All the new and refurbished stations have sub-daily data latency. Atmospheric data products are distributed to researchers using both the Unidata Local Data Manager (LDM) and other web Internet distribution systems. Geodetic data products are available from the UNAVCO public data archive and potential regional data partners in the Caribbean. All of the participants in the project have committed to a free and open data policy.

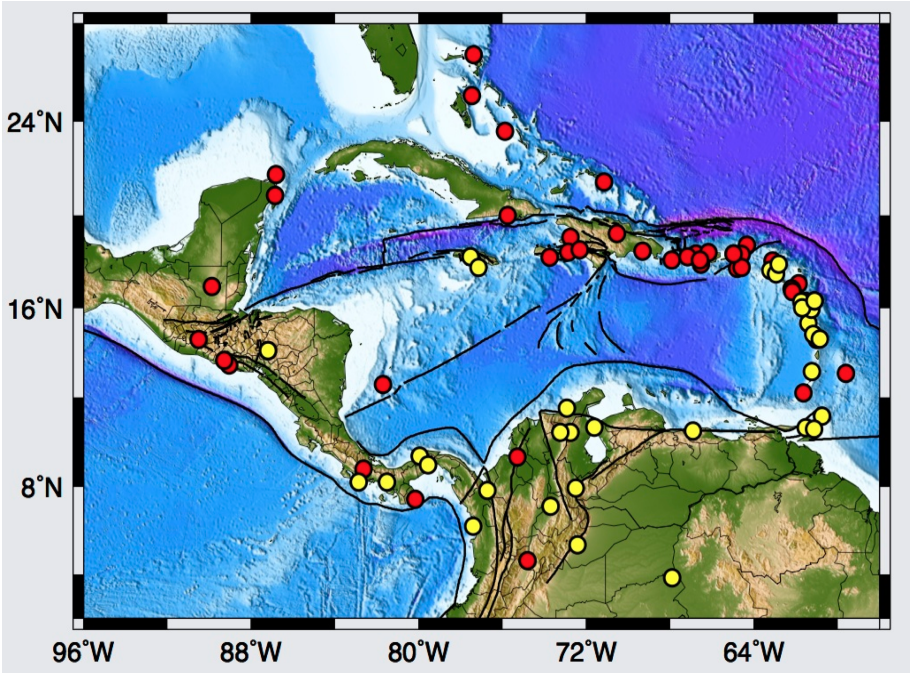

Figure 6.4: COCONet Stations. The 45 red dots represent stations delivering data to COCONet archive. The 32 yellow dots represent stations not yet delivering data to COCONet archive (Courtesy: COCONet)

Some of the reference stations in COCONet distribute high rate 1 Hz data based on UNAVCO′s data archive interface. The stations chosen for this research are Silver Hills (NWBL), Geralds Yard (GERD) and Olveston (OLVN) on the island of Montserrat. Figure 6.5 shows the location of stations. It is expected that the data collected from this network will experience more tropospheric delays than inland data sets such as the ferry data sets described in Section 6.3. There is no online interface to check PW at each station in COCONet, unlike the interactive real-time water vapor data interface of NOAA/FSL. However, one can clearly see, as an example, for the station CRO1, the overall time series of atmospheric moisture and a yearly signature over a few years (see Figure 6.6).

Table 6.1 represents the each station′s coordinate in latitude, longitude and height.

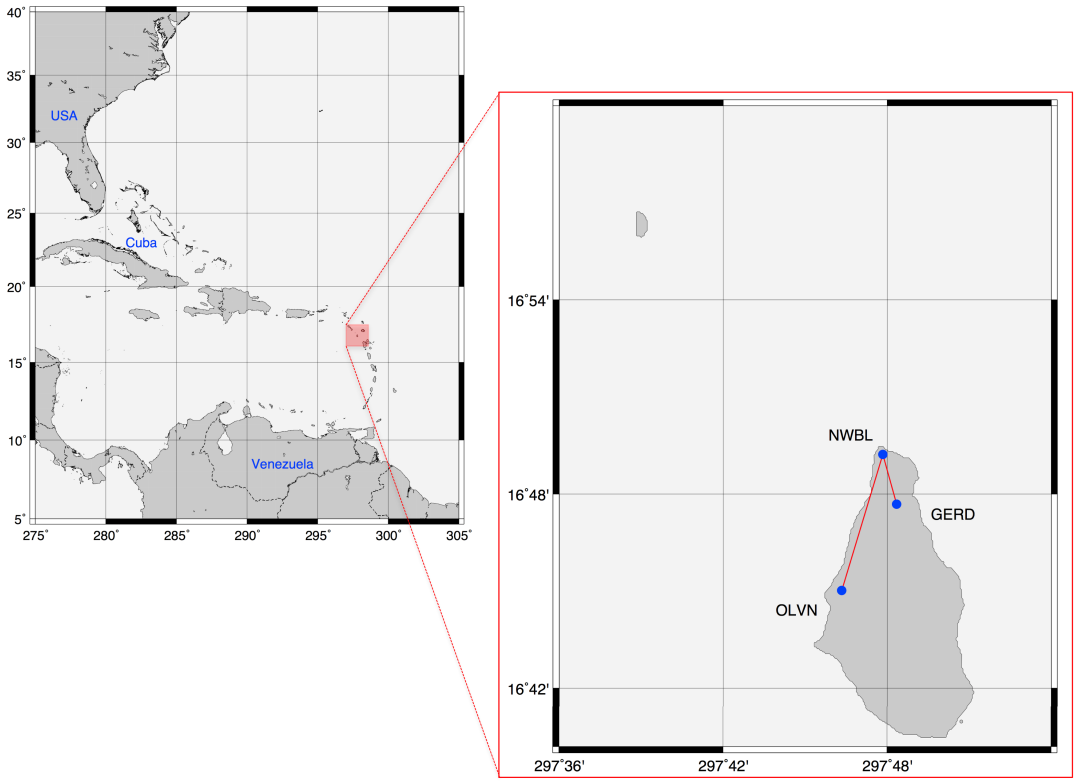

Figure 6.5: Stations location for NWBL, OLVN, and GERD

As is seen, the height difference between stations are over 100 m which is good for investigating the troposphere mitigation.

Table 6.1: Coordinate of NWBL, OLVN, GERD

	Lat.	Long.	height (m)
NWBL	16.82041	-62.20271	147
GERD	16.79482	-62.19430	126
OLVN	16.75040	-62.22773	041

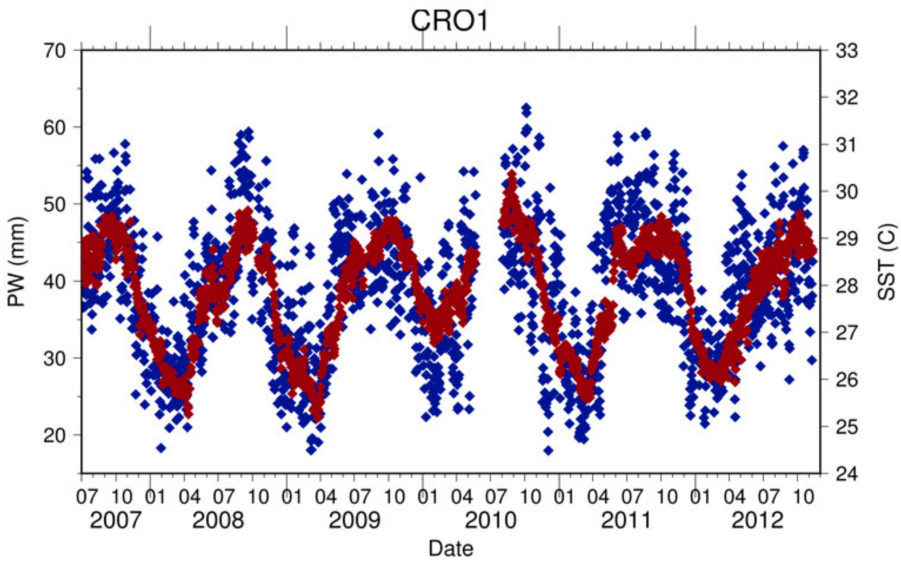

Figure 6.6: Time series of GPS derived amtmospheric moisture (or precipitable water, PW, in blue) and sea surface temperatures (or SST, in red) from St. Croix. The strong coupling of SST and PW is evident (Courtesy: COCONet)

6.3 Field Data with Moving Platform

The University of New Brunswick (UNB) and the University of Southern Mississippi (USM) have collaborated to devise and carry out a long-term experiment in precise GPS positioning over long distances in a marine environment. Pair of GPS reference stations on either side of the Bay of Fundy, Saint John (CGSJ) and Digby (DRHS), and on the ferry, as a part of the Princess of Acadia project, in Eastern Canada, have been deployed with NovAtel′s DL-4 geodetic receivers and GPS-600 antennas (see Figure 6.7). Kinematic GPS data from all three GPS receivers, meteorological stations and tide gauges were collected from November 2003 to December 2004. The ferry travels the same 76 km ferry route two to four times per day, depending upon the season. The Bay of Fundy is located in a temperate climate with significant seasonal tropospheric variations (e.g., temperatures between $-30°$C and $+\ 30°$C).

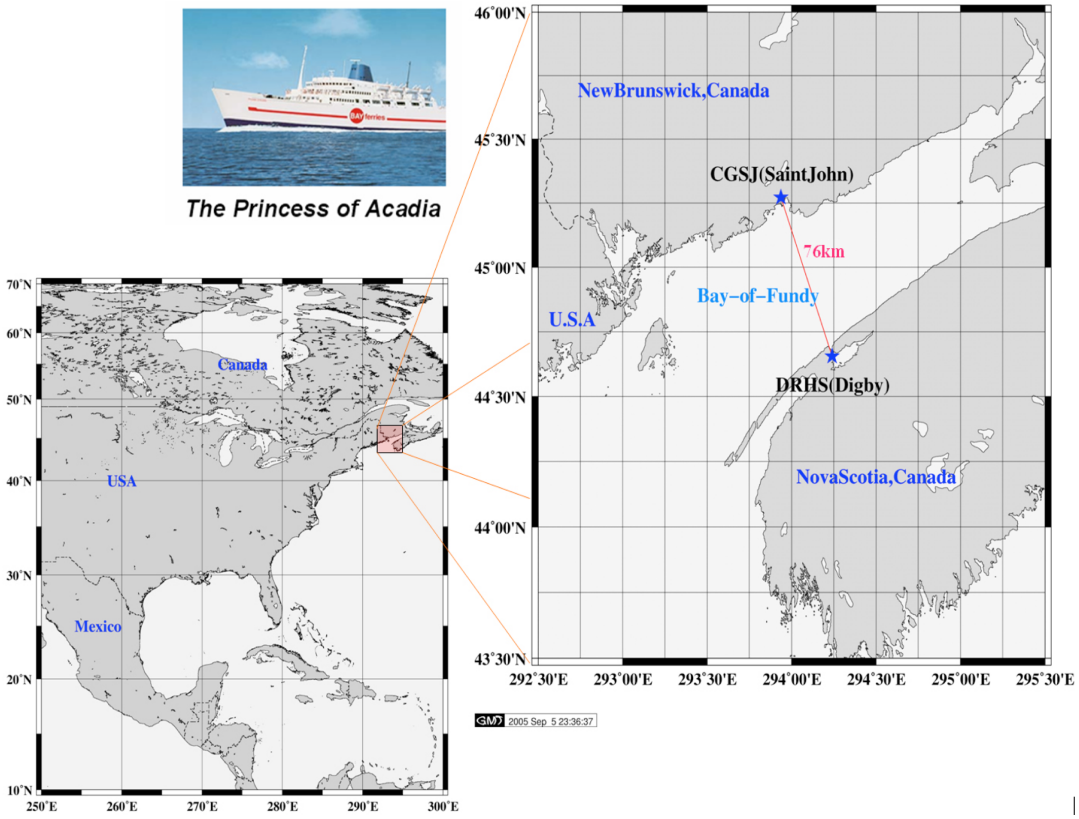

Figure 6.7: Geographic location of the Princess of Acadia project

The primary goal of the study is to advance the science of modeling microwave tropospheric delay over marine areas and to investigate these advances to obtain higher accuracy (centimetre-level) positions [*Santos and Cove*, 2002]. Kim et al. [2004], Santos et al. [2005], Nievinski et al. [2005], Cove et al. [2004] and Cove [2005] demonstrated to advance positioning results with an improved differential tropospheric modeling in this region.

The Bay of Fundy experiences the highest tides in the world, providing additional vertical dynamics to the project. Figure 6.8 represents a typical single baseline GPS trajectory for 24 hours on 13 August 2004 with the ionosphere-free (IF) float solution. Green dots represents the ferry′s trajectory estimated from the IF float where the reference station, CGSJ, was held fixed with ITRF00 coordinates, while red dots

represents the same ferry′s trajectory with DRHS held fixed.

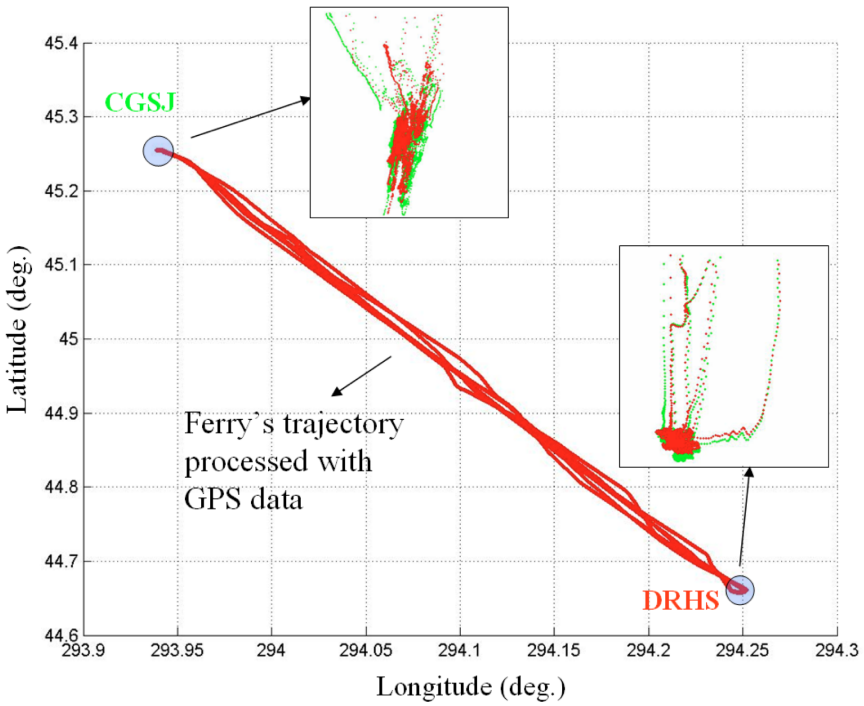

Figure 6.8: An example of the ferry′s trajectory (longitude and latitude component)

As the ferry approaches one of the stations, two solutions from either a long baseline or a short baseline can be estimated. These estimates did not normally agree well mainly due to the increased uncertainties of the long baseline solution as well as mis-modelling of certain parameters in the estimation process. Comparing the two solutions can give an indication of the level of the long baseline unmodelled error as the short baseline solution typically expects better estimates due to correlation of the errors. Figure 6.9 represents the height component during the day which varies about 6∼7 m for the day.

The ferry travels shore to shore so that the collected data of the ferry may experience more tropospheric delays than that of inland. Using the interactive real-time water vapor data interface of NOAA/FSL, it was possible to estimate when the tro-

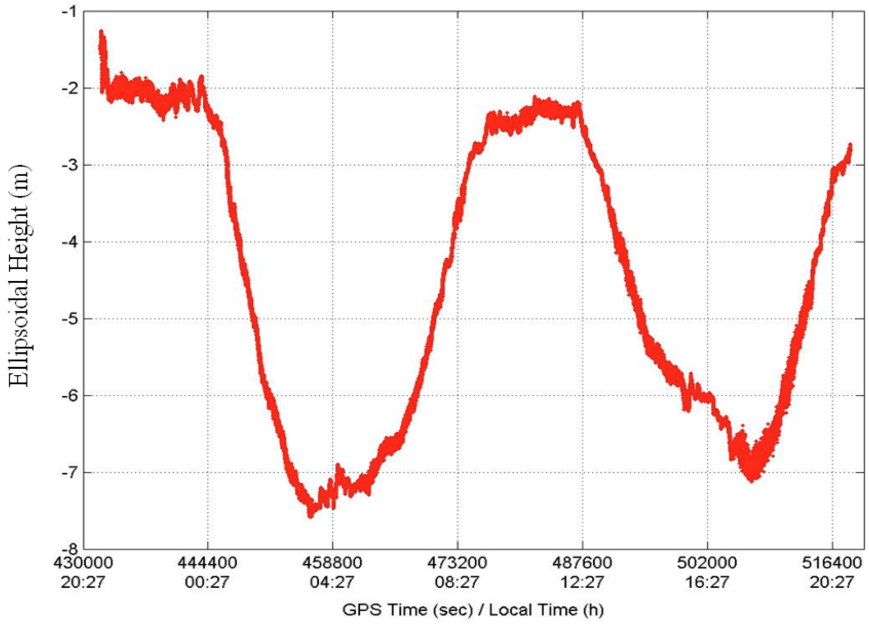

Figure 6.9: An example of the ferry's trajectory (height component)

pospheric effects were relatively prominent. Dates are selected based on weather parameters, such as pressure, temperature, integrated precipitable water vapor (IPW), relative humidity, total delay, and wet delay, to find relatively humid days. Figure 6.10 shows the IPW estimate near the Bay of Fundy, from 3 Aug. to 23 Aug. 2004. IPW reaches about 50 to 60 mm for 13∼14 August, which indicates very humid weather. The blue cross represents EPRT station at Eastport, Maine, USA; the red, Caribou, Maine, USA. Also, hourly data report from local meteorological centre at CGSJ in Canada revealed that it was very humid during the time. As recorded, the time of greatest humidity was from 8:00a.m. to 12:00p.m. on 14 August at CGSJ location. Therefore, this data set can be also an ideal set to test the method for the purpose.

The ionosphere also plays a prominent role in terms of the error sources in GPS. Therefore, the date was carefully selected, as any improvements in accuracy would be masked by the much larger effects of the ionosphere. For the ionosphere, the Kp

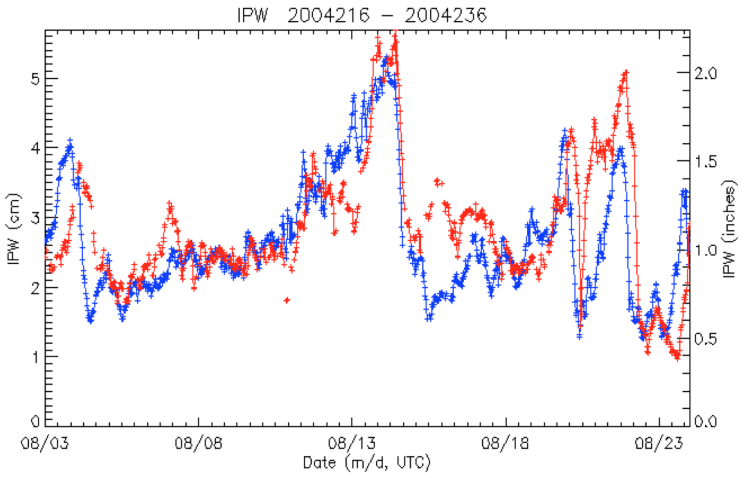

Figure 6.10: IPW values from 3 Aug. 2004 to 23 Aug. 2004 (Courtesy: NOAA)

index is a good indicator of the global geomagnetic activity where the values span an allowed range from 0 to 9. In this research, periods where the Kp index is less than 3 are selected as shown on Figure 6.11, which represents relatively quiet ionospheric activity. Although local values of Kp should be investigated, we can expect non-ionospheric effects for the day.

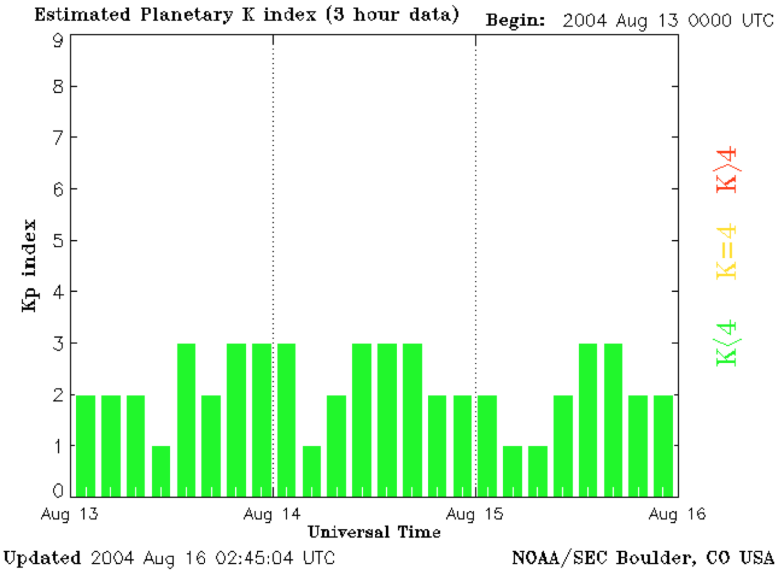

Figure 6.11: Kp index from 13 Aug. 2004 to 16 Aug. 2004 (Courtesy: NOAA)

After carefully analyzing all the parameters mentioned above, data from 8:00a.m. to 09:00a.m. on 14 August 2004 was selected for this research. All of the data were collected by NovAtel DL-4 receiver with GP600 antenna with 1 Hz data rate.

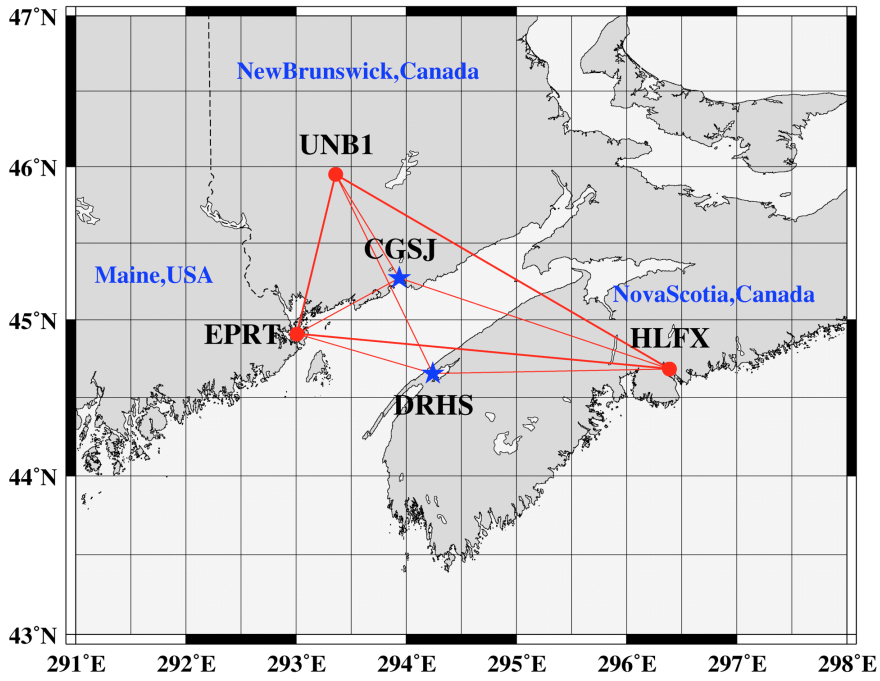

Figure 6.12: Network configuration to estimate the reference coordinates for CGSJ and DRHS

In relative positioning, the fixed coordinates play an important role. If they are wrongly determined then the estimated coordinates may adversely affect other estimated coordinates. Therefore, especially the data from this project were reprocessed to determine the precise reference coordinates. At first, to accurately estimate the coordinates for CGSJ and DRHS, data of 7 days were collected and processed with the Bernese GNSS software. Three permanent IGS stations (UNB1, EPRT, and HLFX) were used for constraining the solution. UNB1 was used until 16 August 2006, and the new site name UNBJ has been used with DOME number 40146M002. UNBJ/UNB1[10] is located in Fredericton, New Brunswick; EPRT in Eastport, Maine,

[10]The details on UNBJ and UNB1 can be found on the following link:

USA, run by NOAA, HLFX in Halifax, is managed by Natural Resources Canada. Figure 6.12 represents the network diagram for the purpose. During the processing with the Bernese software, IGS final SP3 orbit products were used and all three permanent station coordinates were held fixed to their ITRF00 (epoch 97) coordinates to estimate the coordinates of CGSJ and DRHS. The processing sequence of the Bernese software for this purpose included the estimation of receiver clock errors and cycle-slip screening using ionosphere-free linear combination (IF) double-difference phase residuals. After this pre-processing, both the L1 and L2 ambiguities were resolved with stochastic ionospheric modeling. Once resolved the ambiguity these were introduced to create the IF linear combination to fix the ambiguities which gives a more reliable solution than the float solution. Finally, the final coordinates and full covariance matrix are calculated. The Saastamoinen model [*Saastamoinen*, 1972] described in Chapter 3 was used for the tropospheric estimation with elevation-dependent weighting to decorrelate the troposphere on the solution. Antenna phase centre variations were also applied. Final combined estimates of the coordinates for CGSJ and DRHS are summarized in Table 6.2.

Table 6.2: Combined normal equation solutions of the reference coordinates for CGSJ and DRHS for 7 days

		Coordinates determined
CGSJ	X	1824256.0285
	Y	-4109494.8757
	Z	4508639.6075
DRHS	X	1866975.2314
	Y	-4146408.1898
	Z	4457455.0129

http://www2.unb.ca/gge/Resources/UNBJ&UNB1.html

6.4 Summary

This chapter has been provided the details of the data sets to show that why these data sets are especially useful in testing the developed methodology. In Chapter 7, the results of the methodology from the intermediate data sets from Bernese GNSS software and from UNB-RTK software for a 8 km Texas Storm data will be discussed in detail. It will provide the detailed analysis of both static and kinematic scenario case. Further, several other data described in Chapter 6 will be processed with Bernese GNSS software and an open-source RTKLib platform as well as the developed software to see whether the methodology is resistant to the troposphere and therefore it enhances the height solution or not.

Chapter 7

Results

This chapter describes evaluation of the methodology with the data sets described in Chapter 6. Typically, a single reference station GPS relative positioning is limited to less than 10 km for fixing the ambiguities as integers, and to tens of kilometres for ionospheric-free float processing. Since fixing ambiguities allows one to obtain one of the most accurate and reliable GPS positioning solutions, fixing of the ambiguities reduces noticeably the number of unknown parameters and increases the degree of freedom without any other changes; in addition, the a posteriori rms of the observations for the fixed solution is always smaller than that of the float solution. Therefore, the fixed solutions are mainly discussed herein.

7.1 Troposphere Error Mitigation in Kinematic Scenario

Before describing the results, a few different test results are generated. One of them is to evaluate the positioning results with a troposphere estimation in the parameter estimation stage. The other is to evaluate the positioning results based on

the independent result, such as ray-tracing with a NWP model.

7.1.1 Troposphere Delay Estimation during Kinematic Positioning

Even if the tropospheric delay is significant during the day, the DD tropospheric residuals are already at the sub-cm level and the numerical improvement is typically small enough to resolve the ambiguities. As mentioned earlier, however, a kinematic case can be significantly different from a static one. If high dynamics are involved and there are weather fronts, temperature inversions, or other dynamic coastal weather phenomena then the solution may be adversely impacted. As described in Section 4.1, one of the localized anomalies could be observed at Stennis CORS network in Texas, USA. The baseline length is about 2.1 km which is short enough to eliminate the correlated errors in the atmosphere in double difference technique. During the time when there was a localized troposphere anomaly at 20 hours UTC (see Figure 4.1), the residuals reached over a half cycle, thus causing a failure to resolve ambiguities successfully. Using the Bernese GNSS software, the data were reprocessed.

Figure 7.1 shows the epoch-by-epoch kinematic positioning solutions in latitude, longitude and height with 5 min. residual tropospheric delay with non-gradient parameters. The Saastamoinen model with Niell mapping function described in Chapter 3 as an a priori tropospheric delay mitigation was applied. The y-axis in each panel represents the positioning differences. During the tropospheric anomaly around 9:30 (local time), the longitude component deviated by up to 10 cm even for a very short baseline. The height errors varied significantly and were biased by a few cm. Since the geometry of the satellite was not good and number of satellite was

reduced, there was a gap indicating no solution around 10:10 in this plot.

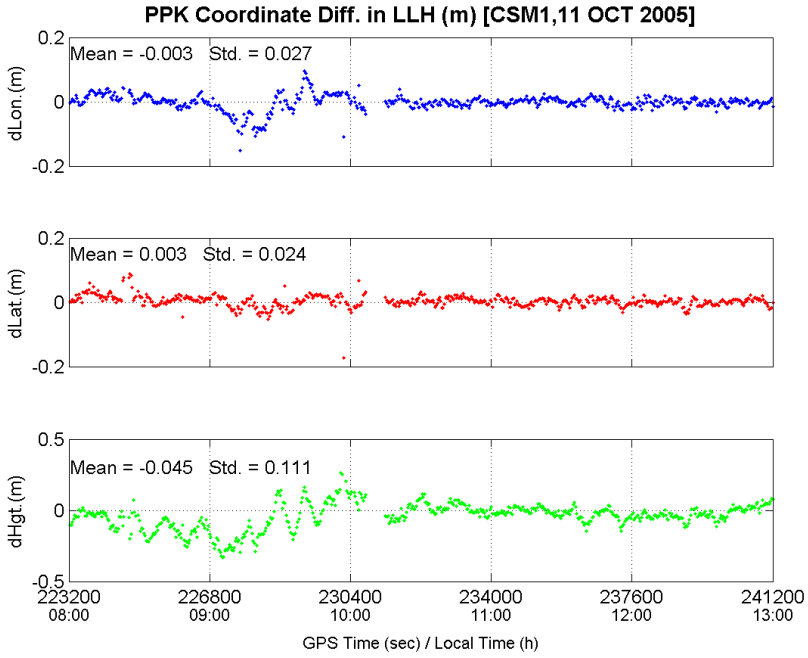

Figure 7.1: Post-processed kinematic (PPK) positioning with every 5 min. tropospheric estimation for rover station CSM1 from the reference station TXSM. Zero ("0") in y-axis represents the differences between the known coordinates of CSM1 and the PPK positioning results.

Figure 7.2 shows the positioning results when the residual tropspheric delay is estimated every 5 minutes, and the gradients are estimated every hour. There is a significant difference when compared with the previous results as shown in Figure 7.1.

Increasing the estimation time for the troposphere delay can dramatically increase the precision of the position solution. Figure 7.3 represents the positioning results with residual tropospheric estimation every 60 min. and it shows better results than the earlier setups shown in Figure 7.1 and Figure 7.2. The best position estimates can be achieved when the residual tropospheric estimation for every 60 min. with 4hr gradient estimation as shown in Figure 7.4.

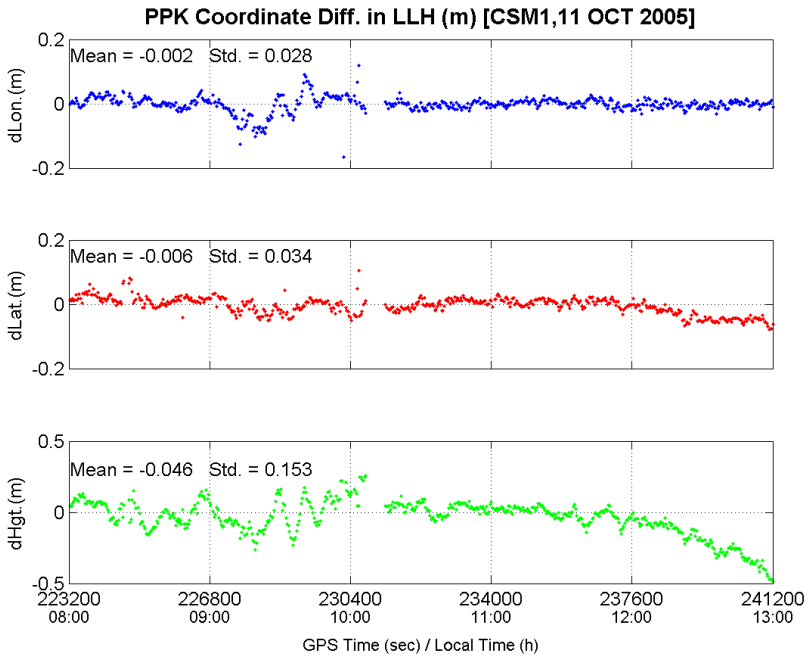

Figure 7.2: Post-processed kinematic positioning with every 5 min. tropospheric estimation with 1hr gradient estimation for the rover station CSM1

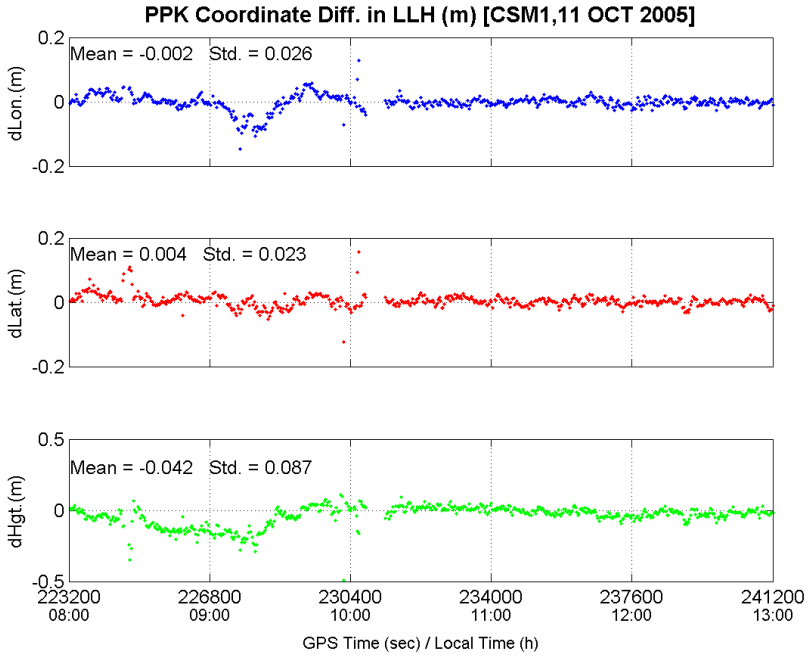

Figure 7.3: Post-processed kinematic positioning with every 60 min. tropospheric estimation for the rover station CSM1

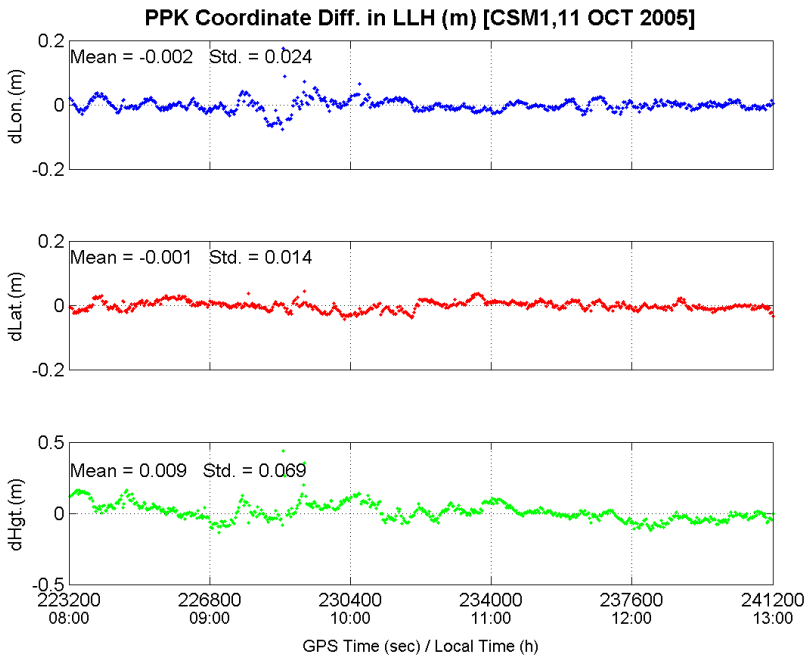

Figure 7.4: Post-processed kinematic positioning with every 60 min. tropospheric estimation with 4hr gradient estimation for CSM1

The static case has enough time to resolve troposphere delay and, in most of the static cases, the dramatic improvement can be seen when including gradient parameters if sufficient time which is typically around 3 hours is given. Table 7.1 represents coordinate results of a few static scenarios from Bernese GNSS software. The baseline is short enough to resolve troposphere parameters, but, due to the uncertainties in the tropospheric model and the difficulty in setting additional parameter estimation in the kinematic scenario, the coordinate estimation result is much worse, especially when compared with the batch estimation.

Another test was performed during the strong typhoon passage as shown in Figure 3.6. Figure 7.5 shows the corresponding epoch wise positioning results when there is no estimation for the residual tropospheric delay. The Sasstamoinen model with the Niell mapping function was used as the a priori mitigation model for the

Table 7.1: Troposphere estimation with Saastamoinen with Niell mapping function

Trop. Est. Interval	Gradient	Lon.(m)	Lat.(m)	Hgt.(m)
5 min.	N/A	0.027	0.024	0.120
5 min.	1 hour	0.028	0.035	0.160
5 min.	4 hour	0.025	0.025	0.106
30 min.	N/A	0.026	0.023	0.106
30 min.	1 hour	0.025	0.031	0.124
30 min.	4 hour	0.024	0.026	0.087
60 min.	N/A	0.026	0.023	0.097
60 min.	1 hour	0.024	0.025	0.077
60 min.	4 hour	0.024	0.014	0.070

troposphere. Figure 7.6 shows the results from the same data when estimating residual troposphere delay every 5 min.. As is shown in a few figures, in the kinematic situation, the estimation of the newer parameters may worsen the entire positioning estimates.

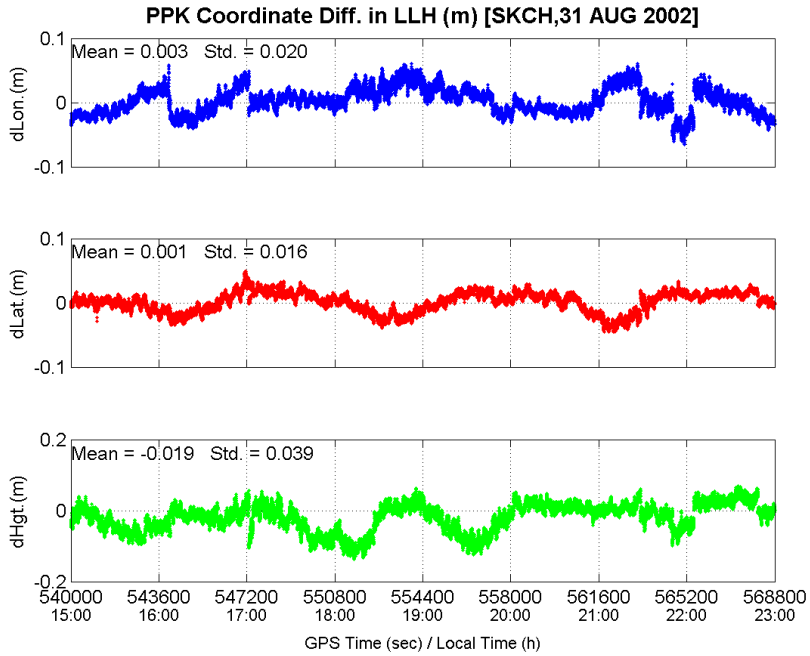

Figure 7.5: Post-processed kinematic positioning with tropospheric mitigation for DAEJ-SKCH-during a passage of typhoon

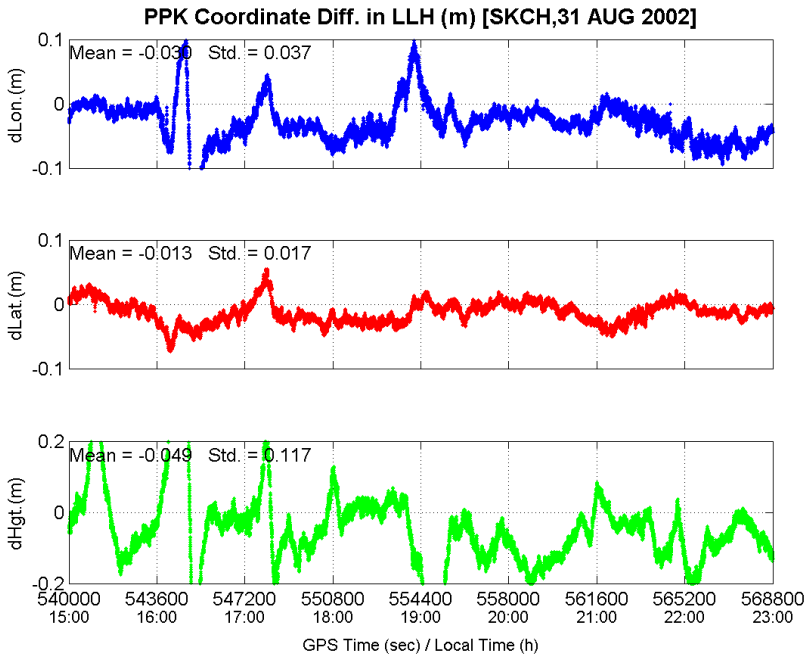

Figure 7.6: Post-processed kinematic positioning with every 5 min. tropospheric estimation for DAEJ-SKCH-during a passage of typhoon

7.2 Results from the Combined Approach

7.2.1 Texas Data

To evaluate the potential improvement of positioning performance by combining the common zenith dependent parameter of the vertical component and the residual tropospheric delay parameter, we analyzed data sets from a severe weather event which is RX1B and RX2B baseline as depicted in Figure 6.2. These data were recorded in Southern Texas on August 21, 2005 by Novariant Inc.. The baseline length was of around 7.8 km. All of the data sets were recorded using the NovAtel OEM4 receiver with a data rate of 1 Hz. The observation time is almost 8 hours and the processing is based on double differences.

Figure 7.7 represents the corresponding kinematic positioning solutions by Bernese

GNSS software version 5.0 in the post processed kinematic (PPK) mode. Again, the zero ("0") in y-axis represents the differences between the known rover coordinates of RX2B and the corresponding PPK positioning results. The Bernese software pre-examines the whole epochs to determine the cycle slips and ambiguities, and also pre-determine stochastic parameters, such as ionosphere. These pre-detemined stochastic parameters and ambiguities can be further used to determine the cleaned results. Even if the whole data span was used in Bernese software, we can still see that the solution is getting worse after 13:00 (local time), especially in the vertical component and reached the worst around 15:00 local time.

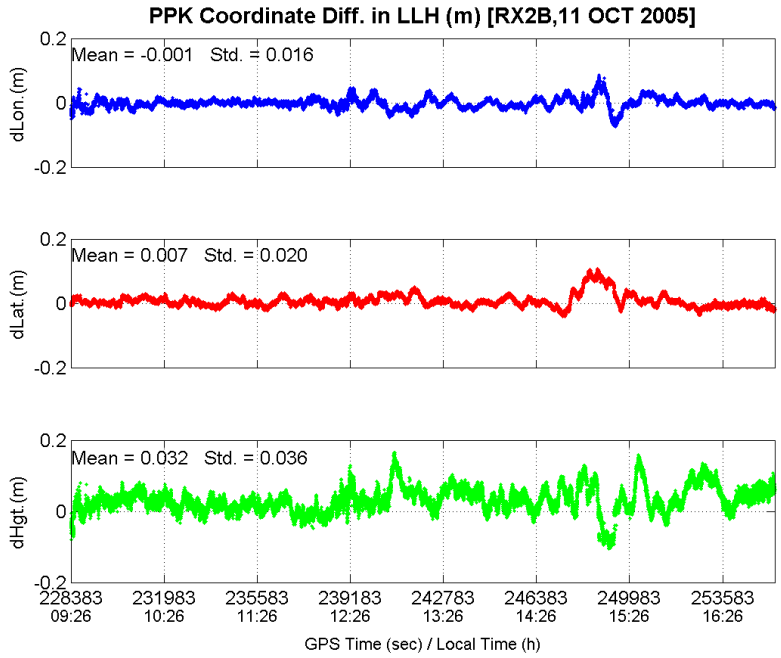

Figure 7.7: Kinematic positioning solutions by Bernese software v5.0 using pre-processed screened results. Zero ("0") in y-axis represents the difference between the known rover position and the corresponding PPK solutions.

During the processing RX1B is used as a reference, and RX2B is selected as a rover. In this case in Bernese software, we introduced the dry Niell mapping function with the Saastamoinen model and estimated 15 minute residual tropospheric delay pa-

rameters. In order to try to obtain a better solution, we tested a few other processing strategies in Bernese software. These strategies included the ionosphere-free linear combination to eliminate the first order ionosphere effect even if the noise level is almost three times higher than that of L1 frequency. Because of this, this processing strategy is not usually favourable on a short baseline processing. We also processed the data using L1 frequency without residual tropospheric estimation, longer estimation periods in CPLF and L2 or wide-lane combination etc. However, the best stable positioning solution which can be achieved is based on the L1 with 15 minutes troposphere estimation in this case.

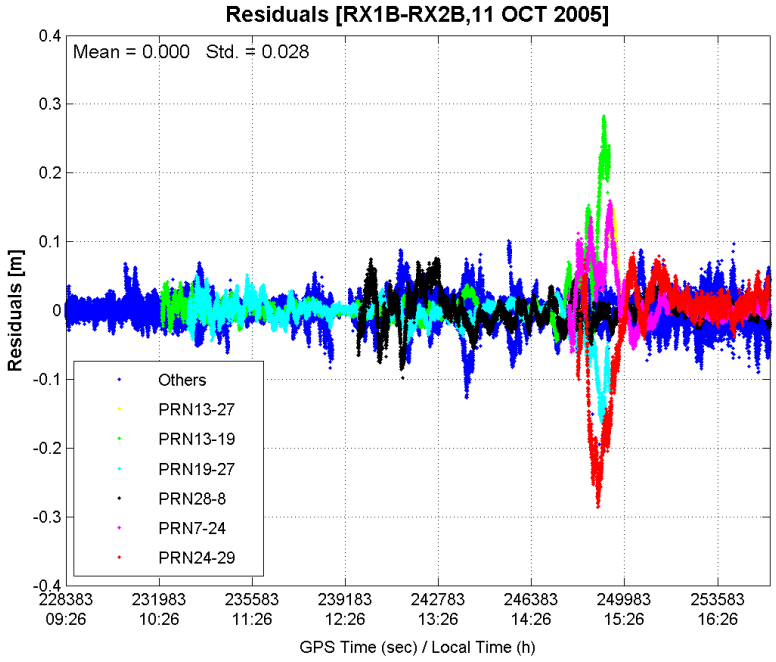

Figure 7.8: Residuals by Bernese GNSS software using pre-processed screened results. Only interested satellite pairs are coloured

As is shown in Figure 7.8, the residuals are still reached up to 100 ppm in a slant direction (or line of sight) during the anomaly period. As is illustrated, the problematic satellites are PRN 24 and PRN 19 which are lower elevation angles, and we found that the corresponding elevation angles are between 15 and 30 degrees.

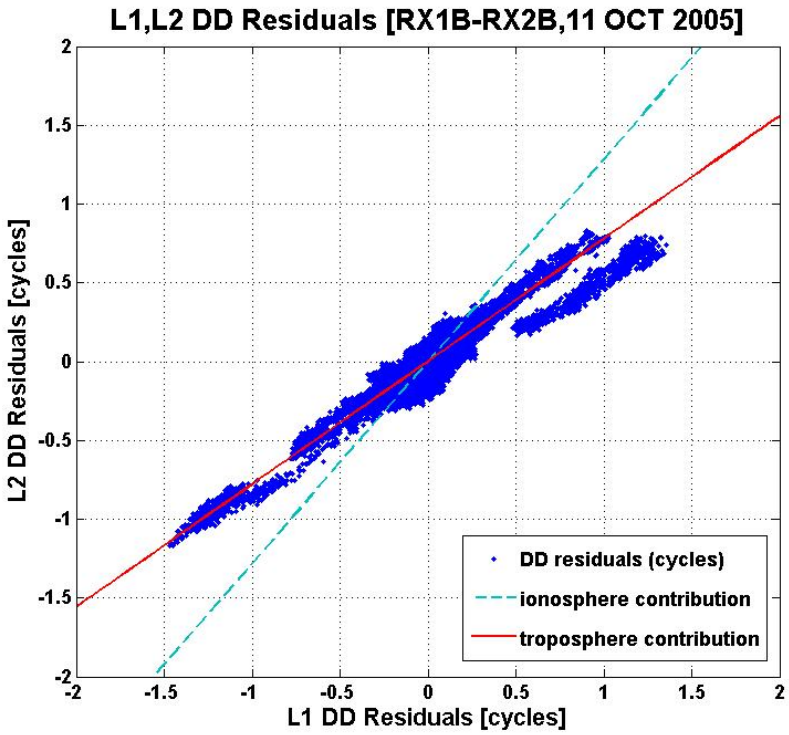

Figure 7.9: L1 and L2 double difference residual comparison by Bernese PPK scenario

Figure 7.9 represents the L1 and L2 double differenced residuals processed by Bernese software as an example. Based on the residual analysis, we can identify whether the residual of the satellite pair is from the ionosphere or from the troposphere. This residual identification can be further used for the weighting scheme. As is shown in Figure 7.9, some of the residuals do not strictly follow the frequency-dependent and non frequency-dependent components, making them somewhat balanced although the reasons are not fully known.

The residual zenith delay of the troposphere and the height component of the positioning solutions are highly dependent on the zenith angle. Due to their correlation, most of the position estimation errors induced by the troposphere are amplified mainly in the vertical component. Depending on weather conditions, a stochastic

modelling approach or parametric estimation has been implemented to mitigate the tropospheric error. In order to solve the issue stated above, we investigate the combined approach which can eliminate inter-correlation among zenith angle-dependent parameters and thus, improve horizontal positioning solutions.

7.2.1.1 Evaluation of the Combined Approach from Bernese Data

To test and evaluate the main methodology, the desired parameters for further analysis were extracted from Bernese GNSS software. Figure 7.10 represents the overall processing scheme for the purpose. Once the baseline was formed, cycle slips were correctly detected and repaired. Then, L1 (and L2) ambiguities were resolved using an ambiguity search process. After all possible ambiguities were resolved, these ambiguities were introduced to obtain the final positioning solutions. At the same time, the residual troposphere parameters at 15 minutes intervals with CPLF were estimated in this case. In order to analyze our methodology, several parameters at single difference level were extracted; Jacobians, reduced observables, ambiguities, satellite positions, elevation and azimuth of the satellites, tropospheric parameters, normal matrices, geometric ranges, receiver clock, etc. Selected parameters are used as input parameters for the algorithm test. The primary reason for choosing this methodology is to minimize uncertainties in the data analysis and maximize the performance analysis in using geodetic software. After reforming the double differences, 100 different values of the parameter α were tested for every epoch. Once the value of the parameter α is selected using a selection criteria, the determined α is used again to obtain the final positioning solution and the residual troposphere delay parameter.

As is in Equation (4.22), if α and ζ are determined, new tropospheric estimates can be retrieved based on the relation: $\zeta = (\Delta u + \alpha)$. During data processing with

Bernese GNSS software, IGS final SP3 orbit products were used to mitigate possible residual orbit errors in order to achieve the highest possible precision in the solution.

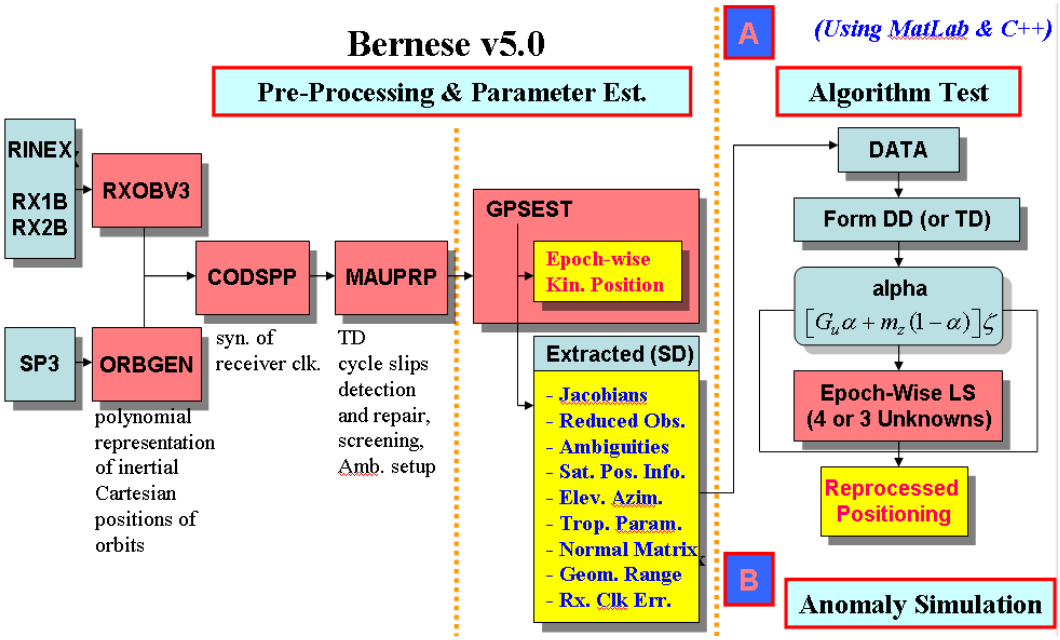

Figure 7.10: Overall processing strategy of the developed methodology using intermediate data from Bernese output

To evaluate the correlation effect between the unknown parameters, the condition number is also examined as is seen from Figure 7.11. The condition number is the ratio of maximal and minimal eigenvalue of a normal matrix. This also represents the degree of the correlation between the parameters. The condition number also increases from 13:00 (local time) which means that the correlation between the unknown parameters is getting higher, resulting in a degraded solution. Typically, introducing a lower satellite can assist in decorrelating the parameters. We can see the solution getting worse after about 13:00 (local time), especially in the vertical component.

Figure 7.12 is a test result of a kinematic positioning solution for a typical esti-

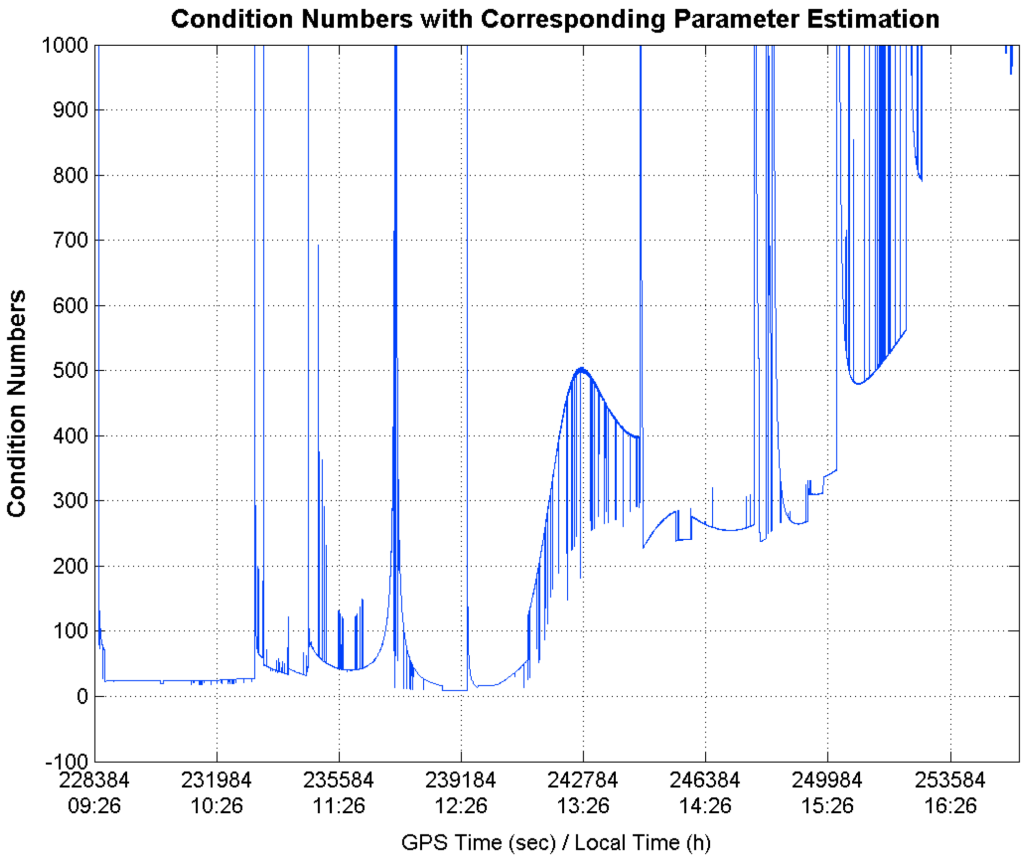

Figure 7.11: Condition numbers from the anomaly troposphere data from Bernese software

mation process where there are four unknown parameters; northing, easting, up as well as residual tropospheric delay. Although CPLF was not used for estimating the troposphere delay in this case, similar positioning result as that from Bernese software in Figure 7.7 can be achieved. However, the reprocessed result shows the high fluctuation of the solution when there is the troposphere anomaly.

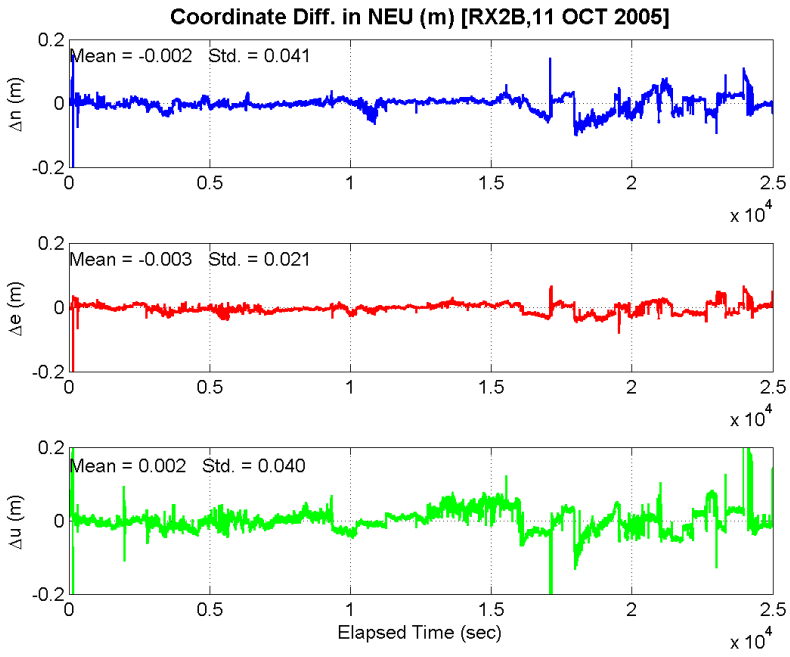

Figure 7.12: The coordinate differences of northing, easting, and up component. This result is from the conventional way for estimating the unknown parameters, without any combination between the parameters

7.2.1.2 Positioning Improvement from the Combined Approach using Optimal Weighting Parameters

Figure 7.14 is a test result from our combined methodology when all of the necessary parameters used are reprocessed. The three parameters that were estimated are northing, easting, and ζ. Once ζ was determined based on the selected α, the vertical component was retrieved. The choice of α coefficient is somewhat arbitrary, and there is no strict numerical way to determine the α coefficient. For a test, we chose α when the norm of the coordinate solutions is at minimum value. For a static scenario where the reference coordinates are precisely known, it is relatively easy to achieve the optimal α compared to that in the kinematic scenario. To make it clear, this static test setup may not be suitable for a direct application for GNSS positioning, but is mainly trying to represent that there must be a certain value which can efficiently decorrelate those two common zenith-dependent parameters. As is

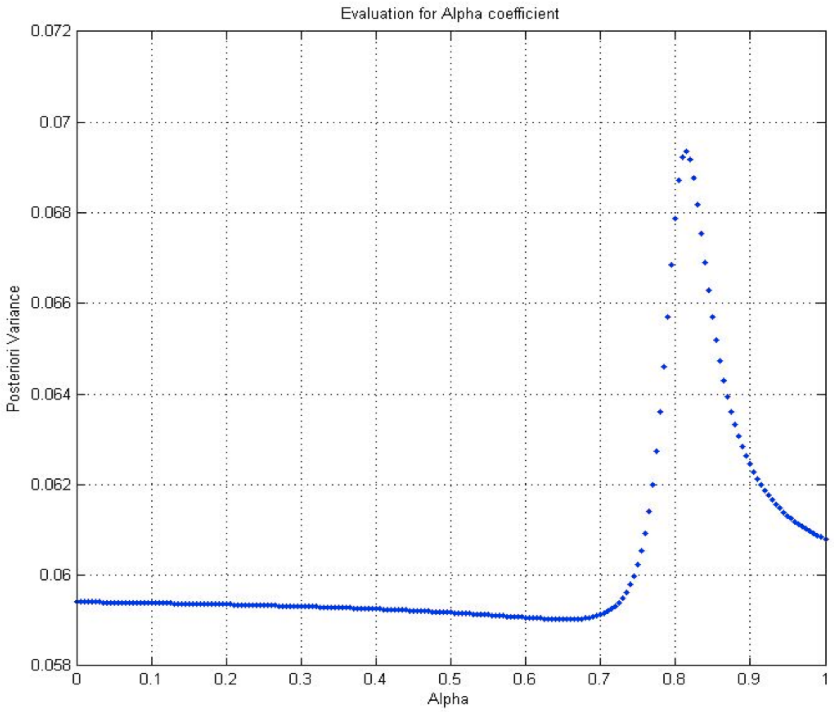

Figure 7.13: An example of the evaluation of the weighting parameter α

shown in Figure 7.14, when α is properly chosen, we can see that the corresponding coordinate solution can dramatically change and converge to the known positioning solution. The rms in the height solution is 0.8 cm in this case. Compared to the earlier plot in Figure 7.12, this shows the reduction of rms in the height component from 4.5 cm to 0.8 cm, over 80% improvement. Kim and Langley [2008] also showed that the height component is significantly improved when the weighting parameter is chosen well, resulting an unbiased solution. In addition, they found that no significant change could be found on the horizontal solution, similar to here. Li et al. [2010] uses a geometry-specified troposphere decorrelation strategy based on a similar idea in order to solve these ill-posed conditions. Using his regularization methodology, he also found that the coordinate solution improves from centimetres to sub-centimetres level for long baseline, especially for the height component.

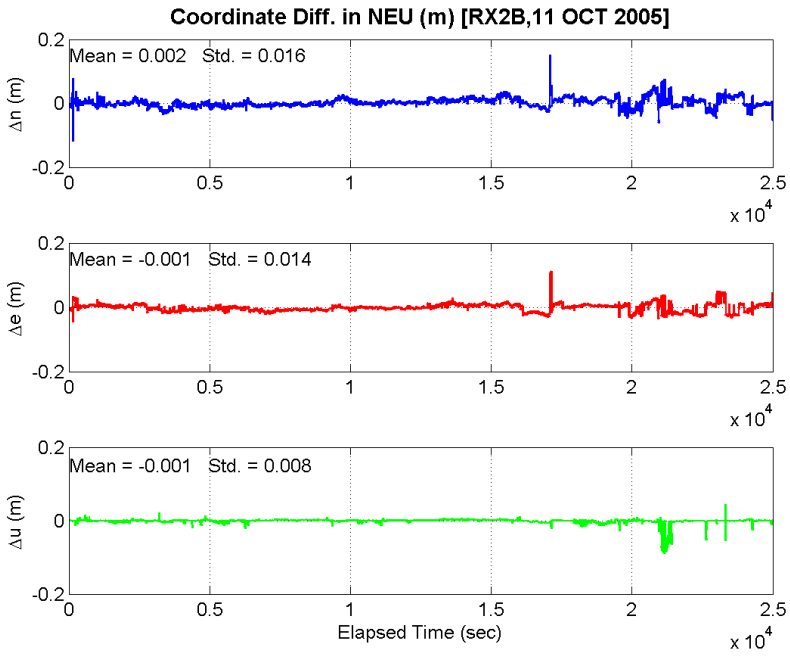

Figure 7.14: The coordinate differences of northing, easting, and up component from the combined case

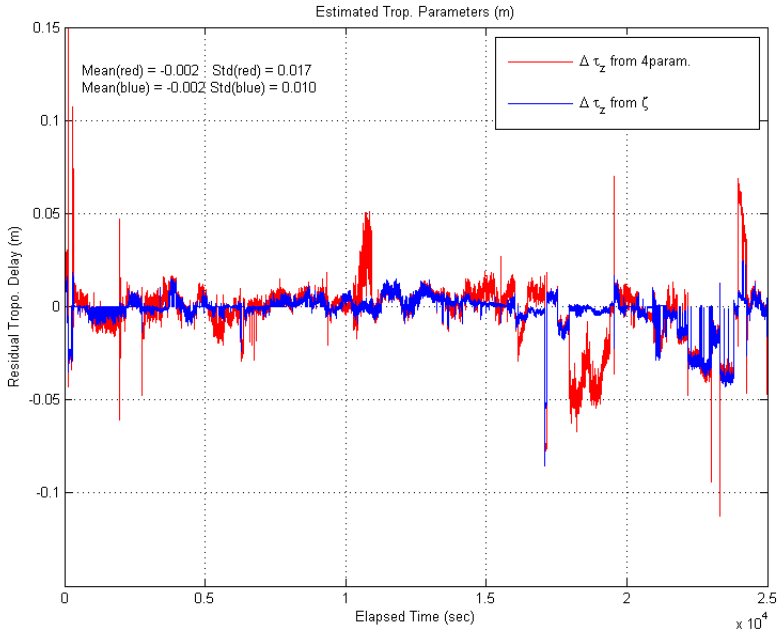

Figure 7.15: Estimated tropospheric parameters from the combined case

Figure 7.15 represents the two estimated tropospheric parameters both from the typical estimation process (red line) and from the combined methodology (blue line). Once ζ was determined based on the selected α, the tropospheric delay parameters can be also retrieved. These values are coloured blue in the figure. As a comparison, the tropospheric delay parameters are also estimated. As is shown in Figure 7.15, there are big differences between the estimated tropospheric delay parameters. By using a different tropospheric weighting scheme based upon α, the estimator seems to enable us to efficiently distinguish the tropospheric delay parameters from the height component if the weighting parameters are chosen well.

From the feasibility test, the developed combined approach could result in the successful de-correlation of both the vertical component and the troposphere delay parameter. Many different coefficients are evaluated and chosen when the norm of the coordinate solutions is at minimum value as there is no strict numerical way to determine the weighting coefficient. While the arbitrary choice of weighting coefficient is somewhat unrealistic, the approach was successful in evaluating our methodology. This could reduce the tropospheric residuals and thus resulted in a dramatic improvement in the solution domain. In post-processed batch solution, this new methodology can thus provide a new analysis method of the data. As this new methodology confirms that it works well under the optimal choice of weighting parameters, the method is further tested in a kinematic scenario when the coordinates of a rover must be estimated at every epoch.

7.2.1.3 Height Comparison from the Combined Approach in a Kinematic Scenario

The second goal of the dissertation has been towards the improvement of kinematic solution during the anomaly period. Although the positioning result could be greatly improved as shown in Figure 7.14, in a practical point of view, the above mentioned way has a limitation to use in a kinematic situation. Instead of using arbitrary choice of the coefficient, the method described in Equation (4.24) is used for the following test herein. Once the double differences were reformulated, different α values for each satellite pairs were applied for every epoch on the weighting scheme. Once the value of α is selected using the selection criteria described in Chapter 4, the determined α is used again to get the final positioning solution. The solution for the vertical component is discussed here.

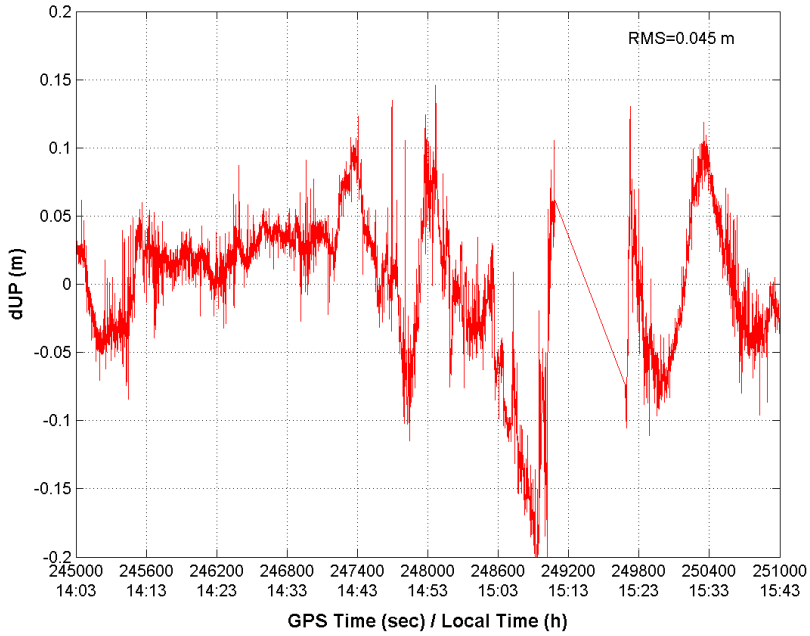

Figure 7.16: Original vertical component determined by UNB-RTK software during the anomaly period

As described in Equation (4.24), if α is determined based on the selection criteria and the actual magnitude of the wet delay to the zenith direction for each satellite pair, new combined parameter, ζ are estimated. Again, the determined weighting can be multiplied to ζ in order to get the final vertical component of the baseline.

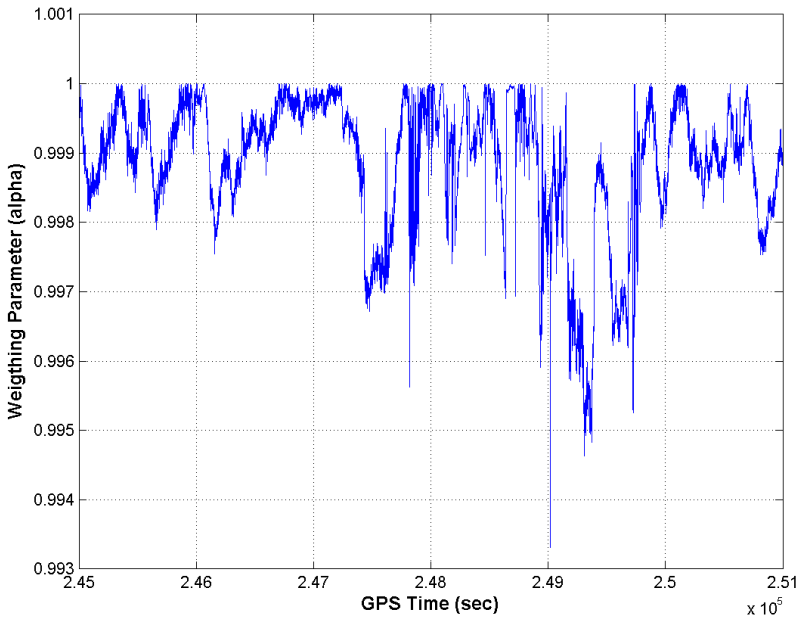

Figure 7.17: Weighting parameters, lower values represent the higher tropospheric contribution

Figure 7.16 represents a test result of a kinematic positioning solution for a typical estimation process for vertical component. Due to the quality control criteria, positioning solution over 600 epochs during the anomaly can not be determined. The vertical component in differences between the known and estimated coordinates is getting worse than -20 cm (but is up to -28 cm) at local time around 15:10 in Figure 7.16. They are probably due to the wrongly fixed cycle slips or wrongly fixed ambiguities due to the anomaly.

Figure 7.18 illustrates the result of the vertical component when the new weighting

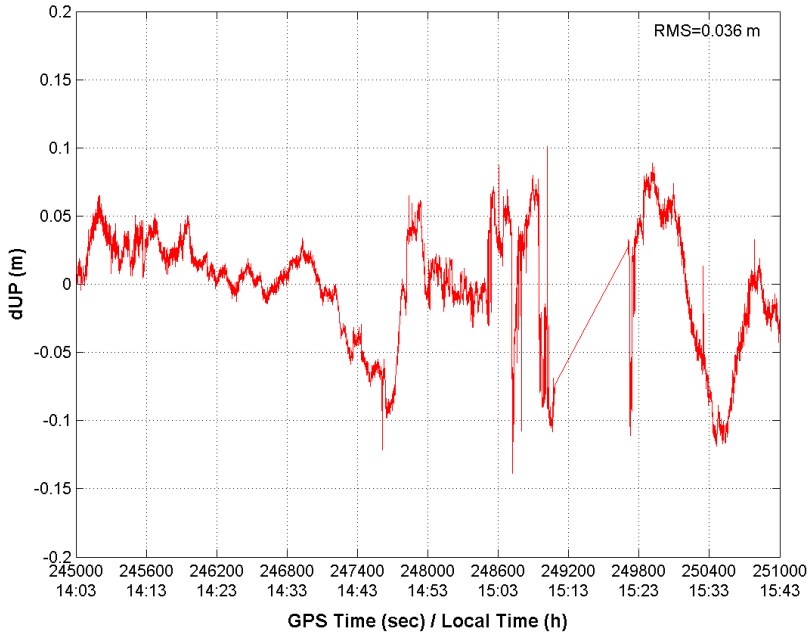

Figure 7.18: Vertical component determined by the proposed weighting scheme during the anomaly period

scheme is applied. Although we could not get a dramatic vertical enhancement in the scenario, some improvement of around 20% in the vertical component can be achieved in our test scenario. More interesting thing is that the anomaly which can reach up to over -20 cm in Figure 7.16 does not exist in our processing result any more. Compared the anomaly area around 15:10 local time between Figure 7.16 and Figure 7.18, we can clearly see some improvement. Our results imply that our weighting scheme based on the residual analysis can be a good alternative for mitigating the unmodeled tropospheric delay. Even if most of the unmodeled tropospheric delay can be eliminated by combined approach with proper weighting, some epochs does not show any improvement. One of the ways of having the best weighting parameter may be from the criteria when the coordinate norm is minimal again. Reversely, we can further compare the best set of weighting parameter from the criteria to the one applied herein to determine the optimal way of determining parameter weighting in different scenarios. Figure 7.17 presents the determined weighting parameter for

this case. Lower values means that the degree of the contribution of the troposphere.

7.2.2 Designed Post-Processed Kinematic Platform

The post-processed kinematic platform has been developed for further tests. Figure 7.19 shows a overall block diagram for the overall software package. The quality control routine is employed to detect cycle slips and to repair them. It also calculates the approximate station′s coordinate from code observables. Then, it forms double differences, and corresponding design matrix with elevation dependent weighting. Double differenced troposphere mapping coefficients are formed. The ambiguity is solved with LAMBDA method. For the test purposes, ambiguity resolution of rounding method is introduced to assist with the software development. After successfully resolving the ambiguities, the positions are calculated at every epoch.

The estimated position from the developed platform is validated with a few software platforms. This includes RTKLib software which is an open source program package for GNSS positioning (see *http://www.rtklib.com*) and Bernese GNSS software. Results confirm that the developed software shows very similar performance to that of RTKLib and Bernese. The Bernese GNSS software is written in Fortran and and most of the software parts are highly sophisticated and somewhat encrypted so that the user can not easily extract any value. Typically, one can achieve the best solution based on batch processing using the Bernese GNSS software. However, the kinematic positioning solution in Bernese software is quite challenging. Meanwhile, the RTKLib software is open-source, written in the C language, and it processes GNSS data with Kalman filtering. Here, the designed software platform is based on both Matlab and C and is designed towards epoch-wise kinematic processing with a least square adjustment. The detailed mathematical formulation for the software

design is described in Chapter 5.

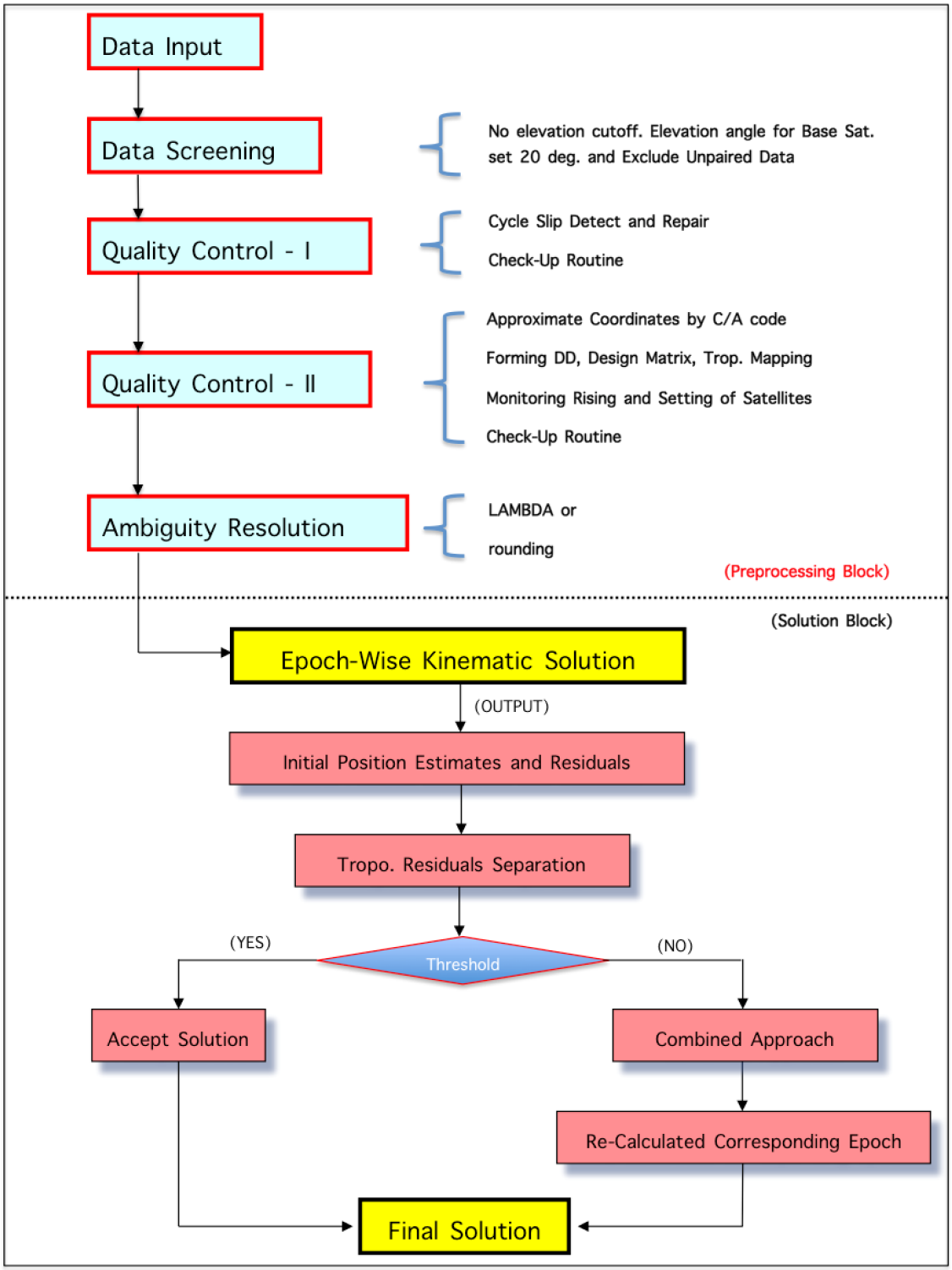

Figure 7.19: Overall processing scheme for the developed software

7.2.3 COCONet Data Result using the Developed Platform

Selected baseline data in the COCONet network in the Caribbean has been processed. Figure 7.20 is the northing, easting and up position result from the developed test-bed software for NWBL-OLVN (around 8 km in length) which is nearly the same distance between RX1B and RX2B in the Texas data. In the software, NWBL is treated as the reference station and OLVN is the rover station. The zero on each panel in Figure 7.20 is the published coordinates from the COCONet. The location of stations, NWBL and OLVN, can be found in Figure 6.5. The data rate is 1 Hz from the Trimble R9 receiver. Figure 7.21 shows GDOP values and the number of satellites. In the developed test-bed software, there are some gaps around 13:42 in the coordinate solutions. This is mainly due to the failure of a statistical test to resolve ambiguities.

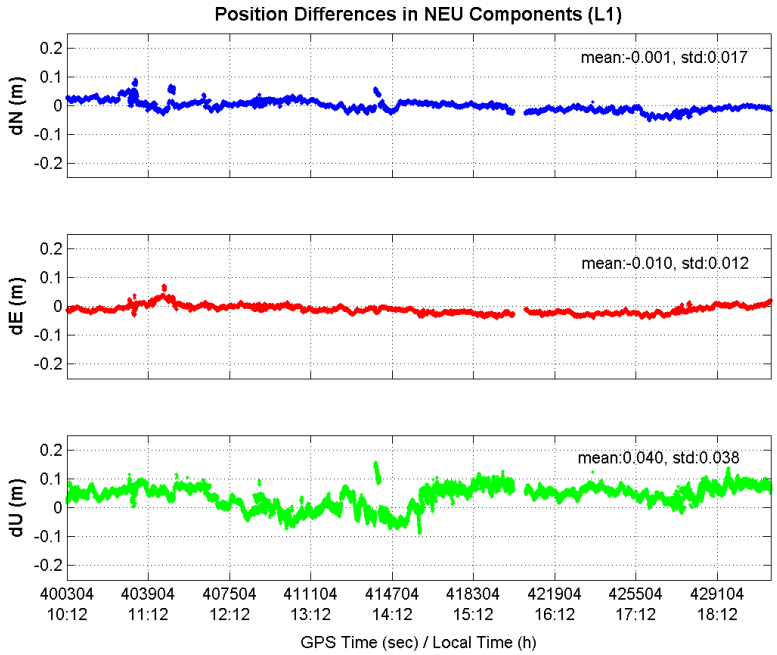

Figure 7.20: L1 positioning solution for NWBL-OLVN from test-bed software

Figure 7.22 and Figure 7.23 is the northing, easting and up position result by

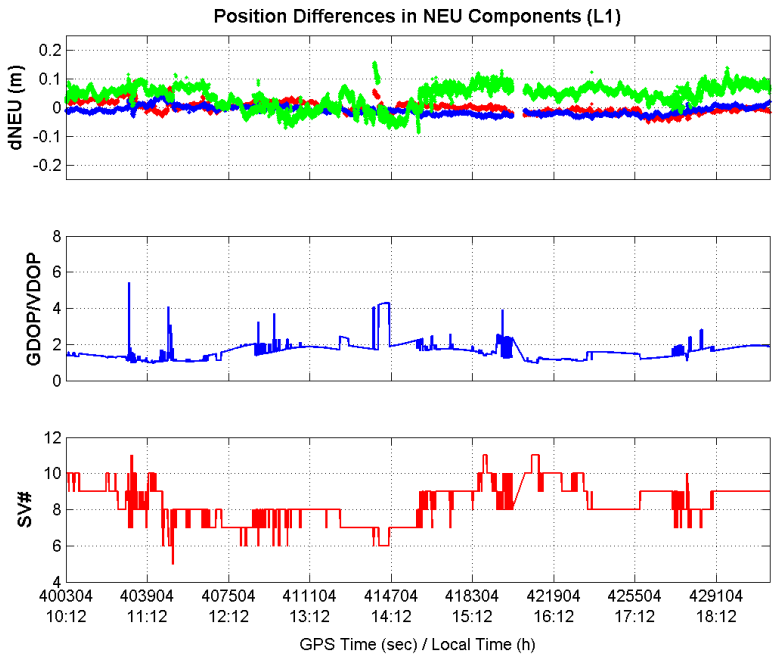

Figure 7.21: L1 positioning solution with DOP and number of satellites for NWBL-OLVN

RTKLib platform and Bernese GNSS software. The results can be compared with the result shown in Figure 7.20 to confirm each software′s performance. Note that the coordinate differences from the Bernese software are from the final estimated coordinates. Therefore, it gives a different result on the mean value. The processing of Bernese software is based on the best estimates for all necessary parameters for all epochs. There is a numbers of different options that can be applied, as with many geodetic software process. Comparing statistics of the position results from the software, we can confirm that the developed test-bed software can generate the very comparable result. After the confirmation, the combined approach as seen in Figure 7.19 was employed to further test the approach with the developed software platform.

Figure 7.24 and Figure 7.25 are corresponding L1 and L2 residuals for the position solution. Figure 7.26 are L1 and L2 contribution signatures from the test-bed

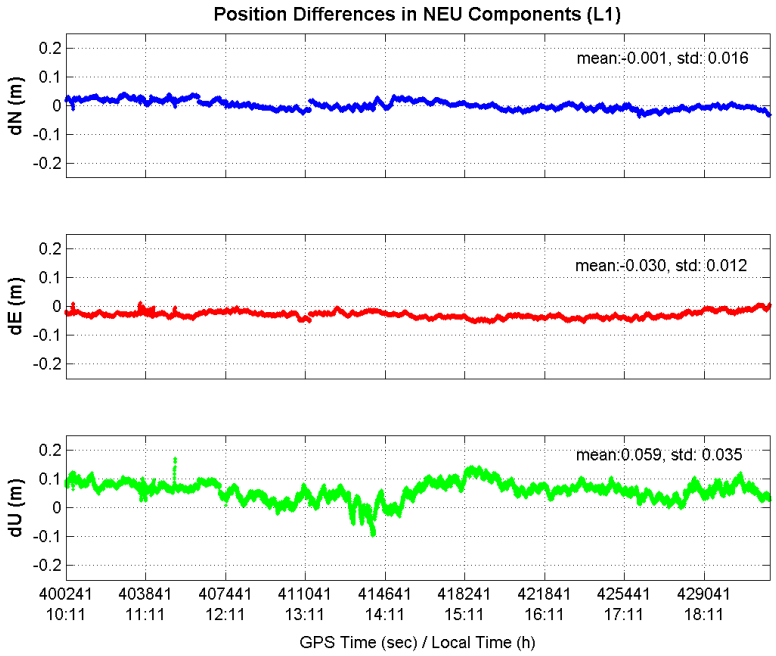

Figure 7.22: L1 positioning solution for NWBL-OLVN from RTKLib

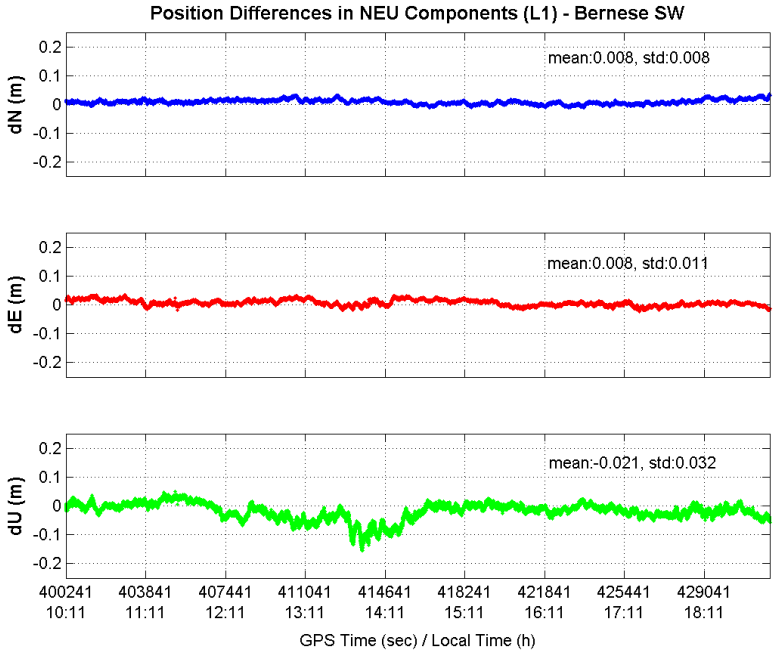

Figure 7.23: L1 positioning solution for NWBL-OLVN from Bernese software

software. As is shown in Figure 7.26, most of the residuals follow well either to the frequency-dependent and non frequency-dependent components, but it seems that some of the residuals are not strictly separable. In this situation, the identification is assumed to have failed and the combined approach is not applicable to the corresponding epochs. Once the troposphere residuals from the residual signature plot in L1 and L2 reaches over 20 ppm in baseline length, the weighting parameters, α based on the residual signatures, is determined. Then, the combined method is applied and recalculates the position solution again to achieve the final solution.

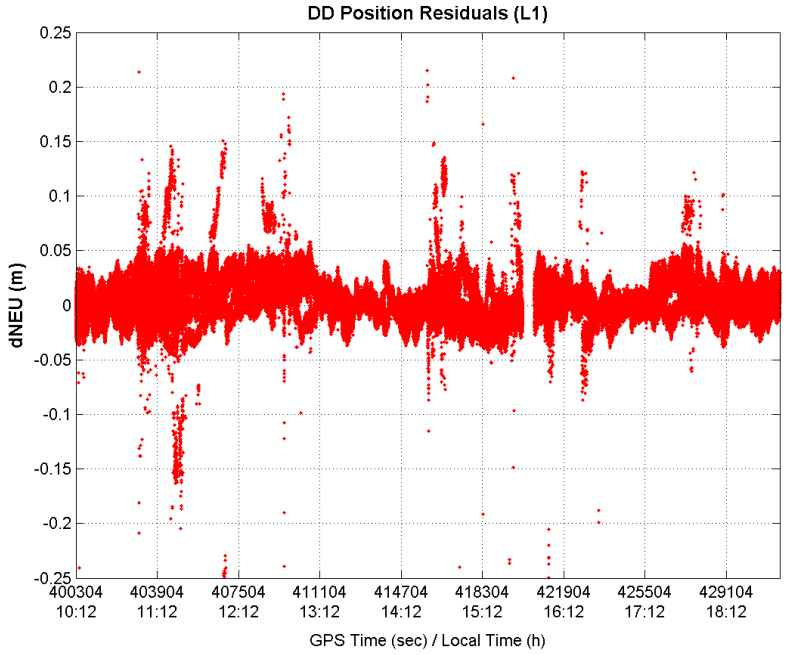

Figure 7.24: L1 residuals for NWBL-OLVN

The Caribbean is generally humid, it may be typical that both stations see almost same troposphere delay. Therefore, we can not see any big improvement in the height coordinate, but in general, the overall performance is better and reduces some biases in the result. This can be seen in Figure 7.27.

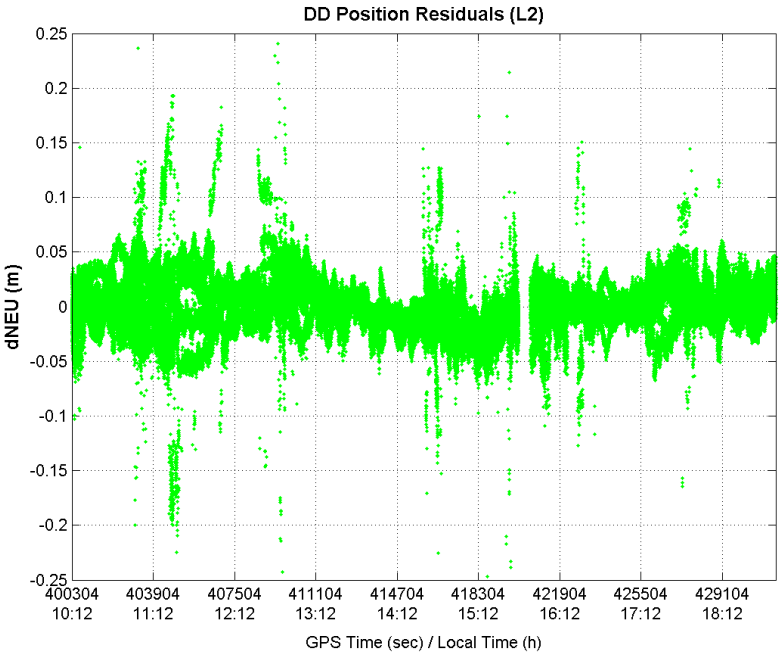

Figure 7.25: L2 residuals for NWBL-OLVN

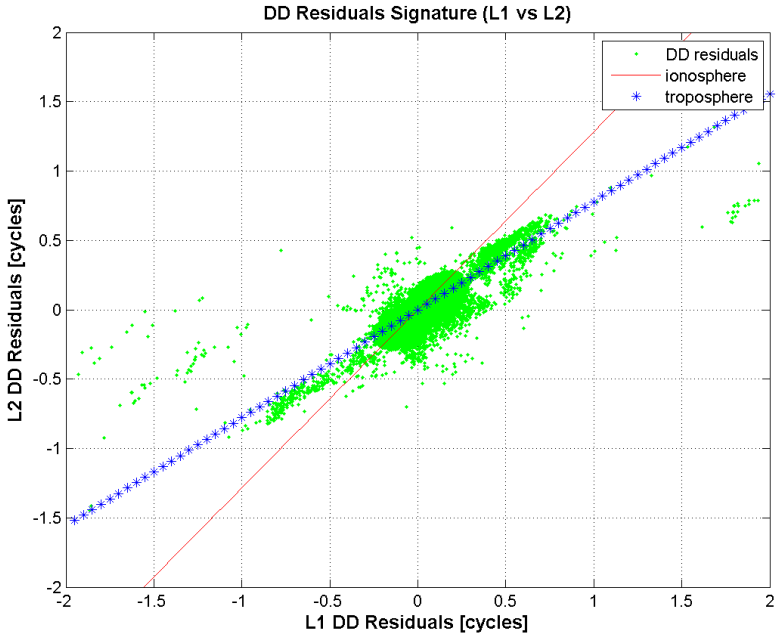

Figure 7.26: L1 and L2 residual signature for NWBL-OLVN

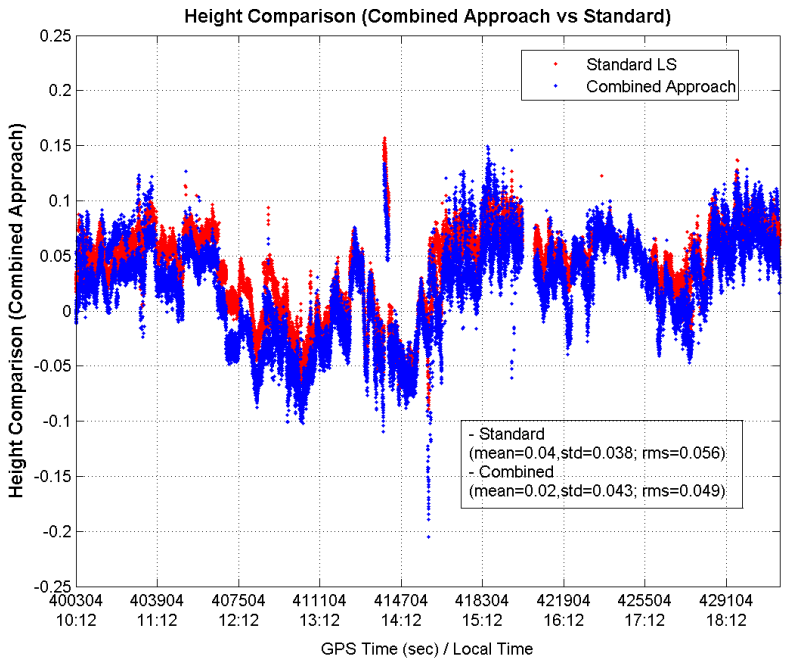

Figure 7.27: Height comparison between the standard (red dot) and combined method (blue dot) for NWBL-OLVN

Figure 7.27 represents the height difference between the standard method and combined approach. The standard method represents when there is no transformation between the cartesian coordinate and local geodetic coordinate, while the coordinates resulting from the combined approach are transformed in Equation (4.20). Figure 7.27 represents the difference between the standard LS which is coloured in red dot and the combined method which is in blue dot. The biggest differences between both methodologies happen in-between 14:12 and 16:12 in local time. As shown in Figure 7.28, the height results from the approach during those epochs show a bigger difference than any other epochs.

Figure 7.29 is the northing, easting and up position resulting from the test-bed software for NWBL-GERD (around 3 km in length). In the software, NWBL is treated as the reference station and GERD is the rover station. The data is also 1 Hz with Trimble R9 receiver. Similarly, the DOP and the number of satellites are

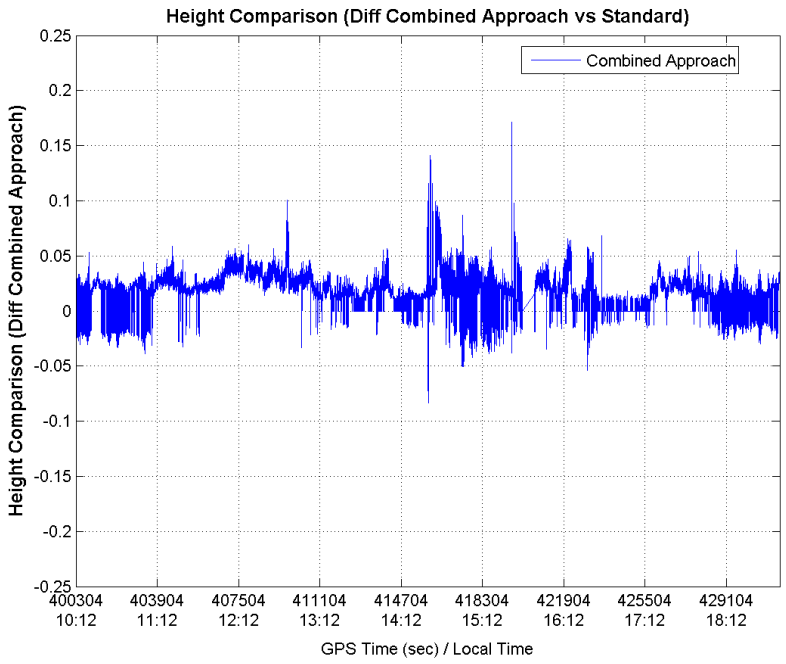

Figure 7.28: Height difference between standard and combined approach for NWBL-OLVN

shown in Figure 7.30 while Figure 7.31 shows the L1 and L2 contribution signature graphs.

Again, Figure 7.32 is the northing, easting and up position results by the RTKLib platform and Figure 7.33 represents the height comparison between the combined approach and standard approach. As can be seen from Figure 7.33, the combined approach reduces overall rms from 4 cm to 3 cm.

Figure 7.34 represents the height difference between the standard and combined approach.

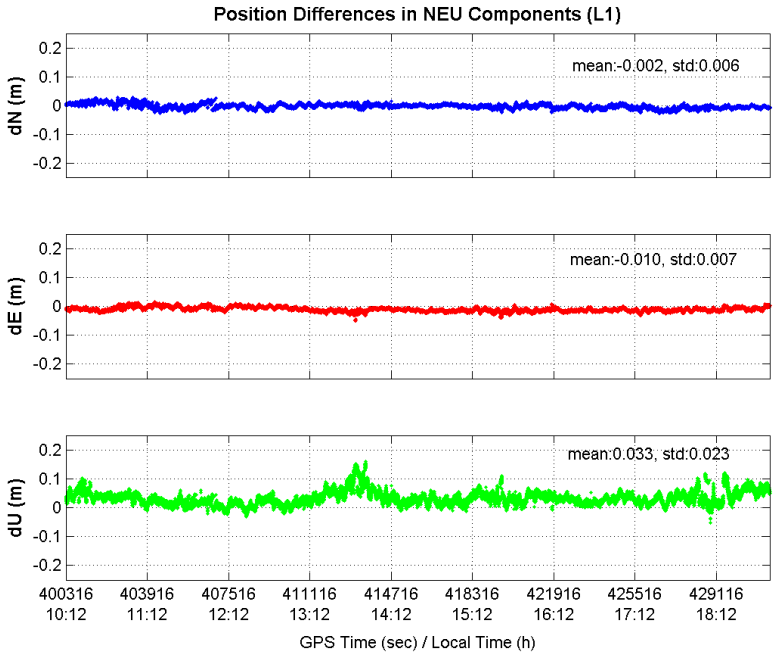

Figure 7.29: L1 positioning solution for NWBL-GERD

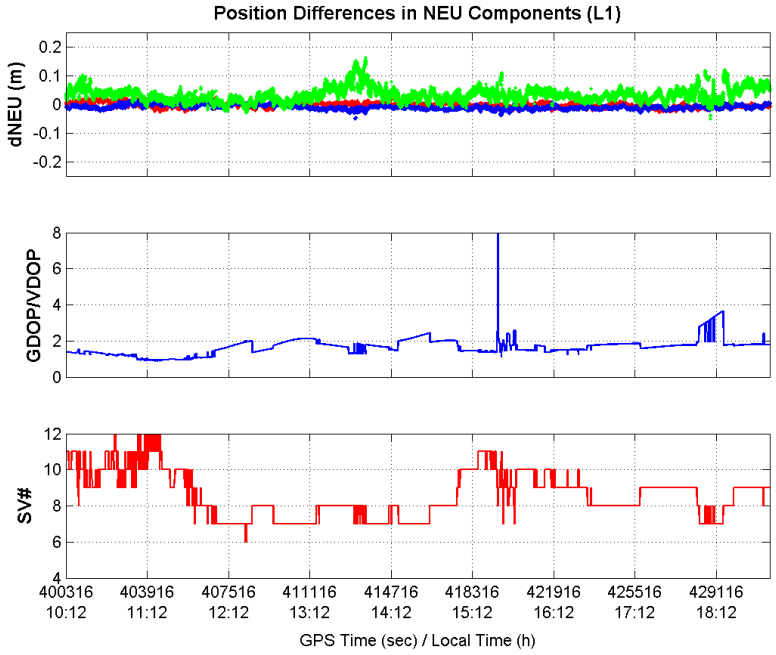

Figure 7.30: L1 positioning solution with DOP and number of satellites for NWBL-GERD

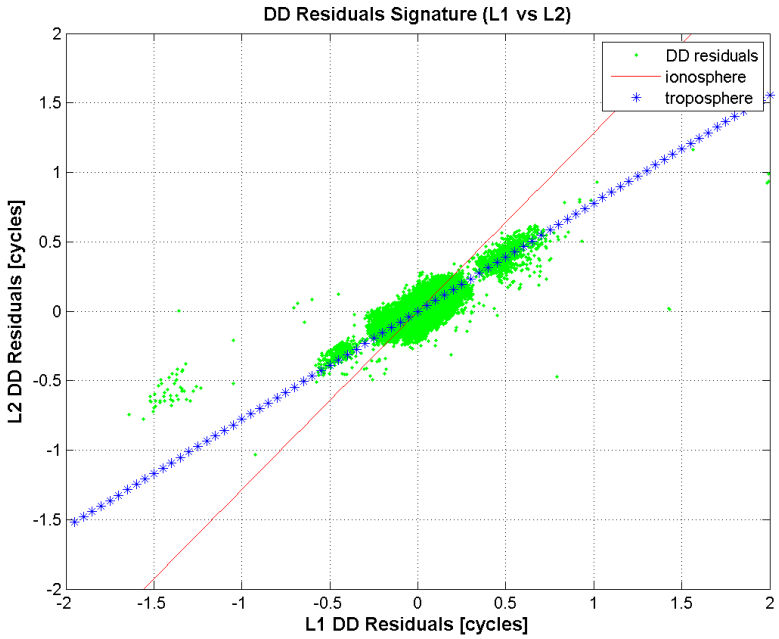

Figure 7.31: L1 and L2 residual signature for NWBL-GERD

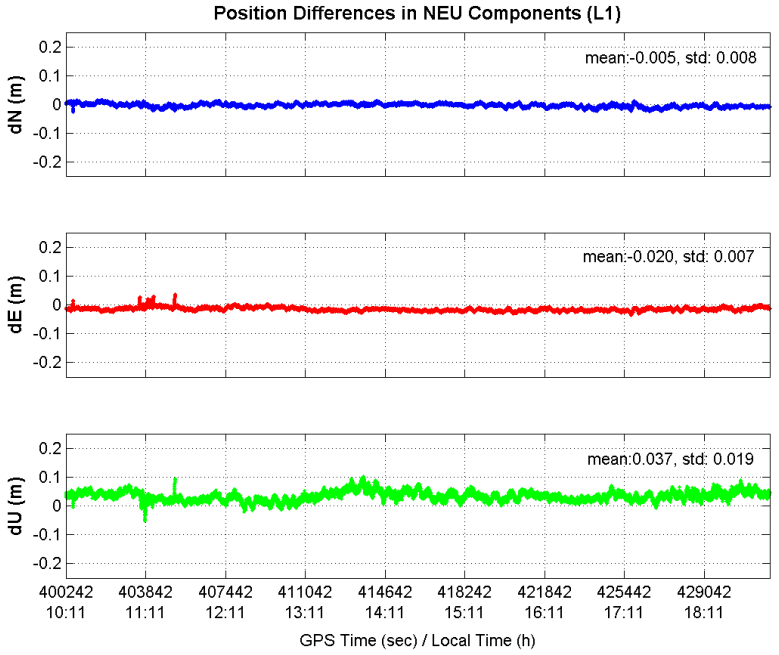

Figure 7.32: L1 positioning solution for NWBL-GERD from RTKLib

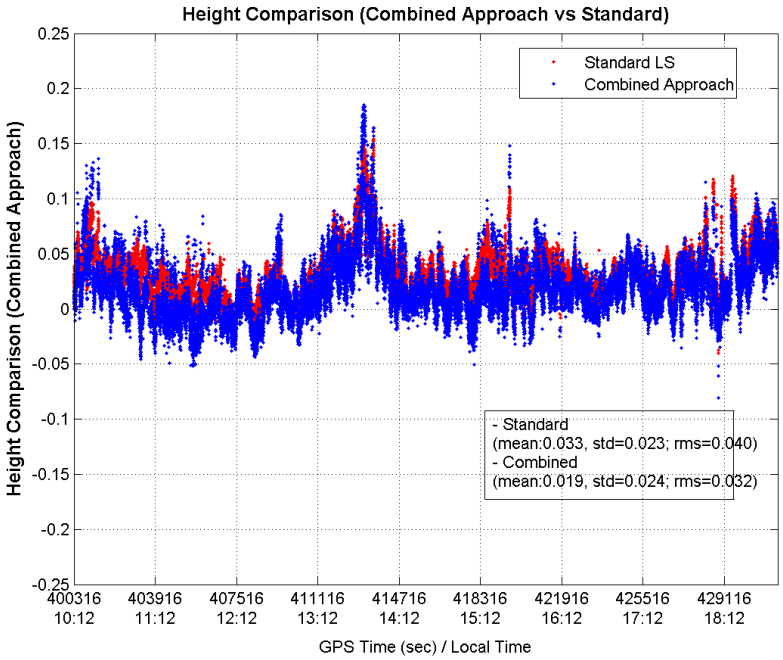

Figure 7.33: Height comparison between standard and combined approach for NWBL-OLVN

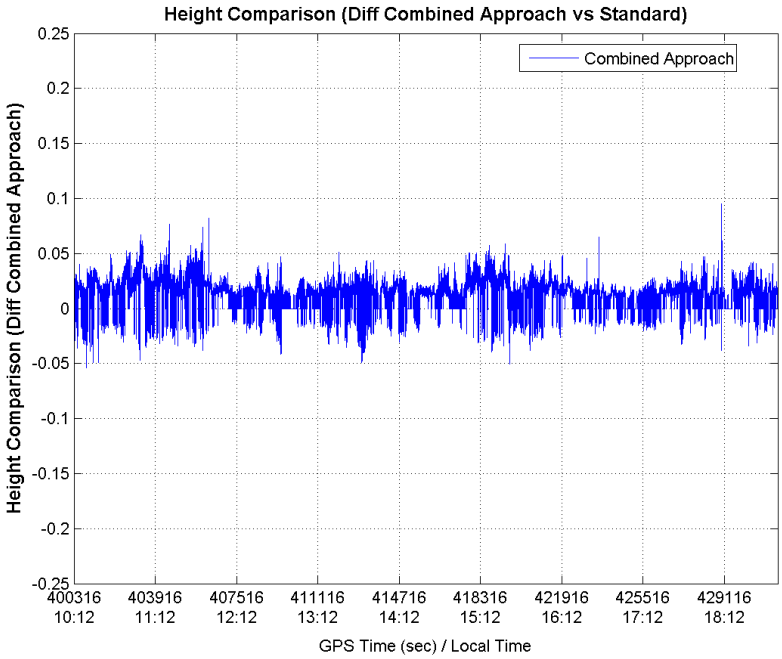

Figure 7.34: Height difference between standard and combined approach for NWBL-GERD

7.2.4 Ferry Data Result using the Developed Software Platform

As discussed in Chapter 6, ferry data is also processed to evaluate the performance of the combined approach. Although the baseline length is short, the determination of the position at cm level for a moving platform is a challenging subject. As the receiver was situated on top of the ferry, most of the error comes through cycle slips.

As the Bernese software can not reliably determine positions of a moving platform at the cm level, and there is no reference trajectory for the vessel, only the positioning result from the RTKLib software was compared with the developed combined approach without detailed statistics. The detailed trajectory for the ferry can be seen from Figure 6.8.

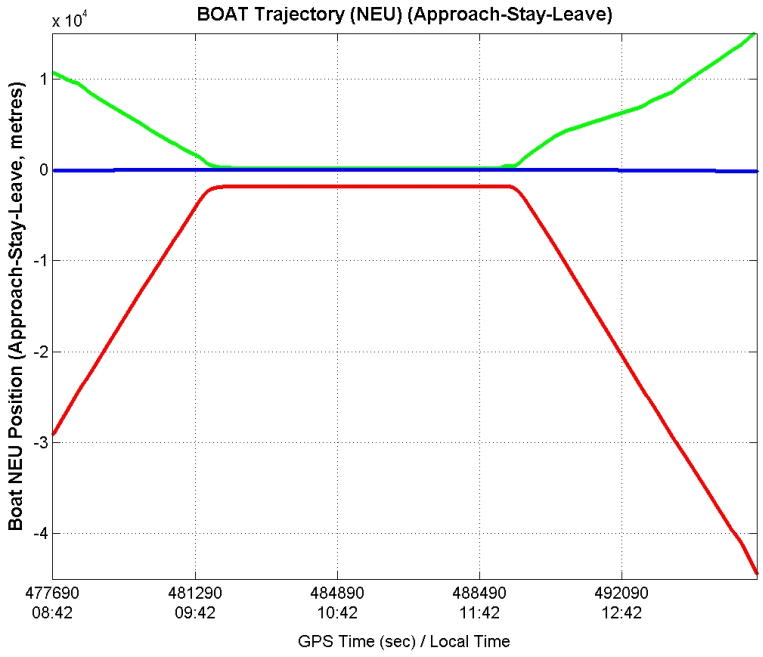

Figure 7.35: Northing, easting and up trajectory for CGSJ-BOAT from the developed test-bed software

Figure 7.35 represents the trajectory of the vessel from the developed software. The data is processed with the test-bed software with the combined approach and the data is 1 Hz from a NovAtel OEM4 receiver. The data were processed when the ferry approached the port and leaves. The longest baseline in this case is less than 5 km from the reference site which is CGSJ. In Figure 7.35, the blue coloured line represents the height component; the green colour the northing, and the red the easting component. The shortest baseline when the ferry stops is around 1.87 km. As there is no reference trajectory for the ferry trajectory, each coordinate solution represents the relative position from the reference station only. The improvement of the height component is the concern of this research through the development of the combined approach.

When the height result is magnified from Figure 7.35, we can see the details of the height changes. This is illustrated by Figure 7.36. The red dot in Figure 7.36 represents the positioning results from RTKLib software when applying the Saastamonen model with the Niell mapping function as the a priori troposphere mitigation. The blue dot represents the result from the developed test-bed software using the combined approach. Quality control routine has worked fine as most of the cycle slips could be detected and fixed in the developed platform and the ambiguity parameters have been determined so that the result of the height component shows overall better performance than RTKLib software.

Figure 7.37 illustrates the height comparison for the ferry from the developed test-bed software and RTKLib software. As illustrated in Figure 7.37, the position difference is due to the wrongly determined height position due to the failure of fixing ambiguities from RTKLib software.

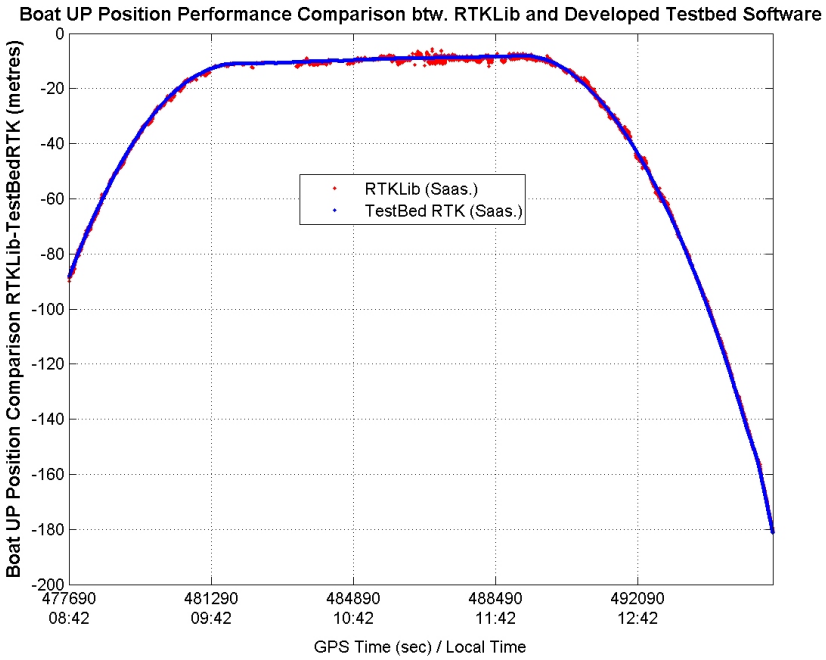

Figure 7.36: Height result for CGSJ-BOAT from the developed test-bed and RTKLib software

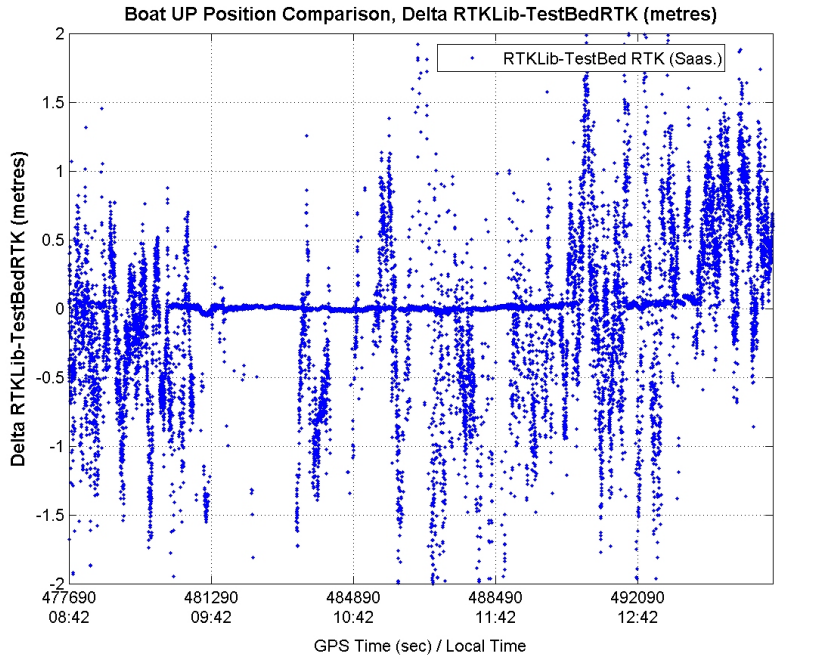

Figure 7.37: Height comparison for a ferry from the developed test-bed and RTKLib software

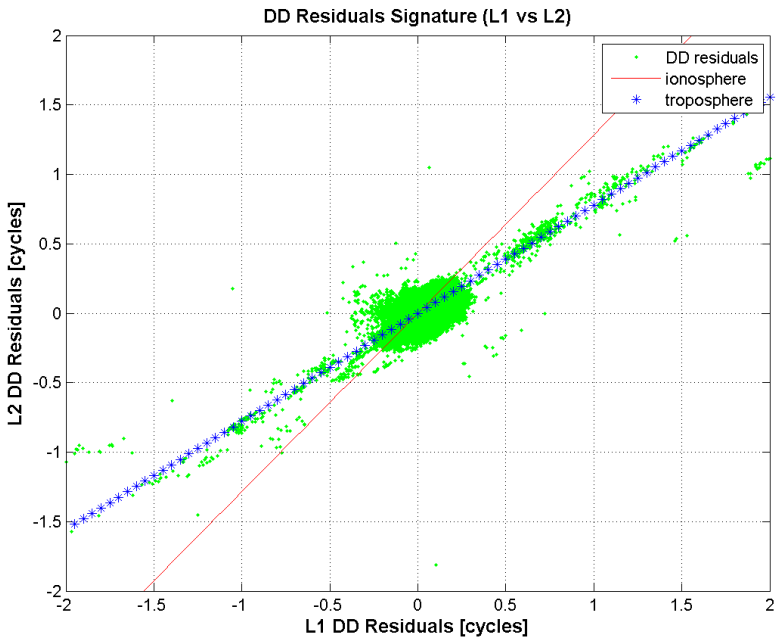

Figure 7.38: Residuals for a ferry from the developed test-bed software

Figure 7.38 illustrates the residuals. Most of the residuals are within 0.5 cycle and hence the combined approach is not employed to many epochs. Therefore an overall improvement for the combined approach can not be easily seen in this case. The reason might be because the distance between them is only a few km and the data may experience nearly the same tropospheric condition where no anomaly is present. In this case, the combined approach does not significantly affect the solution domain, but just has a marginal impact. Some of the results on the plot can be seen.

Figure 7.39 represents the potential height improvement during the moving platform for the ferry. As the residual′s signatures shown in Figure 7.38 has only a few spikes for the troposphere contribution line, only a few comparisons are possible. The red dots represent the height solution from the combined approach due to the higher troposphere contribution in the residuals. The result from the standard LS approach is shown in blue. Assuming the attitude of the moving ferry was not

abruptly changed, the height solution from the developed combined approach is considered to show a more accurate result.

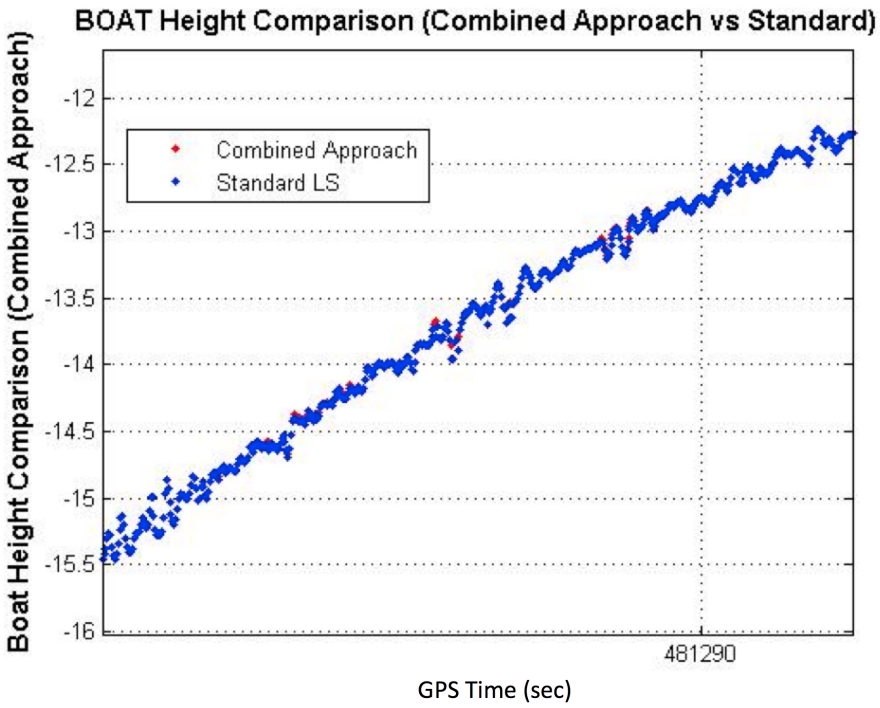

Figure 7.39: Potential height improvement from the combined approach with a moving platform

7.3 Potential Usage of NWP for Long Baseline for Troposphere Error Mitigation

As discussed in earlier sections, the developed combined approach can be a good methodology for a short baseline, especially during the severe troposphere anomaly. For the troposphere mitigation, there are many different approaches as discussed in Chapter 3. One of them is based on a ray-tracing with NWPs. One NWP model was tested in the bay of Fundy to evaluate the PPK performance for the troposphere mitigation for a long baseline case. Test tesults and details of the approach are in-

cluded herein.

RUC20 raw data used in the processing has a horizontal grid of 301 by 225 points, and is based on a 20×20 km grid. It has 37 isobaric levels (with an additional ground surface level) as a three-dimensional gridded field from 1000 hPa to 100 hPa, at intervals of 25 hPa. It also has 92 variables which contain necessary information for calculating refractivity, e.g. geopotential height, relative humidity, pressure, temperature, etc.

The refractivity N from Equation (3.1) at a given distance s along the path is obtained by interpolating the weather parameters at the corresponding three-dimensional position in the NWP gridded fields. N is sampled at as many points as needed to fulfill the tolerance of 1 mm. A typical curve of refractivity versus distance from the receiver in the direction of the satellite (with 1 mm tolerance) is shown on Figure 7.40. This figure shows an example of the refractivity versus slant distance in the zenith direction and at 45 degree elevation angle for CGSJ station at 8:00a.m. on a 14 Aug. 2004 integrated using the RUC20 NWP model. The refractivity reached about 2.6 m in the zenith direction and 3.6 m at 45° elevation angle.

To perform the integration, the coordinates are transformed from the integration space (s) to the interpolation space ($x,\ y,\ H^G$), where x, y represent horizontal coordinates in the Lambert conformal conic projection for RUC20 and H^G is geopotential height. The transformation to the vertical component H^G is based on following equation.

$$H^G = \frac{H \cdot G_{ratio}}{H + R_e} \tag{7.1}$$

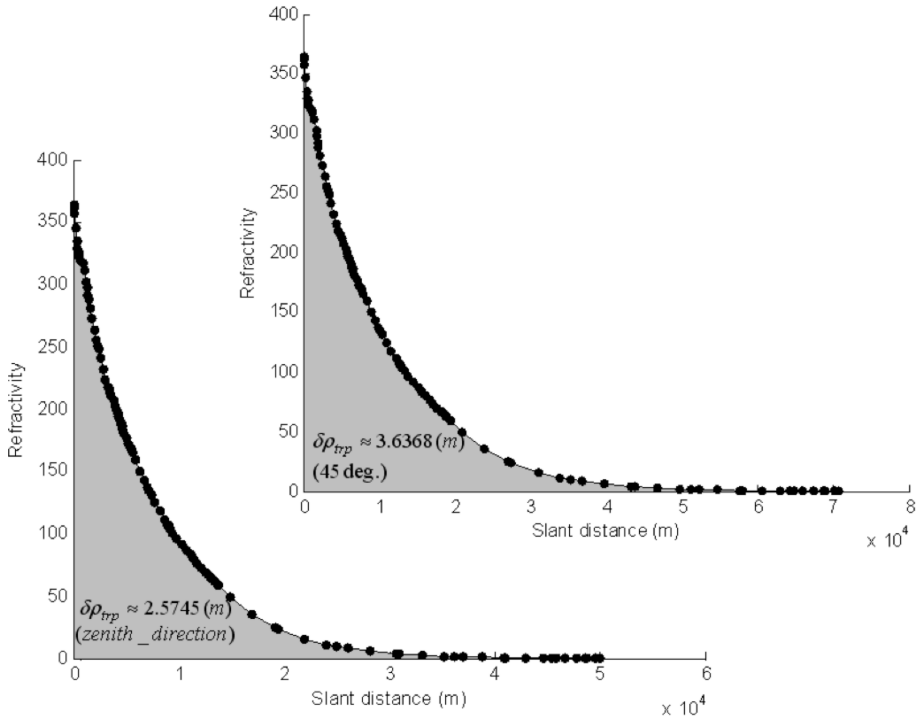

Figure 7.40: Refractivity (mm/km) versus slant distance (m) in the zenith direction and at a 45° elevation angle for CGSJ at 8:00a.m. on 14 Aug. 2004 based on RUC20 NWP. Black dots represent points at which refractivity was sampled [*Ahn et al.*, 2005]

where,

H : orthometric height,

G_{ratio} : the gravity ratio ($g \cdot R_e/9.80665$),

R_e : radius of the Earth at latitude φ, 6371200 m.

The gravity g used in the calculation is a function of latitude φ as follows:

$$g = 9.80616\left(1 - 0.002637\cos(2\varphi) + 0.0000059\cos^2(2\varphi)\right) \tag{7.2}$$

Figure 7.41 illustrates an example of the refractivity profile calculated for each layer from RUC20 raw data. Each level contains refractivity index and isobaric

height covering the whole of the USA, southern Canada, and the northern Mexico region. Node spacing is 20 km apart and each node has detailed meteorological parameters, which can be used for the delay calculations for a specific GPS satellite in view.

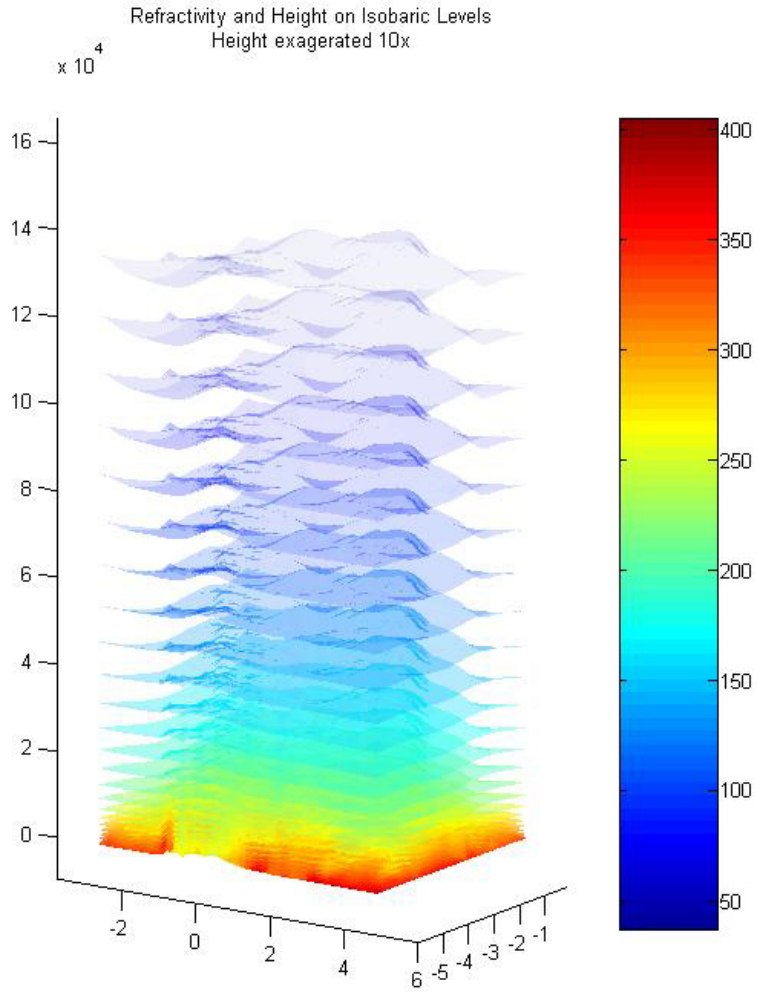

Figure 7.41: Refractivity calculated for each layer from RUC20 raw data

To evaluate Equation (7.1), the hydrostatic delay for UNB1, an IGS station located at UNB, was calculated. For this purpose, pressure values from either meteorological data or NWP were extracted. The pressure values agreed well with a bias of about -0.01 cm and an rms of 0.27 cm, those are consistent with the values observed by

other researchers, e.g. Schuler [2001]. Transformations between geopotential heights and orthometric heights and details of the delay calculations can be found Santos et al. [2005] or Nievinski et al. [2005]. As the RUC20 NWP model only goes up to approximately 16 km in the vertical direction, the COSPAR International Reference Atmosphere (CIRA-86) model [*Fleming et al.*, 1988] was also used as it has values up to 50 km from the maximum vertical direction of the NWP model.

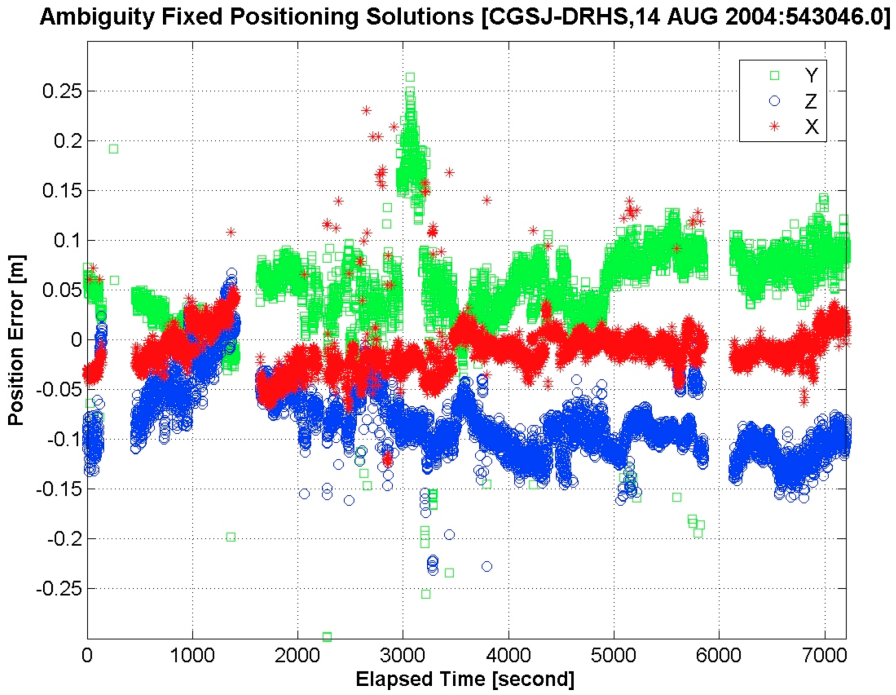

Figure 7.42: Positioning result calculated by the IF fixed solution using UNB3 model as a tropospheric delay model

We evaluated the two tropospheric delays; one is based on UNB3 troposphere mitigation model and the other is a ray-tracing by RUC20 NWP. Static data sets for CGSJ and DRHS (in Figure 6.12) were used and processed epoch by epoch (no need to wait for convergence) for this evaluation. CGSJ was held fixed with the ITRF00 coordinates described in Table 6.2, and DRHS′s coordinates were then estimated for each epoch and compared with a final (combined) coordinate estimate for DRHS in

Table 6.2. Figure 7.42 represents the positioning result using the UNB3 model. The x-axis is the elapsed time in seconds and the y-axis represents the position errors in metres. Note that all the plots herein do not show the combined IF float/fixed solution, but the IF fixed solution only. Figure 7.43 illustrates the result by ray-tracing using the NWP model. As is shown in both Figure 7.42 and Figure 7.43 the improvement using ray-tracing can be seen.

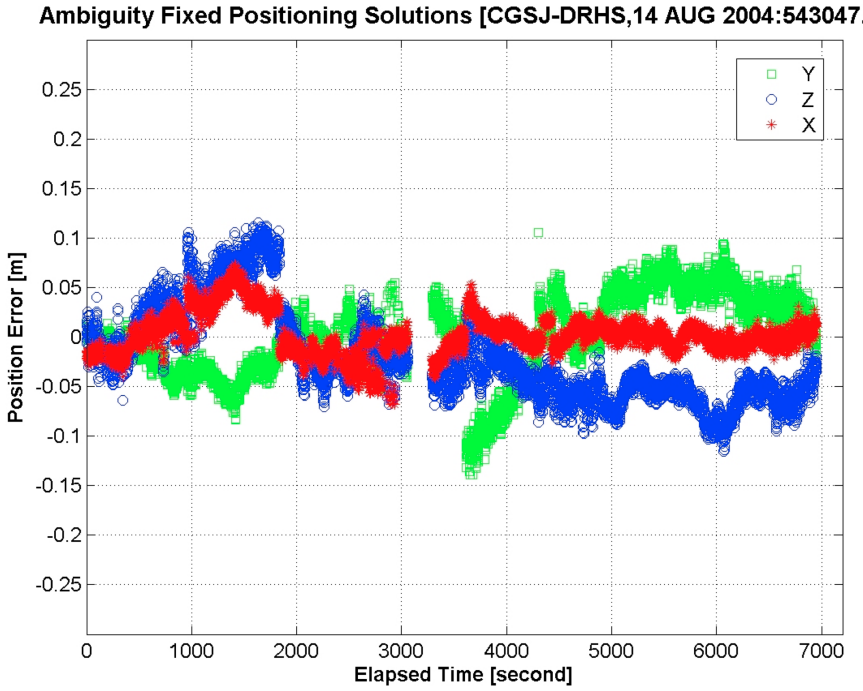

Figure 7.43: Positioning result calculated by the IF fixed solution using ray-tracing as a tropospheric delay model

Table 7.2: Kinematic positioning solutions with troposphere mitigation by a ray-tracing with RUC NWP

		Ray-tracing	
		mean(m)	std(m)
DRHS	X	0.0027	0.0206
	Y	-0.0001	0.0422
	Z	-0.0218	0.0471

The positioning results are based on IF fixed solution, not float solution. A static

test (but kinematically reprocessed) was performed to evaluate the ray-tracing. Table 7.2 gives a summary of the positioning domain results of ray-tracing for the static test. Compared to those two plots (Figure 7.42 and Figure 7.43), the level of improvement with respect to the results by the UNB3 model can be clearly seen. Some wrongly fixed solutions by the UNB3 model are found in Figure 7.42 and the corresponding epochs were rejected. Therefore, instead of giving inconsistent results, only the solution by ray-tracing is shown in the table to verify the performance level.

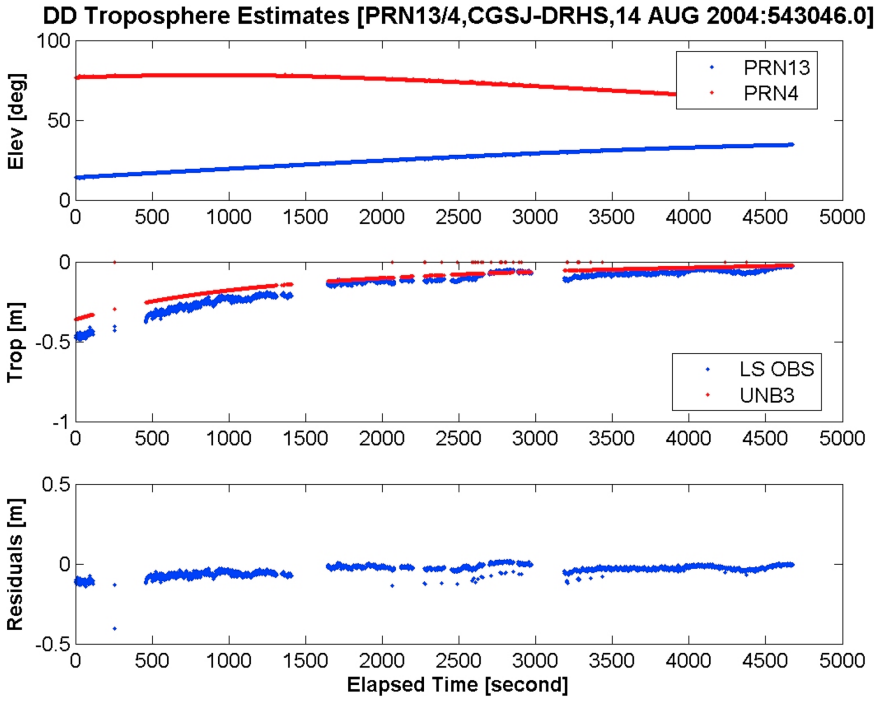

Figure 7.44: Double differenced tropospheric estimates by UNB3

Figure 7.44 and Figure 7.45 show the DD tropospheric estimates and residuals for varying elevation angle using both the UNB3 model and NWP. The red line in the first subplot in Figure 7.44, the elevation angle, represents the reference satellite, i.e. PRN4, and blue line represents the involved satellite, i.e. PRN13. The second subplot represents the double differenced tropospheric delay observables, the red line

represents values predicted by the UNB3 model, while the blue line represents the double differenced tropospheric observables (described in Ahn et al. [2005]) generated using kinematic positioning followed by least-square adjustment. As the satellite goes down to horizon, the differences between UNB3 model and the tropospheric observables become significant. One reason is that since the UNB3 tropospheric model provides essentially a constant prediction value of hydrostatic and wet zenith delay for each day-of-year, the effectiveness of the UNB3 model as similar to other existing model-based approaches will be degraded to some extent by weather fronts, temperature inversions, and other dynamic coastal weather phenomena. Figure 7.45 represents the result from ray-tracing and the residuals are smaller than those for UNB3.

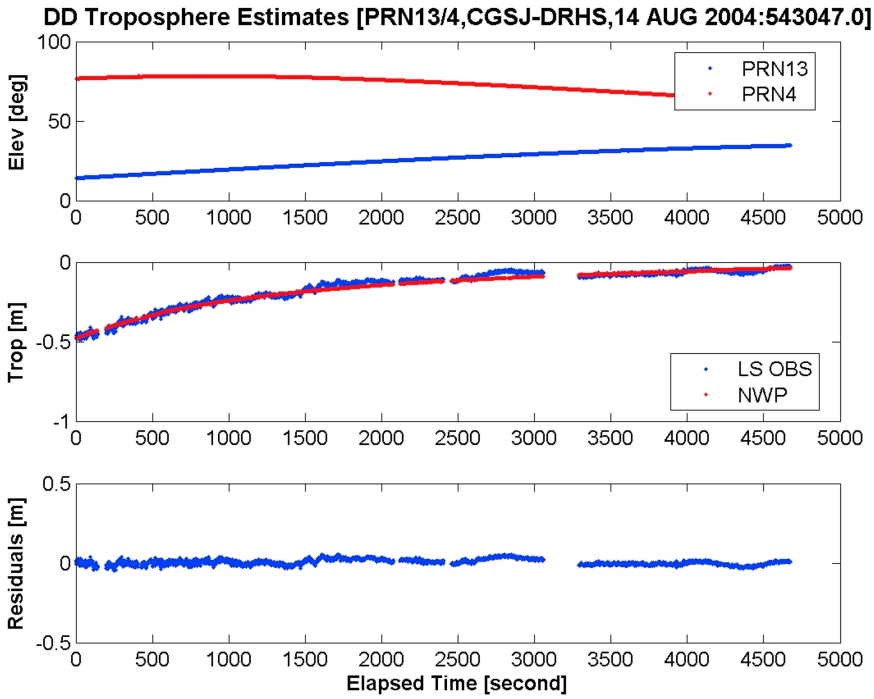

Figure 7.45: Double differenced tropospheric estimates by ray-tracing by RUC20 NWP

The ray-tracing method is beneficial in terms of reducing the tropospheric errors

as an independent source of mitigation method. On the practical side for GNSS data processing, however, ray-tracing has limitations in its use since it is computationally quite demanding. In addition, the current resolution of NWP is more than 10 km which is probably not feasible to use to achieve the goal of this research. However, the NWP provide a great tool to investigate the atmospheric phenomena with a purely mathematical form.

Overall performance of the two tropospheric models shows similar patterns for the processed data sets. For most of the cases in this test, the performance of ray-tracing was more beneficial than UNB3 model in reducing the tropospheric delays and decorrelating the height component. Although the mean values are reduced significantly, the dispersions do not change a lot. One possible reason for the reduction is that the effectiveness of the UNB3 model as well as other model-based mitigation approaches may be degraded to some extent by weather fronts, temperature inversions, and other dynamic coastal weather phenomena. Range difference tests revealed that there are still biases and uncertainties in the solution which may be due to the other effects such as multipath etc.

7.4 Summary

This chapter evaluated the proposed methodology from a few baseline data. Data from a severe troposphere anomaly to typical humid data have been reprocessed to confirm the methodology. Although the height estimate is approximately $1.5 \sim 3$ times worse than the horizontal one due to non-satellite data below the horizon, the solution of this combined approach shows an improvement esp. for the height component, similar to that reported by Kim and Langley [2008] and Li et al. [2010].

In a static case, the proposed methodology with "optimal" weighting parameter provides a dramatic improvement in the height estimate where the height uncertainties of 4 cm go down to 0.8 cm level with ideal weighting parameters. Significantly, the period of the anomaly has been nearly solved with the height estimates using the proposed methodology with the post-analysis method as well as an epoch-wise kinematic solution.

High-precision kinematic positioning is often challenging. The proposed methodology is further tested on a few of data sets to confirm whether helps in kinematic situation or not. Although the test is based on the post-processed platform, the developed software was tested with the Caribbean data as well as a moving vessel.

In summary, the new methodology showed a significant improvement in a static case with proper weighting parameters where the overall rms of 4 cm reduced to 0.8 cm (nearly a 82% improvement) with certain conditions. This means that there must be a certain value at each epoch which can efficiently decorrelate the two common zenith-dependent parameters. In a kinematic scenario, the weighting parameter has been determined using the residual analysis. Overall, the performance on the height component could be seen to have improved by up to 20% (4 cm to 3 cm).

In addition, the potential application using NWP for a long baseline to mitigate the troposphere error is also evaluated.

Chapter 8

Conclusions

The main goal of this research has been to resolve the height position uncertainties during a severe troposphere anomaly. The combined approach proposed in this dissertation (which is not dependent on any external input such as meteorological data) is based on the combination of the common correlated parameters; the height and the troposphere delay parameter.

As the tropospheric delay and the resultant height component are both zenith dependent above 20° elevation angle, that may cause an ill-conditioned case in the normal equations. Those two parameters need to be correctly distinguishable in order to achieve better coordinate solutions. The method is to de-correlate those parameters using different weighting parameters either on the tropospheric delay parameter or on the height component.

The assumption behind the combined method is that the observables are made available in both L1 and L2 (from a dual frequency receiver). To examine the feasibility of this method, anomalous data collected in Southern Texas, USA and COCONet data in Carribean Network as well as data from a moving platform over

a baseline length of less than 10 km were reprocessed.

In order to perform the test, an epoch-wise relative positioning software package has been developed to further analyze the methodology. Consequently, the positioning solution from the new proposed parameter is tested, evaluated, and compared with that from the conventional estimation method. The feasibility of the proposed method has been examined to see whether it is resistant to the anomalous tropospheric case or not. As proposed, new α and ζ coefficients were introduced for combining and decorrelating the cross dependent parameters. If the coefficient is properly selected, the combined zenith-dependent parameter improves the positioning solution especially during a local tropospheric anomaly effect.

In a static case, the analysis shows that the coordinate solution in the severe troposphere anomaly example in Texas can be dramatically improved when the weighting parameter is determined well. The overall rms of the height estimates in this case was reduced from 4 cm to 0.8 cm, which corresponds to around 80% improvement. Therefore, the hypothesis in this dissertation was supported by the results. This also implies that there must be a certain optimal value which can decorrelate the two common zenith-dependent parameters to achieve better solution. This methodology may be especially useful in further analysis of static data to identify the decorrelation parameter in other important applications. In summary, when the weighting parameter has been determined well, a sample static result has revealed that the corresponding coordinate solution can be changed a great deal and converge to the known positioning solution.

There are many different ways to determine the weighting coefficients. In a kinematic scenario, the weighting parameters has been determined based on the residual

analysis. The residuals have been decomposed into two different components to determine the weighting parameter: frequency-dependent and frequency-independent components. The troposphere is of the frequency-independent domain in GNSS signals, and this characteristic is further used as a weighting scheme through the residual analysis. All data were reprocessed to obtain epoch-by-epoch kinematic positioning to test the methodology. Once the frequency-independent component in the residual analysis reaches over 20 ppm, it was assumed that the troposphere is dominant effect and the developed combined approach was employed.

For the severe tropospheric anomaly data in Texas, the overall result in a kinematic scenario showed that the improvement was not as much as the static case, however, the improvement could be still seen especially during a humid period. The improvement of up to 20% could be seen (rms: 4 cm to 3 cm) from the combined approach. The northing and easting components using the proposed method are marginally improved.

For the COCONet Caribbean data, the overall precision based on the combined approach showed that the rms of 5.6 cm was reduced to 4.9 cm for the baseline NWBL-OLVN. For the baseline NWBL-GERD, the overall rms was reduced from 4.0 cm to 3.2 cm.

Data from a moving platform were also reprocessed using the developed software platform. The coordinate results from the developed software and from the RTKLib software are compared. This confirms the performance of the developed software. The ferry data were processed when the ferry closely approached the port, and when it left port. CGSJ was fixed as a reference site. Compared to the RTKLib software, the overall coordinate solutions of the developed software platform in this research

showed better performance in the moving platform of the ferry. Most of the residuals for the processed data were within 0.5 cycles or less, however, an overall improvement for the combined approach could not be seen in this case. Only a few epochs in the trajectory data were affected by the combined approach. Assuming the attitude of the moving ferry was not abruptly changed, the height solution from the developed combined approach is considered to show a more accurate result.

In summary, the developed combined approach is an effective means of minimizing the correlation problem between the height and the tropospheric delay parameters. The overall improvement in the positioning domain shows that the bias and standard deviation of the height component are reduced. By introducing the methodology with the new weighting scheme to de-correlate the height and tropospheric parameters for the purpose of mitigating the mis-modeled tropospheric delay, height positioning improvement of up to 20% can be achieved, even in a kinematic situation. In addition, degradation of the height component during the troposphere anomaly in the conventional approach mostly disappears which was the original motivation of this research.

Chapter 9

Further Direction

The methodology proposed in this dissertation provides a number of different aspect in the analysis of GNSS data sets in terms of position estimation. Especially, the vertical component and the troposphere parameter can be combined together and they can be controlled by a weighting parameter, or simply a scale factor. Once the weighting parameter is determined well, it reveals that the vertical position shows a dramatic improvement. In a kinematic scenario, it still shows improvement but not as much as the static case with the optimally determined weighting parameters. It means that the precision of the coordinate solutions by the combined approach are strongly dependent on the determination of the weighting parameter. In a kinematic scenario, to solve for the parameter, the residual analysis must have been conducted.

Overall, the methodology reveals that the decorrelation between the height and the troposphere parameter is successful especially during a severe troposphere anomaly at one of the GNSS receivers. However, even if most of the unmodeled tropospheric delay can be eliminated by the combined approach with proper weighting, most epochs do not show much of an improvement in the positioning solution unlike the static scenario which can allow us to determine the optimal weighting parameters.

This issue may be from the partial failure of determining the proper weighting parameter to decorrelate those two parameters.

While the developed combined approach and analysis of the data presented in this dissertation can cover a range of topics, there are further research avenues that must be pursued. Some of these include:

- Testing and derivation of the best set of weighting parameters based on the amount of tropospheric anomaly data. The Texas storm data was the only data set for the severe troposphere event examined in this research. With more data sets with severe weather conditions with a number of independent clues, the choice of the weighting parameters can be made more precise and can be generalized. Areas to examine are:
  - Calculation of the weighting parameters based on different DOPs, correlation coefficients, or posteriori variances, residual troposphere observables, and so on,
  - Determination of the weighting parameters based on the external weather data, especially NWPs or radiosondes,
  - A more comprehensive study to make the best functional form of the weighting parameters which can be generally applied for under a variety of conditions in the data sets,
  - A more comprehensive study to separate the frequency-independent component in the positioning residuals, in a static and also in a moving platform environment.
- Comprehensive analysis and evaluation. The analysis of the combined approach in this dissertation was mainly based on the position domain only. Areas to thoroughly examine are:

  - Test and analysis of the improvement in the measurement domain,
  - Analysis of the impact on the ambiguity resolution and success rate,
  - Development of the combined approach with multiple frequencies and PPP.

- Analysis using a wide range of simulation data, e.g. from a hardware simulator. The troposphere anomaly happens from time to time but collecting the relevant data sets to examine is quite challenging. To further study the area, the best way might be to simulate the relevant data sets. As the research is towards cm to mm level accuracy, the simulation has to be fine-tuned from the error-free setting and must apply the relevant but known tropospheric delay in the simulator.

- Analysis of a variety of moving platforms. The analysis presented in this dissertation is based on the post processed kinematic processing. Once the best set or the definitive functional form of the weighting parameters are determined, the effectiveness of the methodology might be checked with a moving platform in real time.

A number of important recommendations given above are indicating that this dissertation is the starting point of the combined approach to the determination of the optimal weighting parameters which may be based on methodologies presented above. Overall, the results from the combined approach presented in this dissertation reveal improvements especially under a severe troposphere anomaly, as well as a humid environment. Therefore, the recommendations described above must be sound, further research topics.

Bibliography

.

Ahn, Y. W., D. Kim, P. Dare, and R. B. Langley (2005), Long baseline GPS RTK performance in a marine environment using NWP ray-tracing technique under varying tropospheric conditions, *Proceedings of ION GNSS 2005*, pp. 2092-2103, Long Beach, CA.

Ahn, Y. W., D. Kim, and P. Dare (2006), Local tropospheric anomaly effects on GPS RTK performance, *Proceedings of ION GNSS 2006*, pp. 1925-1935, Fort Worth, TX.

Ahn, Y. W., D. Kim, and P. Dare (2007), Positioning impacts from imbalanced atmospheric GPS network errors, *Proceedings of ION GNSS 2007*, pp. 2302-2312, Fort Worth, TX.

Altamimi, Z., P. Rebischung, L. Metivier, and C. Collilieux (2016), ITRF2014: A new release of the International Terrestrial Reference Frame modeling nonlinear station motions, *J. of Geophysical Research; Solid Earth, 121*, DOI:10.1002/2016JB01.

Baby, H. B., P. Gole, and J. Lavergnat (1988), A model for the tropospheric excess path length of radio waves from surface meteorological measurements, *Radio Science, 23*, pp. 1023-1038.

Baltink, H. K., H. van der Marel, and A. G. A. van der Hoeven (2002), Integrated atmosphere water vapor estimates from a regional GPS network, *J. of Geophysical Research, 107*, 4025. DOI:10.1029/2000JD000094.

Bassiri, S., and G. A Hajj (1993), Higher-order ionospheric effects on the Global Positioning System observables and means of modeling them, *Manuscripta Geodaetica, 18*(6), pp. 280-289.

Bauersima, I. (1983), NAVSTAR Global Positioning System (GPS) II, *Mitteilungen der Satellitenbeobachtungsstation Zimmerwald, 10*, Astronomical Institute, University Berne, Switzerland.

Beutler, G., I. Bauersima, W. Gurtner, M. Rothacher, T. Schildknecht, and A. Geiger (1988), Atmospheric refraction and other important biases in GPS carrier phase observables, *in Atmospheric Effects on Geodetic Space Measurements, Monograph 12*, edited by Brunner, F. K., pp. 15-43, School of Surveying, Univ. of New South Wales, Kensington, Australia.

Black, H. D. (1978), An easily implemented algorithm for the tropospheric range correction, *J. of Geophysical Research, 83*, pp. 1825-1828.

Blewitt, G. (1990), An automated editing algorithm for GPS data, *Geophyscal Research Letters, 17*(3), pp. 199-202.

Boehm, J., and H. Schuh (2003), Vienna mapping functions, *Proceedings of the 16th Working Meeting on European VLBI for Geodesy and Astrometry*, pp. 131-143, Leizig.

Boehm, J., and H. Schuh (2004), Vienna mapping functions in VLBI analyses, *Geophyscal Research Letters, 31*(1), L01603, DOI:10.1029/2003GL018984.

Born, M., and E. Wolf (1964), *Principles of optics: electromagnetic theory of propagation, interference and diffraction of light*, 2nd eds., Macmillan, New York.

Brevis, M., S. Businger, T. A. Herring, C. Rocken, R. A. Anthes, and R. H. Ware (1992), GPS meteorology: Remote sensing of atmospheric water vapour using the Global Positioning System, *J. of Geophysical Research, 97*(D14), pp. 15787-15801.

Brunner, F. K., and M. Gu (1991), An improved model for the dual frequency

ionospheric correction of GPS observations, *Manuscripta Geodaetica, 16*, pp. 205-214.

Cappellari, J. O., C. E. Velez, and A. J. Fuchs (1976), Mathematical theory of the Goddard trajectory determination system, *Tech. rep.*, Goddard Space Flight Center, NASA.

Chang, X. W., X. Yang, and T. Zhou (2005), MLAMBDA: A modified LAMBDA method for integer least-squares estimation, *J. of Geodesy, 79*(9), pp. 552-565, DOI: 10.1007/s00190-005-0004-x.

Chao, C. C. (1972), A model for tropospheric calibration from daily surface and radiosonde ballon measurement, *Tech. memorandum, 391-350*, pp. 16, Jet Propulsion Laboratory, Pasadena, CA.

Collins, J. P., and R. B. Langley (1996), Mitigating tropospheric propagation delay errors in precise airborne GPS navigation, *presented at IEEE Position, Location and Navigation Symposium*, pp. 582-589, Atlanta, GA.

Collins, J. P., and R. B. Langley (1998), The residual tropospheric propagation delay: How bad can it get?, *Proceedings of ION GPS98*, pp. 729-738, Nashville, TN.

Comparetto, G. M. (1993), The impact of dust and foliage on signal attenuation in the millimeter wave regime, *Proceedings of SPIE, Atmospheric Propagation and Remote Sensing II, 1968*, pp. 81-94.

Cove, K. (2005), Improvements in GPS tropospheric delay estimation with numerical weather prediction, M.Sc.E thesis, Dept. of Geodesy and Geomatics Eng., Univ. of New Brunswick, Fredericton, NB, Canada.

Cove, K. C., M. C. Santos, D. Wells, and S. Bisnath (2004), Improved tropospheric delay estimation for long baseline, carrier phase differential GPS positioning in a coastal environment, *Proceeding of ION GNSS 2004*, Long Beach, CA.

Davis, J. L., T. A. Herring, I. I. Shapiro, A. E. E. Rogers, and G. Elgered (1985), Geodesy by radio interferometry: Effects of atmospheric modeling errors on es-

timates of baseline length, *Radio Science 20*(6), pp. 1593-1607.

Dousa, J. (2001), The impact of ultra-rapid orbits on precipitable water vapor estimation using ground GPS network, *Physics and Chemistry of the Earth 26*(6-8), pp. 393-398.

Escobal, P. R. (1976), *Methods of orbit determination*, John Wiley & Sons, New York, London.

Essen, L., and K. D. Froome (1971), The refractive indices and dielectric constants of air and its principal constituents at 24,000 Mc/s, *Proceedings of the Physical Society 64*(10), pp. 862-875.

Fleming, E. L., S. Chandra, M. R. Schoeberl, and J. J. Barnett (1988), Monthly mean global climatology of temperature, wind, geopotential height and pressure for 0±120 km, *NASA Tech. Memorandum* 100697.

Georgiadou, Y., and A. Kleusberg (1988), On carrier signal multipath effects in relative GPS positioning, *Manuscripta geodaetica, 13*, pp. 172-179, Springer-Verlag.

Glowacki, T. J., N. T. Penna, and W. P. Bourke (2006), Validation of GPS-based estimates of integrated water vapour for the Australian region and identification of diurnal variability, *Australian Meteorological Magazine, 55*(2), pp. 131-148.

Goad, C. C., and L. Goodman (1974), A modified Hopfield tropospheric refraction correction model, *presented paper in AGU Annual Fall Meeting*, San Francisco, CA.

Hannah, B. M. (2001), Modelling and simulation of GPS multipath propagation, Ph.D thesis, Cooperative Research Centre for Satellite Systems, Queensland Univ. of Technology, Australia.

Hansen, A., E. Peterson, T. Walter, and P. Enge (2000), Correlation structure of ionospheric estimation and correction for WAAS, *Proceeding of ION NTM2000*, pp. 454-463, Anaheim, CA.

Herring, T. A. (1992), Modelling atmospheric delays in the analysis of space geodetic data, *Symposium on Refraction of Transatmospheric Signals in Geodesy, Netherlands Geod. Commis. Ser., 36*, edited by J. C. DeMunk and T. A. Spoelstra, pp. 157-164, Netherlands Geodetic Commission, Publications on Geodesy, Delft, The Netherlands.

Hofmann-Wellenhof, B., H. Lichtenegger, and E. Wasle (2008), *GNSS-Global Navigation Satellite Systems-GPS, GLONASS, Galileo and more*, Springer, Wien, New York.

Hopfield, H. S. (1969), Two quartic tropospheric refractivity profile for correcting satellite data, *J. of Geophysical Research, 74*(18), pp. 4487-4499.

Hsieha, C. H., and J. Wu (2008), Multipath reduction on repetition in time series from the permanent GPS phase residuals, *The International Archives of the Photogrammetry, Remote Sensing and Spatial Information Sciences, 37*(B4), pp. 911-916.

Huang, J., and F. van Graas (2006), Comparison of tropospheric decorrelation errors in the presence of severe weather conditions in different areas and over different baseline lengths, *Proceedings of ION GNSS 2006*, pp. 2769-2787, Fort Worth, TX.

Hugentobler, U., P. Fridez, and S. Schaer (2005), *Bernese GPS Software Version 5.0*, Astronomical Institute, University Berne, Switzerland.

Jiang, P., S. R. Ye, Y. Y. Liu, J. J. Zhang, and P. F. Xia (2014), Near real-time water vapor tomography using ground-based GPS and meteorological data: long-term experiment in Hong Kong, *Annales Geophysicae, 32*, pp. 911-923, DOI:10.5194/angeo-32-911-2014.

Kalnay, E. (2003), *Atmospheric modeling, data assimilation and predictability*, Cambridge University Press, Cambridge, New York, Melbourne, Madrid, Cape Town, Singapore, So Paulo.

Kim, D., and R. B. Langley (2003), On ultrahigh-precision positioning and navigation, *J. of Institute of Navigation, 50*(2), pp. 103-116.

Kim, D., and R. B. Langley (2005), Nullification of differential ionospheric delay for long-baseline real-time kinematic applications, *Proceedings of ION 61st Annual Meeting*, pp. 949-960, Cambridge, MA.

Kim, D., and R. B. Langley (2007), Long-range single-baseline RTK for complementing network-based RTK, *Proceedings of ION GNSS 2007*, pp. 639-650, Fort Worth, TX.

Kim, D., and R. B. Langley (2008), Toward the Ultimate RTK: The Last Challenges in Long-Range Real-Time Kinematic Applications, *Proceedings of ION GNSS 2008*, pp. 385-396, Savannah, GA.

Kim, D., S. Bisnath, R. B. Langley, and P. Dare (2004), Performance of long-baseline real-time kinematic applications by improving tropospheric delay modeling, *Proceedings of ION GNSS 2004*, pp. 1414-1422, Long Beach, CA.

Klobuchar, J. A. (1996), *Global Positioning System: Theory and Applications*, American Institute of Astronautics and Aeronautics, pp. 485-515.

Kruse, L. P., B. Sierk, T. Springer, and M. Cocard (1999), GPS-meteology : Impact of predicted orbits on precipitable water estimates, *Geophysical Research Letters, 26*(14), pp. 2045-2048, DOI: 10.1029/1999GL900383.

Langley, R. B. (1997), GPS receiver system noise, *GPS World, 8*(6), pp. 40-45.

Lanyi, G. (1984), Tropospheric delay effects in radio interferometry, Telecommunications and Data Acquisition Progress, *Tech. rep. 42*(78), pp. 152-159, Jet Propulsion Laboratory, Pasadena, CA.

Lawrence, D., R. B. Langley, D. Kim, F. Chan, and B. Pervan (2006), Decorrelation of troposphere across short baseline, *Proceedings of IEEE/ION PLANS 2006*, pp. 94-102, San Diego, CA.

Leandro, R., R. B. Langley, and M. C. Santos (2006), UNB neutral atmosphere

models: development and performance, *Proceedings of ION NTM 2006*, pp. 18-20, Monterey, CA.

Leick, A. (2004), *GPS Satellite Surveying*, 3rd eds. John Wiley & Sons, New York.

Li, B., Y. Feng, Y. Shen, and C. Wang (2010), Geometry-specified troposphere decorrelation for subcentimeter real-time kinematic solutions over long baselines, *J. of Geophysical Research, 115*(B11), DOI: 10.1029/2010JB007549.

Manning, T., K. Zhang, W. Rohm, S. Choy, F. Hurter (2012), Detecting Severe Weather using GPS Tomography: An Australian Case Study, *J. of Global Positioning Systems, 11*(1), pp. 58-70, DOI: 10.5081/jgps.11.1.58.

Marini, J. W. (1972), Correction of satellite tracking data for arbitrary tropospheric profile, *Radio Science, 7*(2), pp. 223-231.

McAdam, M. (2013), Implementation and validation of a UNB Vienna mapping functions service, M.Sc.E thesis, Dept. of Geodesy and Geomatics Eng., Univ. of New Brunswick, Fredericton, NB, Canada.

Mendes, V. B., and R. B. Langley (1994), A Comprehensive analysis of mapping functions used in modeling tropospheric propagation delay in space geodetic data, *Proceedings of KIS94*, pp. 87-98, Banff, AB, Canada.

Mendes, V. B., and R. B. Langley (1995), Zenith wet tropospheric delay determination using prediction model: accuracy analysis, *Cartograpia Cadastro, 2*, pp. 41-47.

Mendes, V. B., G. Prates, M. C. Santos, and R. B. Langley (2000), An evaluation of models for the determination of the weighted mean temperature of the atmosphere, *Proceedings of ION NTM 2000*, pp. 433-438, Anaheim, CA.

Mendes, V. B., J. P. Collins, and R. B. Langley (1995), The effect of tropospheric propagation delay errors in airborne GPS precision positioning, *Proceedings of ION NTM GPS-95*, pp. 1681-1689, Palm Springs, CA.

Montenbruck, O., and E. Gill (2000), *Satellite Orbits: Models, Methods, and Appli-*

cations, Springer-Verlag, New York.

Musa, A., and S. O. Bashir (2013), Prediction of cross polarization discrimination at millimeter wave band due to dust storms, *ARPN J. of Engineering and Applied Sciences, 8*(7), pp. 465-472.

Niell, A. E. (1996), Global mapping functions for the atmosphere delay at radio wavelengths, *J. of Geophysical Research, 100*, pp. 3227-3246.

Nievinski, F., K. Cove, M. C. Santos, D. Wells, and R. Kingdon (2005), Range-extended GPS kinematic positioning using numerical weather prediction model, *Proceedings of ION AM 2005*, pp. 902?911, Cambridge, MA.

Oguchi, T. (1983), Electromagnetic wave propagation and scattering in rain and other hydrometeors, *Proceedings of the IEEE, 71*(9), pp. 1029-1078.

Raquet, J. F. (1998), Development of a method for kinematic GPS carrier-phase ambiguity resolution using multiple reference receivers, Ph.D thesis, Dept. of Geomatics Eng., Univ. of Calgary, Calgary, AB, Canada.

Rieckh, T., B. Scherllin-Pirscher, F. Ladstdter, and U. Foelsche (2014), Characteristics of tropopause parameters as observed with GPS radio occultation, *Atmospheric Measurement Techniques, 7*, pp. 3947-3958, DOI:10.5194/amt-7-3947-2014.

Rocken, C., T. V. Hove, and R. Ware (1997), Near real-time GPS sensing of atmospheric water vapor, *Geophysical Research Letters, 24*, pp. 3221-3224.

Rothacher, M., and G. Beutler (2002), Advanced aspects of satellite positioning, ENGO699.80, Dept. of Geomatics Eng., University of Calgary, Calgary, AB.

Saastamoinen, J. (1972), Atmospheric correction for the troposphere and stratosphere in radio ranging satellites, *The Use of Artificial Satellites for Geodesy, Geophysics Monograph Series, 15*(4), pp. 247-251, edited by S. W. Henriksen, A. Mancini, and B. H. Chovitz, Washington, DC.

Santerre, R. (1989), GPS satellite sky distribution; Impact on the propagation

of some important errors in precise relative positioning, Ph.D thesis, Dept. of Geodesy and Geomatics Eng., Univ. of New Brunswick, Fredericton, NB, Canada.

Santos, M. C., and K. M. Cove (2002), Carrier phase differential kinematic GPS data analysis, *Tech. rep. for Southern Mississippi and NAVOCEANO*, Fredericton, NB, Canada.

Santos, M. C., F. Nievinski, K. Cove, R. Kingdon, and D. Wells (2005), Range-extended post-processing kinematic (PPK) in a marine environment, *Proceedings of ION GNSS 2005*, Long Beach, CA.

Schaer, S. (1999), Mapping and predicting the Earth′s ionosphere using the Global Positioning System, Ph.D thesis, Astronomical Institute, University of Berne, Switzerland.

Schuler, T (2001), On ground-based GPS tropospheric delay estimation, Ph.D thesis, Institute of Geodesy and Navigation, Univ. FAF Munich, Munchen, Germany.

Seeber, G. (1993), *Satellite Geodesy*, Walter de Gruyter, Berlin, New York.

Serrano, L. (2013), Carrier-phase multipath mitigation In RTK-based GNSS dual-antenna systems, Ph.D thesis, Dept. of Geodesy and Geomatics Eng., Univ. of New Brunswick, Fredericton, NB, Canada.

Skone, S. (1998), Wide area ionospheric grid modelling in the auroral region, Ph.D thesis, Dept. of Geomatics Eng., Univ. of Calgary, Calgary, AB, Canada.

Skone, S. (2003), Atmospheric effect on satellite navigation, ENGO633, University of Calgary.

Tachikawa, Y., N. B. Nawarathna, and B. E. Vieux (2003), Hydrologic prediction using weather radar information and distributed hydrological modeling, *The XXIII General Assembly of the International Union of Geodesy and Geophysics*, Sapporo, Japan.

Taff, L. G. (1985), *Celestial Mechanics*, John Wiley & Sons, New York.

Teke, K. (2011), Sub-daily parameter estimation in VLBI data analysis, Ph.D thesis, Institute of Geodesy and Geophysics, Vienna Univ. of Technology, Vienna, Austria.

Teunissen, P. J. G (1993), Least-squares estimation of the integer GPS ambiguities, *IAG General Meeting*, Beijing, China.

Thayer, G. D. (1974), An improved equation for the radio refractive index of air, *Radio Science 9*(10), pp. 803-807, DOI: 10.1029/RS009i010p00803.

Titov, O., V. Tesmer, and J. Boehm (2004), OCCAM v6.0 software for VLBI data analysis, *International VLBI Service for Geodesy and Astrometry 2004 General Meeting Proceedings*, pp. 267-271.

van Diggelen, F.S.T (2009), *A-GPS : Assisted GPS, GNSS, and SBAS*, Artech House, Boston, MA.

Wells, D, N. Beck, D. Delikaraoglou, A. Kleusberg, E. J. Krakiwsky, G. Lachapelle, R. B. Langley, M. Nakiboglu, K. Schwarz, J. M. Tranquilla, P. Vaníček, and D. Wells (1987), *Guide to GPS positioning*, 2nd Eds., Canadian GPS Associates.

Witchayangkoon, B. (2000), Element of GPS precise point positioning, Ph.D thesis, Spatial Information Sci. and Eng., Univ. of Maine, Orono, Maine.

Wübbena, G. (1991), Zur modellierung von GPS beobachtungen für die hochgenaue positionsbestimmung, Wiss. Arb. Univ.

Zhang, Y., and C. Bartone (2006), Single-site carrier phase based troposphere integrity monitoring, *Proceedings of ION NTM 2006*, pp. 530-542, San Diego, CA.

Vita

.

Candidate′s Full Name: Yong-Won Ahn

University Teaching Experience (Univ. of New Brunswick):
- 2016: GGE2012 Advanced Surveying (inc. 3D Laser Scan), 4 ch (credit hours).
- 2015: GGE2013 Advanced Surveying Practicum (inc. 3D Laser Scan), 4 ch.
- 2015: GGE2012 Advanced Surveying (inc. 3D Laser Scan), 4 ch.
- 2012: GGE1001 Introduction to Geodesy and Geomatics, 5 ch.
- 2011: GGE2012 Advanced Surveying, 4 ch.
- 2010: GGE2012 Advanced Surveying, 4 ch.
- 2009: GGE2013 Advanced Surveying Practicum, 4 ch.
- 2009: GGE2012 Advanced Surveying, 4 ch.
- 2008: GGE2013 Advanced Surveying Practicum, 4 ch.
- 2008: GGE2012 Advanced Surveying, 4 ch.

University Attended (Degrees and Diploma Obtained):
- 2011: Diploma in University Teaching (DUT), Univ. of New Brunswick, Fredericton, NB, Canada.
- 2005: Master of Science in Engineering (M.Sc.E), Dept. of Geomatics Engineering, Univ. of Calgary, Calgary, AB, Canada.
- 1997: Master of Science (M.Sc), Dept. of Astronomy & Space Sciences, Chungbuk National Univ., South Korea.
- 1994: Hon. Bachelor of Science (B.Sc), Dept. of Astronomy & Space Sciences, Chungbuk National Univ., South Korea.

Publications (Journals and Proceedings):

· Dare, P, Y. W. Ahn, and A. Cunningham (2015), Experiences in the use of a Terrestrial Laser Scanner at UNB, *Ontario Professional Surveyor, 58*(2), pp. 4-6.

· Ahn, Y. W., D. Kim, J. Bond, and W. S. Choi (2011), Performance Test of the WAAS Tropospheric Delay Model for the Korean WA-DGNSS, *Korean Journal in Aerospace, 15*(4), pp. 523-535.

· Ahn, Y. W. (2009), Positioning Enhancement Based on a New Weighting Scheme to Solve an Ill-Conditioned Case, *Proceedings of ION GNSS 2009*, Savannah, GA,

USA. [*Student Competition Winner*]
· Ahn, Y. W., D. Kim, and P. Dare (2008), Estimation of Troposphere Decorrelation Using the Combined Zenith-dependent Parameter, *Proceedings of ION GNSS 2008*, Savannah, GA, USA.
· Ahn, Y. W., D. Kim, and P. Dare (2007), Positioning Impacts from Imbalanced Atmospheric GPS Network Errors, *Proceedings of ION GNSS 2007*, pp. 2302-2312, Fort Worth, TX, USA.
· Ahn, Y. W., D. Kim and P. Dare (2006), Local Tropospheric Anomaly Effects on GPS RTK Performance, *Proceedings of ION GNSS 2006*, pp.1925-1935, Fort Worth, TX, USA.
· Ahn, Y. W., D. Kim, P. Dare, and R. B. Langley (2005), Long Baseline GPS RTK performance in a Marine Environment using NWP Ray-Tracing Technique under Varying Tropospheric Conditions, *Proceedings of ION GNSS 2005*, pp. 2092-2103, Long Beach, CA, USA.
· Ahn, Y. W., G. Lachapelle, S. Skone, S. Gutman, and S. Sahm (2005), Analysis of GPS RTK performance using external NOAA tropospheric corrections integrated with a multiple reference station approach, *GPS Solution, 10*(3), pp. 171-186, Springer-Verlag, DOI 10.1007/s10291-005-0017-1.
· Alves P., Y. W. Ahn, J. Liu, G. Lachapelle, D. Wolfe, and A. Cleveland (2004), Improvements of USCG RTK Positioning Performance Using External NOAA Tropospheric Corrections Integrated with a Multiple Reference Station Approach, *Proceedings of NTM 2004*, pp. 689-698, San Diego, CA, USA.
· Alves P., Y. W. Ahn, and G. Lachapelle (2003), The Effects of Network Geometry on Network RTK Using Simulated GPS Data, *Proceedings of NTM 2003*, pp. 1417-1427, Portland, OR, USA.
· Cannon, M. E., G. Lachapelle, Y. W. Ahn, P. Alves, P. Lian, J. Liu, A. Morton, M. Petovello ,and J. Schleppe (2004), Improving the Existing USCG DGPS Service: Analysis of Potential System Upgrades and Their Effect on Accuracy, Reliability and Integrity, *Tech. rep.* prepared for U.S. Coast Guard, Portsmouth, VA, USA.
· Park, P. H., U. Chwae, Y. W. Ahn, and K. H. Choi (2001), Preliminary GPS results and a possible neotectonic interpretation for South Korea, *Earth Planets Space, 53*, pp. 937-941.
· Lim, H. C., P. H. Park, J. U. Park, J. H. Cho, and Y. W. Ahn (2001), Precise Orbit Determination of GPS Satellites for Real Time Application, *J. of Astronomy and Space Science of Korea, 18*(2), pp. 129-136.
· Park, P. H., U. Chwae, Y. W. Ahn, H. C. Lim, J. U. Park, and J. H. Cho (2001), A Preliminary GPS result on GPS-neotectonic interpretation for South Korea, *J. of Geological Society of Korea, 37*(3), pp. 455-464.
· Park, P. H., Y. W. Ahn, J. U. Park, J. H. Cho, and H. C. Lim (2000), Crustal Velocities around the Korean Peninsula estimated with GPS, *J. of Korean Geophysical Society, 3*(3), pp. 153-160.
· Ahn, Y. W., C. H. Kim, and P. H. Park (1997), Development of a Software System for Relative Positioning using GPS Phase Observables, *J. of Astronomy and Space Science of Korea, 14*(2), pp. 192-199.

· Several Hardware Simulation Reports and Publications (prohibited)

Publications (Thesis):

· Ahn, Y. W. (2005), Analysis of NGS CORS Network for GPS RTK Performance Using External NOAA Tropospheric Corrections Integrated with a Multiple Reference Station Approach, M.Sc.E thesis, UCGE Report Number 20211, Dept. of Geomatics Engineering, Univ. of Calgary, Calgary, AB, Canada.

· Ahn, Y. W. (1997), Development of a Software System for Relative Positioning using GPS Phase Observables, M.Sc thesis, Dept. of Astronomy and Space Science, Chungbuk National Univ., South Korea.

· Ahn, Y. W. (1994), Determination of Mean Orbital Elements of NOAA-11 due to the Earth′s gravitational potentials $J_2 \sim J_4$, B.Sc. Technical report, Dept. of Astronomy and Space Science, Chungbuk National Univ., South Korea.

Presentations (Oral):

· Dare, P., Y. W. Ahn, and M. Papaioannous (2016), Insights into ancient civilizations and structures through the use of modern technology, *paper presented at Conference of Geomatics Atlantic*, Fredericton, NB, Canada.

· Ahn, Y. W., and P. Dare (2016), De-correlation of Tropospheric Error and Height Component on GNSS using Combined Zenith-Dependent Parameter, *paper presented at Conference of Geomatics Atlantic*, Fredericton, NB, Canada.

· Ahn, Y. W. (2009), Positioning Enhancement Based on a New Weighting Scheme to Solve an Ill-Conditioned Case, *paper presented at Conference of ION GNSS 2009*, Savannah, GA, USA. [*Student competition winner′s presentation*]

· Ahn, Y. W., D. Kim and P. Dare (2008), Estimation of Troposphere Decorrelation Using the Combined Zenith-dependent Parameter, *paper presented at Conference of ION GNSS 2008*, Savannah, GA, USA.

· Ahn, Y. W., D. Kim, and P. Dare (2007), Positioning Impacts from Imbalanced Atmospheric GPS Network Errors, *paper presented at Conference of ION GNSS 2007*, Fort Worth, TX, USA.

· Ahn, Y. W., D. Kim, and P. Dare (2006), Local Tropospheric Anomaly Effects on GPS RTK Performance, *paper presented at Conference of ION GNSS 2006*, Fort Worth, TX, USA.

· Ahn, Y. W., D. Kim, P. Dare, and R. Langley (2005), Long Baseline GPS RTK performance in a Marine Environment using NWP Ray-Tracing Technique under Varying Tropospheric Conditions, *paper presented at Conference of ION GNSS 2005*, Long Beach, CA, USA.

Trained Skills Relevant to Research:

· SPIRENT^{TM} GNSS Hardware Simulator with SimGEN Software, SPIRENT Communication Ltd., Boston, MA, USA, in 2007.

· BERNESE GNSS Software, Astronomical Institute of the University of Berne (AIUB), Bern, Switzerland, in 2005.